Dissertation der Fakultät für Geowissenschaften
der Ludwigs-Maximilians-Universität München

HOLISTIC CORRELATION OF PHYSICAL AND MECHANICAL PROPERTIES OF SELECTED NATURAL STONES FOR ASSESSING DURABILITY AND WEATHERING IN THE NATURAL ENVIRONMENT

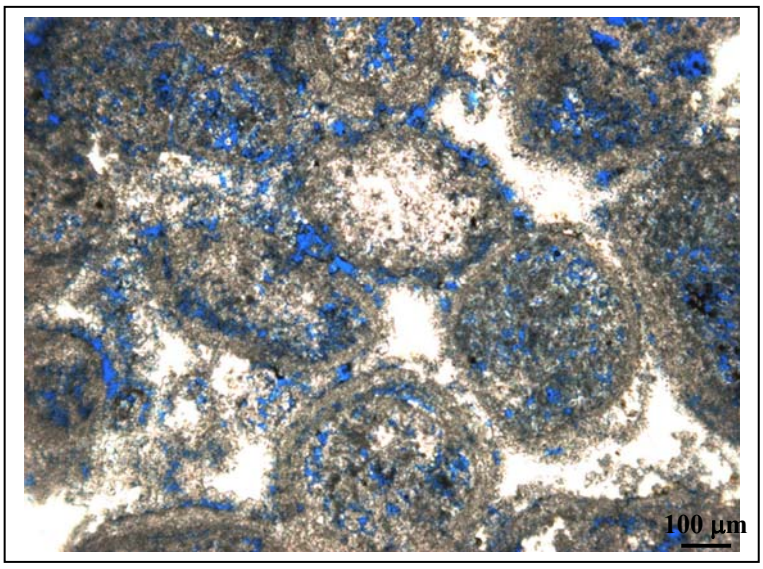

Von
Ann Bourgès

Dissertation eingereicht am 17.03.2006

1. Berichterstatter: Pr. Dr. Rolf Snethlage
2. Berichterstatter: Pr. Dr. Karl Thomas Fehr

Müdlichen Prüfung am 21.06.2006

Introduction

The main purpose of this study is to understand influences of bulk structure of materials on strength behavior as well as water storage and transfer in order to assess durability and weathering.

Therefore, a selection of different methods are applied and compared to optimize the understanding of material structure and physico-mechanical behavior. Optical microscopy (Digital Image Analysis) and scanning electron microscopy as well as water vapor permeability, biaxial flexural strength and ultrasonic velocity are measured on different natural materials: sandstones with clayey, silicious or calcareous binder, oolithic and micritic magnesian limestones and a thermally aged Proconnesian marble. Microstructurales and macrostructurales properties of these materials are studied before and after artificial weathering (freeze-thaw cycles).

First, and in order to validate the efficiency of the digital image analysis to characterize porosity and structure, traditional porosity measurements as water ad- and absorption and mercury porosimetry are crosschecked with the result obtained from digital image analysis. Limits of each methods are also defined. Then, validations of non-destructive and semi-destructive methods are also pursued to evaluate their potential value to replace and complement standardized methods.

By analysis of linear correlations, some essential mechanisms should be underlined, which may connect the macrostructure to the microstructure of the material. A systematic method of analysis should clearly appear and emphasize the role of the structure (grain size, grain contact and pore shape) on physical and mechanical behavior.

The main parameters leading to weathering should then be identified and models of correlations drawn. Correlations between the various physico-mechanical properties could ameliorate the possibilities to assess durability and weathering in the natural environment.

TABLE OF CONTENT

List of Figures

List of tables

List of abbreviations:

A: Surface area (m^2)
A_{om}:Total image area (μm^2)
B: Capillarity rise ($cm/\sqrt{t}$)
BFS: Biaxial flexural strength (N/mm^2)
d: Thickness (m)
DIA: Digital Image Analysis
DRMS: Drilling Resistance Measurement System
DR: Drilling Resistane (N)
DRc: Drilling Resistance corrected (N)
E-Dyn: Dynamic modulus of elasticity (kN/mm^2)
E-Stat: Static modulus of elasticity (kN/mm^2)
F: Load (N)
fo: Displacement (mm)
G: Area of single grain
g: Water flow rate calculated on the plateau (liquid water) during drying kinetics ($g/m^2.h$)
Gc: Grain contact %
GF: Grain area fraction (μm)
Gr: Grain
M: Sample mass (g)
MIP: Mercury Intrusion Porosimetry
N_t: Total porsity (%) or porosity accessible to water
N_{48}: Free porosity (%)
N_F; Porosity of cracks
N_P: Porosity of pores
N_{N2}: Pore radii below 0.1μm calculated from N^2 adsorption
Pc: Capillary pressure (Mpa)
p: Actual vapor pressure
p_o: Vapor pressure at saturation
P_{macro}: Area of single macro pore
p_{macro}: Area fraction of macro pores (μm)
PSD: Pore Size Distribution
Psf: Pore shape factor
Q: Water flow (cm^3/g)
QI: Quality index (%)
S: Saturation coefficient or Hirschwald coefficient
t_c: critical time during drying kinetics, breaking point 1, (h)
t_{eq}: equilibrium time during drying kinetics (h)
V_a: Volume adsorbed at relative vapor pressure p/p_0
V_m: Volume adsorbed forming a monolayer on unit mass of adsorbent
V_p: Velocity of compressive wave (km/s)
V_s: Velocity of shear wave (km/s)
V_p parall: Velocity of compressive wave (km/s) parallel to the stone bedding
V_p perpend: Velocity of compressive wave (km/s) perpendicular to the stone bedding
V_pS: Velocity of compressive wave on water saturated sample (km/s)
V_pD: Velocity of compressive wave on dry sample (km/s)
W: Water uptake coefficient ($kg/m^2/\sqrt{t}$)
β: Coefficient of water vapor conductivity from the surface to the air (h^{-1})
δ: Water vapor permeability (kg/m.s.Pa)
ε: Strain
ε hyd: Hydric dilatation (μm/m)
η: dynamic viscosity ($dynes/cm^2$)
θ: Contact angle (°)

μ: Water vapor diffusion resistance coefficient
ρ: Density (kg/m^3)
σ: Surface tension (N/m)
υ: Poisson coefficient

A. PRESENTATION OF THE STUDY

I. State of the Art

I.1. How to assess weathering

Niesel (1981; 1983) explained in detail that seeking a simple common denominator among the multiplicity of parameters is the most successful approach for holistically assessing behavior of porous material. The first step is to combine all data in order to find the corresponding parameters, which determine the weathering processes (Niesel, 1983).
Acid immersion tests and crystallization tests are the methods frequently used to assess durability of sandstones. These methods require large amounts of material and time (i.e. a few days or weeks). Finding the critical parameters of a stone is integral to finally assessing its durability and degree of weathering. To assess durability, Bell (1988) explained that a measurement of porosity does not serve as an adequate indicator of durability, as it does not provide information on the distribution of pores within the stone. For Bell the saturation coefficient, or Hirschwald coefficient, linked with pore size distribution are the main factors required to assess durability.
Goudie (1999) described experimental studies to assess the importance of modulus of elasticity and other factors in affecting and predicting rock resistance to salt weathering. In general, he observed that high modulus of elasticity is related to high density, low water absorption capacity and the tendency to have greater resistance, while rocks with low modulus of elasticity values, low density and high water absorption capacity tend to be susceptible to weathering. Nevertheless, he highlighted that these factors were not sufficient to explain or predict rock response to salt weathering and that other important factors, such as the pore characteristics, should be included.
Salt weathering is not taken into consideration in this study but can be linked to a certain extent to weathering by freeze-thaw; the approach and the determination of the criteria to assess weathering are of primary importance in this study. Thus, a wide range of rock types is needed to fully evaluate the nature of microscale changes and their influence on rock decay (Nicholson, 2001).

To assess weathering, a different approach can be developed; artificial weathering is an indisputable step. Looking for a simple common denominator from amongst the multiplicity of parameters is of primary concern. Physical as well as mechanical approaches can be carried out, but as the literature (Niesel, 1981;1983; Goudie, 1999) emphasizes, porosity measurements or modulus of elasticity values alone are not enough to assess durability of stone. Therefore, two main needs can be identified:

- To include in the study a wide range of lithotypes
- To determine the various properties common to the different lithotypes and useful to understanding and assessing their behavior when subjected to weathering.

I.2. The use of non-destructive methods

In this paragraph, correlation with dynamic modulus of elasticity will not be described entirely, as it was preferred to link it with mechanical properties and especially with the static modulus of elasticity. Nevertheless, dynamic modulus of elasticity should be considered as a non-destructive method.

Relation of ultrasonic velocity with physico-mechanical properties is only taken into consideration; the evaluation of the efficiency of consolidation treatments by ultrasonic methods is not considered.

I.2.1. Ultrasonic velocity

Since 1972, ultrasonic velocity measurements are applied to determine the quality of stones, especially limestone, in order to demonstrate its homogeneity or its degree of alteration (Mamillan, 1972). Mamillan (1975) applied ultrasonic velocity measurements to stone conservation and diagnostic state of alteration on marble sculptures introducing a new non-destructive methodology to stone conservation. Bouineau (1978) proved the relation between ultrasonic velocity, compressive strength, modulus of elasticity and apparent density of the material. All these regressions are exponential; no linear correlation can be established.
Krtolica and Crnkovié (1979) showed that some strong correlation between longitudinal wave velocity and physico-mechanical properties of carbonates exists. Correlations were especially demonstrated on carbonates samples artificially weathered by freeze-thaw cycles. Porosity decreases exponentially with velocity while compressive strength increases exponentially. Therefore, it was proven that properties of stones change after weathering and can be detected by measuring the longitudinal wave velocity, a non-destructive method.
The following equations (1 and 2) express the relation between the velocities of waves (compressive waves p and shear waves s) and the dynamic modulus of elasticity E-Dyn; υ is the Poisson ratio and ρ represents the density.

$$V_p = \sqrt{\frac{E\text{-}Dyn\,(1-\upsilon)}{\rho(1+\upsilon)(1-2\upsilon)}} \qquad (1)$$

$$V_S = \sqrt{\frac{E\text{-}Dyn}{2\rho(1+\upsilon)}} \qquad (2)$$

Modulus of elasticity, compressive strength and density were the properties that Tassios and Mamillan (1985) developed in relation with ultrasonic velocities in a book on non-destructive testing in order to assess mechanical properties of building materials. In 1989, Guerrero underlined the use of the ultrasonic technique to estimate physico-mechanical properties without the need to measure them. Thus, these authors showed again an increase of the ultrasonic velocities with the apparent density and compressive strength, and a decrease with a raise of the porosity and water absorption in carbonate stones. It seems that these four properties are the main properties to be correlated with ultrasonic velocity.

Generally speaking, ultrasounds are useful to determine the alteration degree of stone, as they decrease with increase in the number of weathering cycles; enhancement of porosity is also assumed; the ultrasonic velocity on a weathered material can be compared to the velocity obtained on unweathered material and also determine structural changes (Accardo et al., 1981; Calleja et al., 1989; Simon, 2001). Such changes in velocity according to the degree of weathering led, in particular, to alteration classification of marble. Galan et al. (1991) and Köhler (1991) related the ultrasonic velocity and the state of degradation of marble (Table 1).

V_p (km/s) after Köhler (1991)	Description	Classification categories
> 4.5	Fresh marble	0
3 - 4.5	Increasing porosity	1
2 - 3	Progressive granular disintegration	2
1 - 2	Danger of breakdown	3
< 1	Complete structural destruction	4

Table 1. Damage classification of marble proposed after Köhler (1991).

Evolution of physical properties during weathering can therefore be correlated with ultrasonic velocity. The increase of large pores during artificial weathering on Carrara marble enhanced the water absorption and is correlated with ultrasonic velocity (Accardo et al., 1981). A good correlation between ultrasonic velocity and water uptake coefficient was also found on weathered marble in the study by Simon (1996).
Nevertheless, ultrasonic velocity cannot be related to pore size before or after alteration (Accardo et al., 1981; Chiesura, 1985). Furthermore, no correlation could be found between grain size and ultrasonic velocity in sandstones (Queisser et al., 1985).

More recently, authors reported an increase of ultrasonic velocity with decreasing total porosity. Sayed et al. (1999) described the exponential relation for stones

Predicting physico-mechanical properties through non-destructive means is still an important concern in stone conservation. Some correlations exist between water uptake or compressive strength, but they are specific to one material, most of the time carbonate rocks; rare is the application to sandstones. Ultrasonic measurement can be used indirectly to define textural properties and, therefore, physico-mechanical properties.

I.2.2. The drilling resistance (DRMS)

Drilling resistance can be qualified as a quasi non-destructive method, which determines drilling resistance profiles in the laboratory as in the field. The drilling resistance gives direct information on the strength of the material and is mainly used to measure the efficiency, depth and durability of consolidation treatments (Leroux et al, 2000; Tiano et al, 2000). Decay profiles, performance of consolidation treatments are established uses of the instrument (Delgado Rodrigues et al 2002).
In term of correlation very few relations between drilling resistance and others mechanical properties are available in the literature. Leonhardt & Kiessl (1990) showed some good relation with flexural strength and Young's modulus. Alfes (1992) showed the correlation between penetration hardness and compressive strength on sandstones. Tiano et al (2000) confirmed the relation of drilling resistance with uniaxial compressive strength (CS), and gave the equation 3:

$$CS\ (Mpa) = 0.1862DRc\ (N) + 25.863 \text{ with } R^2 = 0.82. \quad (3)$$

The correlation will also depend on the type of drill bit: hard steel, widia or polycrystalline diamond; the equation given is for a diamond drill bit.

Studies on correlation between drill resistance and mechanical properties are very poor. The need to link this method to standardized measurements, mechanical properties and textural properties is evident.

I.3. Methods to evaluate porosity: Quantification by Digital Image Analysis (DIA) and relationship with physical-mechanical properties -

Several studies correlated pore size distribution determined from digital image analysis to physico-mechanical properties.

By means of stereological parameters, Christensen and Gudmundsson (1983) described the pore system of sandstone through digital image analysis. The purpose was to describe the pore system with quick measurements and relate it to the storage and transport of moisture. Using automated image analysis software, the perimeter of pores and the mean distance between pores were determined on unweathered and weathered sandstones, proving that weathering leads to an increase of pore volume.

A stereological approach led Chan (1987) to consider grain size distribution in concrete as spherical particles and recreate the sphere size distribution. The author also dealt with the determination of mean spacing between the nearest neighboring air voids in concrete and correlated it with the frost resistance of concrete.

Using digital image analysis Ehrlich et al., (1991) derived five pore types from 16µm to 160µm as a mean diameter in the Cutbank Sandstone. Each pore type is represented by a characteristic shape defined in thin section.
The authors demonstrated the correlation between the defined pores types and the permeability of the Cutbank Sandstone where the smaller pore types (1 and 2 from 16 to 19µm) revealed the lowest permeability while larger pore types (3 to 5 from 50 µm to 160µm) were associated with large throats and increased permeability.
The authors again identified a strong correlation between permeability and pore type in sandstones, showing this relationship as a function of burial depth (Ehrlich et al., 1997).

Fitzner and Basten (1992) cross-linked different methods, such as Mercury Intrusion Porosimetry (MIP), Digital Image Analysis (DIA) and nitrogen sorption in order to characterize pore size distribution. DIA illustrated pores > 4µm and seems to show similar results to MIP in this pore range. The method was therefore proven useful in characterization of large pore sizes.

Meng (1993) characterized the pore size distribution of sandstones by overlapping the results from adsorption isotherms, MIP and DIA. She defined ranges of fractal radii for each method and redefined them as pore size parameters. The author proved the influence of these ranges on the kind of water transport mechanism as the hygric dilatation (pores < 0.1 µm).

Porosity evaluation from Image analysis (DIA), mercury porosimetry (MIP) and water absorption were compared for ceramic bodies (Andreola et al, 2000). The three methods examined gave qualitatively similar results, but some results can be discussed. Image analysis does not distinguish between closed and open pores, while mercury porosimetry resolves open porosity. Therefore, results from mercury porosimetry are necessarily fewer than values obtained from DIA.

Generally speaking, quantified microscopic analysis on thin sections was developed to characterize the composition and state of preservation of building materials.
Indeed, Larbi and van Hees (2000) used an analytical method based on ASTM standard C856-95 involving a point counting system to distinguish binder content from aggregates and pore voids in historic mortars (with the aim to determine binder: aggregates ratios). The authors point out the fact that pores and grain size distribution can be measured without disturbing the structure by chemical methods. Moreover, image analyze improves the knowledge on the composition and state of preservation of the mortar and is in this way helpful to select compatible repair materials.

New software can facilitate the image analysis (DIA) on thin and cross-sections and speed up traditional microscopic methods like point counting. Goins and Reedy (2000) used Image–Pro Plus to characterize grain shape, measure layer thickness and the length of microcracks. The authors applied the system to describe weathered surfaces of volcanic tuff as well as the structure of low-and high-fired ceramics.

Müller and Hansen (2001) performed DIA with the same software Image-Pro plus. Their main purpose was to determine the binder/aggregate ratio in historical mortars and to evaluate pore and grain size distribution. They combined optical microscopy images with images taken with the Environmental Scanning Electron Microscope in order to consider the micropores with a minimum diameter of 0.1μm.
Finally, a recent study (Cultrone et al, 2004) demonstrated that DIA disclosed the evolution of size, shape and connectivity of macropores ($r > 1\mu m$) of brick bodies and that MIP results underestimate the macropore content. However MIP gives a good estimation of the open porosity and of the distribution of pores with $r < 1\ \mu m$.

In summary a systematic, comparison between the different methods used to evaluate porosity and pore size distribution has not yet been carried out in a systematic way for porous material. It has been shown that certain pore ranges are correlated to physical properties in terms of water transport. DIA may give useful results in terms of pore size distribution, and textural properties, such as size and shape of grain. The main problem in this method might be the non-distinction between closed and open pores, DIA taking into consideration the entire pore area visible on the image.

I.4. Physical properties

The main factor influencing physical properties in term of water transport is surely the pore structure. But in fact, this pore structure is strictly dependent on grain size if the theory of packing of grains is taken into consideration (Scheidegger, 1960) (Figure 1). Furthermore, the concept of "largest diameter" of a grain makes sense geometrically. "Stable" packing is represented by one sphere touching at least four neighbours in the same and in adjacent layers such that twelve contact-points are formed (Figure 2). For natural porous materials, grains are rarely spherical, but it is obvious that mean and maximal grain size as well as grain contact are of main importance to determine packing and pore structure (Scheidegger, 1960).

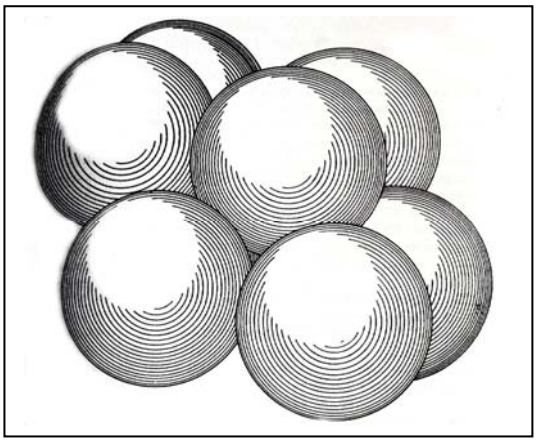

Figure 1. Rhombohedral packing of spheres (after Scheidegger, 1960).

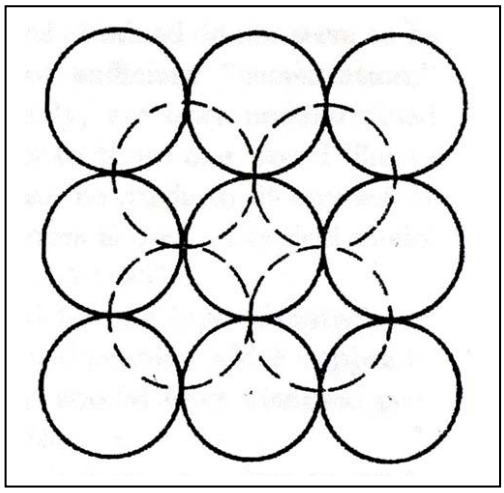

Figure 2. Face-centred cubic packing of spheres.

Niesel (1983) describes the saturation coefficient of sandstones and limestones by the water uptake coefficient and the porosity less than < 5µm variables, which influence both physical properties. The author points out that for many characteristics related to pore structure, sandstones and limestones should be plotted separately. It is interesting to see that most of the time it is difficult to associate different lithotypes on the same linear correlation. Moreover, regression factors are rarely greater than $r^2 = 0.89$.
Apparent density plays an important substitute role for several capillarity parameters. In addition, the water uptake coefficient is related to apparent density following an exponential function; suction dynamics must be considered as directly dependent to material density (Hoffmann et al., 1990).

Valdeon et al. (1992) produced a very interesting study on hydric properties of porous material and their link with petrophysical properties. Close correlation could be determined between hydric properties of dolomite, limestone and sandstones and their textural features. According to the authors, absorption, evaporation and capillarity processes are influenced by open porosity, but even more by the pore throat size. Also, larger pores may lead to accelerate hydric processes, and trapped porosity may slow down water circulation. The configuration of the pore system seems to condition the hydric properties.

Important studies by Hoffmann et al, (1996) on pressed bricks expressed the importance of specific pore volume and porosity (<5μm) in physical properties. Through multiple regression and step-wise regression, the authors determined several relations of these porosity properties with the water uptake coefficient, the water vapor diffusion resistance and the saturation coefficient.
For the water vapor diffusion resistance (μ), it appears that the specific pore volume, up to 75μm, and pore size distribution determined by MIP were the primary indicators, rather than the total porosity.
Finally, the saturation coefficient equation could not determine the influence of pore size distribution. As ice crystals are mainly formed in the coarsest pores, this parameter could not be taken into consideration.

These same authors showed the correlation between evaporation and capillarity behaviors of dry-pressed bricks. The authors mentioned that the open porosity directly influences both measurements. Addition of a fine pore portion participates in moisture filling and evacuating of the material during the second phase of evaporation.

Water vapor permeability may be linked to grain length (Brown, 1993) and according to Shepherd and Brice (1985) permeability is directly correlated to grain size where the higher the grain size the higher the permeability. The same authors pointed out the influence of the shape of the grains in the packing and its effect on permeability and porosity. As already mentioned, spherical grains tend to have a higher porosity and permeability than disc-shaped grains. Once again the contact between these grains is likely one way to evaluate the grain packing.

In general, permeability is linked to open pathways in the rock sample: open pore throats as connections between pores; open cracks; and networks of open pores and cracks (Dürrast, 1999)

Concerning hydric dilatation, swelling of natural stones results from “capillary pressures” set up in the pore system and in cracks of small dimension. This swelling is strongly influenced by the pore size distribution (Felix, 1983). Swelling of clay minerals is an contributing factor of the total swelling of the stone, but no direct relation could be found between the presence of clay minerals and the total swelling. The study of Felix (1983) showed that often swelling is completed after two hours, but some stone (molasse sandstone) may undergo swelling over months. The swelling is dependent on the quantity of water absorbed. The calculation of the softening coefficient (ratio between ultimate compressive strength in wet and dry states) provides valuable measurement of internal cohesion. Stones showing high internal cohesion will show lower volumetric expansion. Influence of pore range < 0.1μm on hydric swelling was often emphasized (Meng, 1993; Alfes, 1994).
Movement and displacement within the structure and changes in the distances between grains are part of decay processes and indicative of an increase in weakness of the intergranular bonds. Snethlage and Wendler (1997) described such a process, explaining the deterioration of stones as expanding spaces in the grain structures where salt can precipitate and ice crystals can also form.

In summary, water transport is influenced by pore structure. The pore structure should integrate grain size, grain shape, and spatial organization of the grain as well as pore network connectivity (open porosity) and pore size distribution. The pore structure is very complex and contains many variables. The hypothesis that textural properties (grain size, grain contact, pore shape) control the pore structure and, therefore, the physical properties requires serious consideration. Through the literature review, it is obvious that some links between structure, porosity and water transport and storage need be studied in more detail.

I.5. Mechanical properties

After Niesel (1983) the two main factors governing weathering of stone are the pore size distribution and the mechanical strength. The understanding of the relationship between these two properties may help to predict the future behavior of stone.

I.5.1. Strength and porosity

In 1734, Rondelet reported in his "Traité de l'art de bâtir" the first instruments used to measure compressive strength of stone. He also improved these instruments and performed more than eight hundred strength measurements on a hundred and fifty different stones. He observed that density, strength and structure in terms of grain compaction, were linked. Moreover, for each type of stone, samples with higher density have greater strength, as well as the finer grains and a more compact structure. Stones with the highest strength show homogeneous grains and structure.

Judd and Huber (1962) crossed various types of stone (siltstone, limestone, granite, sandstone) with a large panel of methods in order to predict physical and mechanical properties of rocks. By the use of multiple regressions, they showed the relation of the compressive strength with impact toughness, scleroscope hardness and modulus of rigidity, all in the same equation. The authors did not prove the relationship between compressive strength and porosity.

Kossev (1970) and Smorodinov et al. (1970) studied separately the relationship between porosity and compressive strength on carbonate rocks (limestone and dolomite), quartzitic rocks (quartzites and quartzites-sandstones) and magmatic rocks. The higher the porosity the lower the strength and both relations are exponential with a correlation factor of around 0.8. Smorodinov et al defined equations for the relation between strength and the porosity of the limestone.
The authors considered the relation of limestone to its strength porosity independently of that of the quartzites, where the relationship is in fact different.

Specific surface area (BET) was also defined as an unusual parameter of porous media related to their volume (Niesel, 1983). Compressive strength decreased as a function of the increase of the specific surface area.

Pore size also seems to have a significant influence on strength, as demonstrated by Alfes (1991). Indeed, sandstones with low porosity demonstrate a higher dependence between mean pore size and strength than higher porous sandstone. Moreover, the mean grain size of sandstones appeared important in the consideration of strength. As porosity decreases, the relation between strength and grain size becomes more important.

Hoffmann et al. (1996) underlined that the compressive strength on dry pressed bricks decreases with an increasing portion of fine pores. Using statistical calculation the authors showed the dependency of the compressive strength with porosity characteristics as porosity < 5µm, specific pore volume and open porosity in a multiple regression.

The decrease in compressive strength with increasing porosity was also illustrated on limestone of the Nile Valley, Egypt, in an exponential regression (Sayed et al., 1999).
The same authors demonstrated the positive relation between strength and apparent density, i.e. an increase in the compressive strength shows an increasing apparent density.

These literature references highlight the influence of grain size, their spatial association and pore size distribution as the principal factors of mechanical properties.

I.5.2. Compressive strength – static and dynamic modulus of elasticity

The correlation between static and dynamic modulus of elasticity has long been a source of great interest in order to predict static modulus of elasticity by non-destructive and field methods. Modulus of elasticity obtained by measurement of sonic wave propagation velocities in laboratory or field tests of rock are usually not comparable to the modulus of elasticity obtained by static load test. There is a clear dependency of elastic properties upon the method of testing. The engineering field is generally interested in reducing the number of tests necessary to evaluate rock reaction under a load. Therefore, if specific correlation factors are established, the results of a relatively simple and economical measurement could be used to extrapolate values and assess modulus of elasticity or others properties (Kaplan, 1959). A wealth of literature exists on the studies of both moduli and their relation to strength.

In 1936, Ide remarked that in a few cases the dynamic modulus was four to twenty percent higher than the static modulus. The author concludes that the cause of observed difference between both methods is due to the presence of cracks and cavities in the rock. Indeed when cracks and pores are present, the closing of such cavities increases the response of the rock to statically applied stresses. Only part of the force is effective in compressing the solid material of the rock. For this reason statically measured values of elasticity are low, and the compressibility of the rock is high.

Judd and Huber (1962) studied the relation of static to dynamic modulus of elasticity through multiple regressions. Indeed, using statistical methods they show that equations can be used to predict rock properties within a relatively narrow range. The authors emphasized that prediction of rock properties cannot only be based on existing and conventional theories of elasticity.

By convention, static modulus of elasticity is measured at one third of the stress-strain curve. It may be possible that other positions on the stress-strain curve could yield better agreement with dynamic modulus of elasticity values.

Then King (1970) confirmed also that the static modulus of elasticity for rocks is generally lower than the dynamic. He also assumed that the reason for that difference is due to the presence of microcracks or microfractures, which affects the strain of the rock during a static measurement more than the propagation of ultrasonics waves during a dynamic measurement. Without microcracks the static modulus approaches the dynamic value.

For the same author (King, 1983), the correlation between compressive strength and dynamic modulus of elasticity is not as good as the relation with the static modulus. In King's opinion, the low correlation factor of only 0.33 between strength and dynamic modulus might be due to the sensitivity of the compressive strength to the orientation and pervasiveness of the microcracks existing in the rocks.

He confirms his hypothesis, showing a relatively good linear regression between static and dynamic moduli with $R^2 = 0.82$ and noticing that with microfracturing rocks specimens tend to fall below the linear regression. He observed also a better relation between the compressive strength and the static modulus of elasticity than with the dynamic modulus, and links this behavior to micro-fracturing existing in the rock.

For Eissa and Kasi (1988) the relation between the two moduli of elasticity is rather low. They underlined a better estimation of the static Young's modulus from the empirical relation between the logarithm of static Young's modulus and the logarithm of the product of the dynamic Young's modulus and density with a coefficient of correlation of 0.96. The study was pointed out on the correlation coefficient and the difference between both moduli was not further investigated.

Guéguen and Palciauskas (1992) explained that static modulus of elasticity is lower than the dynamic modulus because of cracks in the rock, which can be easily closed in compression. For the authors, the porosity is linked to a shape factor, low porosity equals small shape (cracks) while high porosity equals large shape (spherical pores). The first case applies to crystalline rocks, the second to sedimentary. Therefore, they highlight the importance of the porosity geometry and its influence on the modulus of elasticity.

Cylindrical pores cannot be deformed under compression while the cracks closed in compression reduce the static modulus.
Alfes (1992) shows also that moduli of elasticity were dependent on the porosity (a high porosity might correspond to a low modulus).

Christaras et al (1994) compared static and dynamic modulus of elasticity of different rocks, such as limestone, gypsum, basalt and granite. The author observed that the dynamic modulus of elasticity is usually greater than the static, and explained that the response of the sample to the very short duration of strain and low stress is essentially purely elastic.

In any case, good correlation between both methods might allow for determination of the static modulus of elasticity through measurement of the dynamic modulus with non-destructive means. They proposed the equation 4:
E-Stat = -3.16 + 1.05E-Dyn with r = 0.99 (4)

Nevertheless, their mutual variability has led to diverse hypotheses that still need clarification.

Considering the literature, the pore shape seems to be a major issue in the relation between both static and dynamic moduli of elasticity, as well as the relation between strength and moduli. Therefore, determining and characterizing first the pore shape of cracks or pores for each stone studied is a logical and necessary step, which may lead to better understanding of mechanical properties.

I.6. Frost damage on porous material

Understanding the action of frost in porous material has been the motivation for many studies for centuries. Indeed, Brard in 1828 was one of the first to propose an explanation of the frost mechanism (Dethury, 1828). He demonstrated that the expansion strength of ice is the cause of damage. Brard based his theory on fundamental experiment consisting of filling vases of different shapes with water: one with a large opening, the other with a narrow opening. After freezing, he observed that the vase with a large entrance did not show any damage while the one with the narrow entrance broke off. He explained that in the former the ice could extend outward through the opening of the vase without exerting pressure in other directions, while in the latter the ice could not expand through the opening and necessarily exerted great pressure on the vase walls, causing it to break. Brard came to the same conclusions through experiments on fine sand and coarse sand saturated with water and frozen. The surface of the fine sand was deformed, while the surface of coarse sand remained flat (Dethury, 1828). For Brard, ice requires a certain volume to expand; if this volume is too small the material of the container can fail under the pressure exerted by formation of ice. The same mechanisms take place in porous material. Finally, he proposed to study the behavior of stone subjected to salt crystallization in order to assess its susceptibility to frost damage.

Hirschwald (1908) explained similar mechanisms of frost damage in porous material. Indeed, water density is 1g/cm^3 while ice density is 0.9 g/cm^3, thus liquid water that freezes presents a volume expansion of 10%. Hirschwald assumed then that damage might occur if 90% of the porosity of the stone is filled by water. At this point, he conducted many enlightening experiments revealing fundamental mechanisms of damage caused by freezing.
The first experiments consisted of filling to 80% volume of glass vials and capillary tubes of different shapes with water and freezing them (Figure 3). Vials a, b, c, and capillaries e and g were kept open, d and f were closed. The dashed line indicates the level of liquid water. After freezing, vials a, b, c, d, and capillaries e and f, showed a water expansion but no damage of the container. Capillary g, which was connected to a larger volume, was the only one to show cracks of the glass in the lower bulb.
The second experiment of Hirschwald was to completely fill different glass vials with water (Figure 3). After freezing, he states the ice expanded beyond the vial openings in a mushroom form. He concludes that water begins to freeze at the surface.

In general, Hirschwald concludes that if larger pores are inter-connected and reach the surface, ice can be extruded and form on the surface. Also, if capillaries connect larger pores, at full saturation of the pores, ice will exert pressure on the pore walls. Finally, if pores are filled to less than 90%, no pressure will be exerted.

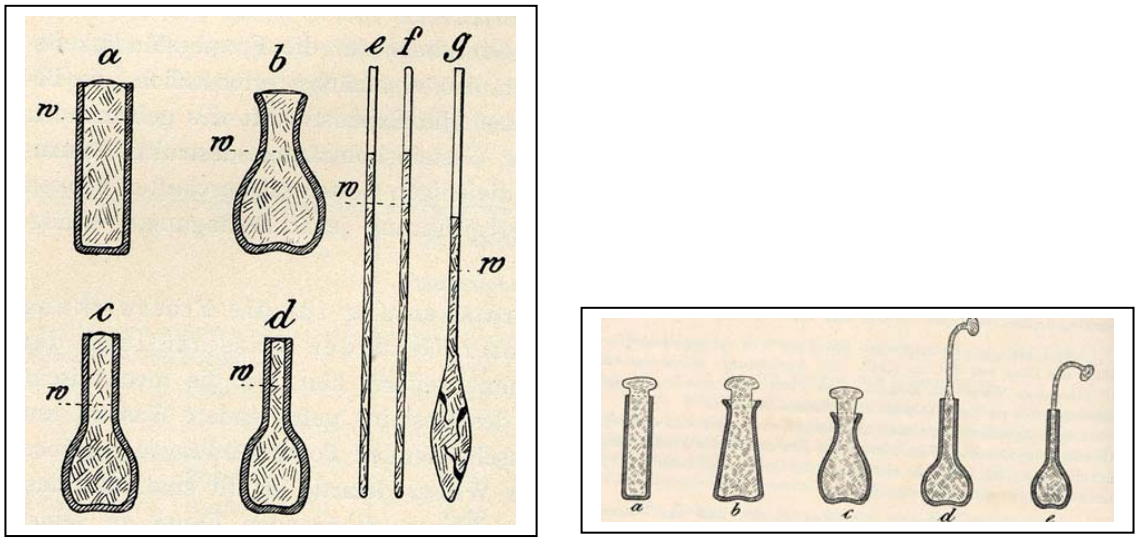

Figure 3. Hirschwald experiements on frost damage – left picture describes the influence of pores connected to capillaries; right picture shows ice extruded through the opening and formed at the surface.

The next approach of Hirschwald was to find a way to estimate the susceptibility of porous material to frost damage. Thus, he measured two kind of porosity: first the free porosity, the water absorption under atmospheric pressure, and then the accessible porosity, the water absorption under vacuum or pressure (Figure 4). He noticed that stronger damage occurs when the stone is fully filled by water. From these experiments, Hirschwald deducted the saturation coefficient (S or Hirschwald coefficient), the quotient of free porosity on the accessible porosity. He determined finally that if this coefficient is higher than 0.8, meaning that the water can fill more than 80% of the stone porosity, the stone is susceptible to frost damage.

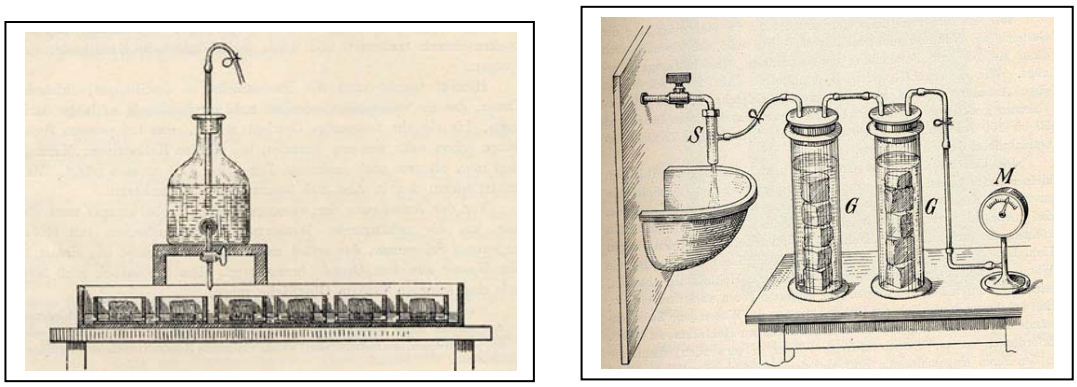

Figure 4. Measurements of the free porosity on the left picture, and of the accessible porosity on the right picture.

Everett (1961) discussed the problem of frost damage from an equilibrium thermodynamics perspective and showed that frost damage is not necessarily connected with expansion, which occurs when water freezes. Fitzner and Snethlage (1982) also developed a description of frost damage through thermodynamics. It has been demonstrated that frost damage is associated with the existence of small pores connected to coarser pores. For thermodynamic reasons the pressure applied on the pore walls is proportional to their size, and mechanical failure may occur if this pressure exceeds the strength of the porous material. The equation 5 shows that the pressure *p* is greater the more the pore sizes of the material are different:

$$p = 2\sigma\,(1/r - 1/R) \qquad (5)$$

where σ is surface tension; r is radius of the small pores; and R is radius of coarse pores. Therefore, liquid water in the smaller pores serves as a substantial reservoir for the growth of the ice crystals in the coarse pores. If the coarse pores are filled with crystals, ice can rupture them and destroy the material.

Since the publication of this work, pore size distribution has been an important factor to consider in order to understand and prevent frost damage in porous material. Through experimental measurements of stones, Everett (1961) showed that poor stones (i.e. those susceptible to frost) are characterized by the presence by a large quantity of pores in the range 0.1-0.5µm. Some interesting studies discuss the pore range, which may lead to greater damage. D'Have and Motteu (1968) came up with the definition of a critical diameter for frost resistance, representing more than 10% of the total porosity of the stone. From bricks analysis, they conclude that if this critical diameter is larger than 3µm, the stone is frost resistant, if inferior to 2µm the stone is not resistant to frost. Evaporation being more important in large pores, it should also play a great role when the critical diameter is higher than 3µm. In general, stone decay is associated with high crystallization pressure due to ice or salt crystallization in a structure where a substantial percentage of small pores (0.005 to 0.5 mm) is present with pores of larger size (Fitzner and Snethlage, 1982; Rossi-Manaresi and Tucci, 1990). This type of structure leads to stone decay. Therefore, pore structure is the main characteristic to assess weathering.
In any case, freeze-thaw cycles cause the displacement of grains relative to each other and contribute to the disaggregation of the grain structure. In the case of partial saturation, freezing may cause a contraction of the pore structure. As ice formation begins in the coarse pores due to thermodynamic reasons, and liquid water is drawn from the fine pores, these pores are emptied and subjected to capillary forces. It causes the contraction of the whole grain structure (Everett, 1961). Thomachot and Jeannette (2002) demonstrated the decrease of fine pores (<2µm) and the increase of large pores by mercury porosimetry; he emphasized the use of mercury porosimetry to identify changes in the pore structure. Freeze-thaw cycles cause the largest dispersion of pore access and accentuate heterogeneity of the porous network. Such changes may lead to a decrease in capillarity within the material.

D'Have and Motteu (1968) showed the use of modulus of elasticity measurements to record the process of decay during freeze-thaw cycles; the modulus of elasticity decreases with the number of cycles, but the relation is not linear.

Aubry and Lautridou (1974) have drawn some correlation between the susceptibility to frost damage and the physico-mechanical properties. Through the study of chalk and limestones, they showed that some slight distinction between the stones could be established; lower total porosity led to higher compressive strength and a better resistance to frost damage. Straight correlations were not established and pore size distribution was not taken into consideration. As has been noted previously, the movement of the grain structure may provide open space where ice crystals may form (Snethlage and Wendler, 1997); hydric dilatation may have an influence on deterioration due to freeze-thaw cycles.
The decrease of uniaxial compressive strength during freeze-thaw cycles seems to be associated to ultrasonic velocity drop off (Topal, 2000).
A variety of pore modifications operate due to weathering, which may be a precursor to more substantial macrodeterioration (Nicholson, 2001). These modifications can be classified as follows:

- Microcraking: propagation of new cracks that may be initiated by internal fluid pressure induced by freeze-thaw.
- Pore enlargement: loose debris contained in pores, probably generated by the break-up of grain contacts (Fitzner, 1988). This debris can be redistributed within the pore structure and therefore improve the pore connectivity without changing the total pore volume. Pore enlargement can also occur through compression of pore walls due to internal growth of ice crystals.
- Dissolution: affects especially limestone and calcitic sandstone.
- Pore compression: collapse or compression of pores may occur, as explained earlier.

Analyses of pore modifications due to weathering indicate that a variety of mechanisms could be responsible for modification of pore structure in limestones (Nicholson, 2001). For Nicholson, the introduction of new voids through pore coalescence and microcraking proceed to substantial rock damage.

The role of the pore size distribution in the resistance or susceptibility of stone to frost damage has been clearly emphasized. Nevertheless, structural changes resulting from freeze-thaw cycles still need further study.
A direct correlation between physico-mechanical properties and their changes due to freeze-thaw cycles may provide an evaluative tool to predict weathering.

In summary:

The literature review shows that textural properties of porous material may be linked to physical and mechanical properties. Indeed, grain size, grain packing, grain contact may control pore shape and pore size and, therefore, determine the physical properties related to water transport and storage. Pore shape seems to be of primary importance in the relationship between dynamic and static moduli of elasticity and strength. Therefore, it appears that textural properties may represent the decisive parameters controlling physico-mechanical properties and weathering behavior. It may be assumed that textural properties are the common denominator between all stone behavior and lithotypes.

Consequently, textural properties represent the first group of variables to be taken into consideration in this study, which will be progressively compared to physical and mechanical properties before and after artificial weathering.

II. Materials and Methods

It appears important in the study to select material that can be measured by all applied methods. In this purpose the choice goes naturally to sandstone and limestone where porosity and physical-mechanical data can be found in the literature and can be as well part of the measurement program representing sufficient diversity in structure and mineralogy.

II.1. Materials of the study

II.1.1. The sandstones, three different binders

All three binders differ in porosity and structure; set of pictures on fresh sandstones and in thin section blue dyed is provided below (the blue dye represents the porosity):

*Sander sandstone (*Figure 5*)*: 78% of aggregates, 8% of a clayey binder and 14% of visible pores (Grimm, 1990). A more detailed composition reveals 54% quartz, 32% stone fragments, 7% plagioclase, 3% alkali-feldspar, 2% muscovite and 2% of divers minerals (Tourmaline, Rutile, Apatite) The is a mosaic of six pictures and shows the structure of Sander sandstone. Sander shows some angular grains homogenously displayed. Through DIA measurements the mean grain diameter can be evaluated around 166 μm. Some floating grains can be observed, as well as some concavo-convex contact and long contact between the grains (e.g.Figure 18). The grain contact has been evaluated around 35%.

Wüstenzeller sandstone (Figure 6): 80% of aggregates, 9% of a siliceous binder and 11% of visible pores (Grimm, 1990). The mineral composition is 69% quartz, 20% stone fragments, 4% muscovite, 2% opal, 3% feldspar and 2% of divers minerals (Chlorite, Calcite, Tourmaline, Rutile). In comparison to Sander the grains are larger with a mean grain size of around 175 μm. The contact between the grains is more a long contact type and may present sometimes some suturated grains. Therefore, the contact between the grains is much higher with 80% of contact.

Regensburger (Green)sandstone (Figure 7) is a calcareous sandstone with 42% aggregates, 47% binder and 11% of visible pores. It contains 45% quartz, 15 to 20% glauconite, 11% of stones fragments, 5% of fossils, 3% of alkali-feldspar and 3% of divers minerals (Chlorite, Zircon, Rutile). Calcitic cement is formed almost exclusively by crystallized calcite, which support the structure. Regensburg reveals grain size close to Sander sandstone with a mean grain size around 150 μm. Grain contact type is more concave-convex or long contact type and floating grains are not observed. The grain contact is slightly higher than Sander with around 45 %.

For all of the sandstones the pore network seems to be composed by spherical pores linked to each other by thinner and longer pores. Wüstenzeller shows long pores with a form of cracks along the grains. The porosity shape might be evaluated by DIA through the aspect ratio measurement.

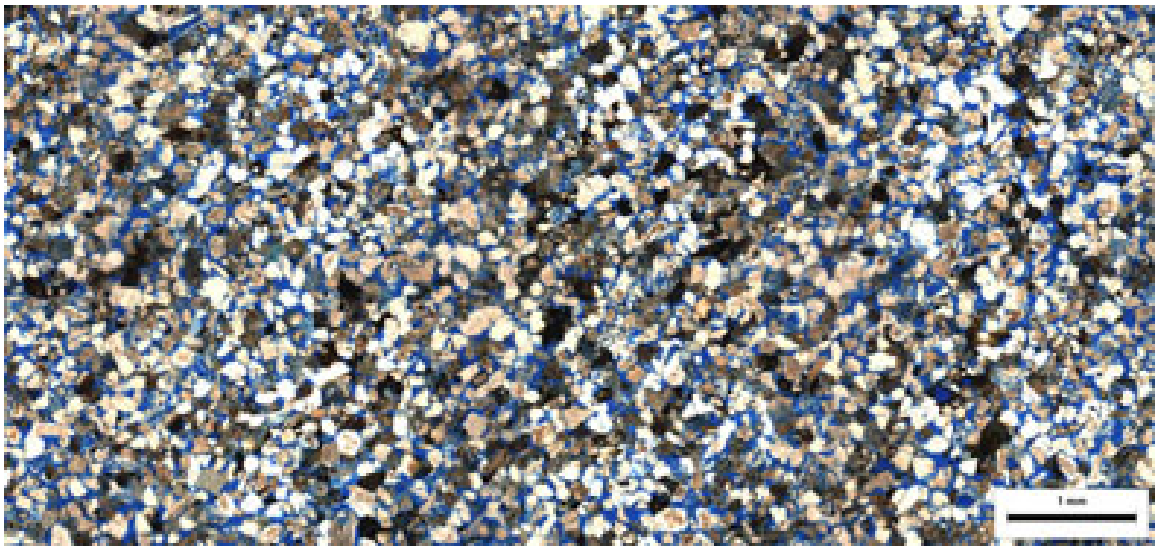

Figure 5. Sander sandstone - mosaic of 6 pictures on optical microscope x 40

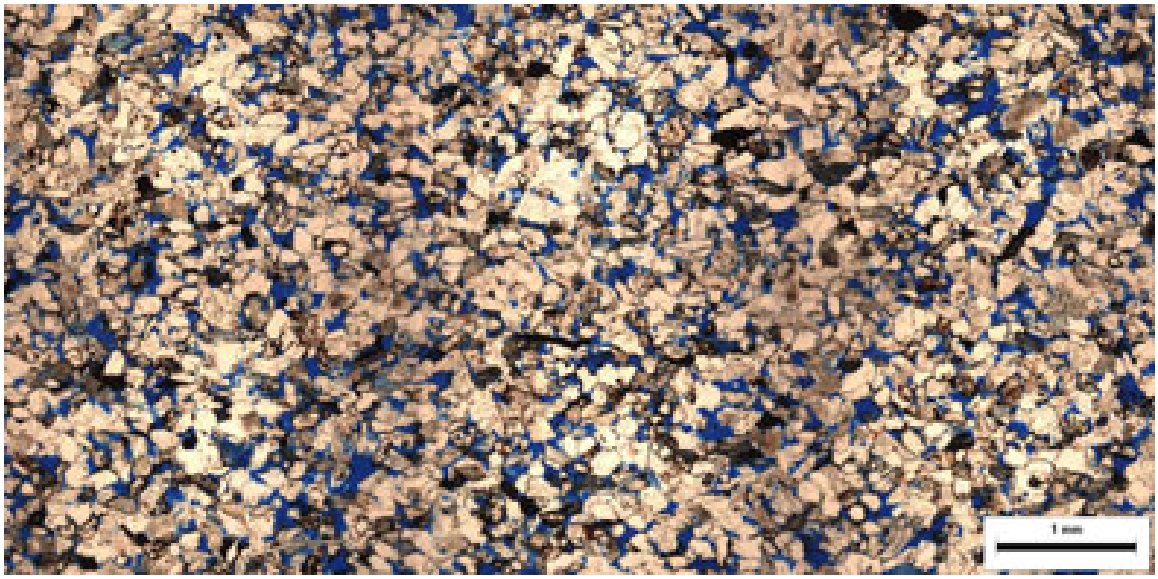

Figure 6. Wüstenzeller sandstone - mosaic of 6 pictures on optical microscope x 40

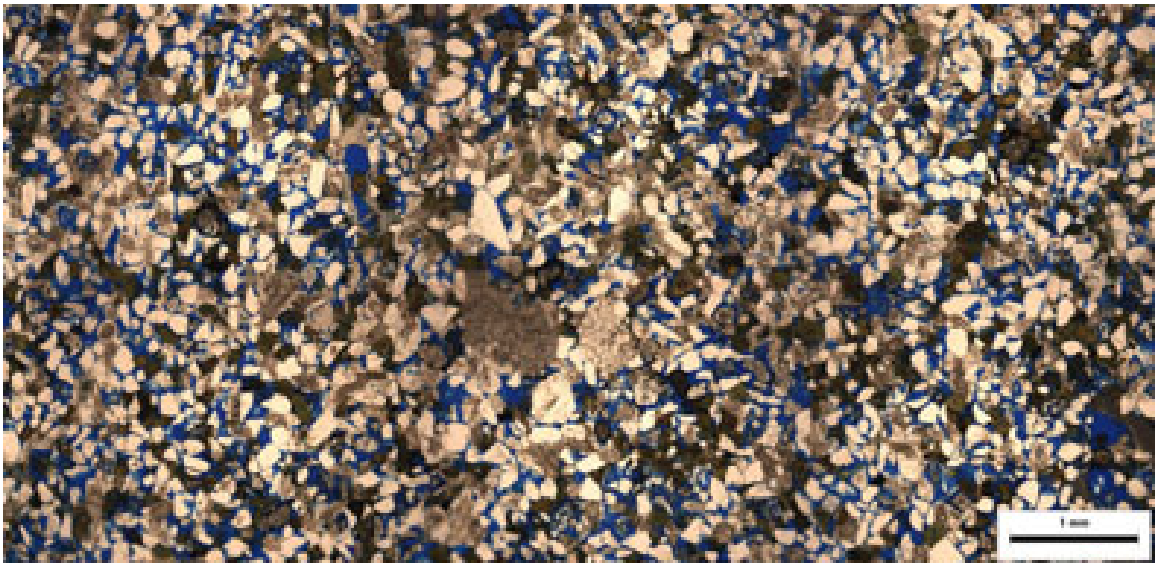

Figure 7. Regensburg sandstone - mosaic of 6 pictures on optical microscope x 40

II.1.2. Classification of sandstones

Textural Nomenclature of Mixed Sediments: Descriptive classification of sandstones is based fundamentally on framework mineralogy, although the relative abundance of matrix plays a role in some classifications.

Unconsolidated siliciclastic sediment is called gravel (dominance of > 2 mm-size grains), sand (600 μm – 2 mm), or mud (<600 μm) depending upon grain size. The lithified rock equivalent of these sediments are conglomerate, sandstone, and shale (mudrock). It might be difficult to decide whether a sedimentary rock composed of nearly equal portion of sand-size and mud-size particles should be called a sandstone or a shale. Various classification schemes have been devised for naming texturally mixed sediments and sedimentary rocks, most of which make use of triangular texture diagrams such as those shown in Figure 8:

The textural classification illustrated in Figure 8A includes particles ranging in size from mud (clay and fine silts) to gravel. Ideally, it might be expected the boundary between gravel and mud-sand to be set at 50 percent; however, this is not always done, as Figure 8A shows. Because particles of gravel size are commonly less abundant than sand and mud particles, geologists consider a sediment with as little as 30 percent gravel-size fragments to be a gravel. If sediments contain only particles of sand size and smaller, a textural classification scheme such as Figure 8B or Figure 8C that uses sand, silt, and clay as end members of the classification is more appropriate. Once the textural nomenclature of siliciclastic sediment or sedimentary rocks has been established, further classification within each textural group can be made on the basis of composition.

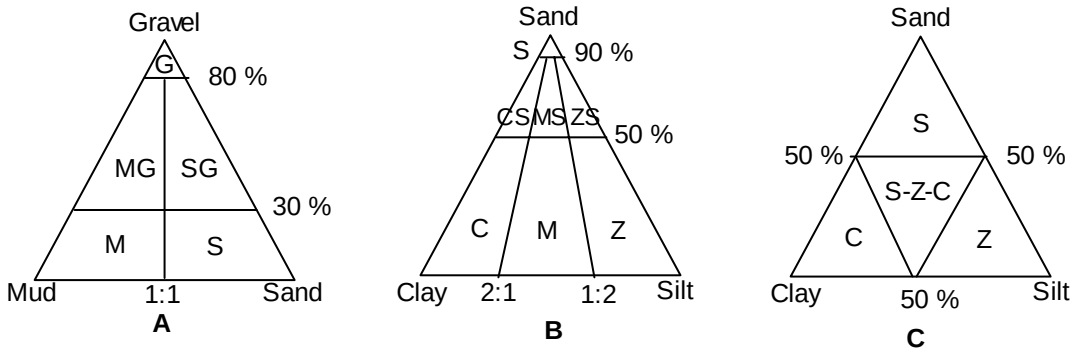

Figure 8. Nomenclature of mixed sediments. A, B. Simplified from Folk (1954).

Mineralogical Classification: Most sandstones are made up of mixtures of a very small number of dominant framework components. Quartz, feldspars, and rock fragments, such as volcanic clasts are the only framework constituents that are commonly abundant enough to be important in sandstone classification. Most of the classifications use triangular diagrams on which quartz (Q), feldspars (F), and rock fragments (R or L) are displayed as end members at the poles of the classification triangle.

One of the simplest and easiest classifications to use is that of Williams et al (1982), shown in Figure 9, which is based on an earlier classification by Dott (1964). In this classification, sandstones that are effectively free of matrix (< 5 percent) are classified as quartz arenites, feldspathic arenites, or lithics arenites depending upon the relative abundance of QFL constituents. If matrix can be recognized (at least 5 percent), the terms of quartz wacke, feldspathic wake, and lithic wake are used instead.

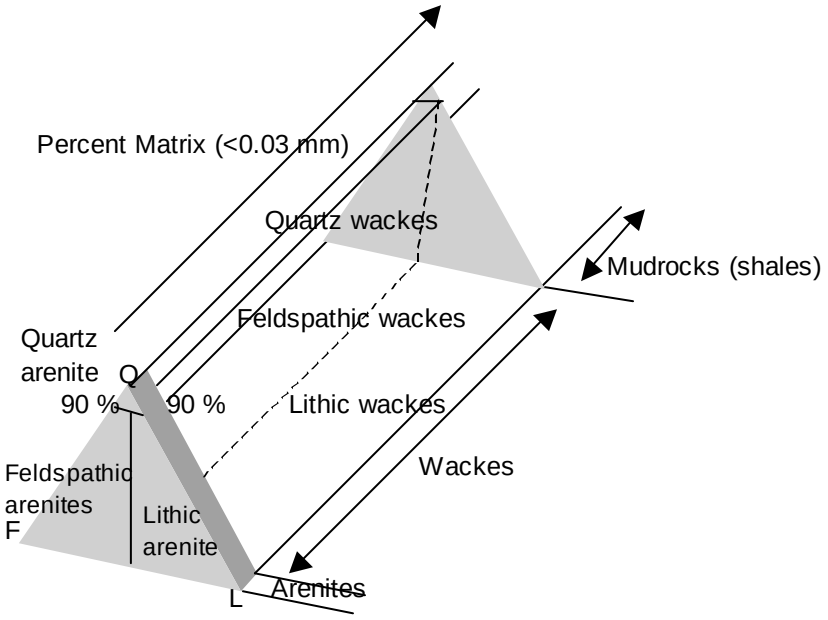

Figure 9. Classification of sandstones on the basis of three mineral components: Q = Quartz, quartzite fragements; F = Feldspars; L = lithic grains (rocks fragments). Points within the triangles represent relative proportions of Q, F, and L end members. A vector extending towards the rear of the diagram represents percentage of argillaceous matrix. The term arenite is restricted to sandstones containing less than about 5 percent matrix; sandstones containing more matrix are wackes, after Williams et al.

II.1.3. The magnesian limestones, three different quarries

The magnesian limestones show a narrow outcrop formation through England of the Permian age (250 million years) (Figure 13). Set of pictures on fresh magnesian limestones and in thin section blue dyed is provided below (the blue dye represents the porosity).

Highmoor quarry: classified as dolo-microsparite. Highmoor is a white magnesian limestone consisting of fine dolomite crystals in micritic cement; some can show rhombic form in thin section. Patches of dark iron oxide can be observed in thin section (Figure 10). Obviously Highmoor presents some spherical pores and the structure is very homogeneous. Due to its micritic structure, the mean grain size is difficult to evaluate as well as the contacts between the grains.

Cadeby quarry: classified as dolo-oomicrite. Cadeby is a light cream-colored stone. The dominant structure visible in thin section is oolithic. Patches of iron oxide are quite common (Figure 11). Ooliths of Cadeby stone are large and elongated around 850 µm diameter, juxtaposed and cemented by a thin calcitic binder along the ooliths.

Hazel Lane quarry: classified as dolo-oomicrite. Hazel Lane is a light cream-colored stone similar to Cadeby stone with an oolithic dominant structure (Figure 12). Ooliths of Hazel Lane are more spherical, around the same size as Cadeby 850 µm, and not juxtaposed as Cadeby. The ooliths are more dispersed in a calcitic matrix. Important calcitic cement joins the ooliths to each other.

Figure 10. Highmoor magnesian limestone - mosaic of 6 pictures on optical microscope x 40

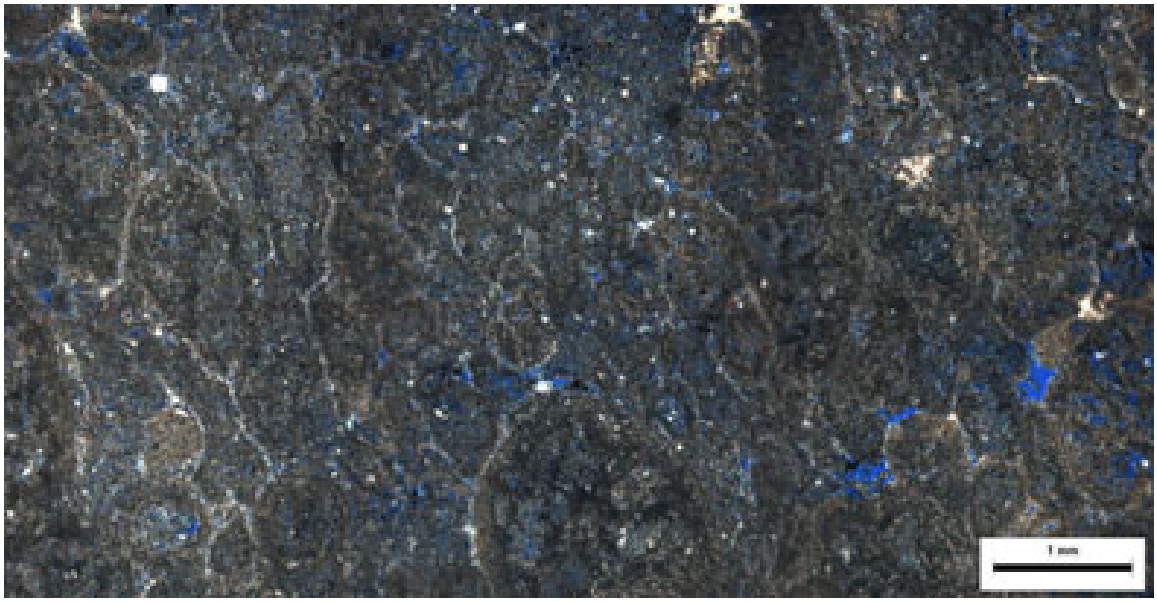

Figure 11. Cadeby magnesian limestone - mosaic of 6 pictures on optical microscope x 40

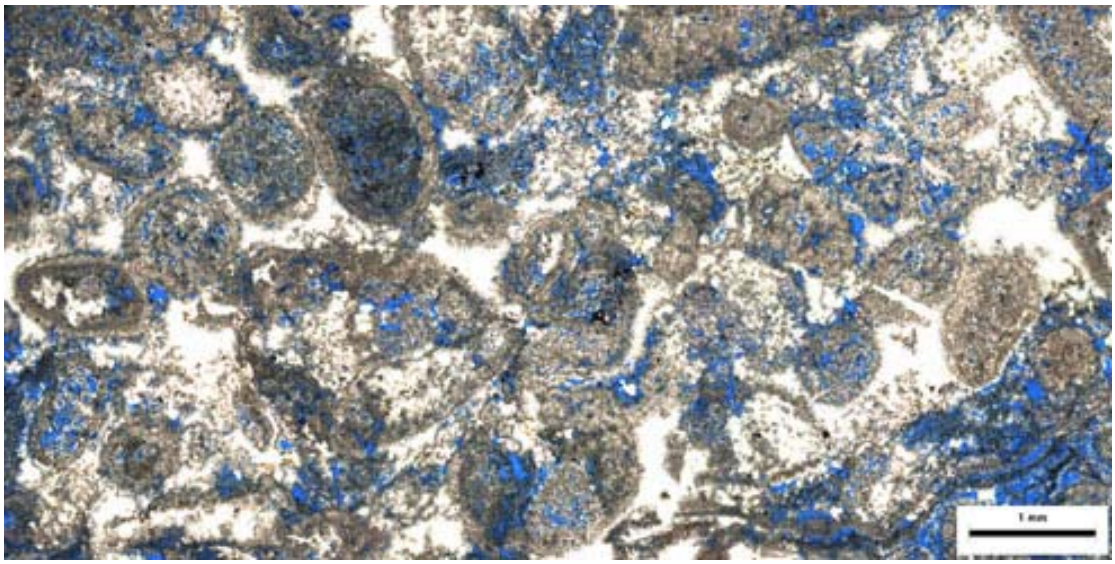

Figure 12. Hazel Lane magnesian limestone - mosaic of 6 pictures on optical microscope x 40

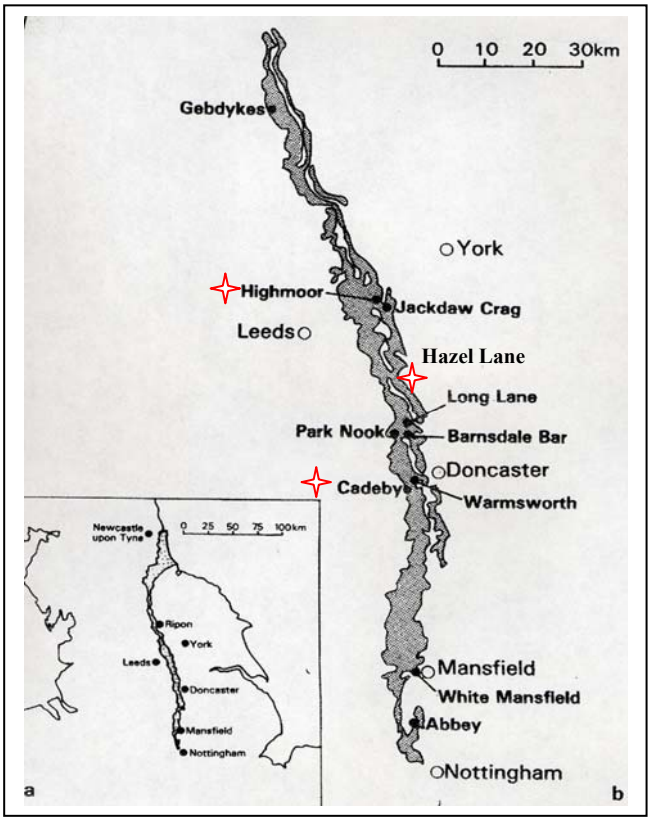

Figure 13: Map showing the narrow outcrop of magnesian limestone in England (Hart D., 1988).

✧ Indicate the quarries

II.1.4. Carbonate classification

The carbonates rocks make up 10 to 15 % of sedimentary rocks. They largely consist of two types of rocks:

- Limestones which are composed mostly of calcite ($CaCO_3$) or high Mg Calcite [(Ca,Mg)CO3]
- Dolostones which are composed mostly of dolomite [$CaMg(CO_3)_2$]

Because carbonates minerals in general are soluble in slightly acidic waters, they often have high porosity and permeability, making them ideal reservoirs for petroleum.
Dolostones tend to weather to a brownish color rock, whereas limestones tend to weather to a white or gray colored rock. The brown color of dolostones is due to the fact that Fe occurs in small amounts replacing some of the Mg in dolomite.

Two classification schemes are in common use by those who work on carbonate rocks: the Folk and Dunham classifications.

The Folk classification divides carbonates into two groups (Figure 14); Allochemical rocks are those that contain grains brought in from elsewhere. Orthochemical rocks are those in which the carbonates crystallized in place. Allochemical rocks have grains that may consist of fossiliferous material, ooids, peloids, or intraclasts. These are embedded in a matrix consisting of microcrystalline carbonate (calcite or dolomite), called micrite, or larger visible crystals of carbonates, called sparite. Sparite is clear granular carbonate that has formed through recrystallization of micrite, or by crystallization within previously existing void spaces during diagenesis.

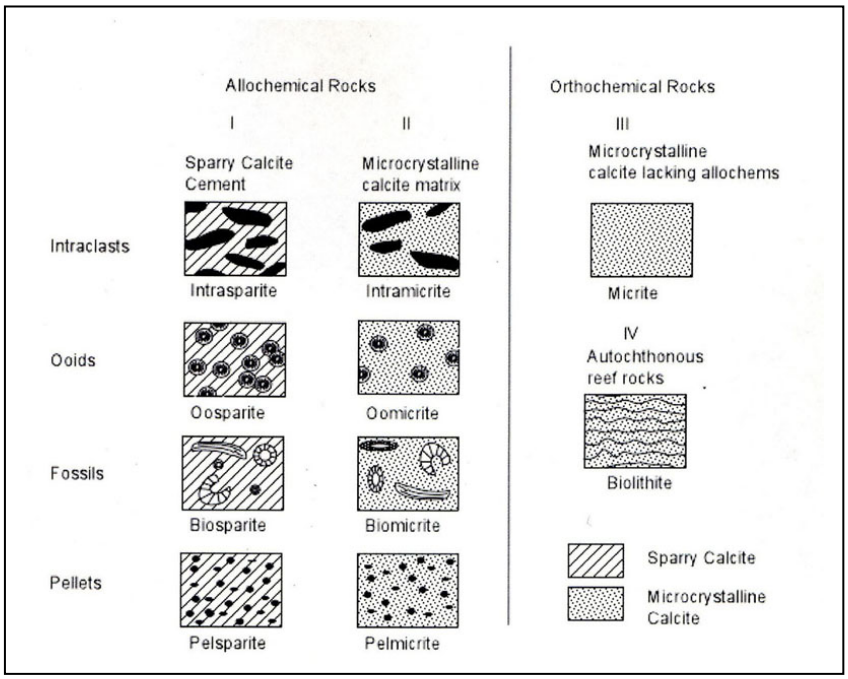

Figure 14. Folk classification of carbonates.

The Dunham classification is based on the concept of grain support (Figure 14). The classification divides carbonates rocks into two broad groups, those whose original components were not bound together during deposition and those whose original components formed in place and consist of intergrowths of skeletal material. The latter group is called boundstones (similar to biolithite of the Folk classification). The former group is further subdivided as to whether or not the grains are mud-supported or grain supported. If the rock consists of less than 10% grains it is called a mudstone. If it is mud supported with greater than 10% grains it is called a wackstone. If the rock is grain supported two varieties of limestone exist:

- packstone, if the grains have shapes that allow for small amounts of mud to occur in the interstices
- grainstone if there is no mud between the grains.

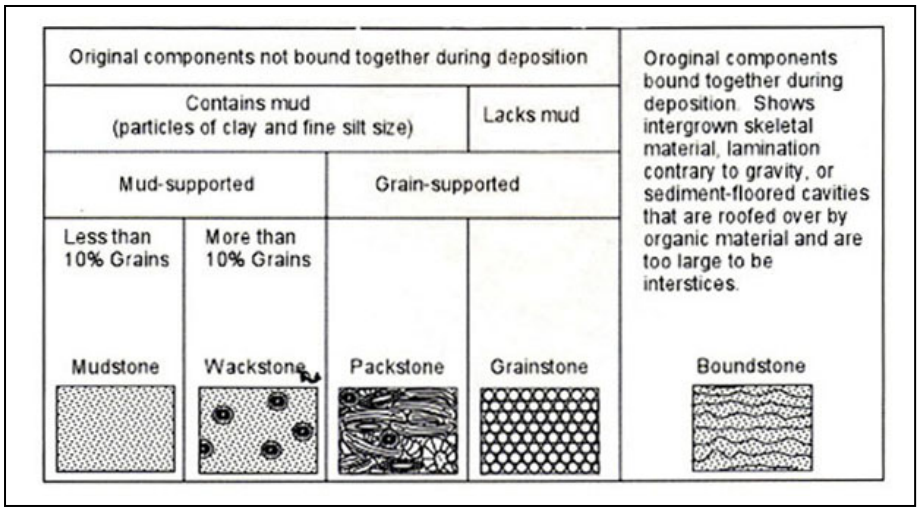

Figure 15. Dunham classification of carbonates.

The grains that occur in carbonate rocks are called allochemical particles or allochems. They are grains often precipitated by organisms that formed elsewhere and became included in the carbonate sediment. Because calcite and aragonite, the main biochemical precipitates, are soft and soluble in water, the distance of transport is usually not very far. Unlike clastic sediments, the degree of rounding and sorting of the grains may not be reflecting the energy of the transporting medium, but may be biologically determined. Grains found in carbonate rocks are as follows:

- Whole or broken skeletons of organisms (fossils). These may range in size from gravel to fine sand, depending on the organism and the degree to which the grains are broken during transport.
- Ooids. These are spherical sand sized particles that have a concentric or radial internal structure. The central part of each particle consists of a grain of quartz or other carbonate particle surrounded by thin concentric layers of chemically precipitated calcite. The layers or coatings are formed in agitated waters as the grain rolls around.

- Peloids. These are spherical aggregates of microcrystalline calcite of coarse silt to fine sand size. Most appear to be fecal pellets from burrowing benthic organisms. As these organisms burrow through the muddy carbonate-rich sediment, they ingest material in search of nutritional organic compounds resulting in waste products containing microcrystalline calcite. The peloids are much easier seen in thin section than in hand specimen because of their small size.
- Limeclasts. These are fragments of earlier formed limestone or partially lithified carbonate sediment. Most are intraclasts, originating within the basin of deposition.

  They may be pieces of partially cemented carbonate mud that were ripped from the seafloor by storms. Some appear to be fragments of partially cemented carbonate mud that originated in intertidal mudflats. Some may also be pieces of limestone carried into the basin from nearby carbonate outcrops.

The matrix of carbonate rocks consists of either fine-grained carbonate mud, called micrite. Or coarser grained calcite crystal formed during diagenesis, called sparite.

The micrite results from recrystallization of carbonate mud during diagenesis or from direct precipitation of calcite, and causes lithification of the sediments. The micrite gives the hazy opaque appearance of most limestones as seen in hand specimen. If the rock consists entirely of fine-grained mud matrix, it implies deposition in a low energy environment just like in siliclastic mudstones. Some of the mud may start out as aragonite needles 5 to 10 mm in length produced by calcareous algae. But, again this becomes recrystallized to a microspar 5 to 15 mm in diameter during diagenesis.

Larger sparry calcite matrix results from diagenesis in the same way that calcite cement originates in sandstones.

II.1.5. Proconnesian marble

Properties on thermally aged Proconnesian marble were integrated in the work in order to cover different kind of pore system and pore shape in the study and identify the influence of the different hydric and mechanical properties. Purpose of the thermal ageing is to increase the porosity and therefore to emphasize its role on the different properties.

Coming from Turkey, it is qualified by Lazzarini (1975) as a large grained marble white or with gray veins. The angular grains of calcite are jointed to each other and present a mean grain size around 800 μm. The 95% contact between the grains allows only a porosity of cracks along the grains. The use of the term of “porosity of cracks” to describe the pore shape instead of “plate-shaped pore” is here voluntary; the term will be often used during the study.
Measurements on thermally aged marbles (artificial weathering) were carried out through previous studies in the laboratory. These measurements were carried out according to methods described subsequently (II.3).
Only properties on thermally aged Proconnesian marble was considered in the study and comparison between fresh and weathered material could not be taken into consideration.

Thermal ageing: Heating to 500 degree Celsius for one hour, then were cooling down in the open oven for 2 hours before being immersed into water.

A uniform temperature increase leads to the expansion of crystal grains, and therefore to compressive stresses. If the temperature is inhomogeneous, then shearing stresses may also arise (Lewin, 1989). High anisotropic thermal dilatation coefficient of calcite is a function of the temperature and induces stress incompatibilities and the grains lose progressively their cohesion, detaching of calcite crystals one from another without their breaking along cleavage planes occur; the final stage being a sugar-like disintegration of the marble (Siegesmund, 2000).

Intermediary, results of heat treatments lead to an increase of the intergranular porosity (Franzini 1984, Zeisig 2002). The name of "marmo cotto" is utilized to describe marble samples showing such degradation.

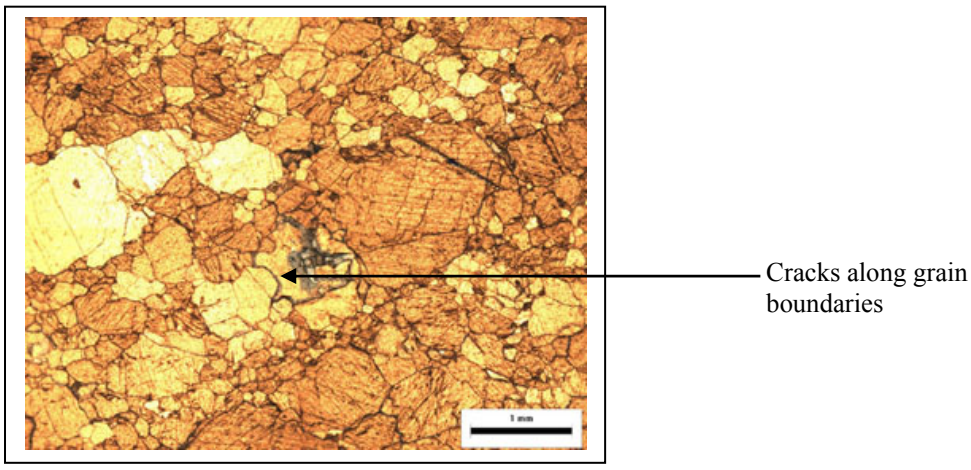

Figure 16. Aged proconnesian marble - mosaic of 4 pictures on optical microscope x 40

II.2. Porosity morphology of porous media

Porosity is probably the most important factor to material properties for many rocks, and there is hardly a physical property of rocks that is not influenced directly or indirectly by porosity. Different kind of porosity must be distinguished.

II.2.1. Intergranular porosity (primary)

Intergranular porosity represents the void space between the grains, particles or fragments of clastic material. It is formed during clastic sedimentation and depends on grain size, sorting of grains, grain sphericity and roundness as shown in Figure 17 (Gebrande, 1982). Intergranular porosity usually decreases during diagenesis due to physical and chemical actions. Different stages can be discerned:

- Packing, whereby the loosely sedimented particles slide into more stable positions under the pressure of increasing overburden, forming more grain-to-grain contacts.

- Compaction, deformation of grains under still increasing overburden pressure, whereby the point contacts between grains gradually change to flat contacts and finally to concave-convex or suturated contacts (Figure 18).
- Cementation, deposition of dissolved material on free grain surfaces, especially around contacts, therefore still reducing pore space and also blocking narrow channels.

II.2.2. Intraganular porosity (mostly secondary)

Intraganular porosity or intercrystalline porosity characterizes the porosity inside the grains. It can develop during changes in the mineralization by chemical dissolution and formation of new mineral species. Occasionally, it can develop into a form of microfissure porosity.

II.2.3. Porosity of cracks (secondary)

Cracks and fissures can develop during shrinking by remineralization, due to temperature changes or by anisotropic pressure release. Adsorption/desorption effects and capillary forces due to evaporation and condensation of liquids in the fissures might enhance effects of dilatation and contraction due to temperature changes.

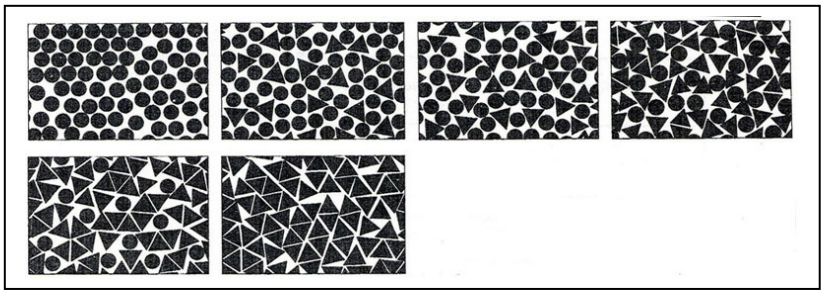

Figure 17. Decrease of tightness of packing for flat circular and triangular discs, depending on the matrix ratio (Gebrande, 1982).

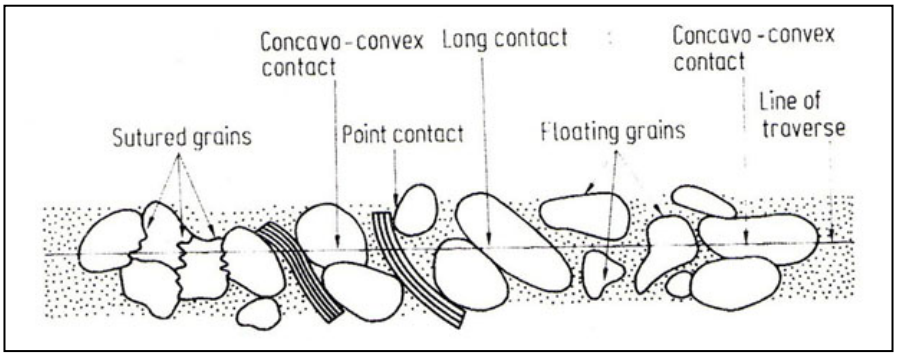

Figure 18. Illustration of grain contacts types (Gebrande, 1982).

To complete this porosity description, few other terms can be added. They are mainly related to connection of the pores to each other (Figure 19).

- Isolated pores are pores presenting no connection to each other; they can also be called closed pores.
- Inkbottle pores are pores linked to the pore network by thin and narrow capillaries. Usually liquid like water can only penetrate such pore under pressure or vacuum.
- Dead end pores are connected to the pore network by only one side, the other one staying close to the network.

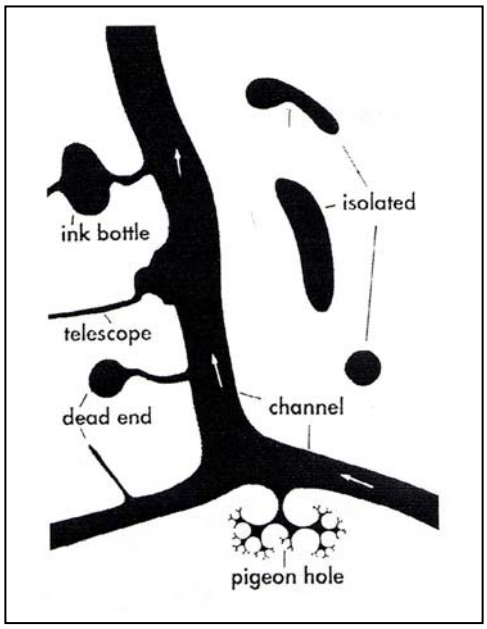

Figure 19. Representation of pore types (after Fitzner B., 1994).

II.3. Investigation Methods

II.3.1. Determination of the porosity

Porosity accessible to water (RILEM I.1)

After drying the samples to constant mass (M_1) (at T°60C), they were placed in desiccators, under vacuum (20 mm MIP) during 24 hours to eliminate the air contained in the pores. Then water was slowly introduced in the vessel, the vacuum was maintained for 24 hours afterwards. Finally the samples were let under water at atmospheric pressure for another 24 hours.
The samples were then weighed in water (hydrostatic weighing: M_2) and in air (M_3).
The porosity (N_t [%]) is expressed as the ratio of the volume of the pores accessible to water to the bulk volume of the sample (equation 6): (M expressed in g)

$$N_t(\%) = \frac{M_3 - M_1}{M_3 - M_2} \times 100 \qquad (6)$$

Free porosity (N_{48}) RILEM II.1

Free porosity at 48 hours, N_{48} (%), allows determining the open porosity accessible to water by capillary under atmospheric pressure and comparable to natural absorption and immersion conditions (equation 7). The sample first absorbs water slowly by capillarity during 2 hours at the atmospheric pressure and then is immersed under water for 48 hours.

$$N_{48}(\%) = \frac{M_{48} - M_1}{V_t} \times 100 \quad (7)$$

M_{48}: mass of the sample after 48h
M_1: mass of the dry sample
V_t: total volume of the sample

The free porosity is comparable with interconnected porosity. From this measurement the Hirschwald coefficient or Saturation coefficient (S) can also be calculated (equation 8), expressing the water saturation of the sample:

$$S = \frac{N_{48}}{N_t} \quad (8)$$

Bulk density and real density (RILEM I.2)

The bulk density (or apparent density): δ_{bulk} [kg/m^3] is the ratio of the mass to the bulk volume of the sample (equation 9).
The real density (δ_{real} [kg/m^3]) corresponds to the volume mass of impermeable material. It is the ratio of the mass to the impermeable volume of the sample (equation 10).
The bulk and real densities were calculated with the mass determined in the experiment for water accessible porosity (M expressed in g):

$$\rho_{bulk} = \frac{M_1}{M_3 - M_2} \times 1000 \quad (9)$$

$$\rho_{real} = \frac{M_1}{M_1 - M_2} \times 1000 \quad (10)$$

Mercury Intrusion Porosimetry

The measurement is based on the non-wetting behavior of the mercury versus the solid surface.
For a cylindrical pore with a radius r_c, the capillary pressure P_c existing between three interfaces (liquid-solid-air) is given by the Laplace law (equation 11):

$$P_c = \frac{2.\sigma.\cos\theta}{rc} \quad (11)$$

P_c: capillary pressure (MPa)
σ: surface tension (N/m)
θ: contact angle mercury-material (°)
rc: radius of the cylindrical capillary (m)

The contact angle θ mercury-material is 140°; the surface tension σ is $480 \cdot 10^{-3}$ N/m.

Mercury Intrusion

As the applied pressure is increased the radius of the pores, which can be filled with mercury decreases and consequently the total amount of mercury intruded increases. The pore volume occupied with mercury at a distinct pressure represents the pore fraction composed by different accessible pore entry radii specified by the Laplace law (equation 11).

Mercury extrusion

During the extrusion some mercury can be trapped in the pore network, which can be due to the ratio pore/throats (the mercury film can crack in thin throats in case of ink bottle pores); the connectivity of the pore network and the roughness (impurities or irregularities) around the grains (Bousquié, 1979).

Limits of the method

The ink-bottle effect

If a small pore of a radius r is connected to a larger pore of a radius R, the mercury can enter in the large pore only when the pressure P_r is reached to enter the smaller pore according to Laplace law. Both pores are invaded simultaneously and the volume considered is only the one of the pore class r. Therefore, large pores can be under-estimated and vise versa, smaller pores class can be over-estimated (Andriani, 2003). The interpretation might be validated by cross-checking the results with other, complementary methods as the Digital Image Analysis (DIA) and BET.

Other effects

Mertz (1991) observed differences between the mercury porosity and the water porosity measured under vacuum (total porosity N_t). Indeed the MIP can deliver higher or lower values than the water absorption method. Higher water porosity can be due to pores on the edge of a small sample, open and directly in contact with the mercury, these pores are not taken into consideration during the calculation of the intruded mercury volume. With higher surface to volume ratio the impact of this effect should gain importance.
In the opposite situation of higher mercury porosity, the microporosity might be not accessible to water during the laboratory experiments (Mertz 1991); also, under water, the swelling of present clay minerals may reduce the wetable pore space.

Moreover, mercury porosimetry does not estimate the real pore space geometry as it is based on the model of cylindrical pores. This point will be discussed later in chapter IV.
A number of factors affect the MIP results. Most important among them is the method of sampling, sample conditioning (oven drying), rate of pressure increase, maximum intrusion pressure applied, assumed values of the contact angle and surface tension of mercury (Kumar, 2004). Kumar used for his measurement on concrete some small cores 25 mm diameter and 15-25 mm in length, and dried the sample at 105-110°C.

Materials used for measurements in this study were dried in the oven at 60°C. This soft drying was selected to not create new fissures in calcitic stones. Water can remain in the pore structure and disturb the measurements. As the maximum cell volume is 1 cm^3, the sample size is limited. As sample should use 50% of the penetrometer volume (Quantachrome requirements), samples of 0.5 cm^3 are used for the measurements.

Measurements were carried out with the Poremaster 60 GT (Quantachrome Instruments). The Pore master 60 is designed to measure pore radii in the range of about 400 to 0.0035 µm. For measuring diameter larger than 7 µm, low pressure and filling station is used. Pressure in the high-pressure station goes from 20 to 6000 psi (140 kPa to 420 MPa).

Specific surface area by Nitrogen

The specific surface area in m^2/g is defined as the sum of the area developed by each particle composing a mass unit of the porous material.
The BET theory was originally elaborated by Brunauer et al (1938). The determination of specific surface by means of the BET theory is based upon the phenomenon of physical adsorption of gases on the external and internal surfaces of a porous material.
The volume of gas is determined as a function of partial pressure from the de-sorption branch of the isotherm after cooling to the liquid nitrogen temperature (BET Nitrogen Adsorption ASTM C1069-86, DIN 66131 modified). Knowing the area occupied by one adsorbed molecule the specific surface area of solids can be calculated after Brunauer et al 1938 equation12:

$$\frac{V_a}{V_m} = \frac{C(p/p_0)}{(1-p/p_0)(1+(C-1)p/p_0)} \qquad (12)$$

Where V_a is the volume adsorbed at relative vapor pressure p/p_0 (p is the actual vapor pressure, p_0 is the vapor pressure at saturation) V_m is the volume of adsorbate forming a monolayer on unit mass of adsorbent and C is a constant related to the energy of adsorption in the first adsorbed layer and consequently its value is an indication of the magnitude of the adsorbent/adsorbate interactions.

Porosity and its distribution by Nitrogen adsorption

The nitrogen adsorption isotherm allows to calculate also the pore size (< 0.1µm) (in the mesoporous region). Pore volume is calculated from the total volume of gas adsorbed at the saturated pressure ($P/P_0 = 1$), after transformation of the gas into a liquid volume (equation 13):

$$V_{sp} = \frac{V_a \times 0.00155}{M} \quad (13)$$

V_{sp}: pore volume (cm^3/g)
V_a: volume total of gas adsorbed at the saturated pressure Po (cm^3)
M: sample mass (g)
The factor 0.00155 represents the change of N_2 density from gas to liquid, with N_2 gas density = 1.2506 kg/m^3 and N_2 liquid density is 0.808 kg/l.
Knowing the apparent density of the sample, total volume (V_t) given by 1 g of sample can be calculated and therefore the porosity N_{N2} (equation 14):

$$N_{N2}\% = \frac{V_{sp}}{V_t} \times 100 \quad (14)$$

The total pore radius calculated from Nitrogen adsorption represent the pore radii below 0.1 µm. Fitzner and Basten (1992) measured also the pore radii by nitrogen adsorption and divided it in two subdivisions, the total porosity < 0.1 µm, a micro porosity < 0.0019 µm and a mesoporosity 0.0019 – 0.1 µm. The authors compared these ranges with other porosity measurements, especially mercury intrusion porosimetry. The same approach was chosen for this study with the same division into pore size categories. The different porosity measurement methods will be compared in a specific chapter.

Digital Image Analysis

Grain size and grain contact

Maximal and mean grain sizes are measured for each stone. Fifty measurements are carried out on three pictures for each stone at a magnification x 40. Datas are exported in Excel and the maximal and mean grain sizes can be calculated.

To evaluate the contact between the grains, the DIA software proceeds by measuring the grain density on the known surface area. From the density of grain on a given area, the contact between them can be estimated; for the sandstones, the binder is not taken into consideration in this calculation, and only the aggregates are measured as for the marble. For the magnesian limestone, it is not possible to distinguish grains, as the stones are mainly composed of micritic cement. Grain size and grain contact could not be evaluated of the magnesian limestones.

Segmentation and components ratio

Mosaic of pictures on blue-dyed thin section should be composed to obtain one image representative of the whole section. The number of pictures to compose the mosaic has still to be determined as a function of the homogeneity of the sample (as an example 12 pictures magnification 40x and resolution 1340x1040 pixels, will give a picture area of 78.6 mm^2). The number of pictures is sufficient when the total pore area fractions converge to a constant value.

Segmentation of pores can be performed by optical microscope, as well as segmentation of the other components as the binder and aggregates (Mueller, Hansen, 2001). Segmentation process would be based on a RGB color cube systems where the minimal pore diameter considered is 25µm at a magnification of 40. The software utilized for the segmentation is Image Pro-Plus**.**

Results are expressed in percent area representative of the component (equation 15 and 16). The area fraction of macro pores (p_{macro} > 25µm) and the grain area fraction (GF) can be determined from the Optical Microscope images considering the total image area (A_{om}) and the area of a single macro pore (P_{macro}) or grain (G):

$$p_{macro} = \Sigma P_{macro} / A_{om} \quad (15)$$

$$GF = \Sigma G / A_{om} \quad (16)$$

The area fraction of the matrix (m) including grains and pores smaller than 25µm can be calculated from the equation 17:

$$m = A_{om} - GF - p_{macro} \quad (17)$$

Pore size distribution

Figure 20 outlines the measuring ranges of the used techniques.
For the pore and grain size distribution only Image-Pro can be utilized. Pore equivalent diameter can be calculated: 18 classes characterize the macro pore and grains (500 to 25µm) and 22 classes for micro pores (25µm – 0.1µm), ESEM-images are needed to evaluate micro pores.

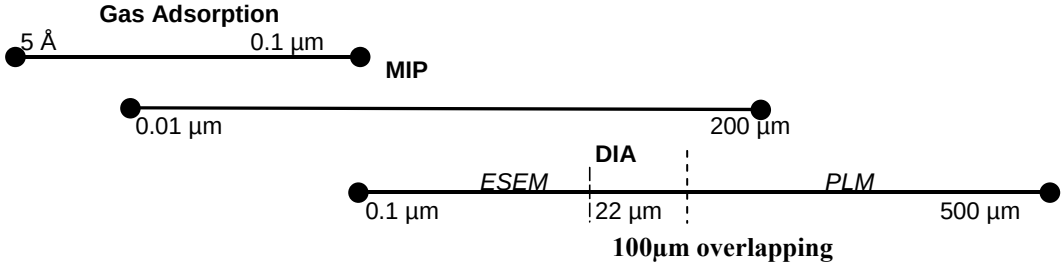

Figure 20. techniques and measuring range

The 40 classes can be grouped in larger pore classes (pore type) in order to be compared with results from mercury intrusion and to evaluate the influence of pore type on the physical-mechanical properties.

Authors quoted as references always considered in digital image analysis the pore size visually measurable by optical microscope. Nevertheless, a first step of the study would consider only macro pores and grains > 25µm detectable by optical microscope. In a second step ESEM images should be acquired to measure the micro pore and also to overlap the measurement taken with the optical microscope (Figure 20).

For each class (n) the maximum pore area (p_n) can be calculated as equation 18 and 19:

$$p_n = \Sigma Pn / A_{om} \quad (18)$$

$$GF_n = \Sigma G_n / A_{om} \quad (19)$$

According to Delesse (1848) the volume fraction of particles embedded in a body can be approximated by their area fraction on the section.

Pore types would be defined from digital image (Ehrlich and al, 1991 and McCreesh and al., 1991) and represent a classification of the optically resolvable porosity. Such pore types defined by digital image can be also distinguished by mercury porosimetry and would allow a direct comparison between both methods.
Pore types can also be translated as pore size parameters and would be used for correlation with water transport properties.

II.3.2. Non-Destructive methods

Ultrasonic velocity measurements and dynamic modulus of elasticity

The aim of the measurement is to determine the time of flight of ultrasonic longitudinal waves V_p as a ratio with the distance between a transmitter and a receiver to the corrected time (time going from the transmitter to the receiver). The velocity is related to physico-mechanical characteristics such as the mineralogical composition, the intercrystalline connections, the porosity, and the moisture content. To determine V_L a portable measurement device USG 20 (Fa. Krompholz Geotron Elektronik, FRG) was used with a 250 kHz emitter (USG -T) and receiver (USE-T).
Determining the Poisson-ratio (equation 21) the dynamic modulus of elasticity is calculated such as equation 20 (from additional shear wave, resonance frequency).

$$E - Dyn = \rho V_p^{\,2} \frac{(1+\upsilon)(1-2\upsilon)}{(1-\upsilon)} \quad (20)$$

With:

$$\upsilon = \frac{1}{2}\frac{\left(\frac{V_p}{V_s}\right)^2 - 2}{\left(\frac{V_p}{V_s}\right) - 1} \quad (21)$$

υ = Poisson coefficient
ρ = apparent density (g/cm^3) (equation 9)
V_p = velocity of compression wave
V_s = velocity of shear wave

II.3.3. Pore shape determination - methods

Cavities in low porosity rocks are usually in the form of cracks, which are situated along cleavages in the minerals or at grain boundaries. When conditions change and the rock is subjected to new temperatures and pressure (as it is the case for the heated marble), internal stress develops and grains crack and tend to shift with respect to one another, resulting in increasing cracks in length and number.

An easy way to differentiate porosity of pores or of cracks is to measure the ultrasonic velocity of water-saturated stones. Indeed, under water saturation, stone characterized by a porosity of pores may not present a significant variation, in comparison to dry state, in its velocity, while a fissured or cracked stone should show a noticeable increase of the ultrasonic velocity (Walsh, 1966; Tourenq and Fourmaintraux, 1971). The water might be fixed on the wall of the cracks linking in a rigid way both sides of the crack. Capillary forces, leading to the closing of the crack, might also be a source of these bridges.
A second approach to separate porosity of pores from porosity of cracks is to calculate the quality index. Tourenq and Fourmaintraux, 1971, have described the calculation of the quality index. Indeed the authors proposed a method to quantify the discontinuities in rocks.
It is based on the comparison of the measured ultrasonic velocity and theoretical ultrasonic velocity values and lead to the Quality Index definition, with equation 22:

$$QI\% = \frac{V_p}{\sum_i Ai.V_p i} \times 100 \quad (22)$$

QI: Quality Index 0 < QI < 100 in % (maximum quality)
Vp: measured ultrasonic velocity (P waves) (m/s)
$\Sigma A_i V_p i$: theoretical ultrasonic velocity (P waves)

The theoretical ultrasonic velocity is calculated from the velocity of each mineral contained in the rock and its concentration.
Tourenq and Fourmaintraux (1971) demonstrated also that the Quality Index could be expressed as equation 23:

$$QI\% = \left(1 - \alpha.N_P - \beta.N_F\right) \times 100 \quad (23)$$

With:
N_P: porosity of pore
N_F: porosity of cracks
α, β: experimental coefficients

The authors defined two equations 24 and 25:

$QI = 100 - 22\ N_F$: rocks containing only cracks (pore porosity $N_P = 0$) (24)
$QI = 100 - 1.6\ N_P$: rocks containing only pores (crack porosity $N_F = 0$) (25)

Le Berre (1975) showed that the porosity of cracks should have a larger importance and transformed the equation to equation 26 and 27:

$QI = 100 - 47\ N_F$ (26)
$QI = 100 - 1.32\ N_P$ (27)

The corrected relation of the porosity of cracks N_F and of pore N_P is illustrated in the Figure 21. All the constants derive from experimental coefficients. Indeed, the authors determined the equation and the constants from the representation of diversified lithotypes in the diagram porosity N_t vs. Quality index QI%.

Looking at the diagram (Figure 21) values of N_F and N_P present two limits clearly drawn; N_F is necessary below 2% ($N_F < 2\%$), while N_P must be below 75% ($N_P < 75\%$) to result QI% above zero.

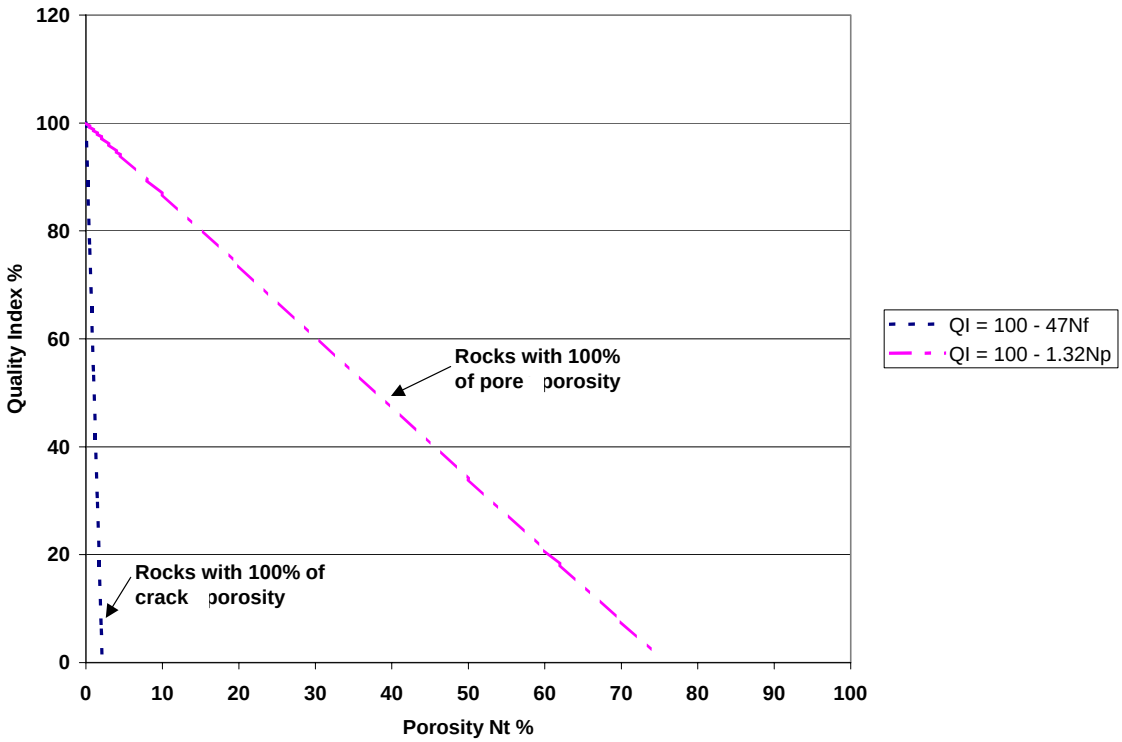

Figure 21. Corrected relation of the porosity of cracks and of pore.

II.3.4. Physical properties

Water uptake coefficient (EN-ISO 15148)

The water absorption coefficient is the mass of water absorbed by a test specimen per face area and per square root of time. The bottom surface of the specimen is in contact with water (level of water 5 mm) and the change in mass of the specimen is measured over a period of time of 24 hours. The measurements are carried out perpendicular to the sedimentation layers of the stone sample and taken after 1 min, 5 min, 10min, 15min, 30 min, 1 h, 2 h, 4 h, and 24 h.
Considering the Hagen-Poiseuille law describing the water flow Q (cm^3/s) in a vertical capillary, as equation 28:

$$Q = \frac{\pi.Pc.R^4}{8.\eta.x} \quad (28)$$

P_c: capillary pressure ($dynes/cm^2$)
η: dynamic viscosity of the fluid ($dynes/cm^2$)
R: radius of the vertical capillary (cm)
x: length of the capillary tube (cm)

The water flow Q through a capillary tube changes according to the radius of the tube. Thus, thinner is the capillary lower the speed of the fluid would be. The relation demonstrates also that it is the cylindrical-like throats, which control the water transport.

Thus, the water uptake coefficient is calculated from the linear part of the curve, as equation 29:

$$W = \frac{m}{\sqrt{t}}\left[kg/m^2/h^{0.5}\right] \quad (29)$$

with:
m: amount of water per area at time t (kg/m^2)

The capillarity rise or B-value, is also linear as a function of the square root of time, as equation 30:

$$B = \frac{h}{\sqrt{t}} \quad (30)$$

with:
h: the water penetration depth in cm

Evaporation kinetics (RILEM II.5)

The evaporation curve of a material is obtained from the density of water flow rate g (t) ($g/m^2.h$) (equation 31) evaporating from the surface as a function of the average moisture content remaining in the material after previous saturation. In the study the value of g included in the correlation is the one calculated on the plateau, when liquid water is conducted to the surface by capillarity (Figure 22).

$$g(t) = \frac{dM}{Adt} \quad (31)$$

With:
g = density of water flow rate ($g/m^2.h$)
M = mass of the sample (g)
t = time (h)
A = evaporation surface (m^2)

During drying, the ambient conditions (air velocity, temperature, relative humidity) must be constant. After 48 hours in total immersion under atmospheric pressure, the sample is sealed on 5 sides by a film of latex. Therefore only one dimensional moisture transport is allowed. Experiments were carried out in the climatic control room at 21°C and 44%RH without wind speed.

As the capillary curve, the evaporation curve is composed in two parts (Figure 22). During the first drying period water is transported to the surface by capillary transfer; the surface of the stone is wet. A plateau (PL) marks this first phase, where g is calculated. Then, a breaking point (P1) marks the phase when the waterfront withdraws from the surface. Evaporation takes place inside the stone by diffusion and the flow rate fall down continuously. A second breaking point (P2) (critical hygric saturation) can be observed at low residual moisture below 10% and when two distinct pore radii maxima are characterized in the stone structure. It represents the residual moisture stored in the smallest pores.

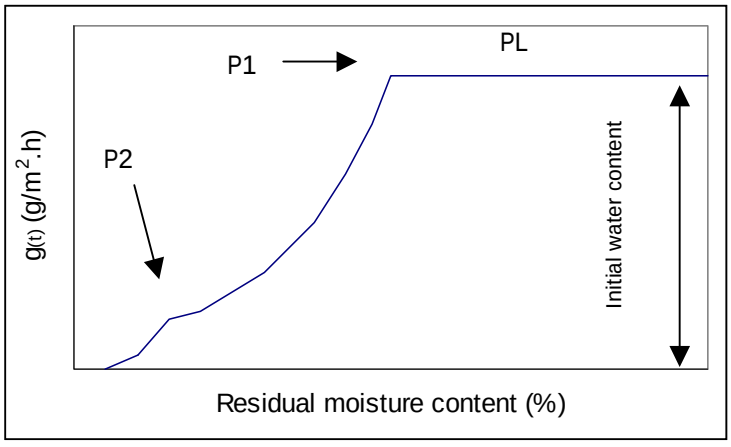

Figure 22. Drying flow rate of a porous material

The coefficient of water vapor conductivity from the surface to that air β can also be calculated from the linear part of the evaporation curve as equation 32 (Snethlage, 1984; Pereira, 1988):

$$\beta = \frac{g}{Ps - Pg} \qquad (32)$$

with g = the water flow rate ($g/m^2.h$) (equation 31)
β = coefficient of water vapor conductivity to the surface (h^{-1})
Ps; Pg = water vapor partial pressure on the surface and in the air (Pa)

Water vapor permeability and diffusion resistance coefficient μ-value (EN ISO 12572)

The water vapor permeability is the quantity of water vapor passing per time unit and surface units through a porous material under isothermal conditions. Fick's law describes this phenomenon (equation 33):

$$\delta = C.\frac{d}{A}.P_{(v)} \qquad (33)$$

With:
δ = water vapor permeability (kg/m.s.Pa)
d = thickness (m)
A = surface area (m^2)
$P_{(v)}$ = difference of partial water vapor pressure on both sides of the material (Pa)
C = coefficient of proportionality between the weight loss and the time

Two units are used: δ = g/m.h.mmMIP or the System International (SI) kg/m.s.Pa
With: 1 g/m.h.mmMIP = $20.8.10^{-10}$ kg/m.s.Pa

The diffusion of the water vapor in the air is not direct and we can also determine the diffusion speed and the water vapor permeability of an air layer, with air pemeability at: 0.09 g/m.h.mmMIP or $1.9.10^{-10}$ kg/m.s.Pa
The water vapor diffusion resistance coefficient of a material is the ratio of the air permeability to its own permeability (equation 34):

$$\mu = 0.09/\delta \qquad (34)$$

This ratio is dimensionless, a material with a μ coefficient close to 1 is a material very permeable to the water vapor, a vapor proof material will be characterized by $\mu = \infty$.
The wet cup procedure is followed with the gradient of 100% RH water H_2O to 45% RH controlled room condition. The sample disc used in the present investigation has a diameter of 40 mm and a thickness of 5 mm.

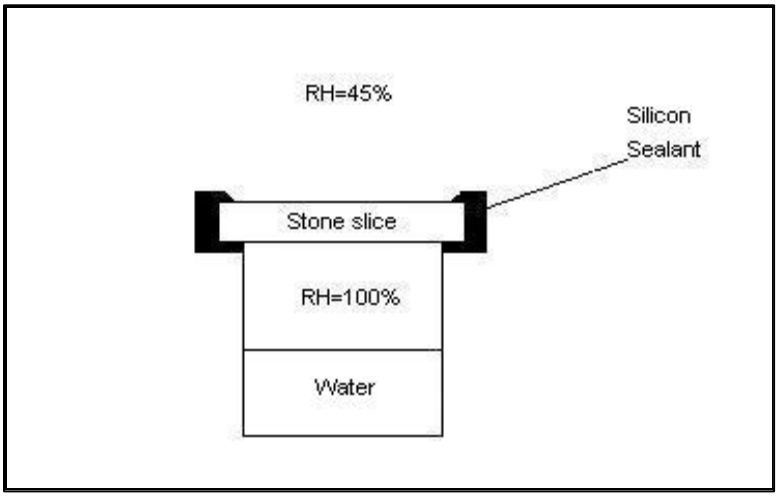

Figure 23. Representation of the water vapor permeability measurement by the wet cup procedure

Hydric dilatation (RILEM II.7)

The aim of the test is to determine the linear strain due to liquid water absorption in a stone. The length variation of the sample due to water absorption is measured as a function of time. Samples are drill core 8 cm x 4 cm, and dried until constant weight. Sample is placed in contact with a LVDT (Low Voltage Transducer) and water is progressively added according to the capillarity properties of the sample, until total immersion. Displacement is recorded as a function of time on a period of 72 hours. Measurement is automatically taken every 5 min for the entire period of the measurement.

The linear dilatation strain ε is given by the equation 35:

$$\varepsilon = \frac{L_1 - L_0}{l_0} \qquad (35)$$

Where: L_1 reading of the total displacement from the tranducer after 72 hours (mm); L_0, initial reading of the transducer (mm); l_0 initial length of the sample (mm). ε is normally given in mm/m.
Measurements have been carried out perpendicular to the stone bedding.

II.3.5. Mechanical properties

Bi-axial flexural strength and static modulus of elasticity

A slice of stone is placed between two steel rings. A load (F) is applied on the sample. First an elastic deformation takes place and allows determining the static E-modulus in kN/mm^2 (E = Young modulus) according to the equation 36. E-stat is not as the Hook law measured from the slope at one third of max load in the stress – strain curve, but is similar and can be used because the sample dimension are always the same. Modulus of elasticity of biaxial flexural strength measurements is different from these measured by uniaxial compressive strength, which is simply the ratio of the load with the strain at one third of the deformation curve. The increase of the load leads to fissures in the sample until its breaking point (maximum load); the bi-axial flexural strength (BFS) expressed in N/mm^2 can be calculated by using equation 37 (Wittmann & Prim, 1983)

$$\text{E-Stat} = 1.5 \frac{F}{f_o} \frac{1}{h^3} (1-\nu^2) [b^2 \ln \frac{b}{a} + \frac{(a^2 - b^2)(3+\nu)}{2(1+\nu)}] \quad (36)$$

$$\text{BFS} = \frac{3F}{4\pi.h2} [2(1+\nu) \ln \frac{b}{a} + \frac{(a^2 - b^2)(1-\nu)}{a^2} \frac{a^2}{R^2}] \quad (37)$$

ν = Poisson ratio (ν= 0.25)
a = Radius of the lower ring (a = 18 mm)
b = Radius of the upper ring (b = 6.5 mm)
f_o = Displacement (mm)
h = Thickness of the slice (mm)
F = Load (N)
R = Radius of the stone slice (mm)

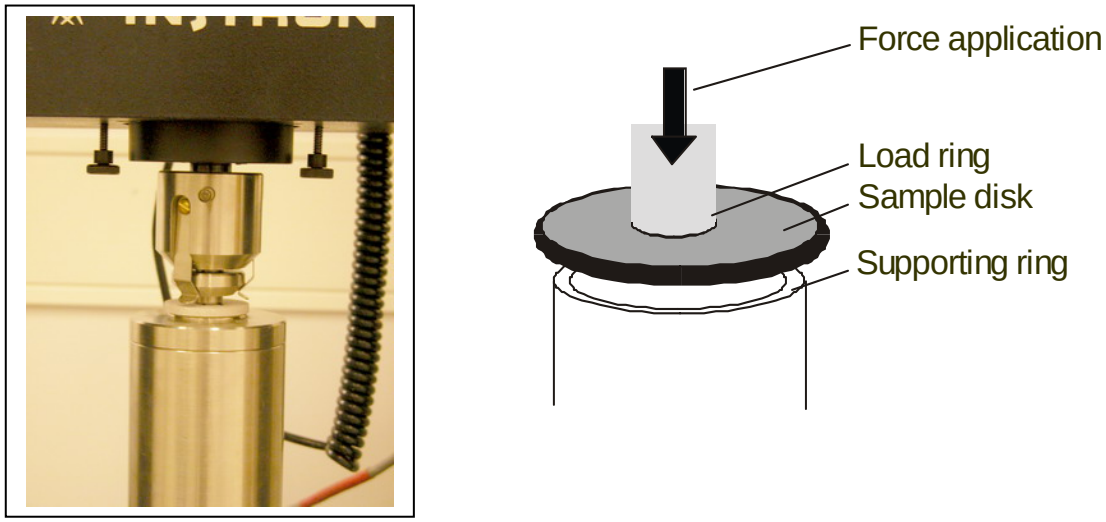

Figure 24. Picture and schema of the biaxial flexural strength set up.

Drilling resistance (DRMS)

The Drill Resistance Measurement (DRMS) is a micro-destructive method, which has been applied to determine the stone hardness. The evaluation of the hardness is related to the drilling penetration force: the force necessary to drill a hole with specific operative conditions such as the Penetration Rate (PR) and the Rotational Speed (RS), which remain constant during the test. The profiles of drilling resistance provide information about the consolidating effect and the penetration depth of a product.
According to the operative conditions (Tiano et al, 2000), the Drill Resistance can be recorded on limestone with a penetration rate (PR) of 20 mm/min and a rotational speed (RS) of 600 rpm, and on the marbles for 5 mm/min and 1200 rpm. Then the values can be corrected according to the formula 38:

$$DRc = DR \frac{20 \times RS}{PR \times 600} \quad (38)$$

The system developed by SINT consists of a precision drilling machine equipped with two precisions motors to keep PR and RS constant, controlled by a computer. In this study diamond drill bits with 5mm diameter were used for both types of stones.

II.3.6. Artificial weathering

Freezing-thawing cycles (DIN EN 12373)

First samples have to be soaked slowly with water by capillarity under ambient pressure. Then, each cycle consists of a six hour freezing period in -20°C ambient environment, followed by a six hour thawing period during where the specimen is immersed in water. The cycles are repeated until the specimen fails or up to a given maximum number of cycles.

The control measurements to determine the freeze/thaw resistance are:

- Visual inspection, which is carry out as followed is done after each cycle:
  - 0 specimen intact
  - 1 very minor change (minor rounding of corners and edges) which does not compromise the integrity of the specimen.
  - 2 one or several minor cracks (< 0.1 mm width) or detachment of small fragments (< 10 mm^2 per fragment).
  - 3 one or several cracks, holes or detachments of fragments larger than those defined for the “2” rating, or alteration of material in veins
  - 4 specimen broken in two or with major crack
  - 5 specimen in pieces and disintegrated

- Measurement of the dynamic modulus of elasticity (Young’s modulus)

By measuring the change in the dynamic modulus of elasticity during the freezing-thawing cycles it is possible to detect some deterioration, such as microcracks. It is necessary to dry the samples to constant mass before performing the measurement.

The percentage decrease in dynamic modulus of elasticity is calculated as follow (equation 39):

$$\Delta E = \frac{(E_0 - E_n) \times 100}{E_0} \% \quad (39)$$

Where E_0 is the initial measurement in a dry condition performed before cycling starts and E_n the measurement in a dry condition after n cycles.
The number of cycles at which the decrease of dynamic modulus of elasticity reaches 30 % shall be noticed.

The test continues until two or more specimen are classed as failed using any of the following criteria:

- the score of the visual inspection attains 3;
- the decrease of dynamic modulus of elasticity reaches 30 %.

For our study the total disintegration is not necessary and the score 2 or 3 at the visual inspection should be sufficient. Moreover the decrease of the dynamic modulus of elasticity appears to be the most accurate measurement to notice start of cracking in the specimen.

II.3.7. Sample size

For all measurements samples are drill cores of 8 cm height x 4 cm diameter. On the same drill cores ultrasonic, dynamic modulus of elasticity, water saturation, water uptake coefficient, and evaporation kinetics are performed. These drill cores are then submitted to freeze-thaw cycles.
A second series of drill core of the same size are taken on the same stone and sliced (slices 4 mm x 40 mm) and used to carry out the water vapor permeability and then the biaxial flexural strength. Broken pieces are used to measure the MIP porosity and BET.

II.3.8. Statistic analysis

In this study different statistic methods are used to determine holistic correlation. The application of the factor analyses is the first method considered. Factor analyses are largely used in statistics as it allows to determine which variables are strongly correlated.
Variables are displayed on a hypersphere of a unit radius, centered on the barycentre of observations. A point on the sphere represents a variable (Figure 25). Coordinates of that point correspond to the coefficient of correlation between these two variables (Lebart et al, 1979).
The interpretation of variables projection position between each other or in relation to factorial axiss is done in term of dependency (correlation), in a disk of diameter relative to a given factorial plane in function of the following rules:

- The better a variable is explained the closer it is to the circle (A), badly explained if the variable is close to the center (B);

- Two variables close to each other are correlated (positive correlation), the closer they are the more correlated (A and C);
- Two variables symmetrically plotted are correlated to each other (negative correlation) (A and D; G and F);
- Two variables well explained (close to the circle) separated by a 90-degre rotation are independent to each other (A and E).

To simplify, entering all data, the software will calculate all the possible linear correlation between the variables. From this calculation several factors will be defined (1 to 4), which represent a group of variables correlated to each other's. The factors (groups of correlated variables) are the axis of the sphere, so each variables are displayed individually as there coordinates are the correlation factor with the factor axis or group of variables.
Plots might be close to one axis and therefore belong to this axis in a certain degree of correlation. The closer they are to 1 or –1, the higher is the correlation factor, as for A, C and D. These three variables belong to the same factor or group of variables but in different ways; A and C are positively correlated, while A and D are negatively correlated.
E belongs to a second axis, so a second group of variable, independent from the first one. G and F are not linked to any of the present two axis; they might be related to a third factor or group of variables.

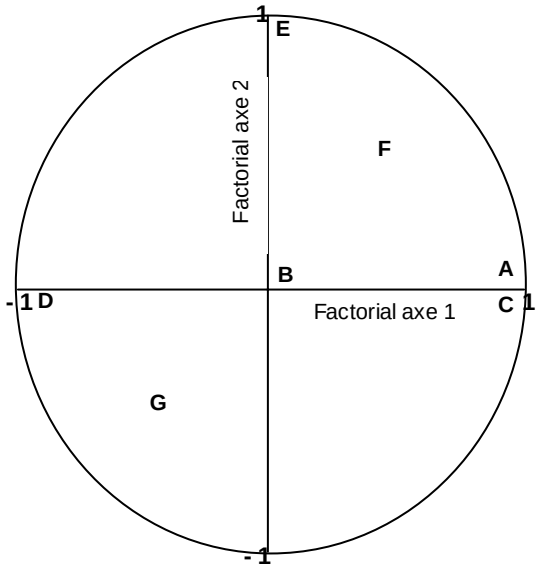

Figure 25. Position of point's representing variables in a correlation disk.

Thus, a direct visualization of the correlation between different variables can be observed on the representation. One variable can be correlated to a group of other variables. In this case a multiple regression can be establish as well as a stepwise multiple regression.
The multiple linear regression analysis is used to derive an equation that can be used to predict values of the dependent variable from several independent variables (Brown, 1993). Any observed variable could be considered to be a function of any other variable measured on the same sample. In multiple regressions, the equation is of the form (equation 40):

$$Y = b_0 + b_1X_1 + b_2X_2 + ... + b_nX_n \quad (40)$$

Where b_0 to b_n are partial regression coefficients, and X_1 to X_n are variables as above.

The stepwise multiple regressions are used to reduce further the number of measured variables and to analyze and remove collinearity that might exist between variables. Stepwise regression uses the same analytical optimization procedure as multiple regressions but differs from the multiple regression method in that a subset of predictor variables is selected sequentially from a group of predictors by means of statistical testing of hypotheses.

II.3.9. Determination of variables

In order to identify holistic correlations for assessing weathering of porous material, it is primordial to have a clear methodology and to determine the main important variables entering in the correlation study. Therefore, the variables can be subdivided into five characteristic categories, which are related to:

- Structure characteristics, with the grain size distribution, mean grain diameter, maximal grain diameter and percentage of grain contact from DIA measurements, and Quality Index.

- Non-destructive methods, with ultrasonic parallel and perpendicular to the bedding and dynamic modulus of elasticity; the drill resistance can also enter in this group.

- Porosity properties, including the different methods to evaluate total porosity and pore size distribution by including pore ranges (BET, water absorption, MIP, and DIA).

- Physical properties, including all measurements related to water transport (capillarity, evaporation, permeability)

- Mechanical properties, which are mainly biaxial flexural strength and static modulus of elasticity, the drill resistance.

The study follows these five groups, each chapter characterizes one of the groups and correlations can be drawn step by step for each lithotype. Correlations are considered mainly through the Factor analyses, multiple linear regression analyses and the stepwise multiple-regression analyses.

B. RESULTS AND DISCUSSION – PART I: PROPERTIES OF FRESH STONES

III. Determination of the structure

In addition the determination of grain size (maximal grain size and mean grain size) and the evaluation of the grain contact by DIA, analysis of the structure should also take into consideration the pore shape. As the literature described, the relation between strength, static and dynamic modulus of elasticity is complex and may be strongly related to a porosity shape factor of pores and cracks. In a holistic correlation pore shape may be an important variable, which may influence physical and mechanical properties as well.
All raw results of the entire study are presented in annex 2.

III.1. Mean and maximal grain size, grain contact

As it has been described in the methods, mean grain size, maximum grain size and grain contact was measured by DIA. Mean grain size varies for the three sandstones from 145 µm (Regensburg) to 180 µm (Wüstenzeller), while their maximum grain size varies from 200 µm (Sander) to 300 µm (Wüstenzeller) as shown in Figure 26 and Figure 24. The range of grain contact is broader. While in Sander grain contact is around 35% of the perimeter, it is 45 % in Regensburg and 80 % in Wüstenzeller. Wüstenzeller grain contact can be qualified as long contact type (Figure 30) while Regensburg shows more concavo-convex contact and few long contacts (Figure 31) and Sander has mainly tangential contact (one contact point between two grains) and concavo-convex contact (Figure 29).
In average, grains of 600 µm compose Proconnesian marble as well as a maximum size grain close to a 1000 µm (Figure 26 and Figure 24). The contact between the grains can be described as the sutured type at 90% grain contact (Figure 28 and Figure 32).
Determination of the grain size and contact of the magnesian limestones could not be measured because of their micritic composition (cf. II. Material and methods p.15).

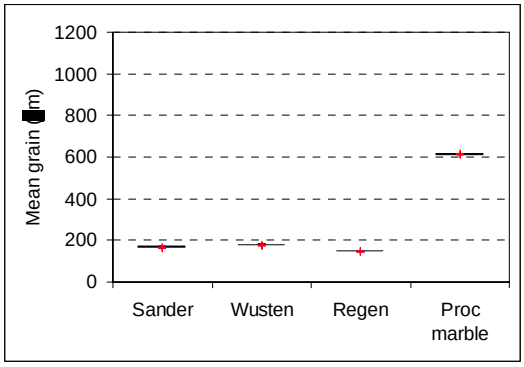

Figure 26. Mean grain size measured by DIA.

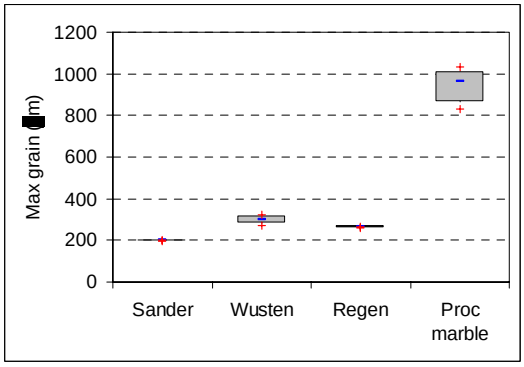

Figure 27. Maximum grain size measured by DIA. Raw results in Annex 2 Table 9

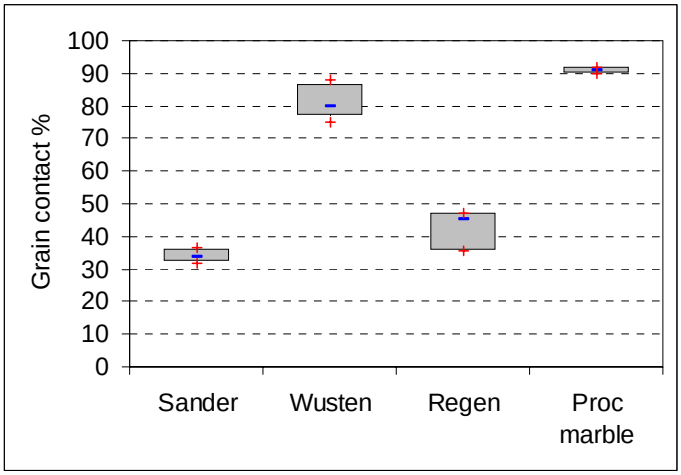

Figure 28. Grain contact evaluation by DIA. raw results in Annex 2 Table 9.

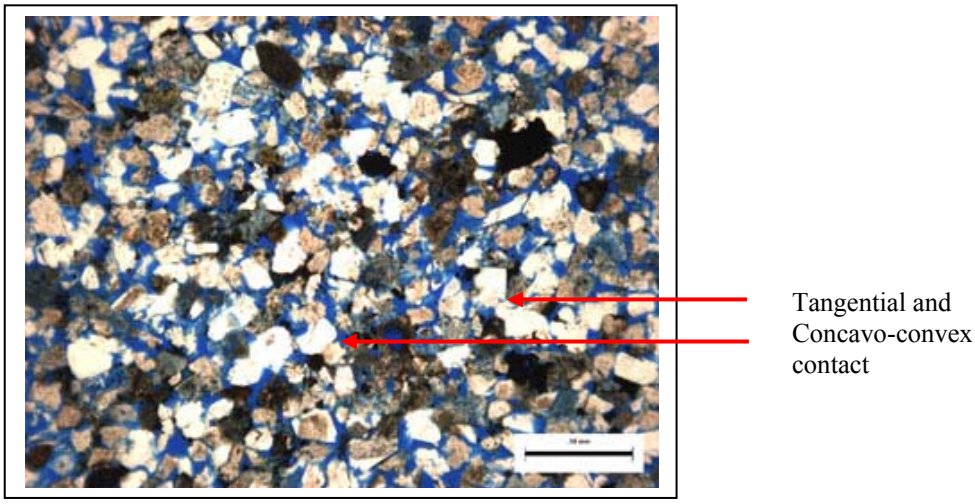

Figure 29. Sander sandstone – thin section blue dyed x 40, the blue is the porosity.

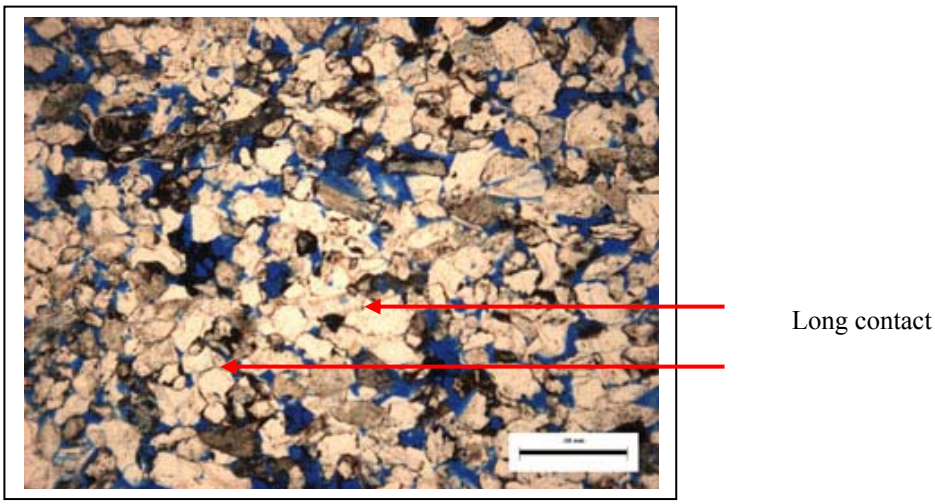

Figure 30. Wüstenzeller sandstone – thin section blue dyed x 40, the blue is the porosity.

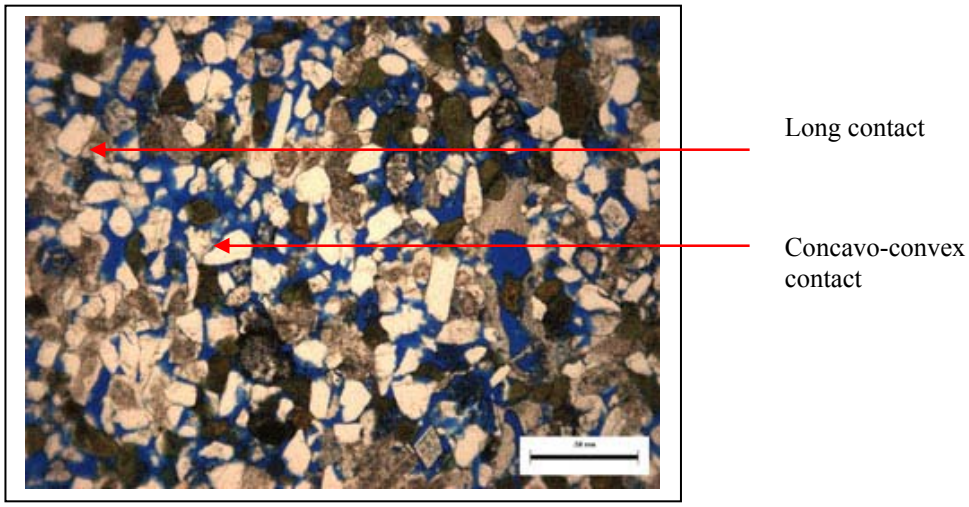

Figure 31. Regensburg sandstone – thin section blue dyed x 40, the blue is the porosity.

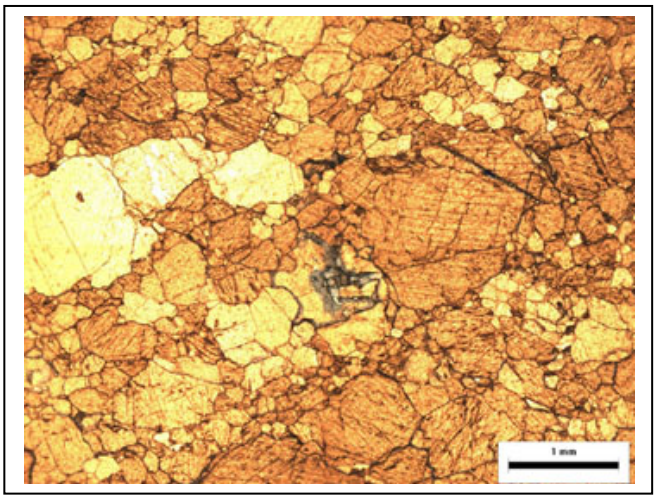

Figure 32. Proconnesian marble aged presenting saturated grain contact - thin section blue dyed x 40

III.2. Grain size distribution of the sandstones

Grain size distribution was determined on the sandstone by Digital Image Analysis (DIA). An average of the measurements is presented in the Figure 33. Three grain classes were defined according to the ASTM D422 norm: silt class 2-80 µm; fine sand class 80-400 µm and the medium sand class 400-2000 µm.

As it can be observed on the Figure 33, the main important grain class of Sander sandstone is the silt class below 80 µm, and the stone does not present medium sand class. Wüstenzeller and Regensburg show three distinct grain classes. Wüstenzeller illustrates similar percentage of fine and medium sand, while Regensburg has same content of silt and fine sand. From these results it may already appear that Wüstenzeller presents the most equilibrated grain size distribution with 14 % of silt class filling the space between fine sand and the medium sand class.

Thus, Sander shows a fine sand fraction dispersed in the silt fraction. For Regensburg it is obvious from the thin section (Figure 7) that only silt and fine sand fraction is in grain contact, medium sand is isolated.

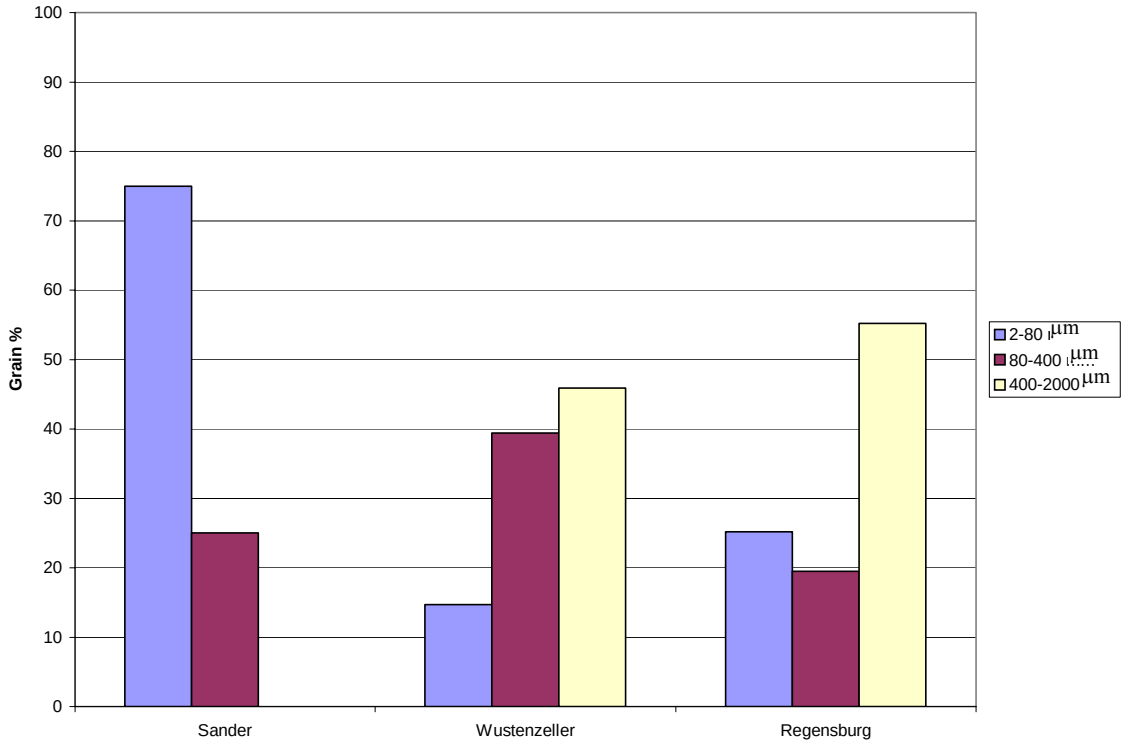

Figure 33. Grain size distribution of the sandstones. Raw results in Annex 2 Table 9

III.3. Pore shape determination

III.3.1. The Quality Index, QI%

For the sandstones, magnesian limestones and Proconnesian marble, the following theoretical velocity values and mineralogical composition was taken from the literature (Gebrande, 1982; Grimm, 1990) to calculate the theoretical velocity and QI:
Calcite : V_p // c = 5710 m/s; V_p // a = 7500 m/s, assuming random distribution of calcite orientation, it is allowed to use the average of calcite ultrasonic velocity.

Quartz :	6060 m/s
Dolomite :	6700 m/s
Calcite (average):	6600 m/s
Opale:	5000 m/s
Muscovit:	6000 m/s
Na-Ca feldspar:	6650 m/s

Sander:	54 % quartz; 42 % feldspar; 2% muscovite; 2% kaolinite
Wüstenzeller:	69% quartz; 25 % feldspar; 4 % muscovite; 2 % opale
Regensburg :	63% quartz ; 22% feldspar ; 15 % calcite
Magnesian limestone:	85% dolomite; 10 % calcite; 5 % quartz;
Marble :	100% calcite

Example of QI calculation:

Proconnesian marble:
The theoretical ultrasonic velocity of a fresh marble (100% crystallized calcite) is 6600 m/s; the measured ultrasonic velocity on the thermally aged Proconnesian marble is 2100 m/s.
Therefore QI % = (2100/6600) x 100 = 31 % (equation 22)

QI on the others specimen are:

Sander:	36.4%	Highmoor :	57.4%
Wüstenzeller:	45.3%	Cadeby	50.3%
Regensburg :	47.7%	Hazel Lane:	64.6%

Sandstones and aged marble have a lower Quality Index than the magnesian limestones. It shows that sandstones and aged marble may have more discontinuities in their structure.
The magnesian limestones are very close to the pore porosity line as well as Hazel Lane and Highmoor (Figure 34). These two stones may be quite entirely characterized by a porosity of pores. On the other hand, the Proconnesian marble is clearly on the opposite, the cracks porosity line. This is completely proved by the heat treatment applied to the marble to increase its porosity by increasing the cracks along the grains. In between, the sandstones seem to be more characterized by a mixed porosity of pores and cracks. Regensburg, Wüstenzeller and Sander occupy distinct areas in the middle of the diagram. Much scattering Cadeby is in the transition between Hazel Lane, Highmoor and the sandstones.

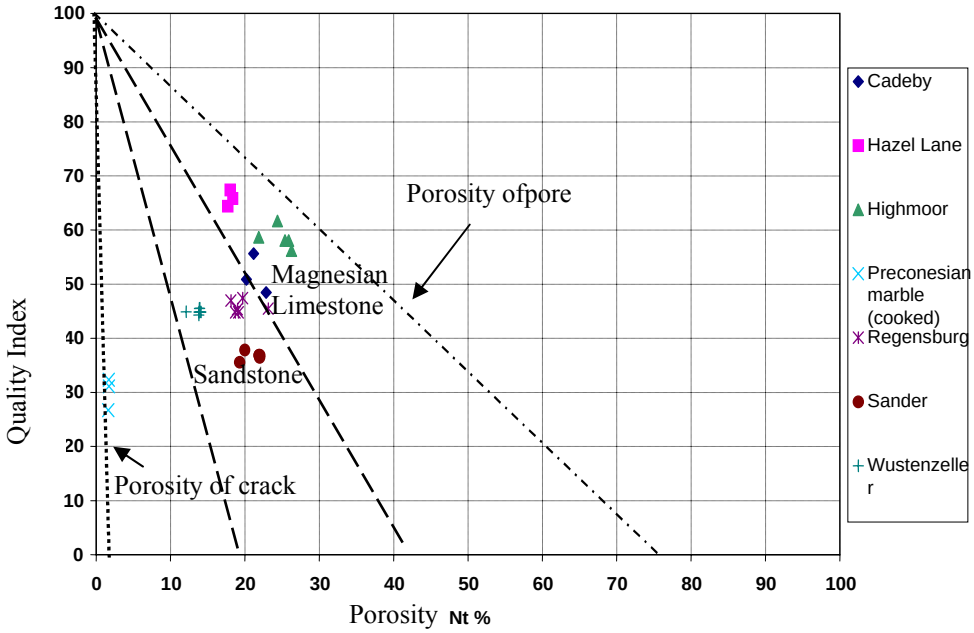

Figure 34. Corrected relation of the porosity of cracks and of pore of the sandstones, magnesian limestone and marble. Raw results in Annex 2 Table 9, Table 14 and Table 19.

III.3.2. Ultrasonic velocity of water saturated samples

Through this measurement the difference between sandstones, limestone and marble can be revealed very clearly (Figure 35). All samples increase their velocity when saturated, but the Proconnesian marble shows the highest increase of velocity by 30 %. The sandstones ultrasonic velocity increase from 20 to 15 %, while the magnesian limestone velocity enhance only from 1 % to 2 % for Hazel Lane and Highmoor and 5 % for Cadeby. Considering that the water saturated velocity increase is in a greater range for a porosity of cracks than a porosity of pores, the marble as well as the sandstones (to a lesser degree), are characterized by a porosity of cracks, while the magnesian limestones are characterized by a porosity of pores. A pore shape factor (Psf) can be calculated from the ratio between the ultrasonic velocity measured on saturated samples (V_pS) and on dry samples (V_pD), (Figure 36), such as equation 41:

$$\text{Psf} = \frac{\left(V_pS - V_pD\right)}{V_pS} \qquad (41)$$

The pore shape factor reflects well the difference between the lithotypes and quantifies the pore shape properties. Therefore, it can be a useful variable to be introduced in the correlation matrix. We can observed that:

0 < Psf < 0.05	Porosity of pore
0.05 < Psf < 0.2 5	Porosity of pore and crack
Psf > 0.25	Porosity of crack

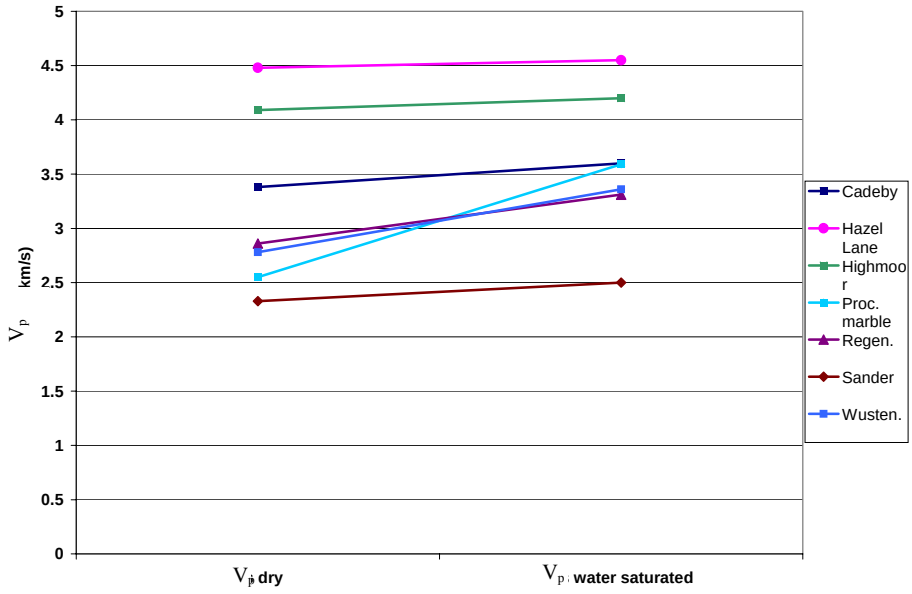

Figure 35. Ultrasonic velocity on dry and on water saturated samples. Raw results in Annex 2 Table 11, Table 15 and Table 21.

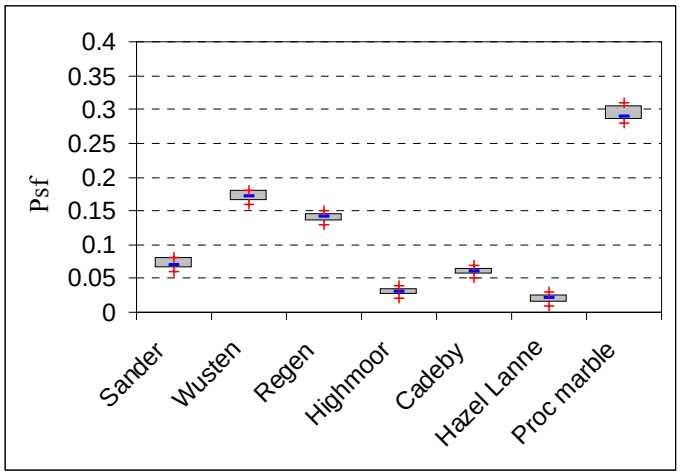

Figure 36. Pore shape factor calculated from ultrasonic velocity on saturated sample and ultrasonic velocity on dry sample. Raw results in Annex 2 Table 11, Table 15 and Table 21.

III.3.3. In summary

The ratio of the ultrasonic velocity measurements before and after water saturation may determine the shape of the pores. The higher the ratio the more crack porosity is prevailing the porosity of pores. A lower ratio indicates a porosity of pores. These results, obtained in a non-destructive way, can be integrated as a fundamental variable in a holistic correlation study.

Quality index (QI%) is also obtained by non-destructive method and indicates the discontinuities in the stone and therefore is seen as an important variable. Pore shape can also be determined when QI is displayed versus the total porosity. The two methods, pore shape factor and QI versus N_t, give similar results. Indeed, both way tend to prove a porosity of pores for the magnesian limestones with Highmoor and Hazel lane ahead; a high proportion of porosity of cracks for the sandstones, Wüstenzeller may present the highest content of crack porosity, while Sander and Regensburg show different results according to the methods applied. In fact, in the QI vs. Nt diagram, Regensburg is closer to the limestones, while in the pore shape factor diagram it is closer to Wüstenzeller (Figure 36).

III.4. Ultrasonic velocity and dynamic modulus of elasticity

Many of the methods to describe the structure of the lithotype are based on ultrasonic velocity measurements, therefore the measurements and the dynamic modulus of elasticity are presented in this chapter.
Ultrasonic velocities are carried out parallel and perpendicular to the stone bedding. In general higher velocity is recorded parallel to the bedding than perpendicular. Two groups of measurements can be distinguished on the Figure 37. Indeed sandstone and aged Proconnesian marble vary from 2 to 3 km/s; the Proconnesain marble can be classified as a level II of alteration ($2<V_p<3$ km/s) (Köhler, 1991).

Magnesian limestones present higher ultrasonic velocities from 3.5 km/s to 4.5 km/s, where Hazel Lane shows the highest values. The gap between sandstones, marbles in one side and the magnesian limestones on the other side is very interesting. It indicates that the magnesian limestone may have much less discontinuities and the direct ultrasonic measurements reflect similar characteristics as the calculation of the Quality Index. Discontinuities in the stone structure may be linked to pore shape. QI displayed versus the total porosity emphasizes the porosity of pores or/and of cracks; limestone, sandstones and marble can be therefore distinguished. Hazel Lane revealing the highest QI = 64.6%, is defined with a porosity of pores and presents then the highest ultrasonic velocity 4-4.5 km/s. Aged Proconnesian marble has the lowest QI = 31%, is close along the porosity of cracks line and shows the lowest ultrasonic velocities 1.8-2.5 km/s. Same considerations can be done for the other specimen. Among the magnesian limestones Cadeby shows lowest values while it also shows the lowest QI and it is closer to the sandstone group in the diagram (Figure 34). On the other hand, Regensburg presents the highest velocities and QI of the sandstones while Sander has the lowest values. It may be assumed that the ultrasonic velocity is more influenced by the shape of the pores than by their quantity in term of total porosity. Cracks create more important discontinuities in the material structure than the spherical pores and sharply decrease elasticity.

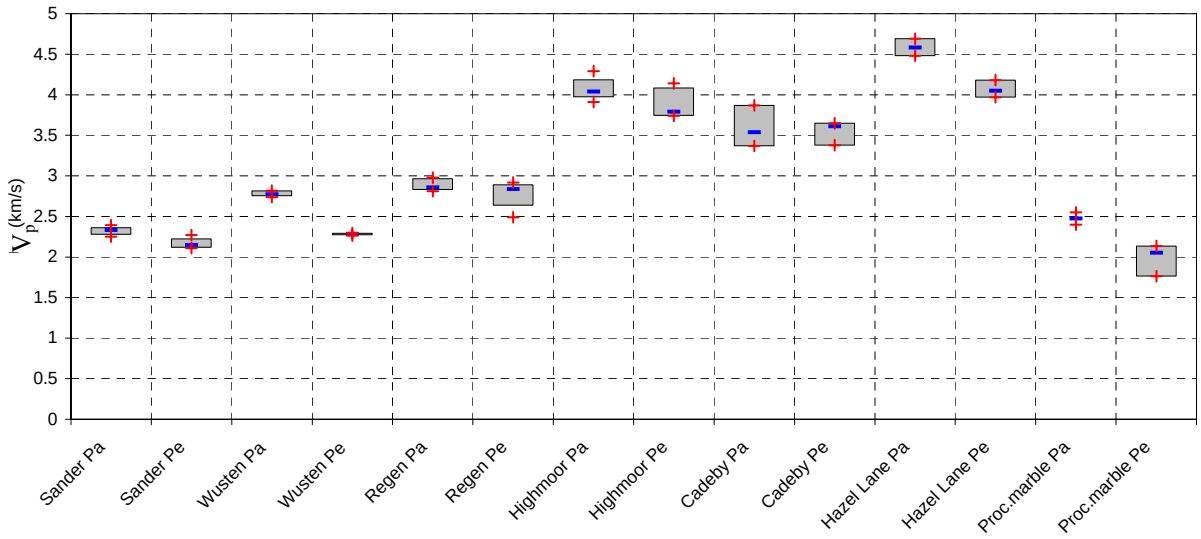

Figure 37. Ultrasonic velocity parallel (Pa) and perpendicular (Pe) to the stone bedding. Raw results in Annex 2 Table 10, Table 15 and Table 20

The dynamic modulus of elasticity shows similar characteristics as the ultrasonic velocities (Figure 38). Magnesian limestone presents the highest values 20 to 30 kN/mm^2; Cadeby has still the lowest value of the three limestones. Sandstones and aged marble have a lower dynamic modulus of elasticity 9 to 15 kN/mm^2, where Regensburg shows the highest results. Again it seems that the pore shape influence greatly the dynamic modulus of elasticity. Moreover, Regensburg is free of interstitial clay. Glauconite occurs in form of grains only. Further considerations will be developed in the analysis of the mechanical properties.

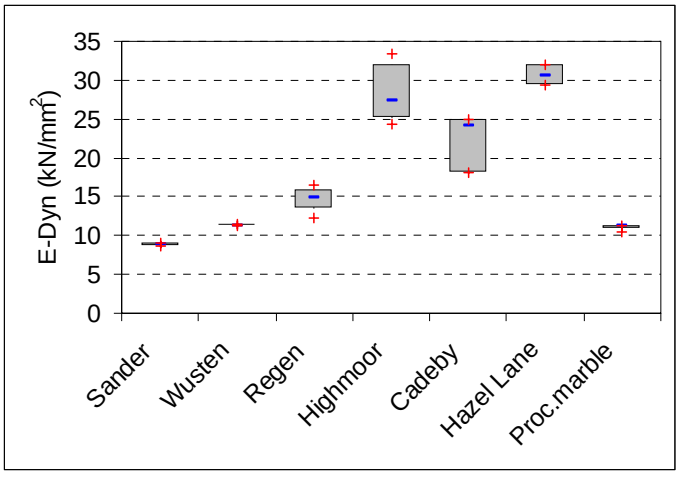

Figure 38. Dynamic modulus of elasticity of the different lithotypes. Raw results in Annex 2 Table 11, Table 15 and Table 21

IV. Porosity – Comparison of different methods

In the field of conservation digital image analysis (DIA) may facilitate and speed up the characterization of porosity and structure of a material. Methods commonly used to characterize the pore structure need time and require a certain amount of material (e.g. Rilem methods) or are not easily accessible as the mercury intrusion porosimetry (MIP). Even if these traditional methods deliver irreplaceable information, DIA might improve the results on the material structure in an easy and fast way.
A porosity classification using the DIA criteria was defined and related to physical-mechanical properties of materials (Ehrlich et al, 1991).

IV.1. Accuracy of DIA measurements

IV.1.1. Surface area needed for DIA

First step of the study of DIA is to determine the surface area needed to evaluate the porosity in volume or the pore size distribution in an accurate manner. Mosaicing images are the solution to increase the area analyzed appropriately. The number of pictures sufficient to compose the mosaic is achieved when the calculated total porosity converges to a constant value. In the case of sandstones, limestone and marble, mosaics of 6, 12 and 20 pictures were studied, considering respectively a total picture area of 39.3, 78.6, 131.1 mm^2 (magnification x40) (Table 2). Measurements of the total porosity as well as the pore size distribution showed that a mosaic of 12 pictures gives equivalent results to larger mosaics. Moreover, mosaic of 6 and 12 pictures are easy and fast to analyze, while the software due to the number of pixel to count usually cannot handle a mosaic of 20 pictures.

	Total porosity % - 6 pictures	Total porosity % - 12 pictures	Total porosity % - 20 pictures
Highmoor	19.7	19.9	19.2
Cadeby	18.7	23	24.6
Hazel Lane	29.7	29	29.7
Sander	17.8	21.2	19.9
Wüstenzeller	7.9	12.5	11.1
Regensburg	12.8	20.3	21.5

Table 2. Comparison of porosity measured by DIA on different mosaiques.

IV.1.2. Overlapping of two magnifications x 40 and x 100 – comparison of the range of pores 5-40 microns

In order to exclude the risk that the limit of 22 μm (Figure 39) measured by optical microscopy is due to a decreasing methodological sensitivity, an overlap of both measurements is needed. Indeed, by increasing the magnification of the optical microscope at x100 the definition by pixel on the picture is also increased. Therefore, at x100, 1 μm is represented on the picture by 1.2 pixel, while at x40 1 μm was only represented by 0.47 pixel.

By increasing the ratio μm/pixel the limits of pore size measurable by optical microscopy change, and the range of detection goes from 2 μm to 180 μm. This third magnification at x 100 overlaps the range 5 – 40 μm of the pores size distribution taken by both methods as it is shown in the Figure 39.

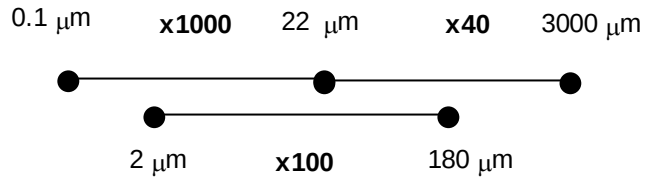

Figure 39. Pore size range measured with optical and electronic pictures.

The two-magnifications x40 and x100 are overlapped and for better comparison, the percent porosity volume for the pore range 5-40 μm is counted for each sample and magnification (Table 3). By overlapping the measurements taken from optical and electronic picture with a third magnification, the accuracy of DIA results is testified.
All following DIA results will derive from measurements from counting on optical pictures at x40 and electronic picture at x1000.

5-40 microns	Wüstenzeller	Highmoor
Por.Vol% x 40	1.4	13.9
Por.Vol% x 100	1.7	14

Table 3. Porosity volume for each magnification and samples for the pore range 5-40 μm

IV.2. Total porosity through water saturation (N_t), mercury intrusion (MIP) and DIA

Before any comparison between the different methods to evaluate porosity volume, it may be important to consider that different methods may give different kind of results. Therefore the pore throats influence the mercury porosity, as this method characterizes more the pore entry size than the total diameter of the pores. In the other hand the DIA also takes into consideration the closed pores and the intercrystralline porosity, not accessible to fluid or gas transport. Higher DIA porosity values than those determined by mercury intrusion and under water saturation might reveal a high closed porosity.

Concerning the sandstones, all methods seem to give very similar porosity result (Table 4). The three methods (water saturation, MIP and DIA) are comparable and in the same range of result for each sample. It is confirmed with the factor analysis, which shows clearly only one main group of correlation (Figure 40). Only one factor could be obtained and therefore only one group of variables exists.

Water absorption porosity results are also similar to the data mentioned in the literature; the literature refers to N_t (%) values from 17 % to 20 % for Sander, from 11 to 14% for Wüstenzeller and around 20% for Regensburg (Sattler, 1992; Grimm, 1990; Meng, 1993).
The pore size distribution is emphasized later (IV.3).

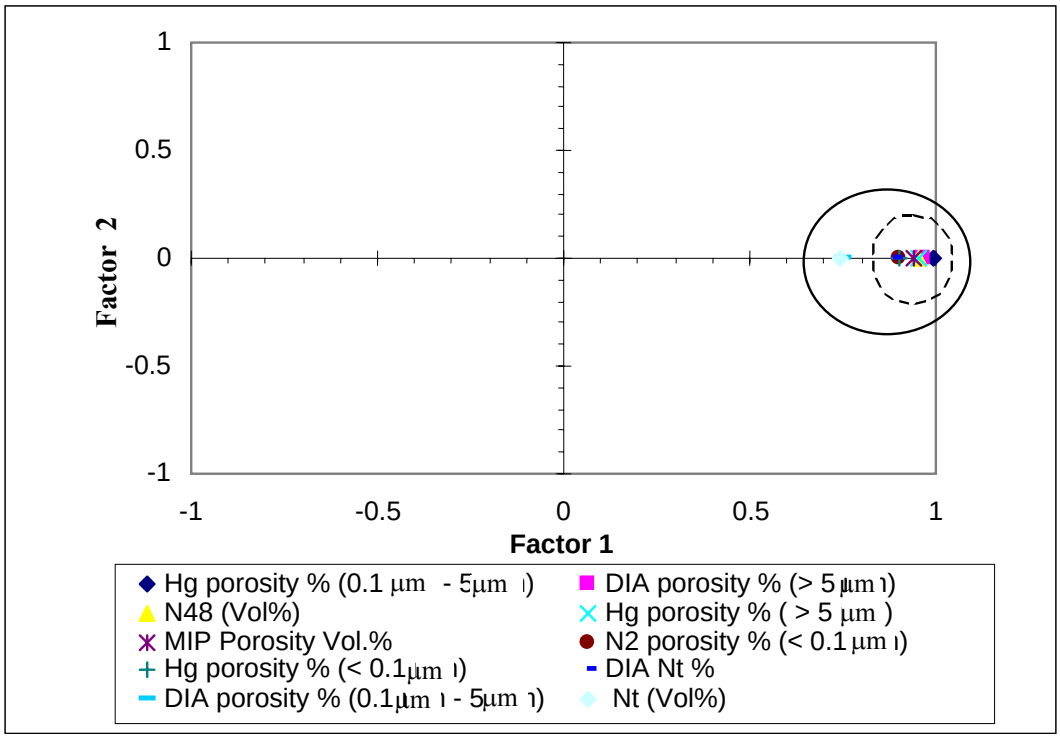

Figure 40. Factor analysis considering the different methods to evaluate porosity and pore size distribution of the sandstones. Raw results in Annex 2 Table 10.

Nevertheless, the best relation that has been obtained on the three sandstones to evaluate porosity by DIA is described by a stepwise multiple regression (equation 42):

$$DIA\ (\%) = 2.29 + 0.48N_t(\%) + 0.58N_{48}(\%) \qquad \pm 1.93 \qquad R^2 = 0.8 \qquad (42)$$

It shows the dependency of the DIA porosity with total and free porosity measured by water absorption. Direct relation can be established between DIA and the other methods to evaluate porosity, but cannot be reduced to one variable.
Mercury porosimetry is influenced by free porosity and therefore by the pore network connectivity (equation 43).

$$MIP\ (\%) = 3.5 + 1.1N_{48}\ (\%) \qquad \pm 2.32 \qquad R^2 = 0.75 \qquad (43)$$

On the other hand, the magnesian limestones reveal some disparities between the methods. The factor analysis illustrates that the three methods are displayed in different places (Figure 41). To explain such a result each magnesian limestones should be taken in consideration individually.
Highmoor stone presents a water saturated porosity higher than the mercury porosity and the DIA. Indeed, it is proved that Highmoor stone presents a very low saturation coefficient and

as well a low open porosity measured at 48 hours. These two measurements illustrate the poor connection of the pores. It can be also observed on optical image (chapter II.I.2) where many of the spherical pores are independent to each other and without connection**.** Therefore, it shows that mercury porosimetry has a realistic limit of intrusion for the pores below 6 nm. This pore range is accessible to sorption isotherm. As it is described in the pore size distribution the pore range < 0.1 μm seems to be underestimated by MIP (Figure 43). Moreover, a higher correlation between the open porosity and mercury porosity exists, than with the total porosity (N_t).
A stepwise multiple regressions considering only the magnesian limestones shows clearly the relation between the two methods; N_t, N_{48} and DIA were the variables selected and only N_{48} remains in the equation 44:

$$MIP\ (\%) = 3.9 + 1.14N_{48}\ (\%) \qquad \pm 1.76 \qquad R^2 = 0.85 \qquad (44)$$

It shows that mercury porosity is influenced by the open porosity and the pore connectivity. Well-connected porosity facilitated the evaluation of the porosity by mercury intrusion.

Additionally, the Proconnesian marble characterized by a specifically well-connected pore network (open porosity N_{48} almost equal to total porosity N_t) presents an equal result between total porosity, mercury porosity and open porosity (Table 4). The significant open porosity of the marble gives a perfect result of the porosity by mercury porosity. DIA is also surprisingly low and comparable to MIP value. However, the aged Proconnesian marble will not be considered as the magnesian limestone and the sandstone and will not be analyzed by factor analysis. Indeed, it will not be accurate to make factor analysis and establish correlation on only one kind of marble. The Proconnesian marble will be only considered for its different shape of pores (porosity of crack) and compared in this way with the limestone (porosity of pore).

As it is visible on the picture from the thin section, spherical pores of Highmoor are mainly the only porosity visible on the image (Figure 10). Connectivity by capillaries is not perceptible on the section. Therefore, it can be assumed that DIA measurement doesn't allow to distinguish capillaries and the whole porosity network at magnification x 40. DIA porosity of Highmoor is also lower than water porosity and porosity is probably underestimated by DIA. Mertz (1991) explained that higher water porosity than mercury porosity can be due to pores on the edge of a small sample, open and directly in contact with mercury. These pores are not taken into consideration during the calculation of the intruded mercury volume.

Hazel Lane presents also an important difference in porosity measurements. Indeed, the DIA porosity is 1.5 higher than the porosity measured under saturated water and mercury. With a look at the structure of Hazel Lane limestone such a disproportion is easily understandable. The oolithic forms characterizing the structure show an important internal porosity (figure chapter II.I.2). The ooliths are very porous and have lost their calcitic binder. Therefore the DIA measurements taking into consideration the entire pore surface, closed and open pores (Andreola, 2000) on the image raised the total porosity counted.
The ooliths also present in Cadeby limestone don't have the same structure and are filled by the micritic grains (figure chapter II.I.2).

The best correlation factor, which can be obtained for the magnesian limestones by a stepwise multiple regressions, is such as equation 45:

$$DIA\ (\%) = 65.03 - 1.26N_t(\%) - 0.69MIP(\%) \qquad \pm 1.5 \qquad R^2 = 0.92 \qquad (45)$$

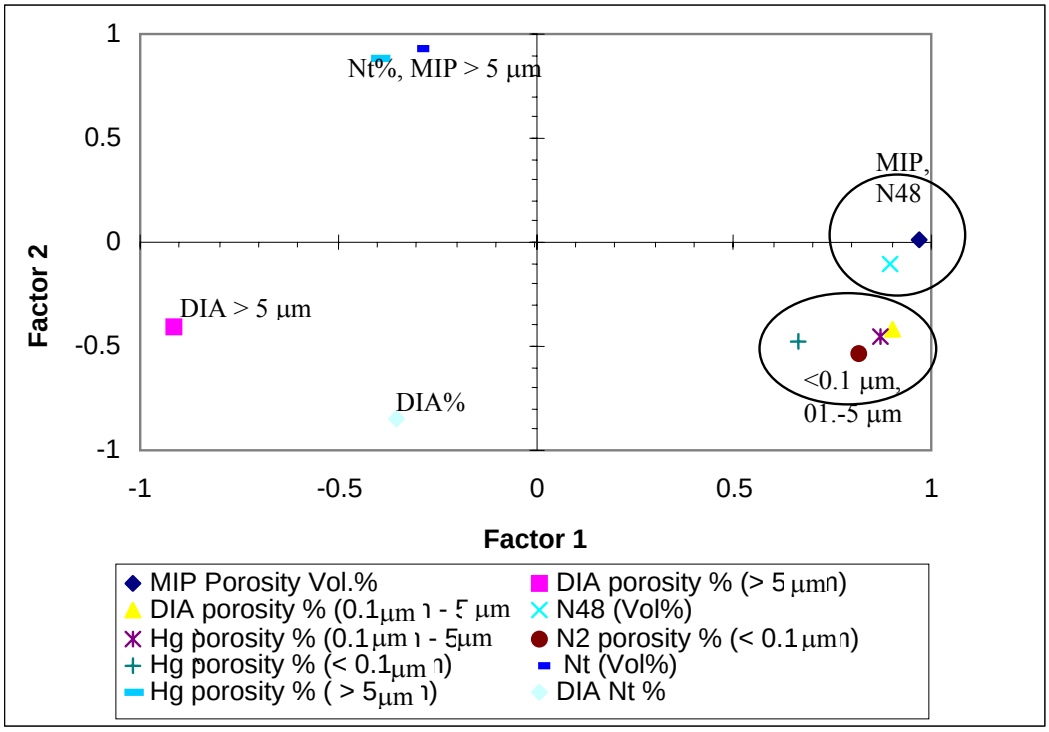

Figure 41. Factor analysis considering the different methods to evaluate porosity and pore size distribution of the magnesian limestones. Raw results in Annex 2 Table 14.

In terms of measuring the total porosity, water absorption, mercury intrusion and DIA may appear comparable. However DIA does not distinct open porosity to close porosity, while the pore network (pore connectivity) largely influences mercury porosity. DIA is reliable to three-dimensional object only if there is no pronounced orientation in the grain structure. It may appear as a useful method to evaluate the porosity of a material but can be mainly influenced by the close porosity; the results may not be accurate. Grouping the three lithotypes the best relation obtained between the different methods is such as equation 46:

$$MIP\ (\%) = 0.99 + 1.31N_{48}\ (\%) \qquad \pm 2.1 \qquad R^2 = 0.91 \qquad (46)$$

MIP measurements can be calculated from this last equation and can be therefore derived from others methods. Free porosity N_{48} appears to be of a main importance as it enters in almost all equations and is directly related to MIP porosity.

Each of the methods gives different kind of results and is therefore not completely exchangeable. Each method might also be related in different ways to physical-mechanical properties and it may be interesting to evaluate their influence on the diverse properties according to each lithotype as will be shown later.

IV.3. Pore size distribution – comparison of pore size entry by mercury intrusion, pore size distribution by nitrogen adsorption and area of pores by DIA

In holistic correlation, it is primordial to define appropriate pore ranges, reflecting the use of the three methods. The results are presented in the Table 4. Unit of the different pore ranges are in % of the total porosity in vol % (ex: 5.2 % of pores 0.1-5 μm of the 22 % total porosity).

Therefore, three pore ranges are determined according to Nieminen and Uusinoka (1988):

- < 0.1 μm where capillary condensation takes place;
- 0.1 – 5 μm representing the capillary pores
- > 5 μm range allowing the free water to penetrate the porous material (Nieminen and Uusinoko., 1988).

On a first view the three methods seems to show similar results for the sandstones, magnesian limestones and Proconnesian marble; Hazel Lane magnesian limestone shows huge difference, which are mainly linked to its oolithic structure including many closed pores (Table 4; Figure 44; Figure 45; Figure 46).

Stones	Methods	Total Porosity (Vol %)	< 0.1 (µm)	0.1 - 5 (µm)	> 5 (µm)
Sander	N_t	22 ±1.81			
	N_{48}	17.8 ±0.47			
	N_2-Sorption	3.8 ±0.32	3.8		
	MIP	23.7 ±2.5	1.6 ±0.11	5.5 ±0.38	16.6 ±0.74
	DIA	21.8 ±1.47		4.2 ±0.21	17.6 ±0.59
Wustenzelle	N_t	13.9 ±1.12			
	N_{48}	10.1 ±0.01			
	N_2-Sorption	1.1 ±0.03	1.1		
	MIP	13.4 ±0.72	0	0.4 ±0.15	13 ±0.84
	DIA	13.3 ±0.29		1.1 ±0.26	12.2 ±0.62
Regensburg	N_t	19.1 ±0.62			
	N_{48}	12.1 ±0.38			
	N_2-Sorption	1.5 ±0.04	1.5		
	MIP	18.2 ±1.53	0.3 ±0.03	4 ±0.97	13.9 ±1.56
	DIA	20.3 ±3.18		6 ±0.64	14.3 ±0.36
Highmoor	N_t	25 ±1.76			
	N_{48}	12.6 ±0.86			
	N_2-Sorption	0.6 ±0.08	0.6		
	MIP	18.4 ±0.95	0.4 ±0.16	6.5 ±1.29	11.6 ±1.32
	DIA	19.3 ±0.36		4.5 ±0.11	14.8 ±0.36
Cadeby	N_t	21.5 ±1.33			
	N_{48}	19 ±2.3			
	N_2-Sorption	0.9 ±0.13	0.9		
	MIP	25.9 ±1.81	0.7 ±0.2	19.2 ±2.39	6 ±2.06
	DIA	20.2 ±0.4		14.6 ±0.22	5.6 ±0.92
Hazel Lane	N_t	18.5 ±0.33			
	N_{48}	15.8 ±0.48			
	N_2-Sorption	0.8 ±0.06	0.8		
	MIP	19.6 ±1.75	0.5 ±0.23	15 ±1.8	4.3 ±0.93
	DIA	28.7 ±0.51		9.4 ±0.1	19.3 ±0.51
Proc. Marble (cooked)	N_t	1.7 ±0.04			
	N_{48}	1.5 ±0.09			
	N_2-Sorption	0.11 ±0.02	0.11		
	MIP	1.5 ±0.08	0	0.6 ±0.16	0.9 ±0.11
	DIA	1.3 ±0.22		0.4 ±0.26	0.9 ±0.18

Table 4. Table grouping total and free porosity, and pore size distribution according to each method – 3 pore ranges are selected – values presented are averages of 5 measurements. Raw results in Annex 2 Table 10, Table 14 and Table 20.

At this point it is essential to remember that the two methods provide different kind of results. As it has been demonstrated, the mercury porosimetry measures the size distribution of the pore entry, while the DIA presents the cross section of pores on the thin section and is probably reliable to 3D pore model only if there is no preferential orientation.

The distribution given by MIP measurement reveals the pore throats as it is linked to the pressure necessary for the MIP to penetrate the pores. DIA considers the porosity represented by a surface area and must include pore area and capillary tube area as well. Therefore in terms of pore distribution, both methods are not comparable, but remain complementary and may be linked to different physical-mechanical properties.
Moreover, the MIP measurements consider a cylindrical pore model (cf. I.3). The model of independent cylindrical pores is a great simplification of real systems of interconnected pores (Boucher, 1976). Indeed, pore geometry in sandstone is much more complex and different geometries can be distinguished. First, the nodal pores are supposed to be spherical, the sheet-like throats supposedly flat and the tube-like throats with a circular cross-section (Bernabe, 1991) (Figure 42). For the sheet-like throats the model applied to calculate the pore size is different taking into consideration the distance d between the two walls instead of the assumed radius r. Therefore, pore shapes and pores size are correlated in sandstones and some specific studies demonstrated that nodal pore size ranges from 20 to 100 μm and throat size from 0.8 to 14 μm (Wardlaw, 1979). According to the authors the throats control the transport properties, whereas the nodal pores command the storage capacity. Therefore, the cylindrical model used to calculate pore size by MIP may be not accurate for the sheet-like throats, which can be below 14 μm, as the mechanisms of filling and emptying are completely different: multilayer formation in one hand and capillary evaporation on the other (Gregg and Sing, 1982).

Moreover, in natural stone the sides of the sheet-like throats will be rarely parallel or planar and some plates can touch their neighbors and produce as well wedge-shaped pores.

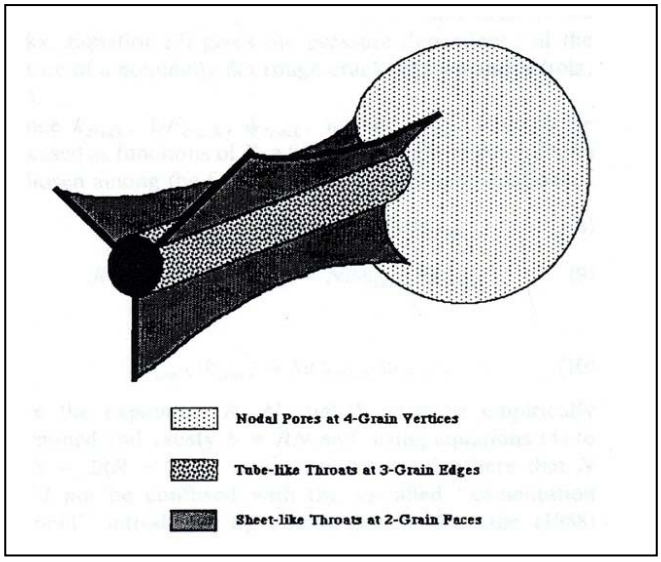

Figure 42. Schematic representation of the pore geometry of sandstones (after Bernabe, 1991).

On the other hand, mercury porosimetry can overestimate smaller pores and underestimate larger pores in the case of inkbottle pores. If a small pore of a radius is connected to a larger pore of a radius, the mercury can enter the large pore only when the pressure to enter the smaller pore is reached according to Laplace law. Both pores are invaded simultaneously and the volume considered is only the one of the smaller pore class. Therefore, large pore class can be underestimated and vice-versa, smaller pores class can be overestimated (Andriani and Walsh, 2003). This is even more relevant for a bimodal pore radius distribution.

The Figure 43 presents the N_2 adsorption isotherm of the different magnesian limestone and the sandstones.
Through the classification differences between the stones in each lithotypes are visible.

Sander with clay reach binder presents the highest quantity of pores below 0.1 µm (Table 4). Moreover, Sander and Regensburg show a similar percentage of capillary pores in the range 0.1-5 µm, around 5%, while Wüstenzeller is for the same pore range below 1% (Table 4). Sander stone also shows the highest percentage of pores > 5 µm (17%), while Wüstenzeller and Regensburg are similar for the same pore range, between 13-13.5%. Sander has therefore a wide pore range and Wüstenzeller shows a real unimodal pore size distribution (Figure 45).
The factor analysis clearly shows that all methods to evaluate pore size distribution are grouped and correlated to each other (Figure 40).

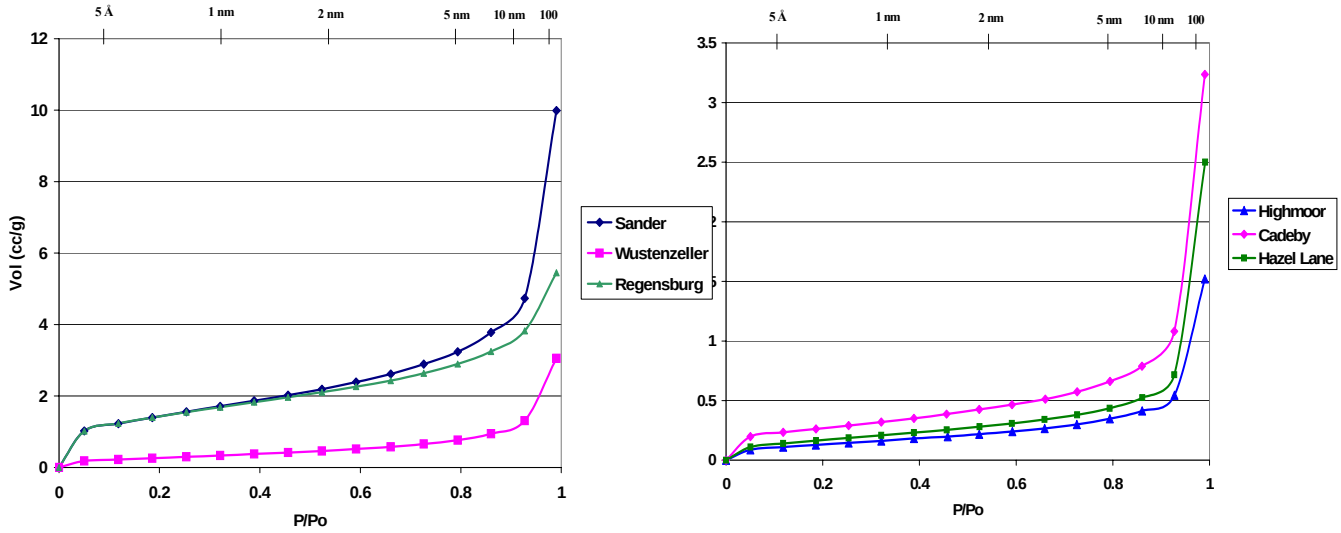

Figure 43. N_2 adsorption isotherm of the sandstones and magnesian limestones.

Concerning the magnesian limestone their N_2 adsorption shows an adsorption close to Regensburg and Wüstenzeller sandstones. Some distinctions between each limestone are manifest and reveal a highest porosity < 0.1 µm of Cadeby stone, while Highmoor presents the lowest. Because of the soft preconditioning drying at 60ºC most microporosity may not be accessible to N_2. The microporosity might be revealed only after drying above 110ºC, which is not feasible for calcitic stones, because of creating new fissures in the material. However the factor analysis proved a good correlation between N_2 and MIP for the same pore range < 0.1 µm.
Highmoor has the lowest quantity of pores in the capillary range 0.1-5 µm (5-6% for Highmoor; > 10% for Cadeby and Hazel Lane) as well as for the range < 0.1 µm. On the other hand, Highmoor shows the highest percentage in the range > 5 µm (> 12%), probably nodal pores evident on DIA, while Cadeby has only around 6% (Table 4). Hazel Lane also illustrates a high quantity of nodal pores > 5 µm in DIA, but they are mainly closed inside the ooliths.

Differences in pore size distributions with Highmoor on one side and Cadeby and Hazel Lane on the other might contribute to low pore connectivity of Highmoor and low free porosity with many nodal pores connected to few capillary pores. The high amount of capillary pores of the two other stones may increase the pore network connectivity and lead to a higher free porosity. Concerning the gap between both methods for Hazel Lane magnesian limestone, it can be explained by its porous oolithic structure. Indeed, DIA measurement reveals already an over estimation of the total porosity because of the important intern porosity of the ooliths. This miscalculation is also present in the DIA > 5 µm pore size distribution, which corresponds with the size of the ooliths intern porosity.

The factor analysis reveals the separation of the pore size > 5 µm as a function of the methods used (Figure 41). Indeed, pore range < 0.1 µm and 0.1-5 µm are correlated to each other and are grouped together, while pore DIA > 5 µm is isolated and MIP > 5 µm is linked with total porosity N_t. It shows the particularity of this pore range, which is probably due to spherical pores of Highmoor and Hazel Lane. The addition of closed pores in Hazel Lane in the DIA > 5 µm separates it from the MIP > 5 µm.

The aged Proconnesian marble shows a very low porosity < 0.1 µm at 0.11% and a bimodal pore size distribution with two mainly equal ranges at 0.1-5 µm and > 5µm.

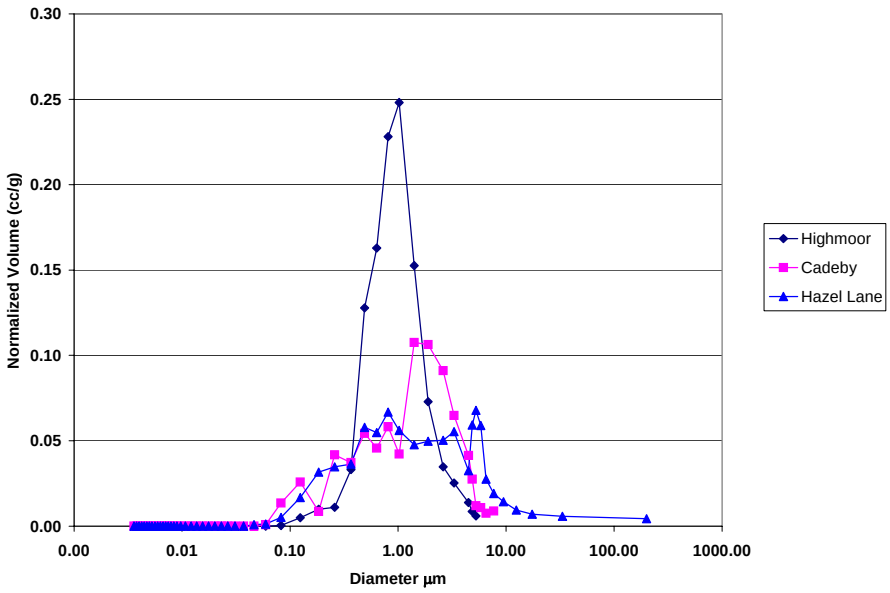

Figure 44. Pore size entry distribution by mercury porosimetry of the three magnesian limestone.

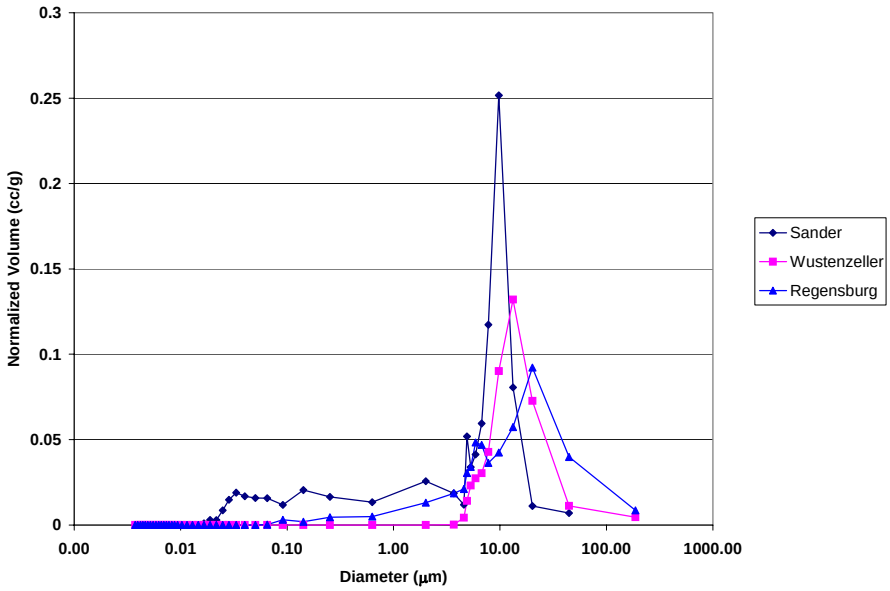

Figure 45. Pore size entry distribution by mercury porosimetry of the three sandstones.

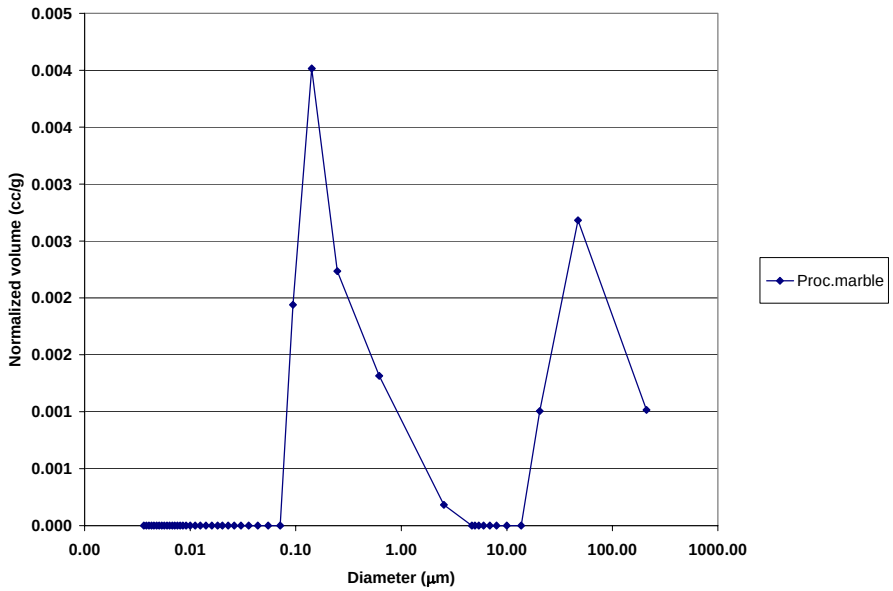

Figure 46. Pore size entry distribution by mercury porosimetry of the Proconnesian marble cooked.

In conclusion, DIA might be a good tool to evaluate nodal pore > 5 µm by measuring its surface, when the specimen presents spherical pores and unimodal pore size distribution or closed porosity. Moreover, DIA < 5 µm might not be really accurate as the pore may be difficult to discern to each other and the blue dye used for the thin section may create a "halo" around the pores. Open spherical pores control the water storage. MIP, through the cylindrical pore model, might be more accurate to evaluate the tube-like throats 0.1-5 µm and therefore the transport properties.

Concerning the sheet-like throats they might be not well discerned by MIP measurements, as they are included in the cylindrical model. This observation obviously has an influence on sandstone where some sheet-like throats may be formed between the joint grains and especially for the Proconnesian marble, where the porosity is mainly of this kind. Finally, pores < 0.1 μm measured by N_2 adsorption are always superior to MIP measurements. It might demonstrate that MIP measurements is very precise in a range 0.1-0.01 μm but inaccurate close to the limit of the measurements < 6 nm, where N_2 measurements are the most precise.

IV.4. Correlation porosity properties vs. structure characteristics and ultrasonic velocity

Relationships can be established between the structure characteristics and the porosity properties just determined. The use of factor analyses underlined clearly the different group of variables, which are associated. Unit of the different pore range are in % of pore vol.

The magnesian limestone

Factor analysis displays two groups on each extremity (Figure 47). The first one is composed by the pore ranges < 0.1 μm and 0.1-5 μm and is directly opposed to the air trapped porosity or inkbottle pores (calculated from the difference between the total porosity N_t and the free porosity N_{48}). It shows that an increase of capillary pores between 0.1-5 μm reduced the inkbottle pores (equation 47).

$$\text{Air Trapped \%} = 18.93 - 0.81\ \text{MIP 0.1-5 μm} \qquad \pm 2.38 \quad R^2 = 0.85 \qquad (47)$$

Concerning the total porosity N_t, it is correlated with pore volume MIP > 5 μm.; large pores increase the total porosity extensively according to the equation 48:

$$\text{Nt (\%)} = 17.45 + 0.66\ \text{MIP} > 5\ \mu\text{m} \qquad \pm 1.78 \quad R^2 = 0.72 \qquad (48)$$

The factor analysis shows the direct association of QI with ultrasonic velocities measurements (equation 49). QI representing the discontinuities in the structure and calculated from the ultrasonic measurements is logically correlated with this non-destructive method. QI is perfectly related with the ultrasonic velocity measured parallel to the stone bedding, while with the ultrasonic velocity perpendicular to the bedding the correlation factor is only of 0.79. It proves that discontinuities revealed by the QI follow the bedding of the stone.

$$\text{QI\%} = 14.37\ V_p\ \text{parall (km/s)} \qquad R^2 = 1 \qquad (49)$$

Along the same axis a third group can be drawn with the DIA > 5μm and the dynamic modulus of elasticity. This relation is weak but can have an influence on the elasticity properties of the magnesian limestone. Indeed, porosity measured by DIA > 5 μm illustrate more nodal pores well determined by this method, which is efficient in measuring large and distinct surface area.

In the same time, pore shape factor (ratio water saturated ultrasonic velocity vs. dry ultrasonic velocity) presents a negative relation with the ultrasonic measurement and even more with the DIA > 5 µm and the dynamic modulus of elasticity. DIA > 5 µm and pore shape factor are graphically opposed and show that higher is the factor, more important is the crack porosity and lower is the DIA > 5 µm. It demonstrates that DIA > 5 µm characterizes a porosity of pores and that crack porosity reduces ultrasonic velocities and dynamic modulus of elasticity, while pore porosity enhances them. The pore shape is therefore of a main importance to evaluate and assess dynamic modulus of elasticity of the magnesian limestone. Indeed, QI seems also to be related to the pore shape factor (opposed on the same axis) but does not present a direct correlation as the two variables are opposed on the same side of the axis (no symmetry). On the other hand QI is related to the pore volume DIA > 5 µm. Therefore, an indirect relation can be established which demonstrates that the Quality Index may be linked to the pore shape and to the dynamic modulus of elasticity according to the following equation, 50, 51 and 52 and Figure 48:

$$Psf = 0.07 - 0.003DIA_{>5\mu m} \quad \pm 0.01 \quad R^2 = 0.8 \quad (50)$$

$$E\text{-}Dyn\ (kN/mm^2) = 19.96 + 0.58DIA_{>5\mu m} \quad \pm 2.97 \quad R^2 = 0.65 \quad (51)$$

$$QI\% = 46.95 + 0.85\ DIA_{>5\mu m} \quad \pm 3.1 \quad R^2 = 0.8 \quad (52)$$

For the magnesian limestone the structure characteristics play a great role in the porosity properties and the ultrasonic transmission. Spherical pores illustrated by the pore shape factor and the DIA > 5 µm increase the dynamic modulus of elasticity and is indirectly linked to the QI, which underlines discontinuities inside the structure.

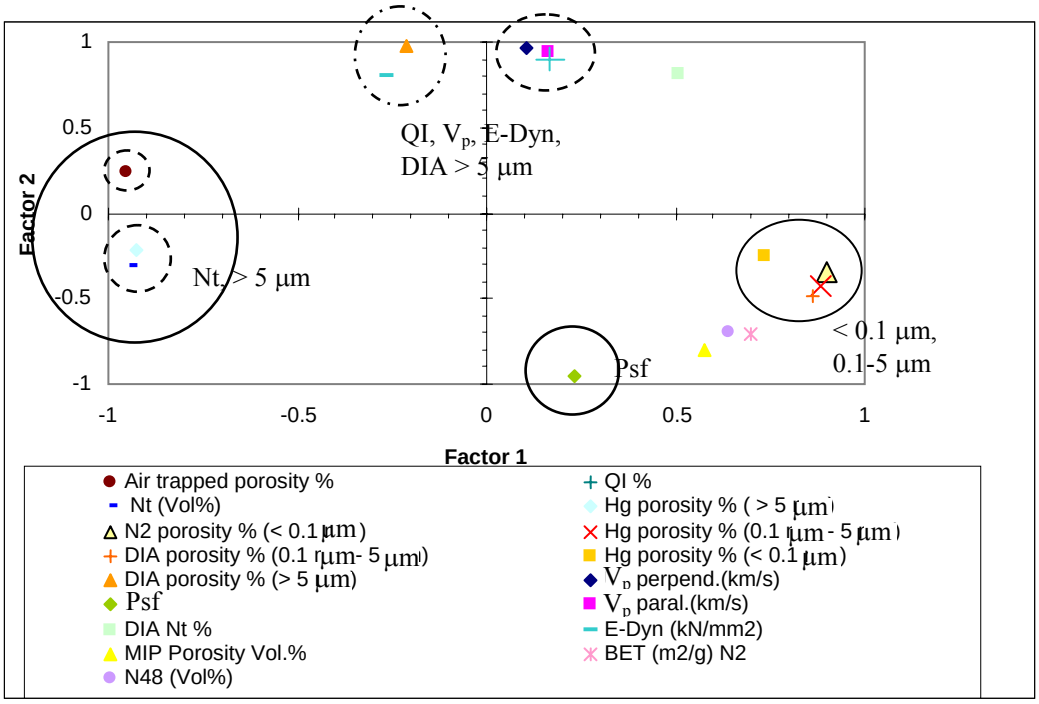

Figure 47. Factor analyses considering the structure characteristics and the porosity properties of the magnesian limestone.

If the aged Proconnesian marble is integrated in the correlation pore shape factor versus DIA > 5 µm, it confirms that DIA > 5 µm corresponds to a porosity of spherical pores (Figure 48). Indeed, the Proconnesian marble is characterized by a porosity of crack (III.3.1) and shows a DIA > 5 µm closed to zero; the aged Proconnesian marble and the magnesian limestone are totally opposite in the diagram.

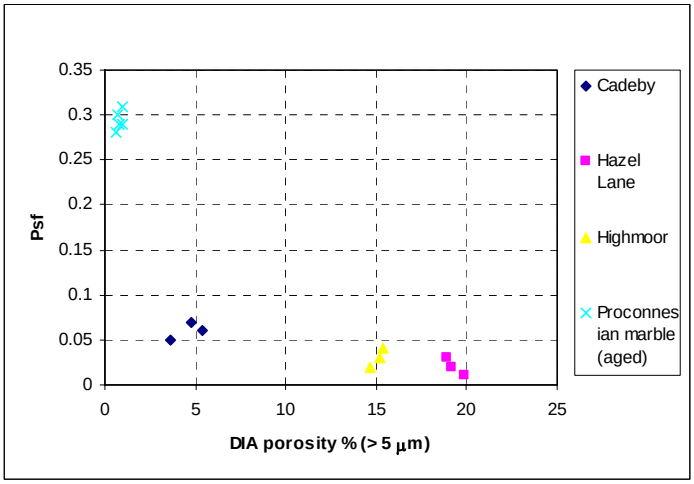

Figure 48. Scatterplot of the magnesian limestone and the aged Proconnesian marble on the diagram Psf versus DIA > 5 µm. Raw results in Annex 2 Table 14 and Table 20.

The sandstones

Concerning the sandstones two groups of variables are clearly opposed. One is composed by different structure characteristics, the other one by many of the porosity properties (Figure 49). However, finest distinctions can be established.

QI is, as for the limestone, correlated with the ultrasonic velocity measurements and also with the dynamic modulus of elasticity as well as the large grain size 400-2000 µm (medium sand class, ASTM D422) (equation 53, 54 and 55). Such a group of variables, all correlated, demonstrate that large grain size contributes to increase the ultrasonic velocity inside the material, improve the QI and therefore decrease discontinuities inside the structure, and finally increase the dynamic modulus of elasticity. As it is shown in the following equation, QI is still perfectly correlated with the ultrasonic velocity parallel to the stone bedding and reveal the preferential orientation of the discontinuities inside the structure. Ultrasound perpendicular to the bedding present a correlation coefficient with the QI of only 0.5.

$QI\% = -2.27 + 16.82\ V_p$ parall (km/s) ±0.36 $R^2 = 1$ (53)

$QI\% = 36.79 + 0.18$ Gr400-2000 µm % ±0.86 $R^2 = 0.97$ (54)

E-Dyn (kN/mm^2) = 8.54 + 0.1 Gr400-2000 µm % ±1.29 $R^2 = 0.80$ (55)

On the other hand, others variables may decrease the dynamic modulus of elasticity, ultrasonic velocity and therefore the QI. These variables are represented in the opposed group and are composed with small pore volume < 0.1 μm, the free porosity N_{48}, and the fine grain size between 2-80 μm, the silts section (equation 56 and 57). It shows the intimate relation between pore size distribution and grain size distribution, where smallest pore volume is closely related to the presence of silts. These grains increase small pore volume but also are probably the main factor introducing discontinuities and decreasing ultrasonic velocity as the following equation show.

$$MIP < 0.1\ \mu m = 0.02\ Gr2\text{-}80\ \mu m\ \% \qquad \pm 0.15 \qquad R^2 = 0.93 \qquad (56)$$

$$QI\% = 46.55 - 6.31\ MIP{<}0.1\ \mu m \qquad \pm 1.37 \qquad R^2 = 0.92 \qquad (57)$$

When QI and pore shape are in a negative correlation for the limestone (porosity of crack creating discontinuities), they are positively correlated for the sandstones; QI is enhanced in the same time that the crack porosity (pore shape factor increased). This crack porosity does not create discontinuities in the structure to decrease the QI. As it was observed and determined for QI correlations, pore shape factor and ultrasonic velocity is increased with the medium sand class 400-2000 μm and decreased with the silt portion 2-80 μm. For instance, Wüstenzeller presents the lowest grain percentage in the range 2-80 μm, low free porosity and also plate pore shape. Relation between porosity properties and the pore shape factor could have been directly simplified to one variable the free porosity (N_{48}) and show that the pore connectivity decreases with an increase of plate shape pore such as equation 58:

$$Psf = 0.29 - 0.01 N_{48}\% \qquad \pm 0.01 \qquad R^2 = 0.94 \qquad (58)$$

Finally, pposed to this group are the porosity properties. Large pores > 5 μm as well as MIP 0.1-5 μm and MIP porosity are also dependent on grain size and pore shape, but also grain contact. The higher are these porosity ranges and the lower is the grain contact. This last variable is correlated with the grain class 80-400 μm representing the fine sand. It demonstrates that this grain class has a specific role in filling the space between the larger grains and therefore improves the contact between all the grains according to the equation 59:

$$Gr\ 80\text{-}400\ \mu m = 0.5\ Gc\ \% \qquad R^2 = 0.98 \qquad (59)$$

Large grains do not necessarily enhance grain contact but it is how the grains are spatially distributed and fill the empty space. As well Wüstenzeller shows an important class of grains in the range 80-400 μm associated with an important amount of grains in the class 400-2000 μm and a small quantity of grains in the range 2-80 μm. The equation 60 emphasizes the correlation between the grain contact and the pores 0.1-5 μm:

$$Gc\ (\%) = 82.87 - 8.76\ MIP\ 0.1\text{-}5\ \mu m \qquad \pm 6.0 \qquad R^2 = 0.94 \qquad (60)$$

Finally, the grain class 80-400 μm plays a last role in reducing the specific surface area (BET). It can be assumed that presence of fine sand in the material may contribute in reducing the micro porosity such as equation 61:

Gr 80-400 µm = 46.1 – 4.8 BET (m^2/g) ±2.9 $R^2 = 0.94$ (61)

The study of the sandstones underlines the intimate relation existing between the spatial arrangement of grains and their size with the determination of pore size distribution as well as with the conduction of ultrasonic waves, dynamic modulus of elasticity and grain contact. Therefore, DIA is probably of a great interest to evaluate grain size distribution. Indeed, determination of grain size is not as affected by a 3D representation, as the pore size distribution could be. Moreover, grain size might be related to others properties (water transport, mechanical properties) and thus might be a key element to assess general material behavior in a simple and rapid way.

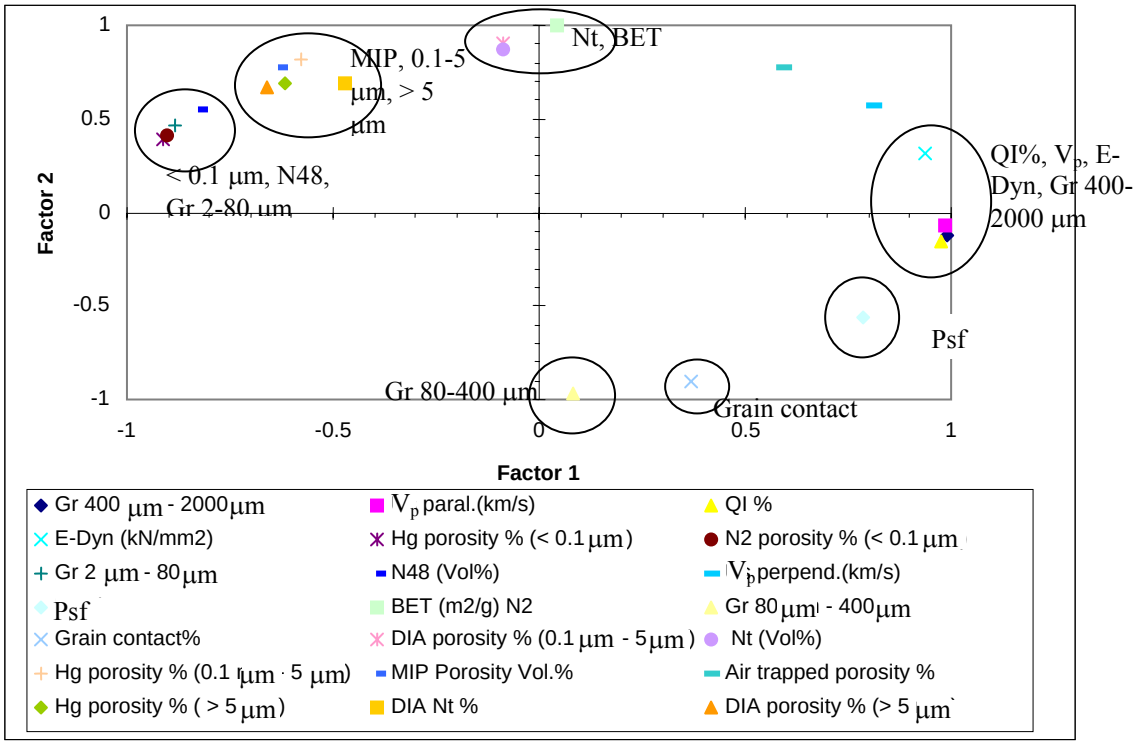

Figure 49. Factor analyses considering the structure characteristics and the porosity properties of the sandstones.

IV.4.1. In summary

For the magnesian limestone, pore shape factor defines the pores measured by DIA > 5 µm and can influence slightly the dynamic modulus of elasticity (equation 50 and 51). Moreover, spherical pores or nodal pores improve the elasticity properties, as they are less deformable than porosity of cracks (Guéguen and Palciauskas, 1992).
On the other hand, discontinuities in the structure are directly illustrated with the Quality Index and is linked to the pore shape and to the dynamic modulus of elasticity.

For the sandstones, structure characteristics are closely linked to each other. A logical and clear association is drawn where grain size distribution determines special arrangement of the

grain, their contact (fine sand 80-400 μm), the shape and the size of the pores and the pore network connectivity; sandstone correlations prove that all variables influence each other and therefore that all properties can be deducted from selected variables.

V. Physical properties

As Hoffmann (1996) said truly "because all characteristics are coupled anyhow one with another – directly or indirectly – each small value is for the time being a step in the direction of the sought objective to explain behavior of a stone by its physical-technical data, to forge a link between a porous material's structure and its intrinsic characteristics".

V.1. Physical properties characterization

V.1.1. Saturation coefficient, S

The saturation coefficient or Hirschwald coefficient potentially indicates the susceptibility of stone to frost damage. As a reminder Hirschwald coefficient ranges are: $S > 0.85$ susceptible; $0.75 < S < 0.80$ moderate resistance; $S < 0.75$ frost resistant. Theses ranges correspond to the water saturation of the pore network and are therefore directly linked to the free porosity measured at 48 hours and the pore connection.
The measured saturation coefficient of the various stones are given in the Figure 50 and in the Table 14. Sander sandstone has a saturation coefficient of 0.8, meaning that 80% of its porosity can be saturated by water and enters therefore in the moderate resistant frost category. On the other hand, Wüstenzeller and Regensburg present a saturation coefficient between 0.6-0.7 and may be considered as well frost resistant. Literature data of Sattler, (1992), Schuh (1987) and Grimm (1990), confirm the results.
The magnesian limestone illustrates great differences between each other. Indeed, Highmoor stone reveals a saturation coefficient of 0.5, which results from its poor pore connectivity. Hart, (1988) published same saturation coefficient (Figure 50). Hazel Lane stone has a saturation coefficient of 0.8, while Cadeby presents a saturation coefficient equal to 0.9; the whole pore network can almost be water saturated. Here again the literature data confirm the results.
Finally, the aged Proconnesian marble also shows a saturation coefficient of 0.9. Artificial ageing created cracks along the grains and open the pore network such as the entire porosity may be water saturated.

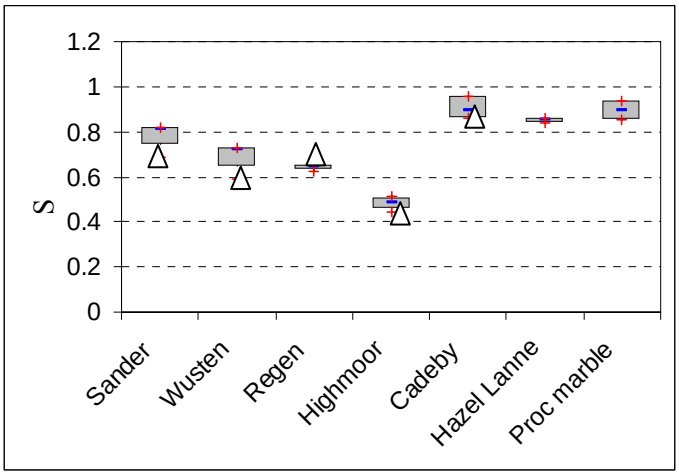

Figure 50. Saturation coefficient of the three lithotypes according to equation 8. Raw results in Annex 2 Table 9, Table 14 and Table 19

△ Literature data Sattler 1992, Schuh 1987, Grimm 1990 and Hart 1988.

V.1.2. The water uptake coefficient

The capillary curves of Sander and Regensburg present two distinct parts as shown in Figure 51. The first part of the curve is linear as a function of the time root, while the second part of the curve shows a sort of plateau (Figure 51). The linear part of the curve represents the water absorption by the free porosity, open porosity to water capillary. The second part of the curve occurs when the free porosity of the material is saturated and the capillary rise reach the top of the sample. The micropores continue to be slowly filled especially for Sander sandstone, which present many micropores (Figure 44), but no more important water uptake happens and the curve runs horizontally.

For the sandstones, Sander shows the highest water uptake coefficient (4 $kg/m^2/h^{0.5}$) (equation 29) and also an important water penetration coefficient (B = 2.8 ± 0.2 $cm/h^{0.5}$) (equation 30) (Figure 52 and 52). Regensburg presents a water uptake in the same range (3.5 ± 0.5 $kg/m^2/h^{0.5}$) and the highest water penetration coefficient, B = 4.1 ±0.1. Both stones show the starting point of the plateau and prove also a fast saturation of the free porosity after 6h for Sander and 4 h for Regensburg. Finally, Wüstenzeller with a low water uptake coefficient (1 $kg/m^2/h^{0.5}$) doesn't show after 24h a saturation of the free porosity, the curve is still linear. The water front has not reached the surface.

B-values from the literature confirmed the measurements (Sattler, 1992; Schuh, 1987); with a B-value of 2.2 $cm/h^{0.5}$ has been measured for Sander and 2.34 $cm/h^{0.5}$ for Regensburg.

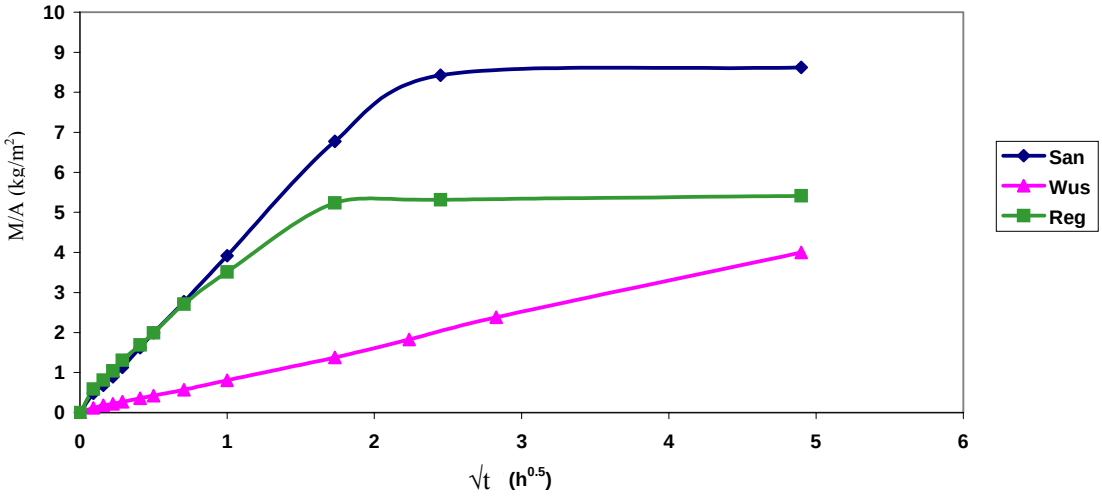

Figure 51: capillary curves of the sandstones

As well we can consider that the difference between the three sandstones in their capillary behavior is linked to a variation in the throat radius and the pore network. Indeed, Wüstenzeller presents the lowest percentage of capillary pores in the range 0.1-5 µm with 0.4% ± 0.1 while Sander and Regensburg have respectively 5.5 % ±0.4 and 4 % ±1 of pores in this range (Table 4). Moreover Sander shows the highest porosity < 0.1µm as well as the highest proportion of pore > 5 µm. Evaluating the pore range influencing the water uptake of the sandstones is an important factor to understand water transport properties. Indeed, looking at the pore entrance distribution of Wüstenzeller (Figure 44) the high proportion of pores > 5 µm should contribute to a high water uptake. Nevertheless, it will be proved in the factor analysis and the correlation that the pore range > 5 µm was also considered and did not show a good correlation with the water uptake coefficient. Only the pore range 0.1-5 µm was correlated with the water uptake. Therefore it emphasizes that it is this pore range 0.1-5 µm, which influence the most the water uptake coefficient and confirm the low coefficient of Wüstenzeller.

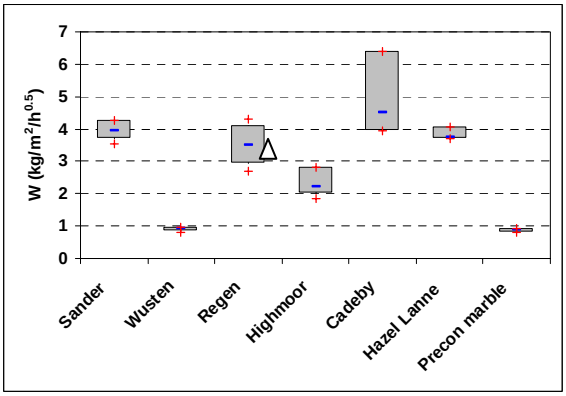

Figure 52: Water uptake coefficient W of the sandstone, limestone and marble

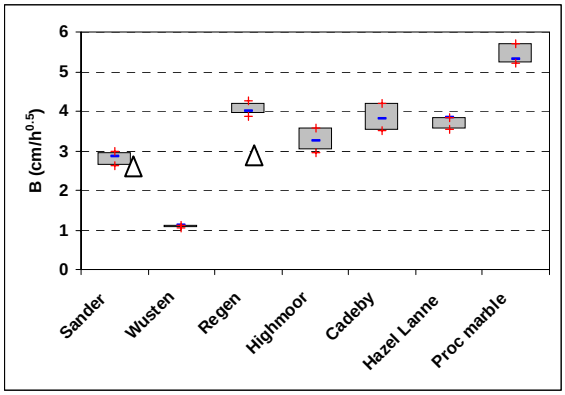

Figure 53: Water penetration coefficient B
Δ literature data Sattler 1992, Schuh, 1987

Raw results in Annex 2 Table 11, Table 16 and Table 21.

Similar consideration can be made for the magnesian limestones, where Highmoor presents the lowest water uptake and capillary rise (Figure 52 and Figure 52) and presents the lowest quantity of capillary pores 0.1-5 µm, around 6.5% ± 1.3. The low pore connectivity of Highmoor stone has been already described (IV.2) and may also influence the water uptake. Highmoor with its high percentage of nodal pores, probably > 5µm, are connected to a low percentage of capillary pores 0.1-5 µm; the stone is also not entirely saturated after 8 hours. On the other hand, Cadeby shows the highest porosity values in the range 0.1-5 µm with 19.2% ±2.4 and a low porosity > 5µm with 6% ±2 (Table 4). The connection between the different ranges of pores is as well optimized with more capillary pores than large pores.

Hazel Lane capillary curve being similar to Cadeby, they may have a similar percentage of pores in the range 0.1-5 µm as the mercury porosimetry suggested it (Table 4). Nervertheless, a distorsion of the curve of Cadeby can be observed and can be due to a slow filling of its microporosity. Cadeby has the more important porosity < 0.1µm between 0.7-0.9%. Cadeby and Hazel Lane have reached complete saturation.

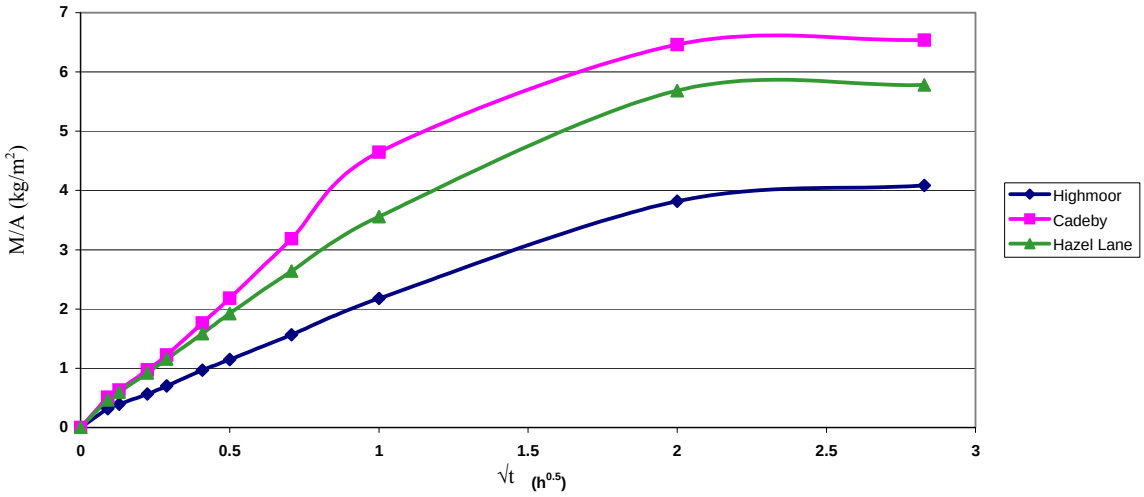

Figure 54: capillary curves of the magnesian limestones

The Proconnesian marble with a water uptake around 0.8 kg/m^2/h$^{0.5}$ is presented in a separate graphic because of the scale difference (Figure 55). The low porosity of the Proconnesian marble leads naturally to a low water uptake coefficient. The porosity is also equally divided between the two pore ranges 0.1-5 µm and > 5 µm (Table 4), which may lead to a good pore connection and an important free porosity measured at 48 hours. N_{48} = 1.5% Vol while N_t = 1.7 %Vol. The low porosity of the aged Proconnesian marble involved a low water uptake coefficient, while the volume of large pores and their good connection lead to a fast water absorption and a high capillary rise. The capillary rise was not measured but calculated from the saturation point of the water uptake coefficient measurement.

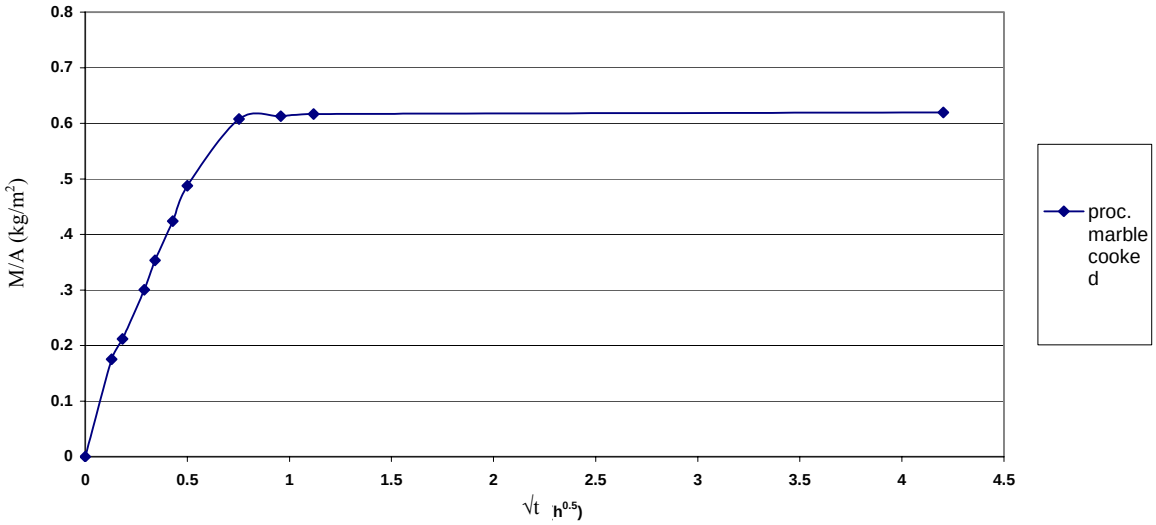

Figure 55: capillary curve of the Proconnesian marble.

V.1.3. The drying kinetics properties

Wüstenzeller and Regensburg seems to have similar drying curves and especially water flow rates (measured on the plateau, liquid phase), respectively 120 and 130 g/m^2.h (Figure 56 and Figure 57); a large plateau and a slow decrease of the water flow rate. Sander stone indicates a very high water flow rate > 250 g/m^2.h. In term of pore size distribution, Sander has the highest quantity of pores > 5µm (16.6% ±0.7), while Wüstenzeller and Regensburg presents lower percentage of pores in these two ranges (respectively 13 % ±0.8 and 13.9 % ± 1.5 > 5 µm).

Water vapor conductivity coefficient from the surface to the air (Figure 58) is varies from 0.2 to 1.05 as a function of the sandstones (Figure 58) (equation 32). Sander shows the highest (β = 1.05) and Regensburg presents values close to Sander (β = 0.9 ± 0.05), while Wüstenzeller has the lowest coefficient (β = 0.2). At this point it is difficult to link this coefficient to a specific porosity but Sander and Regensburg showed already a high specific surface area and an important range of pores < 0.1 µm, which may lead to high surface conductivity. This observation will be further investigated in the chapter.

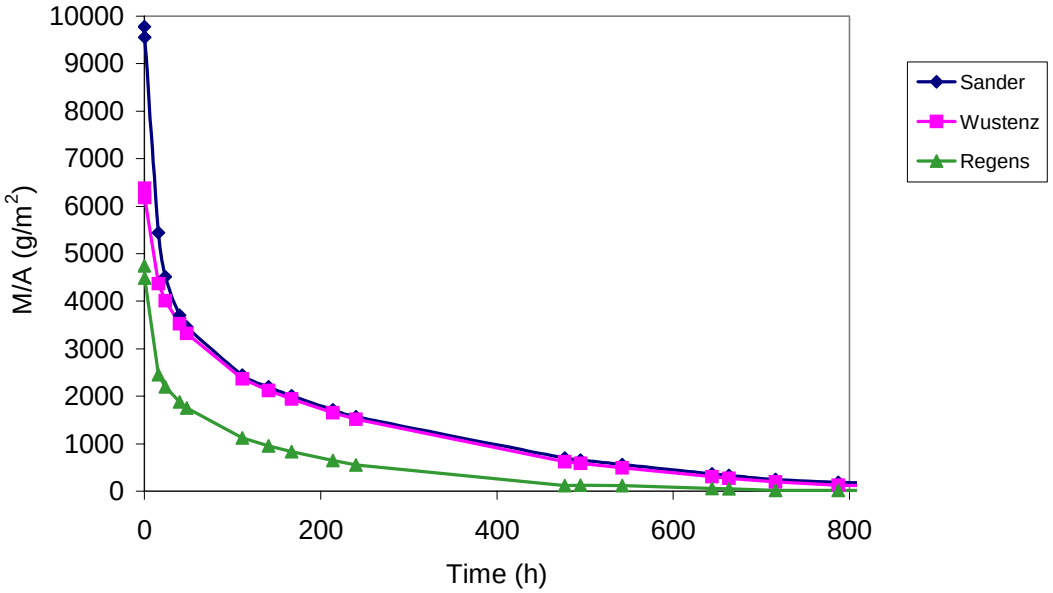

Figure 56: Drying curves showing the loss of the mass M normalized to the area A as a function of time of the sandstones.

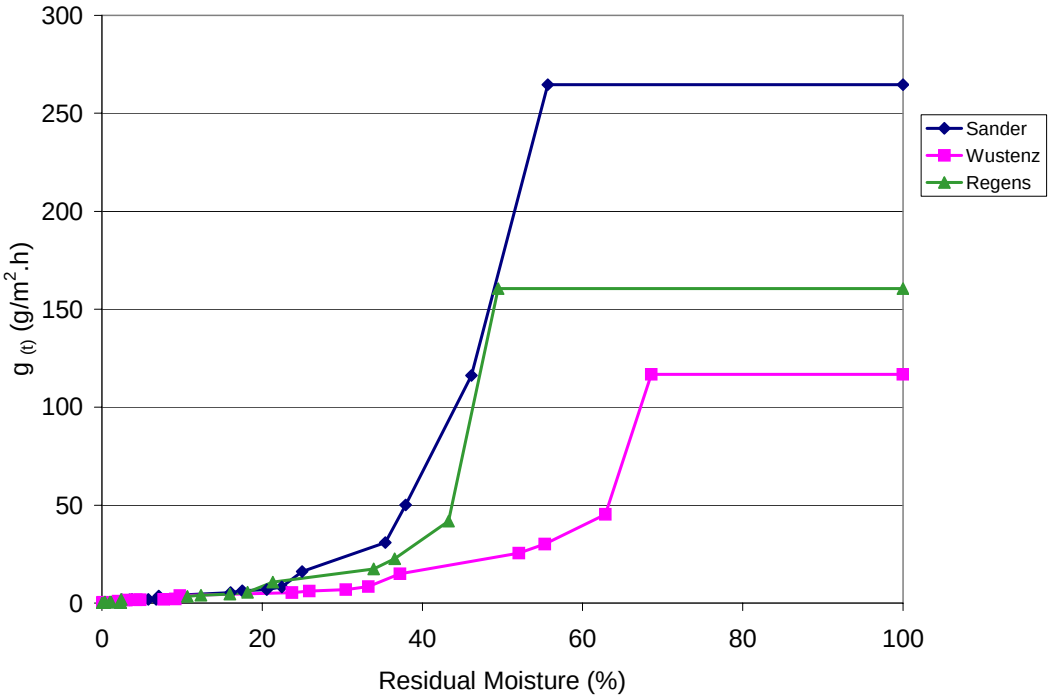

Figure 57: Water flow rate g as a function of the residual moisture of the sandstone according to the equation 31.

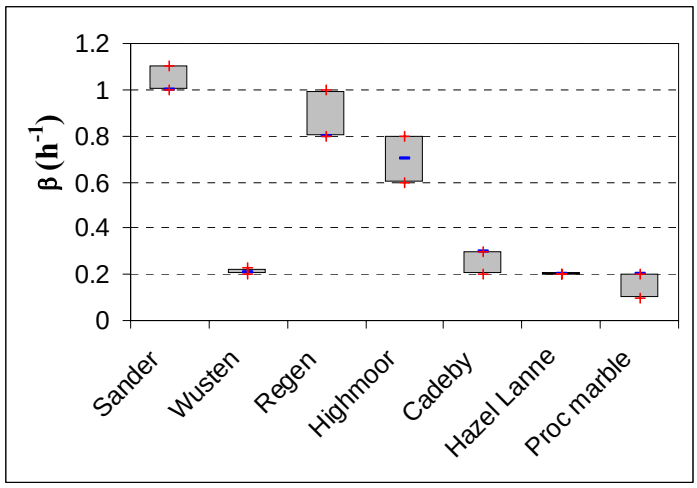

Figure 58. Water vapor conductivity coefficient β from the surface to the air according to equation 32. Raw results in Annex 2 Table 11, Table 16 and Table 21

During the drying kinetics, Cadeby and Hazel Lane show similar curves while Highmoor stone with lower water content, presents a shorter drying curve (Figure 59). Thus, Cadeby and Hazel Lane stones illustrate parallel water flow rate curves with a plateau, the first breaking point around 60% moisture and a discontinuous decrease of the water flow rate until samples are dry (Figure 60). On the other hand, Highmoor reveals the longest plateau, a first breaking point around 45% moisture which illustrate a faster drying and a more continuous decrease of the flow rate until the stone is dry.

Again, the shape of the water flow rate curves may be related to pore size distribution. Indeed, Highmoor with a high portion of pores > 5 µm (11.6 % ±1.3) illustrates the longest plateau and a second phase of drying decreasing continuously. That range of pores have a specific influence on the drying kinetics of the limestones to conduct liquid water to the surface, while smaller pores may slow down the drying and store the water longer in their structure.

The water vapor conductivity coefficient from the surface to the air confirms the highest conductivity of Highmoor. Only the sandstones will provide good correlation between β and other variables.

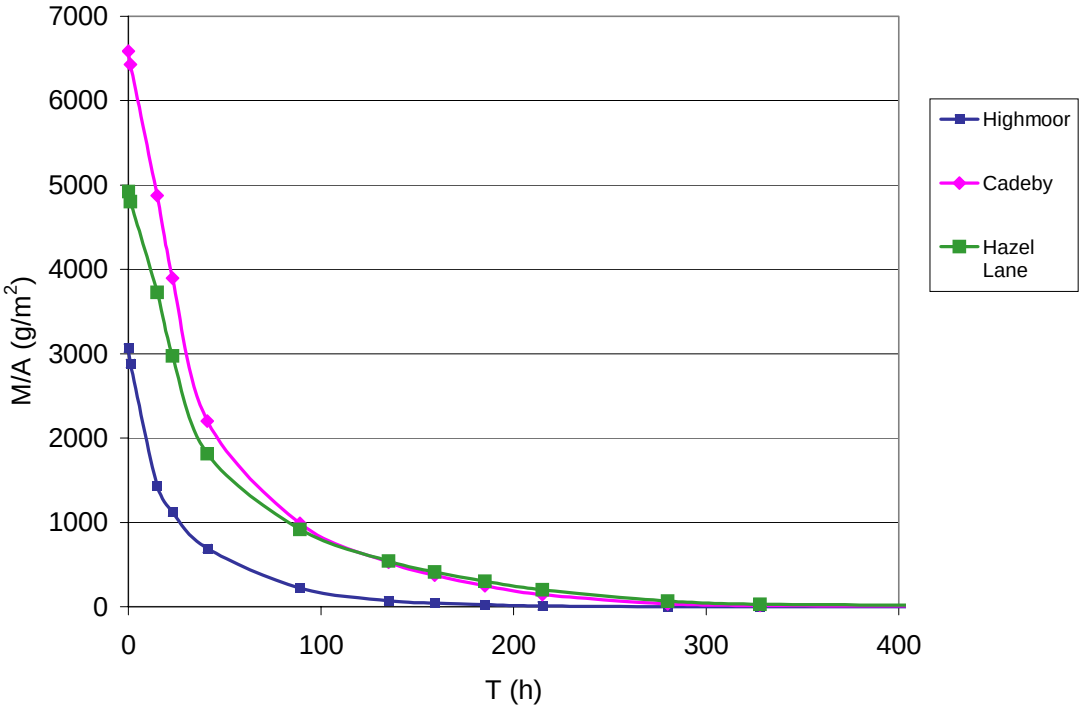

Figure 59: Drying curves showing the loss of water content as a function of time of the magnesian limestones.

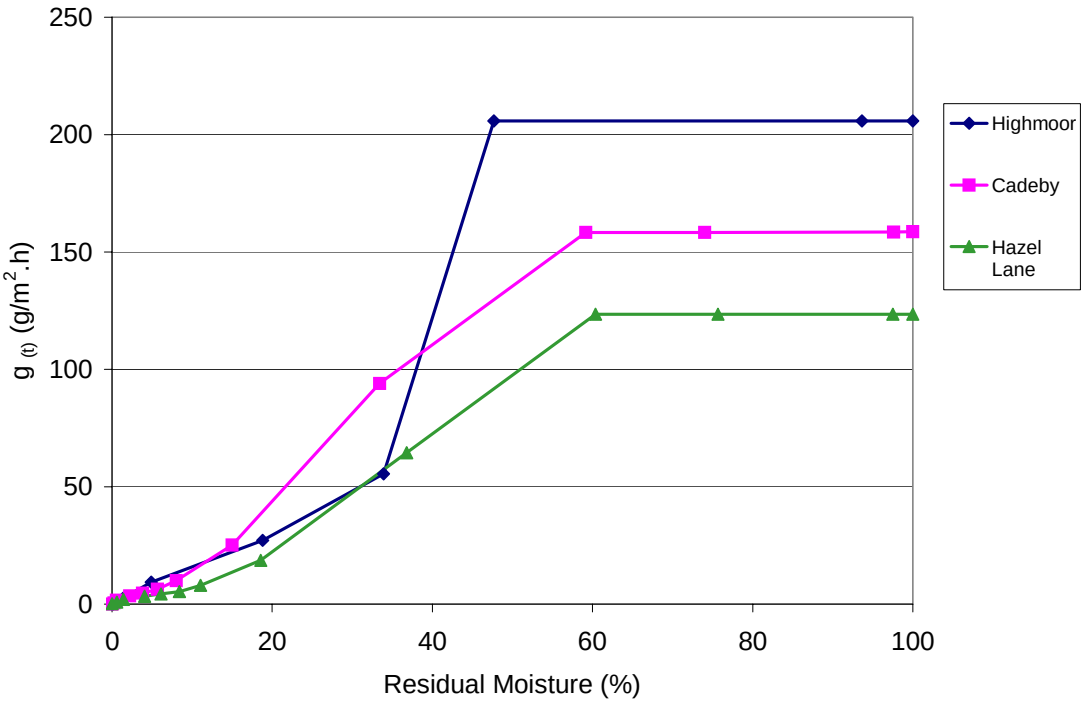

Figure 60: Water flow rate g as a function of the residual moisture of the limestone according to equation 31.

Weathered Proconnesian marble shows a fast and continuous drying. The high water flow rate at the plateau (g = 115 g/m^2.h) is rapidly followed by a straight decrease. That decrease seems to slow down around 5 % of water content to approach the base line (Figure 61 and Figure 62). The Proconnesian marble is mainly composed of interconnected pore (free porosity and the total porosity are almost equivalent). Moreover the pores are equally distributed in the range 0.1-5 µm as well as in the range > 5µm, which may lead to optimal pore network.

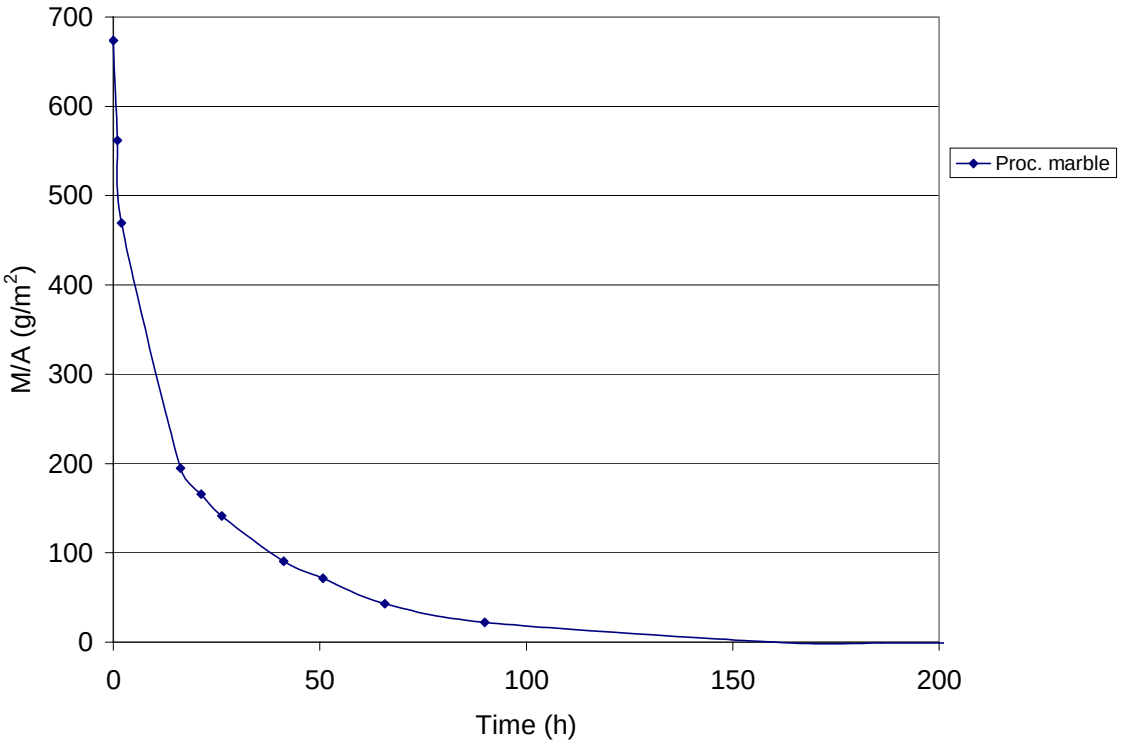

Figure 61. Drying curves showing the loss of water content as a function of time of the aged Proconnesian marble.

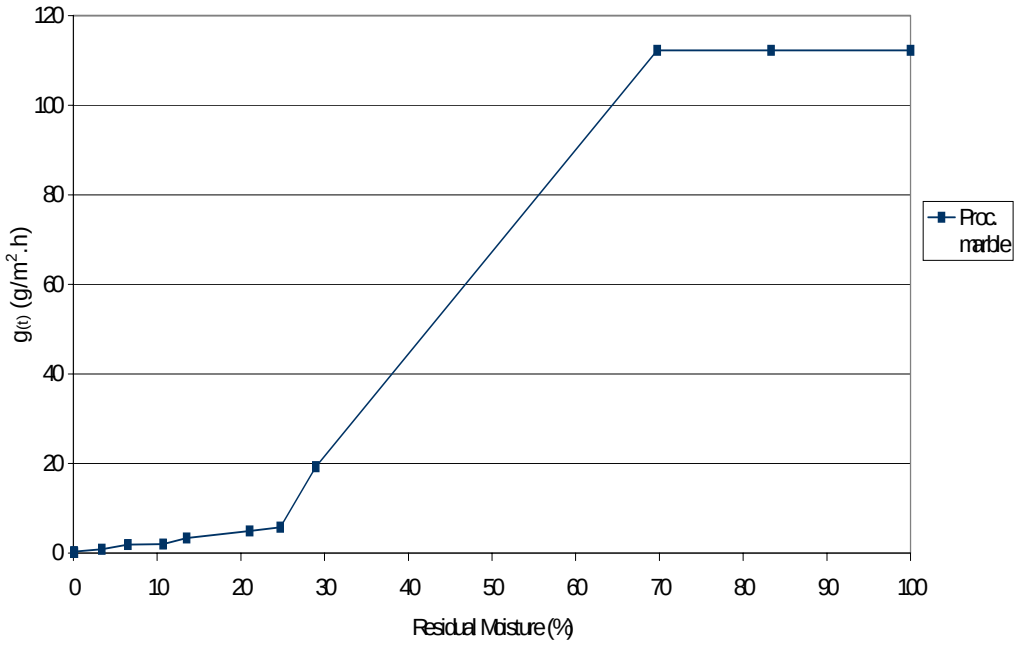

Figure 62: Water flow rate g as a function of the residual moisture of the Proconnesian marble according to equation 31.

V.1.4. The water vapor diffusion resistance coefficient, μ

The water vapor diffusion resistance coefficient μ varies with the different stone types (equation 34). As well, the sandstones reveal a lower μ-value than the magnesian limestones and the aged Proconnesian marble. For the sandstones, Wüstenzeller shows the highest μ around 32 ± 2, while Sander and Regensburg have a similar μ around 20 ±1. In term of porosity, Wüstenzeller demonstrates the lowest total porosity (13%) but its saturation coefficient S is similar to Regensburg sandstone (0.6-0.7).
In comparison with the pore size distribution, Wüstenzeller presents the lowest percentage of pores in the range 0.1-5 μm (Table 4). This variable may have an influence on the permeability even if the structure of the lithotype should be also taken into consideration.
The magnesian limestones illustrate also some difference between each other. Hazel Lane shows the highest μ 48 ±4, followed by Highmoor 40 ±4 and then Cadeby with the lowest μ at 30 ±2. One hypothesis may be that the lowest total porosity of Hazel Lane (N_t = 19%) and the low pore connectivity of Highmoor (S = 0.5) could play a role in the water vapor permeability of the stones.
Finally, the aged Proconnesian marble presents a μ-value over 200. It can be assumed that the low porosity of the marble leads to such a high μ-value.

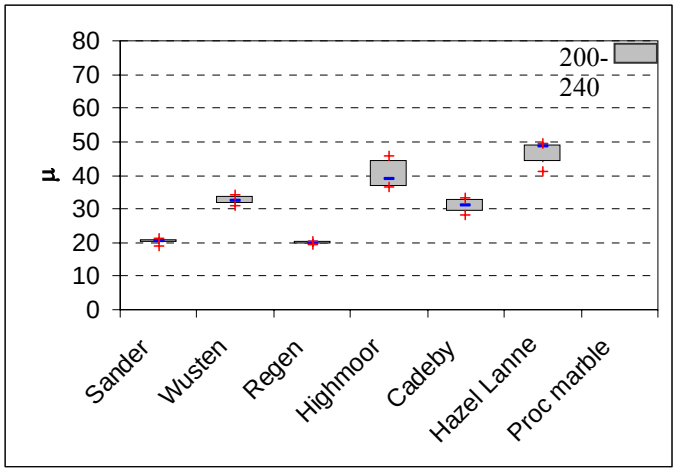

Figure 63. Water vapor diffusion resistance coefficient μ of the three lithotypes according to equation 34. Raw results in Annex 2 Table 11, Table 16 and Table 21.

V.1.5. The hydric dilatation, ε-hyd

Hydric dilatation (immersion into water) results are shown for the sandstones (Figure 64). The results are comparable to literature data, where clay rich sandstones showed the highest hydric dilatation (Sander – clayey binder dilatation between 1000 and 2000 μm/m; and Wüstenzeller containing some clay in its binder, dilatation between 600 and 1000 μm/m). Calcitic sandstones always revealed lower hydric dilatation and were usually measured below 500 μm/m.

In the present investigation Sander presents the highest dilatation 800 μm/m, then Wüstenzeller around 500 μm/m, and Regensburg around 100 μm/m.

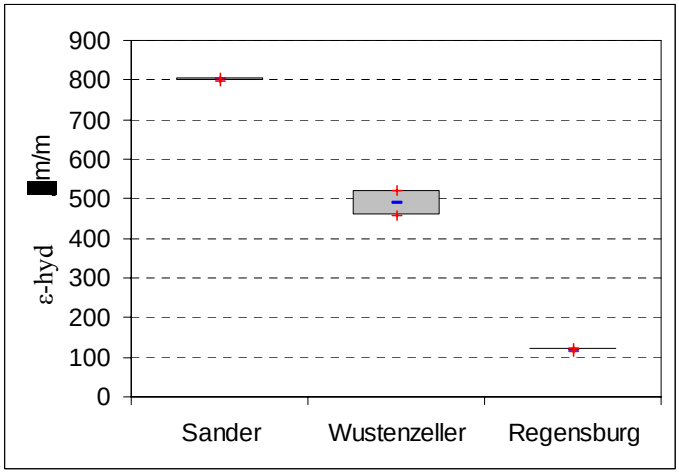

Figure 64. Hydric dilatation of the sandstones. Raw results in Annex 2 Table 11.

V.2. Correlation of the physical properties vs. porosity properties and textural characteristics

V.2.1. The magnesian limestones

Factor analysis demonstrates that many different relations exist between the physical properties versus the porosity properties (Figure 66). A first large group of variables is composed mainly by capillarity transport properties associated to different pore ranges. As well, the water uptake coefficient W-value is associated to pore range 0.1-5 µm, the free porosity N_{48}, the saturation coefficient S and the pore range < 0.1 µm. Thus the capillarity depends especially of the tube like throat (cylindrical) as it was defined in the porosity study and of the network connection of these pores.
A multiple regression (equation 62) shows the link between these variables:

$$W\ (kg/m^2/h^{0.5}) = -0.39 + 0.14\ N_{48}(\%) + 3.38\ S - 0.99\ N_2 < 0.1\ \mu m \pm 0.34 \quad R^2 = 0.92 \qquad (62)$$

The equation can be simplified and emphasizes the role of the free porosity and the tube like throat such as equation 63 and 64:

$$W\ (kg/m^2/h^{0.5}) = 0.23 N_{48}(\%) \qquad \pm 0.42 \qquad R^2 = 0.83 \qquad (63)$$

$$W\ (kg/m^2/h^{0.5}) = 1.38 + 0.14\ MIP0.1\text{-}5\ \mu m \qquad \pm 0.46 \qquad R^2 = 0.81 \qquad (64)$$

High pore connectivity can be deducted from a high free porosity. The higher are these variables the more important might be the pore range 0.1-5 µm and higher will be the water uptake coefficient and the saturation coefficient (equation 64 and 65). The pore range 0.1-5 µm and then the tube like throat particularly influence the saturation coefficient.

$$S = 0.27 + 0.03\ MIP0.1\text{-}5\ \mu m \qquad \pm 0.07 \qquad R^2 = 0.9 \qquad (65)$$

For the magnesian limestone these pore range as well as the free porosity was not well associated to structural characteristics. However, the saturation coefficient reveals a weak link with the QI and the pore shape (equation 66).

$$S = -3.86 + 0.14\ QI\% + 3.88\ Psf \qquad \pm 0.14 \qquad R^2 = 0.67 \qquad (66)$$

Two others groups can be distinguished. Opposite to the capillarity properties, the water vapor diffusion resistance coefficient µ is grouped with the DIA > 5 µm (equation 67). Usually, the resistance to water vapor diffusion may decrease with porosity. But it has been demonstrated that DIA > 5 µm may correspond to nodal pores but also to the closes porosity of Hazel Lane; therefore this pore range should probably not be taken into consideration for water vapor transport properties. There is an increase of µ with the porosity only in the case of closed porosity.

$$\mu = 26.8 + 1.06\ DIA{>}5\mu m \qquad \pm 3.1 \qquad R^2 = 0.86 \qquad (67)$$

As it has been shown earlier, DIA > 5 µm is related to the dynamic modulus of elasticity, ultrasonic velocities, QI and indirectly to the pore shape factor (for Psf < 0.1; porosity of pores). As well, µ should also be linked to these variables (Figure 67). Discontinuities in the structure are linked to the water vapor diffusion resistance coefficient; higher is the quality index (>20), higher is the water vapor diffusion resistance (equation 70).

$\mu = 51.88 - 316.4Psf$ ±4.3 $R^2 = 0.67$ (68)

$\mu = -18.8 + 14.51V_p\,perpend$ ±3.2 $R^2 = 0.82$ (69)

$\mu = -18.59 + 1.01QI\%$ ±3.43 $R^2 = 0.79$ (70)

Water vapor diffusion resistance can be assessed in a non-destructive way determining the quality index or just in measuring the ultrasonic velocity perpendicular to the stone bedding. Moreover, a high shape factor indicates the presence of a porosity of cracks, which reduces the water vapor diffusion resistance and therefore increases the water vapor permeability. The shape of the pores is a factor influencing the water vapor transport in the limestone.

If the aged Proconnesian marble is included in the correlation DIA > 5µm versus µ, the relation is totally changed (Figure 65). It is not the spherical pores, which contribute to a high resistance to water vapor diffusion for the aged proconnesian marble. Marble with a porosity of crack presents a DIA > 5 µm closed to zero, but shows an extremely high value of µ. It can be assumed that specifically high grain contact (> 90 %) and the very low porosity (1.5 %) of the marble is the main factor influencing µ.

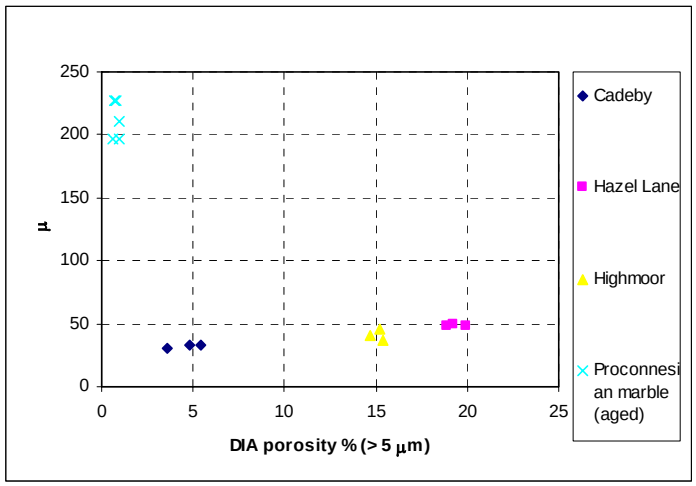

Figure 65. Scatterplot of the magnesian limestone and the aged Proconnesian marble in the diagram DIA > 5 µm versus µ. Raw results in Annex 2 Table 16 and Table 21.

Finally, water flow rate during evaporation kinetics g, (calculated on the plateau when g is constant) is associated to total porosity N_t and MIP > 5 µm. The best relation is obtained with the total porosity N_t (%), as equation 71:

$g\ (g/m^2/h) = 7.95N_t\ (\%)$ ± 17.03 $R^2 = 0.75$ (71)

Tube like throat in the range 0.1-5 µm are filled first during liquid water absorption and determine the water uptake coefficient, while larger pores > 5µm are emptied first during drying and determine the liquid water flow rate during evaporation.

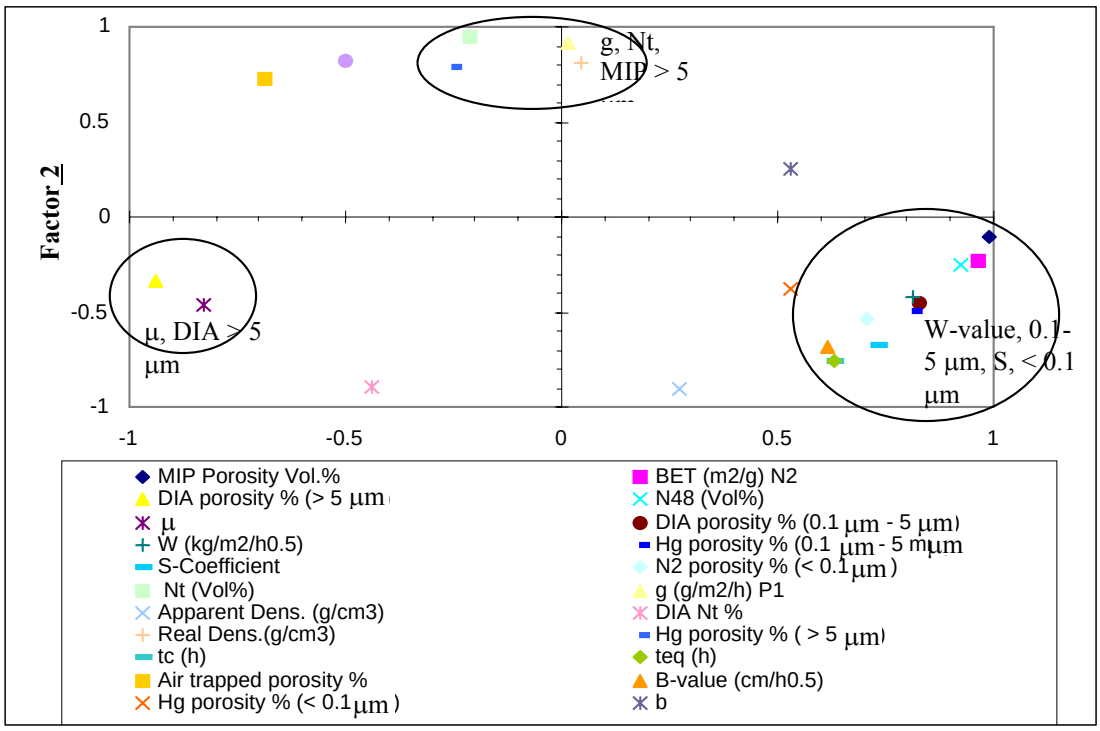

Figure 66. Factor analysis of the physical properties versus the porosity properties of the magnesian limestones.

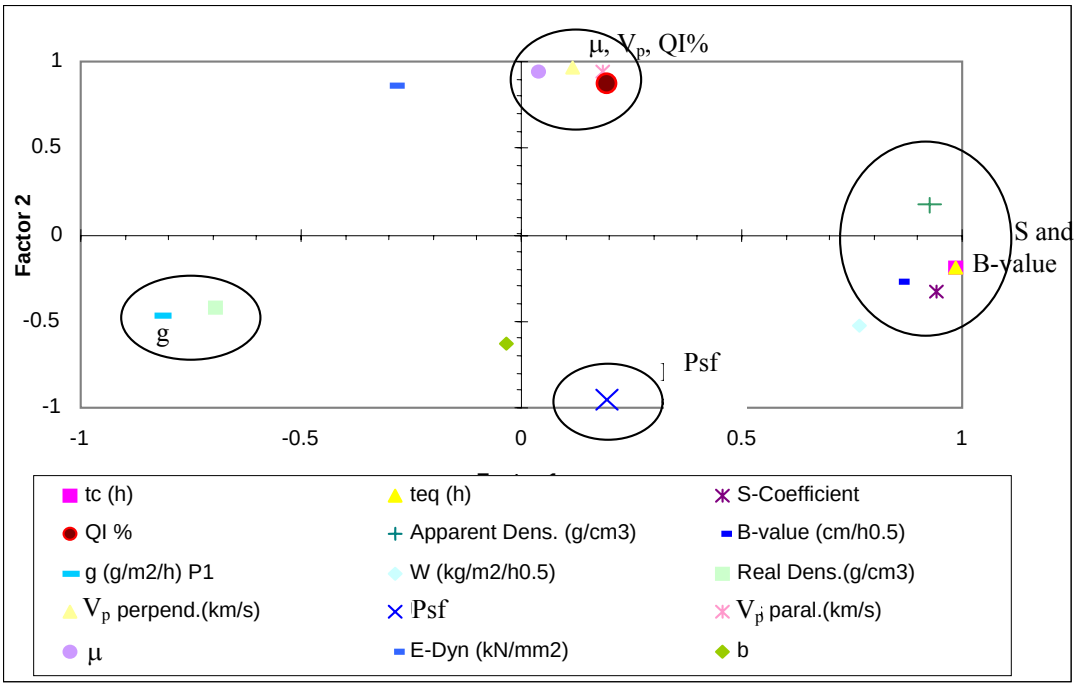

Figure 67. Factor analysis of the physical properties versus the structure characteristics of the magnesian limestones.

V.2.2. The sandstones

For the sandstones most of the variables are associated in the same group (Figure 68). Indeed, along the x axis, W (kg/m^2/h$^{0.5}$) as well as β (water vapor conductivity to the surface) are closely associated with MIP 0.1-5 µm and the larger pore ranges > 5 µm (Figure 68). Still in the same group is liquid water flow rate g (g/m^2/h) linked with the pores < 0.1 µm and the free porosity N_{48}.

As for the limestone, the pore range 0.1-5 µm determining the tube like throat, controls the capillarity and therefore the water uptake coefficient. In the porosity study (IV.3) Wüstenzeller showed an important volume of pores > 5 µm but the lowest water uptake coefficient. The pore range > 5 µm was considered in the correlation but did not reveal a good correlation with W. Only the pore range 0.1-5 µm is well correlated and confirms its impact on the water uptake coefficient, such as equation 72:

$$W\ (kg/m^2/h^{0.5}) = 0.86 + 0.55\ MIP\ 0.1\text{-}5\ \mu m \qquad \pm 0.54 \qquad R^2 = 0.87 \qquad (72)$$

The capillary rise, B is more distant of the group, but can still be linked to pore ranges (equation 73). However, it cannot be reduced to one variable and the pore range < 0.1 µm shows a primary influence.

$$B\ (cm/h^{0.5}) = 2.1 - 1.01\ N2{<}0.1\ \mu m + 0.73\ MIP0.1\text{-}5\ \mu m \qquad \pm 0.52 \qquad R^2 = 0.85 \qquad (73)$$

Water vapor conductivity to the surface is also related to the same pore range (equation 74). The range of pores 0.1-5 µm controls the capillarity as well as the water vapor transport.

$\beta\ (h^{-1}) = 0.19 + 0.15$ MIP0.1-5 μm ±0.11 $R^2 = 0.92$ (74)

As it has been demonstrated previously (IV.4), the structure characteristics are all grouped and control most of the pore ranges as well as the free porosity. Therefore, capillary properties should also be related to these characteristics (Figure 69). Indeed, the W and β are associated to the grain class 80-400 μm and the grain contact (equations 75,76, 79 and 80). More important is the class 80-400 μm, the higher is the grain contact, the lower is the porosity and the lower is the network connectivity. Thus capillarity as well as water vapor transport is decreased. The grain class 80-400 μm plays a main role, closely related to the pore size distribution and controlling the water transport properties.

$W\ (kg/m^2/h^{0.5}) = 6.13 - 0.12$ Gr 80-400 μm ±0.74 $R^2 = 0.79$ (75)

$W\ (kg/m^2/h^{0.5}) = 6.05 - 0.06$ Gc. (%) ±0.6 $R^2 = 0.87$ (76)

$B\ (cm/h^{0.5}) = 3.9 - 0.09$ Gc % + 25.8 Psf ±0.55 $R^2 = 0.85$ (77)

$B\ (cm/h^{0.5}) = 5.43 - 0.1$ Gr 80-400 μm ±0.69 $R^2 = 0.75$ (78)

$\beta\ (h^{-1}) = 1.59 - 0.02$ Gc. (%) ±0.1 $R^2 = 0.94$ (79)

$\beta\ (h^{-1}) = 1.56 - 0.03$ Gr 80-400 μm ±0.17 $R^2 = 0.82$ (80)

The water flow rate g ($g/m^2/h$) is included in the same group (Figure 68). It is more related to fine pores < 0.1 μm and free porosity N_{48}. As well, good pore network conductivity may increase the water flow rate (equation 81).
The important part of pores < 0.1 μm in the sandstones also increases the water flow rate and may be due to the presence of clay increases the surface area. The multiple regression cannot be reduced to one variable; both variables are necessary to describe the water flow rate.

$g\ (g/m^2/h) = -15.26 + 12.73\ N_{48} + 38.67$ MIP<0.1μm ±8.27 $R^2 = 0.99$ (81)

Again, pore ranges defining the water flow rate are related to the structure characteristics (Figure 69). However, the water flow rate is related to the two-grain classes 2-80 μm and 400-2000 μm because these grain classes define a specific pore size distribution (IV.4). The water flow rate is first correlated with a pore distribution and then, indirectly with a grain size distribution. Silt class 2-80 μm may increase the water flow rate, while the medium sand class may decrease the evaporation (equations 82 and 83).

$g\ (g/m^2/h) = 82.6 + 2.36$ Gr 2-80 μm ±10.7 $R^2 = 0.98$ (82)

$g\ (g/m^2/h) = 262.3 - 2.6$ Gr 400-2000 μm ±26.3 $R^2 = 0.88$ (83)

Then and logically, water flow rate is correlated with ultrasonic velocity and QI. Higher is the quality index and the velocity, lower the water flow rate will be.

$g\ (g/m^2/h) = 805.2 - 14.8\ QI\%$ ±22.8 $R^2 = 0.90$ (84)

$g\ (g/m^2/h) = 823.6 - 242.9\ V_p\ parall$ ±27.5 $R^2 = 0.85$ (85)

The water flow rate will increase with a porosity of pores and decrease with the introduction of more cracks in the structure. Pore shape and grain contact are related; high grain contact involves a porosity of crack (less spherical pores) and decreases the free porosity (and thus pore connectivity). Therefore, the water capillarity and the drying kinetics are decreased. A porosity related to pores causes higher water conductivity and thus allows water to evaporate faster (equation 86).

$g\ (g/m^2/h) = 367.8 - 1499.4\ Psf$ ±20 $R^2 = 0.92$ (86)

Finally, the μ-value is opposed to the first described group (Figure 68). Therefore, capillary pores 0.1-5 μm decreases the resistance to water vapor diffusion. More this pore range is important in the pore structure, higher is the water vapor permeability. Tube like throat is the most important variable in the water vapor transport (equation 87).

$\mu = 32.4 - 2.3\ MIP0.1\text{-}5\ \mu m$ ±2.3 $R^2 = 0.87$ (87)

As β is correlated with the grain contact, the water vapor diffusion resistance also is (Figure 69). If lower grain contact and important pore volume 0.1-5 μm increase water vapor transport, the same variables influence the μ-value. The grain class 80-400 μm plays again a main role and increases the water vapor diffusion resistance coefficient, μ (equations 88 and 89).

$\mu = 9.38 + 0.53\ Gr\ 80\text{-}400\ \mu m$ ±1.6 $R^2 = 0.94$ (88)

$\mu = 10.04 + 0.27\ Gc\ (\%)$ ±1.64 $R^2 = 0.94$ (89)

The hydric dilatation (ε hyd) is also related to fine pores, < 0.1 μm and 0.1-5 μm (equation 90). The equation cannot be reduced to one variable. In fine pores, high capillary pressure is exerting, which may weaken the bound between the grains and increase the distance between them, increasing the dilatation (Snethlage and Wendler, 1997).

$\varepsilon\ hyd\ (\mu m/m) = 471.8 + 600.3\ MIP{<}0.1\ \mu m - 98.35\ MIP0.1\text{-}5\ \mu m$ ±93.9 $R^2 = 0.91$ (90)

It is therefore associated with grain size distribution, ultrasonic velocity measurements, the quality index as well as with the grain contact and the pore shape factor. Grain class 400-2000 μm reduces pore volume < 0.1 μm as it was mentioned earlier, but also may play a role of stabilizer limiting the movement of the entire structure. As it can be observed in other natural material enriched in clay minerals, addition of larger aggregates may reduce the dilatation and shrinkage of the material. Medium class sand may reinforce the whole structure.

As dynamic modulus of elasticity is already correlated with the same grain class, hydric dilatation also shows a relation with the modulus (equations 91 and 93).

ε hyd (μm/m) = 828.2 – 10.8 Gr 400-2000 μm ±112.1 $R^2 = 0.87$ (91)

ε hyd (μm/m) = 2576.6 – 865.1 V_p parall ±107.7 $R^2 = 0.86$ (92)

ε hyd (μm/m) = 1763.2 – 110.9 E-Dyn ±48.3 $R^2 = 0.97$ (93)

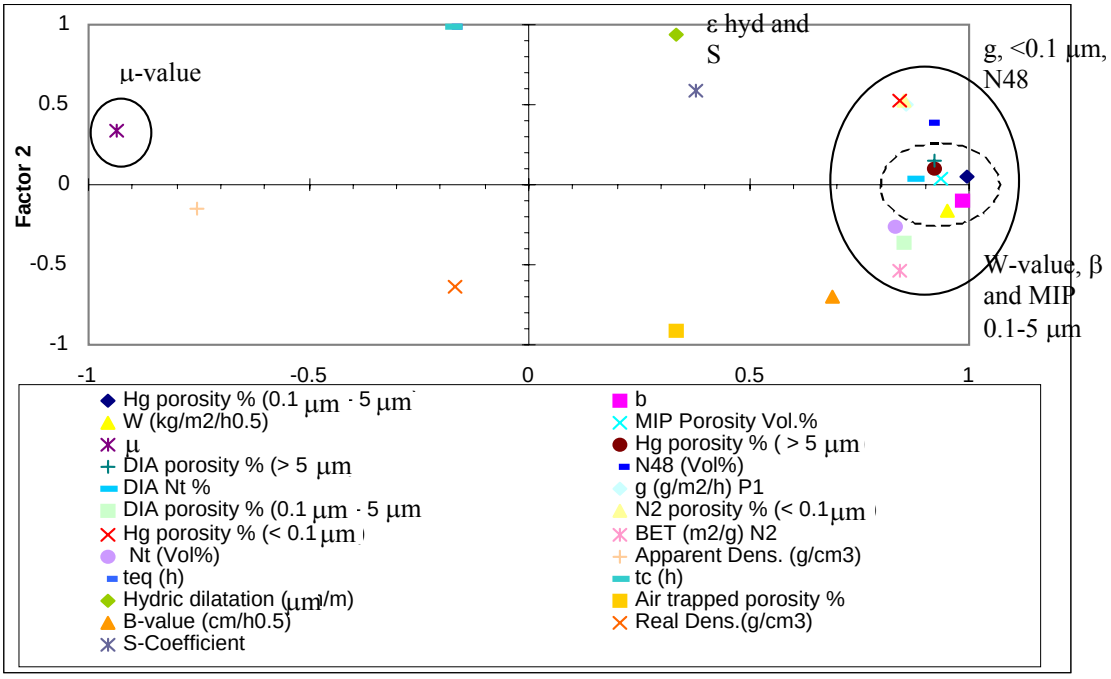

Figure 68. Factor analysis of the physical properties versus the porosity properties of the sandstones.

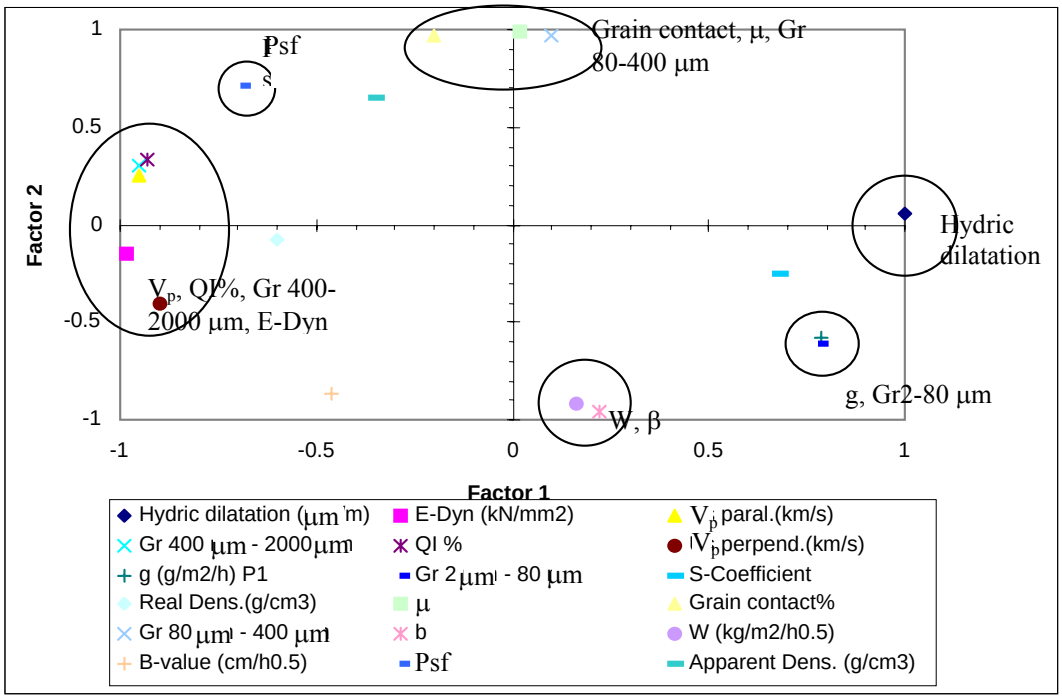

Figure 69. Factor analysis of the physical properties versus the structure characteristics of the sandstones.

V.2.3. In summary

For all lithotypes, a correlation exists between the free porosity measured at 48 hours (N_{48}) and the water uptake coefficient W. This correlation between the two properties emphasizes the importance of the free porosity and the interconnected pore, accessible to water by capillarity in the determination of the water uptake coefficient W (equation 94). The higher is the free porosity, the higher the water uptake coefficient would be.

$$W\ (kg/m^2/h^{0.5}) = 0.2\ N_{48}\% \qquad \pm 0.76 \qquad R^2 = 0.73 \qquad (94)$$

Structure characteristics seem to control most of the physical properties of the limestones as well as the sandstones.

For the magnesian limestone, the water transport properties are well controlled by pore size distribution measured by MIP. Indeed, pore range 0.1-5 µm, which may correspond to tube-like throat, determines capillarity and water vapor transport and confirms literature references Wardlaw (1979); Bernabe (1991). Moreover, pore > 5 µm representing the nodal pores and the water storage capacity enhances the drying kinetics as these pores increase the water flow rate g measured on the plateau.

On the other hand, physical properties are not easily linked with structure properties as very few variables could have been defined to describe the structure of the magnesian limestone.

Only QI representing the discontinuities in the structure, and the pore shape ratio could have been determined.
The pore shape ratio as well as the quality index may have an influence on the permeability. Cracks porosity added to pores porosity may better drive water vapor, while a higher QI may reduce the permeability. Therefore, more discontinuities in the structure enhance the water vapor permeability.

For the sandstones more parameters describing the structure characteristics can be taken into consideration, as the grain size distribution and the grain contact; a clear mechanism is drawn linking the structure to the porosity and the water transport properties. It is the grain size, which influences the grain contact, and therefore controls most of the hydric properties. High grain contact, increased by the fine sand class 80-400 μm, reduces pore ranges and therefore decreases water transport liquid and vapor. The same pore range as for the limestone, measured by MIP, 0.1-5 μm controls capillarity and permeability, while pore connectivity with the free porosity and pore < 0.1 μm influence the drying positively.

Water distribution in the porous material is clearly underlined by correlation analysis and the mechanism is illustrated in the Figure 70.
Through this illustration, it is obvious that fine sand fills empty spaces and creates more contact, not only in term of number of contact but even more in term of surface in contact between the grains. Therefore, it is evident that higher grain contact will decrease the pore space and thus the water transport and storage capacity of the porous material.

Capillarity and permeability seems to follow the same law for the limestone and the sandstones. The results also confirm some of the literature, as Niesel (1983) who find a relation between the saturation coefficient and water uptake of sandstones and limestones with the porosity < 5 μm. The drying may differ between the lithotypes, where the large nodal pores of the magnesian limestone are the most important factor, while the pore network connectivity and the finest pores of the sandstones take the major place. After Valdeon (1992) the configuration of the pore system conditions the hydric properties. Grain contact, pore shape, grain size and QI are all connected variables for the sandstones, for the limestone QI and pore shape are dissociated. It shows that the pore shape of the limestone does not create discontinuities and confirms the idea that porosity of pores present fewer discontinuities in the structure than a porosity of cracks.
Shepherd (1985) linked the permeability to grain size but even more to grain contact as he mentioned that spherical grains tend to have a higher porosity and permeability than disc-shaped grains. The present study proved for the sandstone that grain size is obviously linked to grain contact and influences strongly the water vapor transport.
Therefore as Scheidegger (1960) mentioned the main factor influencing physical properties in term of water transport is surely the pore structure, strictly dependent of grain size distribution and the theory of packing of grains.

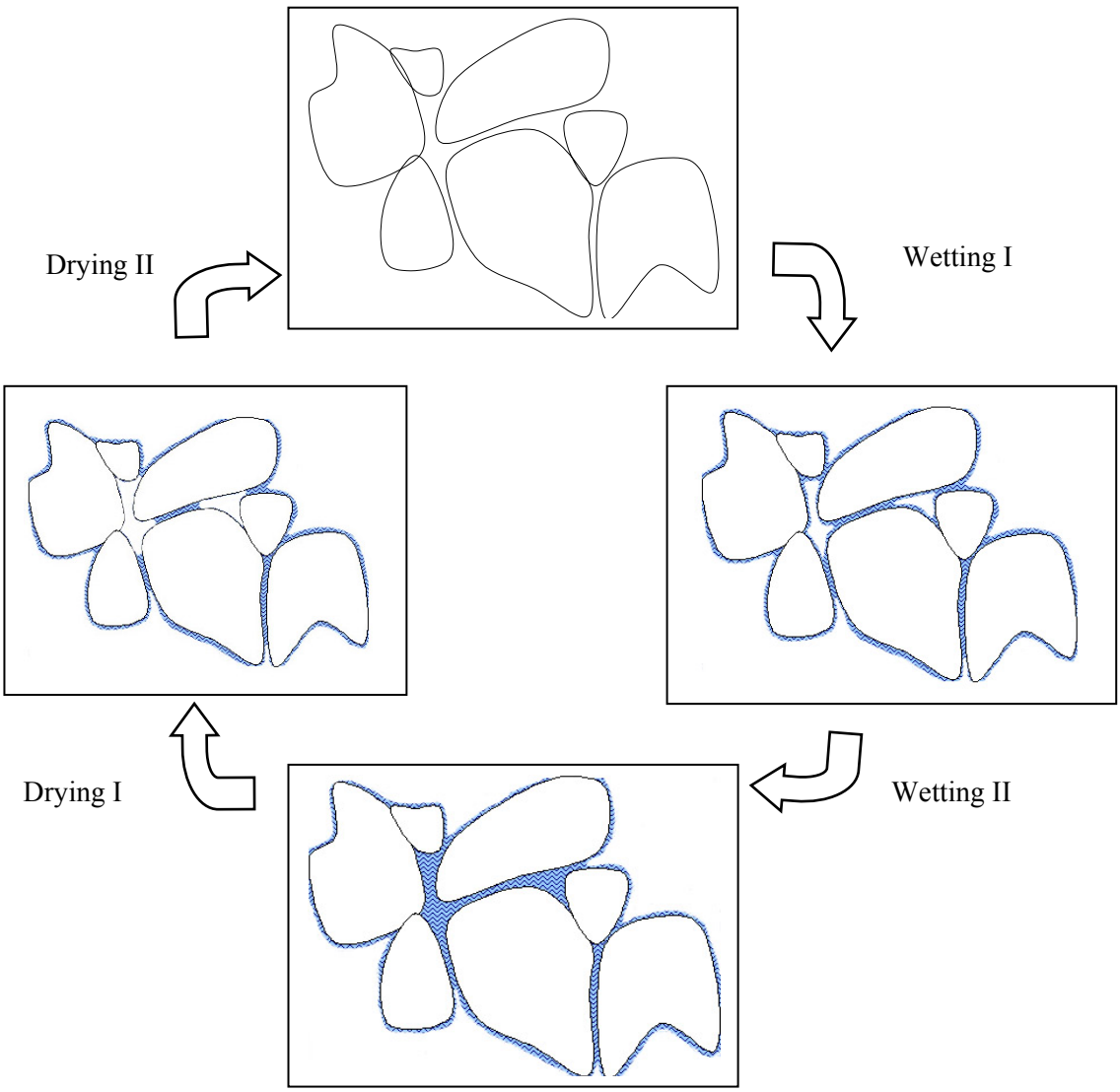

Figure 70. Water distribution in a porous body.

VI. Mechanical properties and their relationship to fresh materials

VI.1. The bi-axial flexural strength/ moduli of elasticity

Considering the three sandstones, Wüstenzeller presents the highest biaxial flexural strength (8 N/mm^2) while Sander and Regensburg are lower (4 N/mm^2 and 3 N/mm^2) (Figure 71). For the magnesian limestones Highmoor reveals the highest strength (8 to 10 N/mm^2) whereas Cadeby is the lowest (< 6 N/mm^2). For the sandstone, Wüstenzeller shows the highest modulus of elasticity, while Cadeby presents the lowest modulus for the limestones. Even though biaxial flexural strength seems to be comparable to static modulus of elasticity, it can be noticed that Regensburg doesn't show an important gap with Wüstenzeller, as it was the case for the strength.

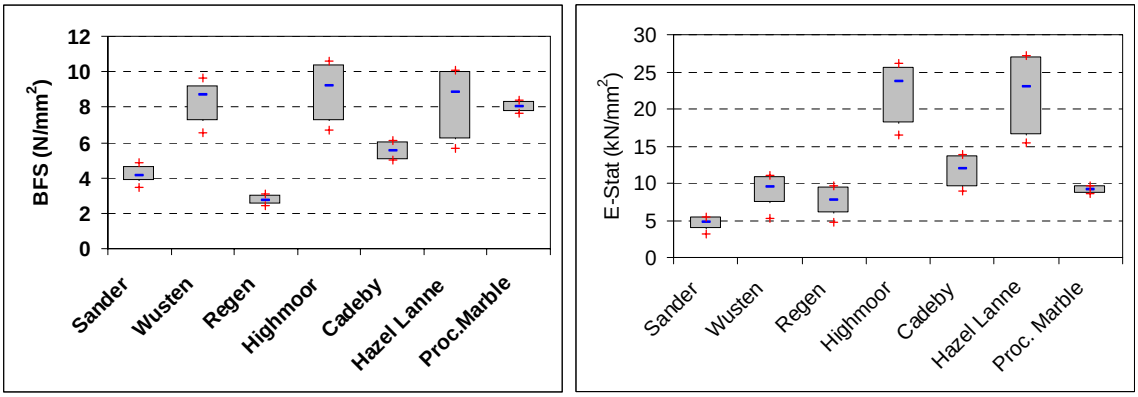

Figure 71: Bi-axial flexural strength of the sandstone, Figure 72. Static modulus of elasticity magnesian limestone and aged Proconnesian marble, according to equation 36 and 37. Raw results in Annex 2 Table 11, Table 16 and Table 21.

The stress-strain curves illustrate the deformation of the different stones (Figure 73). After maximum load has been reached, the stress-strain curve falls steeply or gradually. In fact, two curves can be obviously distinguished from the others, Hazel Lane and Highmoor magnesian limestones. These two stones prove a straight linear elastic deformation, while the others show a curvilinear elastic deformation.

Walsh and Brace (1966) proved the behavior of cracks and pores in rocks. They showed that the application of a non-hydrostatic load would first close the cracks and then allow the cracks to slide relative to one another; they are open to friction. In the other hand, pores do not close under moderate stress; the material containing only pores may be considered, as a linear elastic body, while the one containing cracks may not. Therefore, the stress at which fracture is initiated will be lower in a sample containing cracks than in one containing pores.

Stress-strain curves demonstrate such a characteristic by the deformation curves of the two magnesian limestone which are displayed on the highest extremity of the correlation, Hazel Lane and Highmoor. These two limestones seems to be exclusively composed with a porosity of pores and the stress-strain curves show a typical linearly elastic deformation.

Therefore, the results illustrate that the Highmoor and Hazel Lane magnesian limestones composed by a porosity of pore reach the highest strength and lowest deformation.

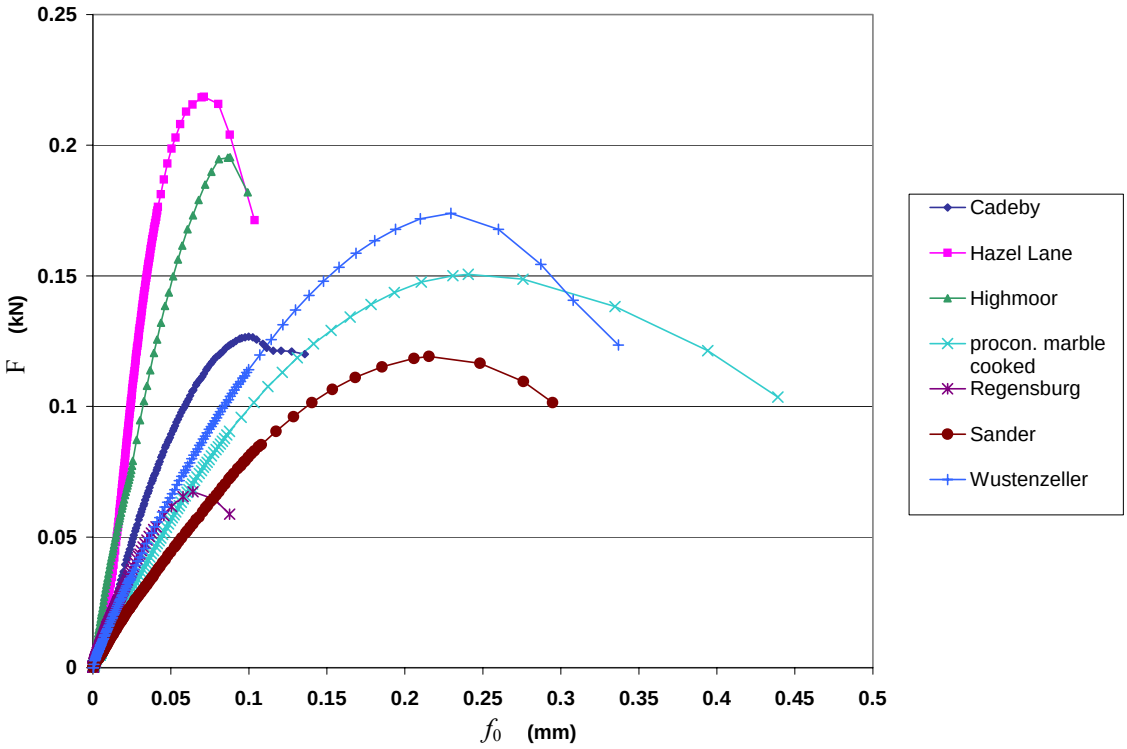

Figure 73. Deformation curves from the biaxial flexural strength. The magnesian limestones show a linear elastic behavior, especially Hazel Lane and Highmoor stones.

VI.2. Drilling Resistance

Drilling resistance measurements raw and corrected (cf. II.3.4) are presented in the Table 5. the correction follows the equation (Tiano et al, 2000) (cf. Equation 38):

$$\text{DRc} = \text{DR}\,\frac{20 \times RS}{PR \times 600}$$

The purpose of the correction formula is to compare drilling resistance to standard conditions of the reference sample ARS 600 RS and 20 PR. The selected parameters are as advised by the literature (Tiano et al, 2000), such as:

	Rotation speed (rpm)	Penetration rate (mm/min)
Reference sample ARS	600	20
Sander	600	10
Wüstenzeller	1200	5
Carrara Marble	1200	5

Therefore, Sander and Wüstenzeller results could be compared to literature data (diamond drill bit) (Tiano et al, 2000). Both stones give very similar results to the literature (Table 5), where Sander non-corrected was measured around 20.7 N ± 2.2 and DRc at 41.2 N; Wüstenzeller was measured around 43.0 N ± 14.8 non corrected and DRc at 344.8 N.
Sander presenting a biaxial flexural strength between 4 and 5 N/mm^2, Regensburg and Cadeby was measured with the same drilling parameters as Sander. Wüstenzeller showing a BFS between 8 and 9 N/mm^2, Highmoor and Hazel Lane followed the same drilling parameters as Wüstenzeller.
Finally, the aged Proconnesian marble was measured using the Carrara marble parameters. A fresh Carrara marble may present a DR 37.3 N ± 11.6 and DRc 298.4 N. The aged Proconnesian marble shows a normal value of DRc 141.1 N.

	Sander	Wustenzeller	Regensburg	Highmoor	Cadeby	Hazel Lane	Aged Proc. Marble
DR (N) Mean Literature	20.7	43					
StD Literature	2.2	14.8					
DRc (N) Mean Literature	41.2	344.8					
DR (N) Mean	18.0	51.1	15.1	45.7	20.5	28.6	17.6
StD	0.9	7.5	2.3	5.9	5.8	3.3	0.9
DRc (N) Mean	35.9	408.8	30.3	365.8	41.0	228.5	141.1
StD	1.7	59.7	4.6	47.0	11.6	26.4	7.6

Table 5. Drilling resistance measurements raw (DR) and corrected (DRc). Raw results in Annex 2 Table 11, Table 16 and Table 21

VI.3. Correlation mechanical properties versus porosity properties and structure characteristics

VI.3.1. The magnesian limestones

According to the factor analysis a first group describes mechanical properties, all correlated to each other (Figure 75). Biaxial flexural strength is well correlated with the static modulus of elasticity, as well as with the drilling resistance (equations 95, 96 and 97).

$$BFS\ (N/mm^2) = 1.92 + 0.3\ E\text{-}Stat\ (kN/mm^2) \quad \pm 0.72 \quad R^2 = 0.88 \quad (95)$$

$$BFS\ (N/mm^2) = 5.36 + 0.012\ DRc\ (N) \quad \pm 0.9 \quad R^2 = 0.81 \quad (96)$$

$$E\text{-}Stat\ (kN/mm^2) = -11.44 + 1.17\ E\text{-}Dyn\ (kN/mm^2) \quad \pm 2.93 \quad R^2 = 0.77 \quad (97)$$

The variable DIA > 5 µm appears in the same group as the mechanical properties (Figure 75). Logically the porosity cannot increase the strength. However, as it was already mentioned that this pore range is probably representative of nodal pores, with a poor connection to each other's or even no connection at all, in the case of closed pores. Therefore, these spherical and independent pores cannot be a source of cracks propagation.
Biaxial flexural strength and even more static modulus of elasticity are related to the pore shape factor. The magnesian limestone characterized by a porosity of pores presents few discontinuities and high modulus of elasticity.

It emphasizes the hypothesis that spherical pores, less deformable than cracks, increase the static modulus of elasticity and the biaxial flexural strength (equations 98 and 99). For the magnesian limestones the pore shape factor should be in the range $0.01 < Psf < 0.07$.

$$BFS\ (N/mm^2) = 11.2 - 87.6\ Psf \qquad \pm 1.1 \qquad R^2 = 0.71 \qquad (98)$$

$$E\text{-}Stat\ (kN/mm^2) = 30.65 - 286.15\ Psf \qquad \pm 3.1 \qquad R^2 = 0.78 \qquad (99)$$

When the aged Proconnesian marble is completely out of the correlation Psf versus E-Stat of the magnesian limestone (Figure 74). The marble with a porosity of crack does not follow the relation of the magnesian limestone, which shows clearly an increase of the static modulus of elasticity as a function of the roundness of the pores. The marble represents only one group and thus its strength and elasticity properties cannot be related to a structural property.

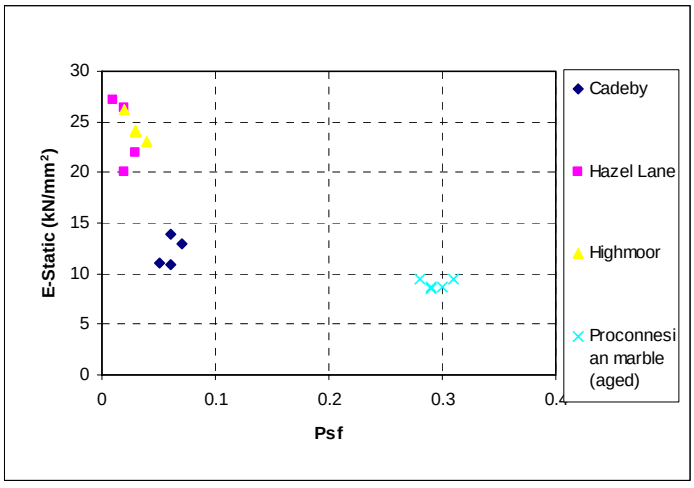

Figure 74. Scatterplot of the magnesian limestone and the aged Proconnesian marble in the diagram pore shape factor versus static modulus of elasticity. Raw results in Annex 2 Table 16 and Table 21.

On the other side, opposite to the mechanical properties, are the free porosity N_{48}, the MIP and the BET; these three variables decrease the strength, the modulus of elasticity and the drilling resistance (equations 100, 101 and 102). Mercury porosimetry is influenced by the connectivity of the pore network. Therefore if the nodal or closed pores can enhance the strength and the elasticity, the pore network connectivity is a main factor decreasing strength and elasticity. A good connection of the pore network may favor fracture propagation.

Moreover, the specific surface area (BET) is even better associated with the biaxial flexural strength and the drilling resistance than the MIP (equations 103 and 104). It may show that microporosity characterized by the BET measurements could play a role in the pore connectivity as well as in the presence of micro defects in the structure. The specific surface area is also dependent of the mineral roughness. Such defects related with a good pore connection are source of crack propagation (for magnesian limestones BET should be < 1 m^2/g).

E-Stat (kN/mm^2) = 51.35 – 1.39MIP% ±2.9 $R^2 = 0.8$ (100)

BFS (N/mm^2) = 17.44 – 0.42 MIP% ±1.15 $R^2 = 0.70$ (101)

DRc (N) = 948.1 – 33.38 MIP% ±71.4 $R^2 = 0.79$ (102)

BFS (N/mm^2) = 14.26 – 8.89 BET (m^2/g) ±0.7 $R^2 = 0.74$ (103)

DRc(N) = 781.51 – 847.5 BET (m^2/g) ±47.1 $R^2 = 0.9$ (104)

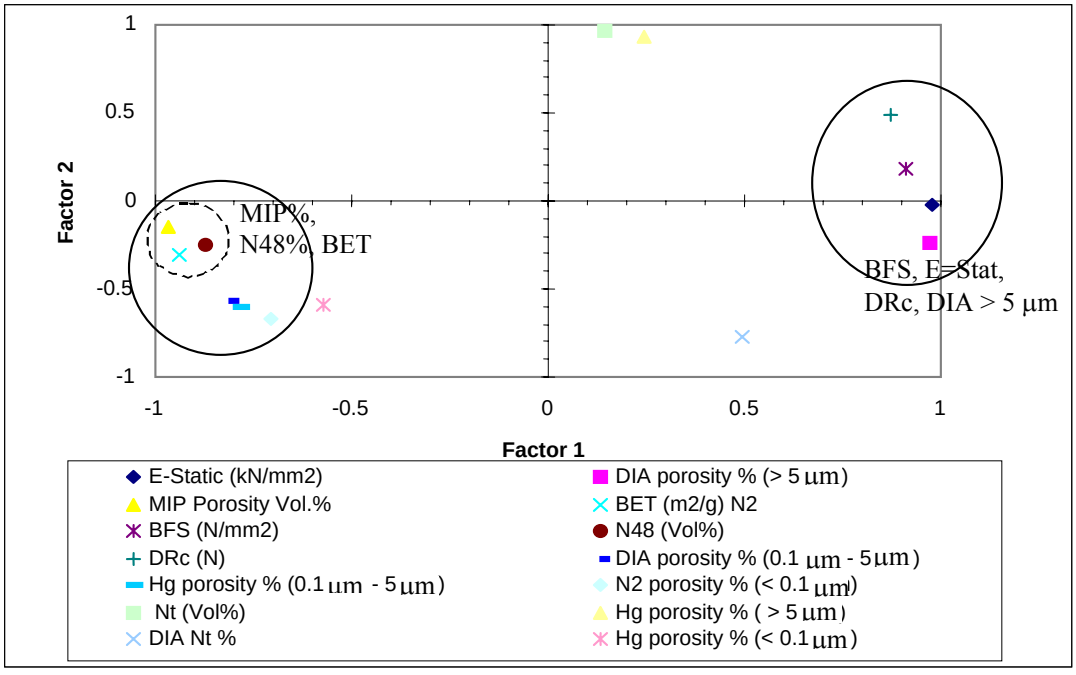

Figure 75. Factor analysis of the mechanical properties versus the porosity properties of the magnesian limestone.

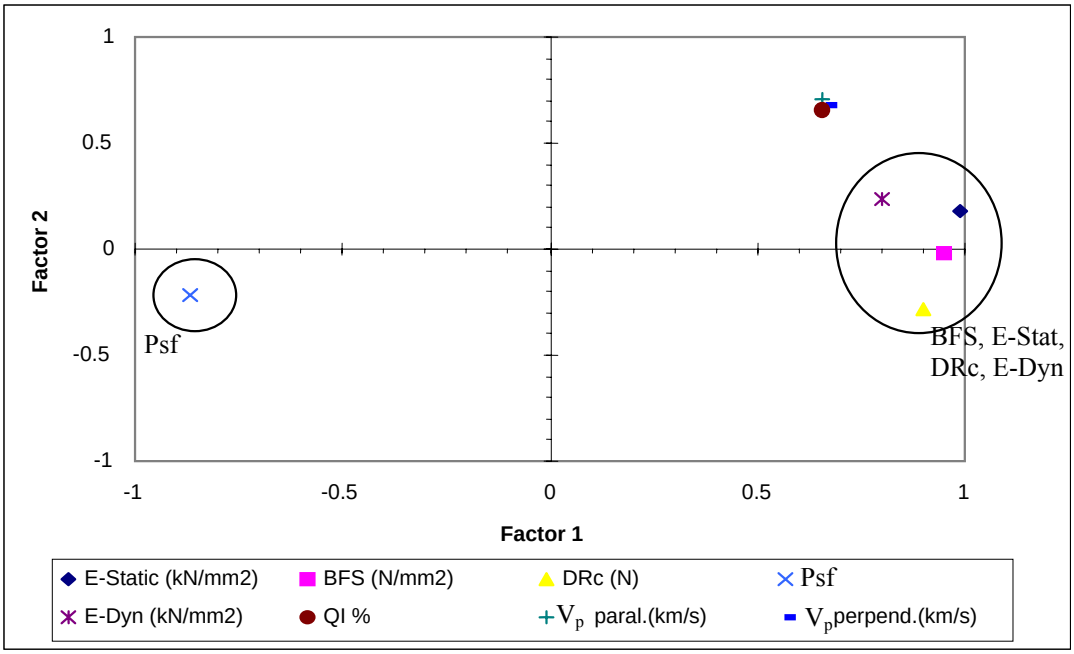

Figure 76. Factor analysis of the mechanical properties versus the structure characteristics and non-destructive methods.

VI.3.2. The sandstones

In the factor analysis showing the correlation between mechanical properties and porosity of the sandstone, strength (BFS) and static modulus of elasticity are dissociated. It doesn't mean that strength and static modulus of elasticity are not correlated, but that one sandstone may present a different relation between strength and modulus than the other sandstones. This is exactly the case when all stones, from the different lithotypes are displayed in one diagram (Figure 77). Sander and Wüstenzeller sandstones are linearly associated with the aged Proconnesian marble, while Regensburg sandstone is linked to the group of the magnesian limestone along a line with slope 1. Moreover, the dynamic modulus of elasticity is also isolated, in the factor analysis, from the static modulus and the strength for the same reason. The relation observed for the correlation static modulus and strength is repeated for the relation strength and dynamic modulus of elasticity as well as for the relation static and dynamic moduli of elasticity (Figure 79). Errors are represented for each data point and reflect the error of the method. A 3% of error was calculated for the biaxial flexural strength and static modulus of elasticity (manual measurement of sample size, error of the instrument), 1% of error for the dynamic modulus of elasticity.

As King (1983) illustrated, microfracturing rocks tend to fall below the linear regression static vs. dynamic modulus of elasticity. It confirmed our results where the stones characterized by a porosity of crack (Proconnesian marble) or a porosity of pores and cracks, seem to present a separate linear regression below the linear regression of the magnesian limestone, which might be more characterized by a porosity structure of pore, and calcareous sandstone. Therefore, the idea to divide the relation in two distinct regressions is justified. Thus, for the correlation strength - static modulus of elasticity as well as the relation strength - dynamic modulus of elasticity, two groups can also be distinguished in each relation.

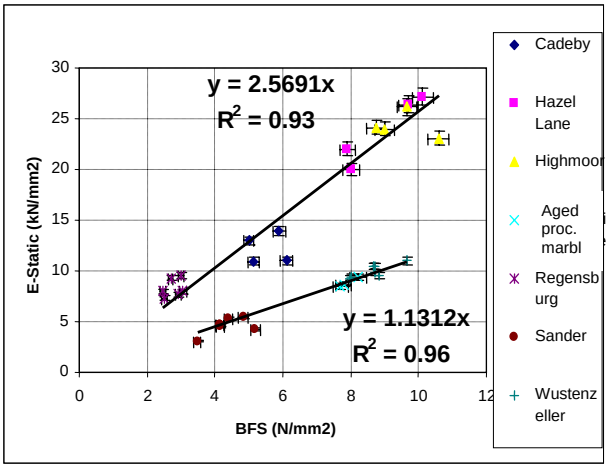

Figure 77: static modulus of elasticity versus BFS

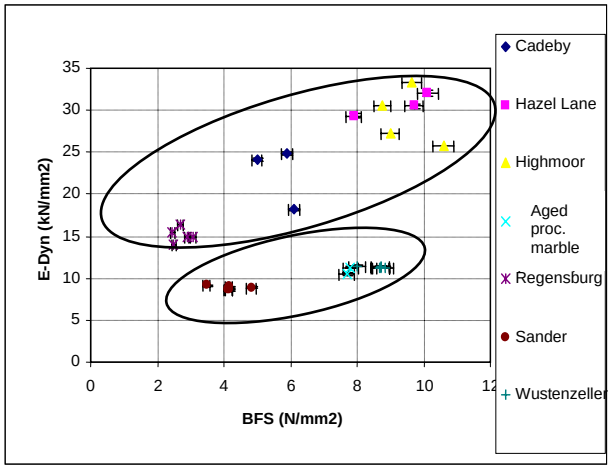

Figure 78: BFS versus E dynamic

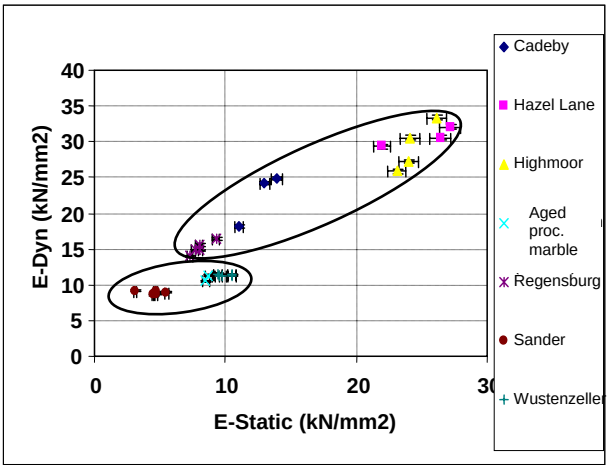

Figure 79: correlation between the static and the dynamic modulus of elasticity. Raw results in Annex 2 Table 11, Table 16 and Table 21.

If we consider that the pores cannot be deformed, the consideration of Ide (1936) is only valid in case of cracks and a low static modulus may be related to the presence of cracks in the stone more than the presence of pores. Moreover the volume of a spherical pore is enormously greater than that of a crack.

Thus, if porosity is used as a basis of comparison, the effect of cracks upon modulus, and other properties as well, is much greater than the effect of pores (Walsh and Brace, 1966).
However, such relation may also be related to other parameters than only pore shape. Indeed, one group is apparently composed by limestone (porosity of pores) and sandstone (porosity of pores and cracks) with calcitic binder. The origin of the dispersion in the relation between strength and moduli or between the two moduli, and the formation of distinct groups, might be related to a mineralogical composition, as one group is composed of calcareous stones.

On the other hand, the biaxial flexural strength is still correlated with the drilling resistance, as it was determined for the magnesian limestone (equation 105). A direct relation is therefore drawn between the two variables, where drilling resistance increases linearly with the strength. As it was also observed for the magnesian limestone, the specific surface area (BET) reduces the biaxial flexural strength as well as the drilling resistance (equations 106 and 109). The presence of micro defects in the structure may be the factor initiating crack propagation along the grain boundary. As it was defined earlier, fine sand grain 80-400 μm increases the contact between the grains. Thus, grain contact increases directly strength and drilling resistance (equations 108 and 111). The load acting on a grain is transmitted to the adjacent grains that support it, at various arbitrary angles depending on the shape of the grain and therefore of the type and number of grain contact (Derski et al, 1989) (Figure 83).

Fine sand 80-400 μm increasing contact between the grains may improve consequently the mechanical properties, the distribution of vertical load is better spread, while the micro defects may reduce grain contact as it decreases the strength parameters.

$BFS\ (N/mm^2) = 3.16 + 0.01\ DRc\ (N)$ ±0.86 $R^2 = 0.90$ (105)

$BFS\ (N/mm^2) = 9.79 - 1.15\ BET\ (m^2/g)$ ±0.57 $R^2 = 0.95$ (106)

$BFS\ (N/mm^2) = -0.67 + 0.22$ Gr 80-400 μm ±1.0 $R^2 = 0.87$ (107)

$BFS\ (N/mm^2) = 0.1$ Gc% ±1.24 $R^2 = 0.79$ (108)

$DRc\ (N) = 480.25 - 82.2\ BET\ (m^2/g)$ ±57.9 $R^2 = 0.91$ (109)

DRc (N) = -299.6 + 16.8 Gr 80-400 μm ±52.3 $R^2 = 0.93$ (110)

DRc (N) = -271.4 + 8.26 Gc% ±47.42 $R^2 = 0.95$ (111)

The static modulus of elasticity of the sandstone is related with the pore connectivity, reflected by the free porosity N_{48}, and the pore range < 0.1 μm. Therefore, it is still small pores as well as the connectivity between these pores that reduce elasticity properties. When pore range is larger as defined by the BET measurement (< 2nm), it can be assumed that the defects decreasing elasticity properties are of a larger size than those reducing the strength. Static modulus of elasticity is also linked to grain size and pore shape. Static modulus of elasticity is decreased by the silt grain class 2-80 μm introducing small pore volume < 0.1 μm (equations 113 and 114).

E-Stat (kN/mm^2) = 16.8 – 0.9 $N_{48\%}$ ±0.75 R^2 = 0.91 (112)

E-Stat (kN/mm^2) = 11.33 – 1.85 N2<0.1 µm % ±0.87 R^2 = 0.89 (113)

E-Stat (kN/mm^2) = 10.4 – 0.07 Gr 2-80 µm % ±0.72 R^2 = 0.91 (114)

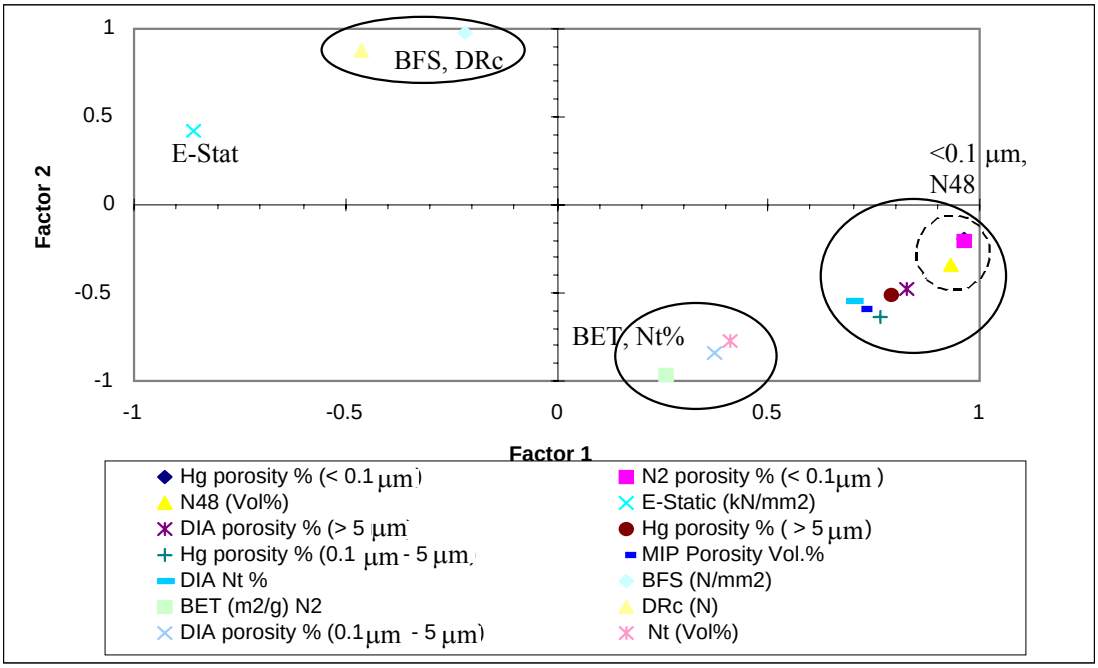

Figure 80. Factor analysis of the mechanical properties versus the porosity properties of the sandstones.

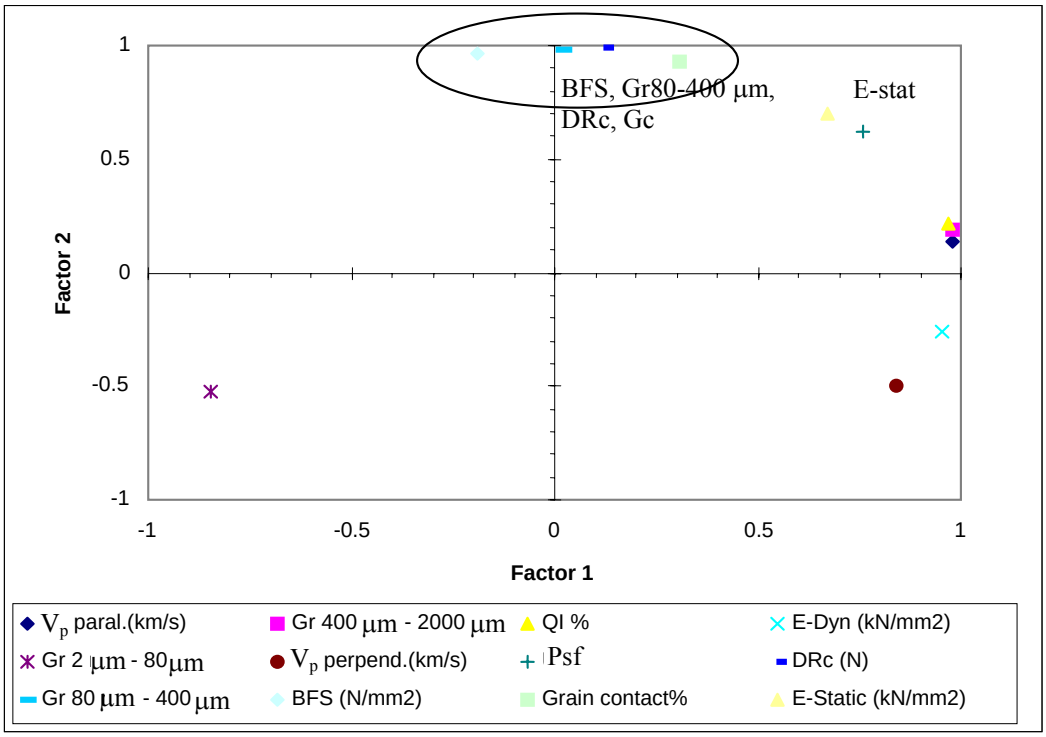

Figure 81. Factor analysis of the mechanical properties versus the structure characterisitics and non-destructive methods of the sandstones.

Finally, some relation between mechanical properties and water transport could have been defined, as pore ranges and even more grain contact are the common elements of these two groups of properties. When water uptake coefficient and water vapor conductivity to the surface are increased the strength parameters (BFS and DRc) are reduced (equations 115 to 118).

The sandstones show a noticeable circle of correlation where all properties are in one way or another related to each other's. Water transports as well as mechanical properties are therefore linked to the pore structure but even more to one common variable, the grain contact.

$$BFS\ (N/mm^2) = 9.61 - 1.55\ W\ (kg/m^2/h^{0.5}) \quad \pm 1.26 \quad R^2 = 0.77 \quad (115)$$

$$BFS\ (N/mm^2) = 9.53 - 6.04\ \beta\ (h) \quad \pm 1.28 \quad R^2 = 0.77 \quad (116)$$

$$DRc\ (N) = 496.92 - 120.83\ W\ (kg/m^2/h^{0.5}) \quad \pm 67.23 \quad R^2 = 0.88 \quad (117)$$

$$DRc\ (N) = 492.88 - 471.63\ \beta\ (h) \quad \pm 58.79 \quad R^2 = 0.91 \quad (118)$$

VI.3.3. In summary

The correlation study of the mechanical properties emphasizes the relation between strength and drilling resistance. The drilling resistance can be considered as a semi-destructive method, but can also be used as a laboratory test as well as a field measurement.

Therefore, it is primordial that the drilling resistance can be related with strength of the material and even, in the case of the limestone, its elasticity properties. Profile of decay can be obtained as well as efficiency of consolidation treatments. The different lithotypes present a better correlation factor when they are considered individually. However, fresh lithotypes of limestone and sandstone can be associated in the same equation such as equation 119:

$$BFS\ (kN/mm^2) = 3.9 + 0.01\ DRc\ (N) \qquad \pm 1.33 \quad R^2 = 0.77 \qquad (119)$$

The second important observation concerning the mechanical properties of the different lithotypes is the relation between mechanical properties, grain size distribution, specific surface area and pore network connectivity. It is shown that for all lithotypes the strength parameters decrease as a function of the pore connectivity. The higher is the pore network connectivity, the easier is the propagation of cracks in the material structure. Moreover, this cracks propagation seems to be directly linked to the specific surface area, emphasizing the presence of micro defects in the structure. The propagation of cracks depends on the geometry of the cracks and the presence of neighbor cracks. Each propagation crack develops two new crack on its extremities. Interaction and anisotropy lead to local cracks concentration from where a macroscopic fissure appears (Figure 82).

Microporosity enhances pore connection and is the initiator of crack propagation through the structure. On the other hand, addition of fine grain sand 80-400 μm enhances the contact between the grains and the strength is therefore increased.
The role of pore size distribution in the strength decrease was underlined in the literature, emphasizing the effect of pores < 5 μm (Alfes, 1991; Hoffmann, 1996). The influence of BET measurement on the decrease of strength was faintly mentioned (Niesel, 1983). It appears clearly through the correlation study of the sandstones that pore size distributions as well as grain size distribution are the main properties influencing the strength parameters.
Nevertheless, the method of strength measurement may be relevant. Indeed, the reduced sample size (40 mm x 5 mm) as well as the small loaded area may lead to a higher friction between the compressed surface and the grains. Since strength testing is based on the assumption of an isotropic structure, small defects or heterogeneities are supposed to influence the results. It might be the reason why the role of micro defect implied by the BET are clearly revealed in the strength measurements. The biaxial flexural strength might be a method “sensible” to detect propagation of fissures.

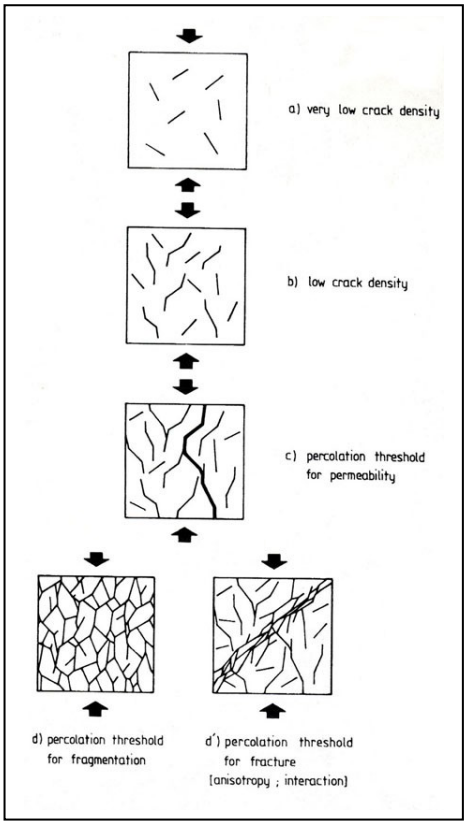

Figure 82. Development of cracks per propagation (after Guégen and Palciauskas, 1992)

For the limestone, the presence of spherical or nodal pores prevents from crack propagation. These pores are poorly connected to each other and less deformable. The pore shape is the main property that increases strength and elasticity.
On the other hand, mechanical properties of the sandstone may be more optimized by a relevant grain contact. The numbers of contact but even more the type of contact (long or tangential contact) may influence strength parameters.

The distribution of vertical loads is mainly dependent on the position of the grain contacts (Figure 83). The load P_A acting on the grain is transmitted to the two adjacent grains that the forces P_B and P_C affect in different magnitude and direction (Derski et al, 1989). The inequality coefficient of load distribution is defined as equation 120:

$$k = P_C/P_B = l_B/l_C \qquad (120)$$

Therefore, the value of this coefficient k depends of course of the grain size and on layer thickness.

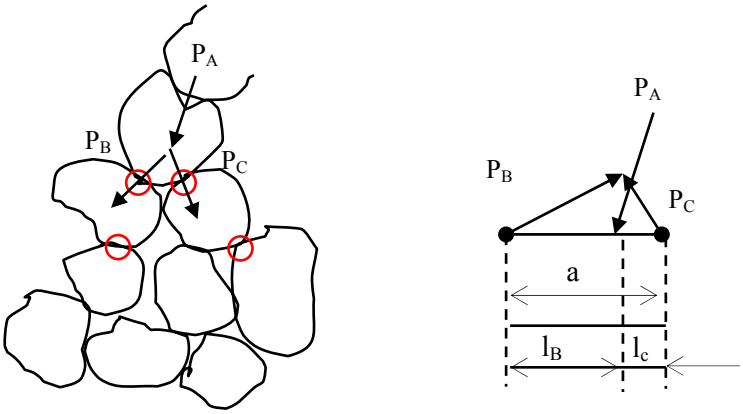

Figure 83. Interaction between grain contact and the vertical load distribution, a is the grain size.

The common point between the lithotypes is the connection of the pore network. In one case it can be decreased by spherical pores, in the other case, it can be reduced by long grain contact. Nevertheless, the aged Proconnesian marble presenting large grain and high grain contact still illustrates a significant pore connection, as the size of the porosity created by weathering is larger than the porosity influenced by the grain contact.

Finally, the relation strength and moduli of elasticity seems complex and not necessarily depending on the lithotypes. The pore shape may be an important factor defining the relation between each property. Indeed, the literature refered intensively to the type of porosity of pores or cracks (Judd and Huber, 1962; Guéguen and Palciauskas, 1992; Christaras et al, 1994). Many authors observed that the microcracks tend to decrease the static modulus versus the dynamic modulus (King, 1983). Certainly, the response of the sample to the low stress involved by ultrasound (dynamic modulus) is essentially purely elastic, while deformation is more important under static compression load. Moreover, cylindrical pores are not as deformed under compression as the cracks, which close in compression and reduce the static modulus. Therefore, the difference between static and dynamic moduli of elasticity might be related to the pore shape. However, other parameters can influence these elasticity properties.
The study also shows that static and dynamic moduli of elasticity are influenced by two different grain sizes; the silts class 2-80 μm decreases the static modulus, while the dynamic modulus is increased by the medium sand class 400-2000 μm. Such a characteristic may change the relation strength – moduli, or the correlation between the two moduli.
Nevertheless, Christaras et al (1994) obtained a very good correlation between the static and the dynamic modulus of elasticity for limestone, basalts, granite and andesite (Figure 84). The range of the measurements of Christaras et al (1994) was from 30 kN/mm^2 to 110 kN/mm^2 for both moduli, but raw datas were not available (the static modulus was measured from uniaxiale compressive strength and the dynamic modulus from ultrasonic velocity). The equation was determined such as equation 121:

$$\text{E-Stat (kN/mm}^2\text{)} = 1.05\text{E-Dyn (kN/mm}^2\text{)} - 3.16 \qquad R^2 = 0.99 \qquad (121)$$

The results of the magnesian limestone, sandstones, and aged Proconnesian marble (lithotypes presented in this study and discussed in Figure 79) are in a lower range from 5kN/mm^2 to 30 kN/mm^2, and show a lower correlation but are closer to zero and then closer to the theory. Datas of magnesian limestone, sandstones and aged Proconnesian marble are obviously below the slope of Chistaras et al (1994), and is such as equation 122:

E-Stat (kN/mm^2) = 0.74 E-Dyn (kN/mm^2) $R^2 = 0.88$ (122)

When all lithotypes are grouped (Christaras et al, 1994, and magnesian limestone, sandstones and aged Proconnesian marble) on the same diagram, a single linear correlation can be drawn passing by the origin. The coefficient of 0.94 let assume that static modulus of elasticity can be assessed through the measurement of the dynamic modulus, in a non-destructive way. The equation is such as equation 123:

E-Stat (kN/mm^2) = 0.89 E-Dyn (kN/mm^2) $R^2 = 0.94$ (123)

However, it can be noticed that the coefficient of E-Dyn is the lowest for the equation grouping only the sandstones, magnesian limestone and aged Proconnesian marble (equation 122). This coefficient goes from 1.05 for Christaras et al (1994) (equation 121), to 0.89 for the equation linking reference results and new results (equation 123), to 0.74 for only the new results (equation 122). These new results provide a more exact equation (equation 122) than Christaras et al (1994) (equation 121) even if the correlation factor is lower.

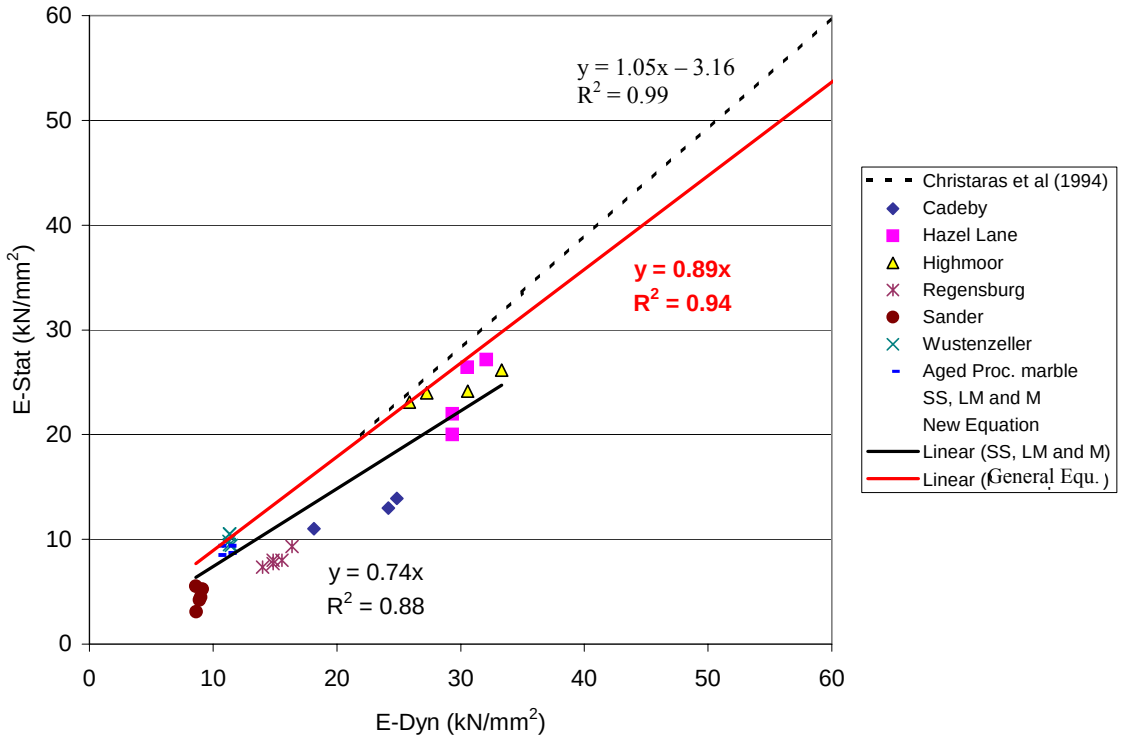

Figure 84. Correlation static and dynamic moduli of elasticity grouping Christaras et al (1994) datas and the data of the study.

VII. Synthesis

As a synthesis, the main results obtained on fresh magnesian limestone and fresh sandstone shall be reiterated in a schematic form. Indeed, the synthesis is focused on the determination of models that can be relevant to the study of artificially weathered stones. By clearly exposing the different material properties dependent to each other, it would be easier to identify the impact of decay on the various properties and therefore to draw a new model that can assess weathering and should be a link with the second part of the study, after artificial weathering.

For the magnesian limestone, two independent models can be drawn (Figure 85). One illustrates more the physical properties as the water transport in the material; the other one describes the mechanical properties. The two models underline the role of the structure characteristics in relation with the porosity properties, the water vapor transport, the strength and the elasticity properties of the limestone.
Water transport properties (capillarity, evaporation) are well correlated and explained by porosity properties but could not be integrated in the entire scheme. The study on the magnesium limestone point out precise and interesting characteristics. It seems that the most important result is the association between spherical pores that are less deformable under static compressive load and the pore connection properties. Lower pores network connection as well as lower specific surface area and therefore microporosity (<2nm) lead to higher strength of the material by reducing micro defect and micro cracks propagation through the structure. It seems that this is the major association of properties that may lead to a better understanding of weathering in natural environment.
The second model may also be interesting to follow through alteration as the quality index (QI) and the ultrasonic velocity may predict the water vapor diffusion resistance. Changes in the water vapor transport may play a relevant role in the weathering velocity.

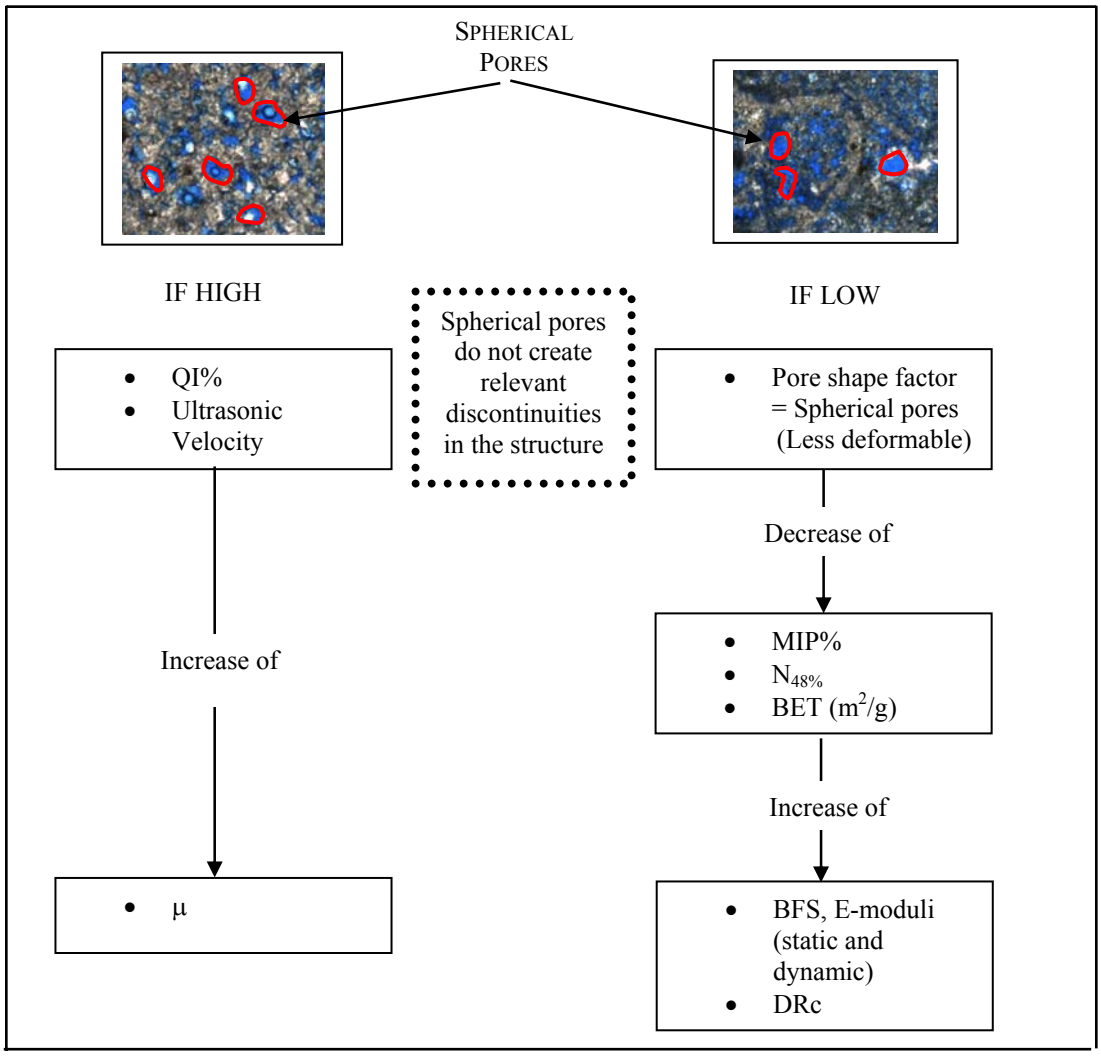

Figure 85. Correlation model for the magnesian limestone.

For the sandstone, the three different grain classes define different models. However, fine sand 80-400 μm determines one major model (Figure 86). It is important to underline here the key role of the grain size distribution in all physical and mechanical properties. Grain class 80-400 μm enhances grain contact and therefore controls pore size distribution and especially pore volume directly correlated with water transport liquid and vapor as well as strength properties (BFS, DRc). All variables are interdependent in the model.
Therefore, the structure characteristics control physical and mechanical behavior of the material. Relevant grain contact may also reduce pore network connection and propagation of cracks through the structure initiated by an applied force (biaxial or drilling).
However, two others models exist and are controlled by the two others grain classes. High percent of medium sand 400-2000 μm increases the quality index, ultrasonic velocity and dynamic modulus of elasticity and consequently reduces hydric dilatation (Figure 87); on the other hand, silts class 2-80 μm influences negatively the pore shape, increases pores below 0.1 μm, enhances water flow rate during evaporation and decreases static modulus of elasticity (Figure 88).

Thus, it can be observed that the two modulus are in separate models, one depending more of the medium sand class (dynamic modulus), the other one related to the silt class and the shape of the pores (static modulus).

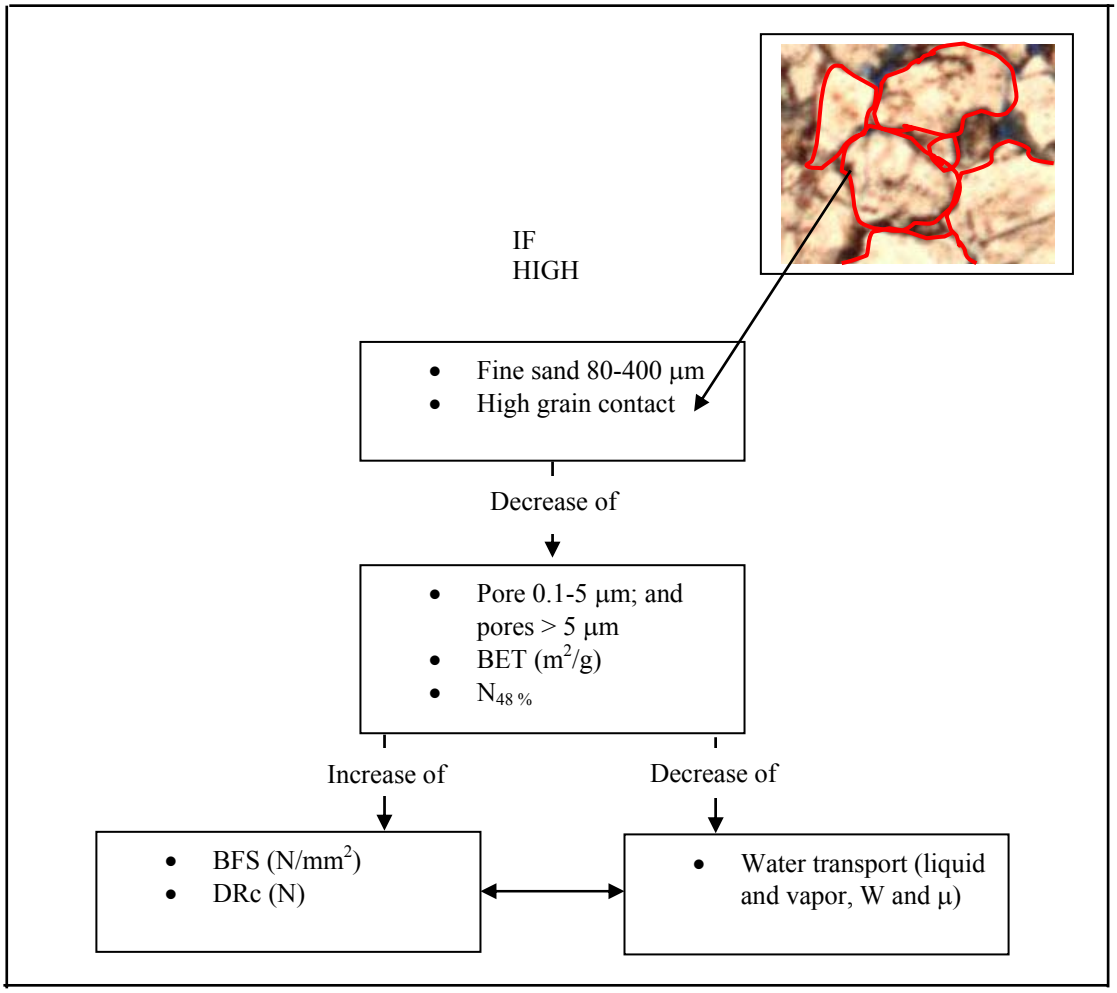

Figure 86. Major correlation model for the sandstone where fine sand class control main of the properties.

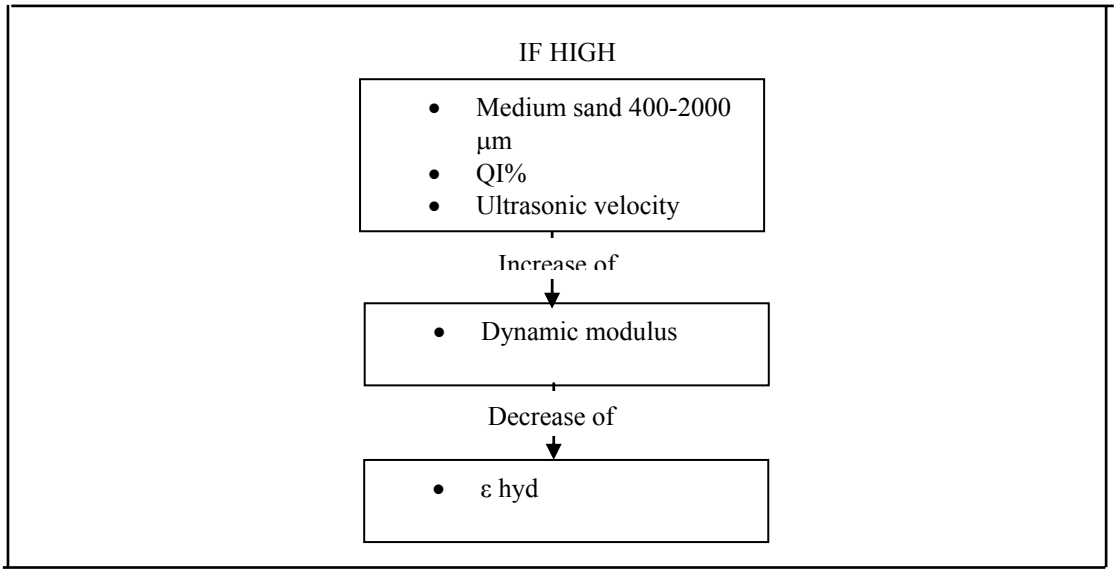

Figure 87. Correlation model for the sandstones where medium sand class control some properties.

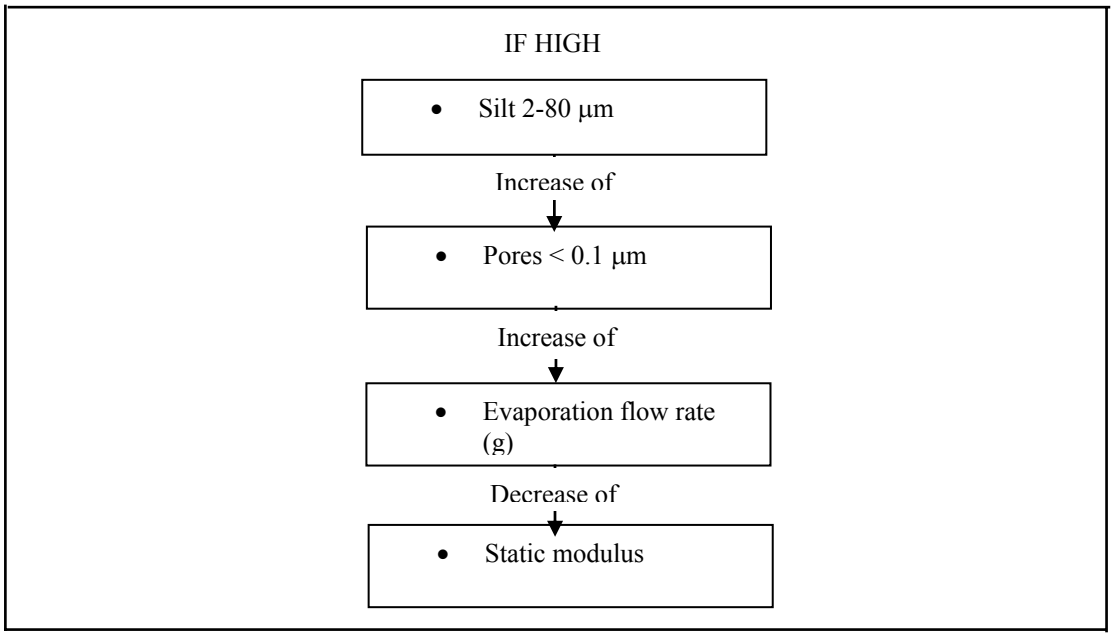

Figure 88. Correlation model for the sandstones where silt class influence some properties.

Magnesian limestone and sandstone have in common some of their water transport properties as the pore volume 0.1-5 µm, tube like throat, which controls capillarity for both lithotypes. Moreover their mechanical behaviors are pretty similar. Both show a direct relation between strength and drilling resistance, and the two properties seem to be associated with the microporosity and the specific surface area as well as the pore network connection.

C. RESULTS AND DISCUSSION – PART 2: PROPERTIES OF STONES AFTER FREEZE-THAW CYCLES (F-T)

The following chapter describes and explains the changes that occurred on the different lithotypes after artificial weathering by freeze-thaw cycles.
State of the alteration by freeze-thaw cycles were followed and evaluated according to the DIN EN 12373 (cf. II part I). Visual examination and measurement of dynamic modulus of elasticity were carried out. Artificial weathering has been stopped for all lithotypes after 100 freeze-thaw cycles even if all of them were not visually deteriorated. This choice was made in order to distinguish the variables leading to deterioration from the variables leading to durability. Moreover, in order to be able to measure most of the physical and mechanical properties, samples should have remained in one piece and in an alteration state reasonable to carry out the measurements. Once state 2 or 3 of visual alteration was reached (before specimen broke), artificial weathering was stopped.
This last chapter would establish relation between variables before and after freeze-thaw cycles in order to assess weathering in natural environment.

VIII. Changes in structure

VIII.1. Visual inspection

From the six lithotypes, four reached a visual alteration of degree 2 or 3 (Table 6), Sander and Regensburg sandstones (Figure 89 and Figure 88) and Cadeby and Hazel Lane (Figure 91 and Figure 90) magnesium limestone (degree 2: one or several minor cracks (< 0.1 mm width) or detachment of small fragments (< 10 mm^2 per fragment); degree 3 by one or several cracks, holes or detachments of fragments larger than those defined for the "2" rating, or alteration of material in veins, see Table 6). Wüstenzeller sandstone as well as Highmoor magnesium limestone didn't reveal any cracks through the sample.

The Sander and Regensburg sandstone show a clear crack transversal to the sample (Figure 89 and figure 2). The crack of 2 mm width follows the stone bedding, parallel to the surface.
The magnesium limestones reveal smaller cracks which are still parallel to the stone bedding. Even if only macro cracks can be observed on the specimen it can be easily assumed that micro cracks exist simultaneously parallel to the stone bedding. Clearly the specimens are not homogenously decayed and the macro cracks are obviously not present on the entire sample. No specific enrichment of clay minerals could have been observed around the cracks. The explanation for a specific failure in the middle of the stone sample and without spalling off parallel to the surface might be a preferential level of wetting and drying. Indeed, samples are entirely immerged under water and the saturation occurred only by capillarity at 20 °C; it is a partial saturation. Then, during the freezing period, samples are frozen in the air. It can be assumed that a partial drying of the sample occurs and that a preferential liquid water rise is present in each material. During the freezing period it may create a preferential location of ice crystallization and applied specific stress on the material.

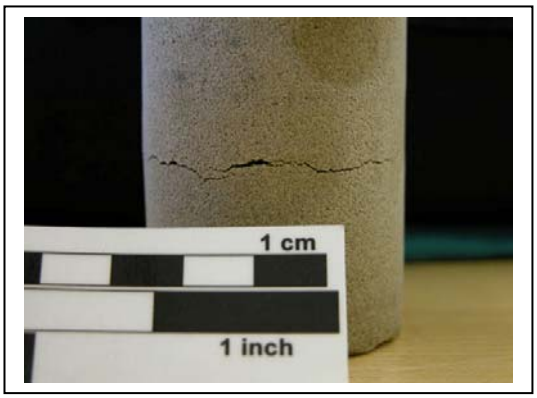

Figure 89. Picture of Sander sandstone after 100 F-T.

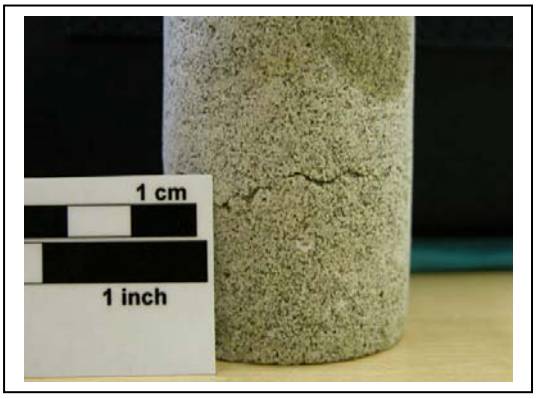

Figure 90. Picture of Regensburg sandstone after 100 F-T cycles.

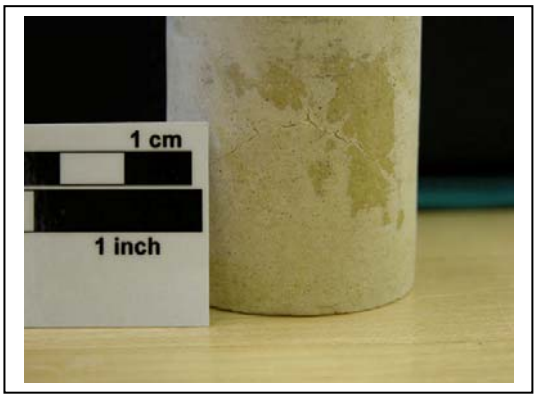

Figure 91. Picture of Cadeby Mg-limestone after 100 F-T.

Figure 92. Picture of Hazel-Lane Mg-limestone after 100 F-T.

Degree of alteration	Description	Sample after weathering
0	Specimen intact	Highmoor Wüstenzeller
1	Very minor change (minor rounding of corners and edges), which does not compromise the integrity of the specimen.	
2	One or several minor cracks (< 0.1 mm width) or detachment of small fragments (< 10 mm^2 per fragment).	Cadeby Hazel Lane
3	One or several cracks, holes or detachments of fragments larger than those defined for the "2" rating, or alteration of material in veins	Sander Regensburg
4	Specimen broken in two or with major crack	
5	Specimen in pieces and disintegrated	

Table 6. Classification of the decay after freeze-thaw cycles (DIN EN 12373).

VIII.2. The quality index, QI %

A decrease of the quality index (QI%) is observed for all lithotypes (Figure 93), except Wüstenzeller sandstone, which seems to illustrate a slight increase of its quality index.
When the quality index is plotted versus the total porosity (Nt%) the data point indicate the pore shape of the lithotypes (Figure 94); data points are more or less closer to the line defining the porosity of pores then the line defining the porosity of cracks. When data after artificial weathering are compared to the data obtained on the fresh stones, it can be easily noticed that the decrease of the quality index corresponds to the appearance of cracks in the material. Indeed, the data points are shifted to the center of the graphic and move away from the line of pore porosity.
The highest changes in the quality index are shown for Sander and Regensburg sandstone and Cadeby and Hazel Lane magnesium limestone. These four stones present the more important alteration with the appearance of clear macro cracks. However, Highmoor magnesium limestone, which do not show macro cracks, still presents a decrease in the quality index. It may prove that micro cracks exist in the specimen. On the other hand, Wüstenzeller sandstone does not illustrate a significant change of the quality index. The slight "increase" may be due to heterogeneity of sandstone samples.

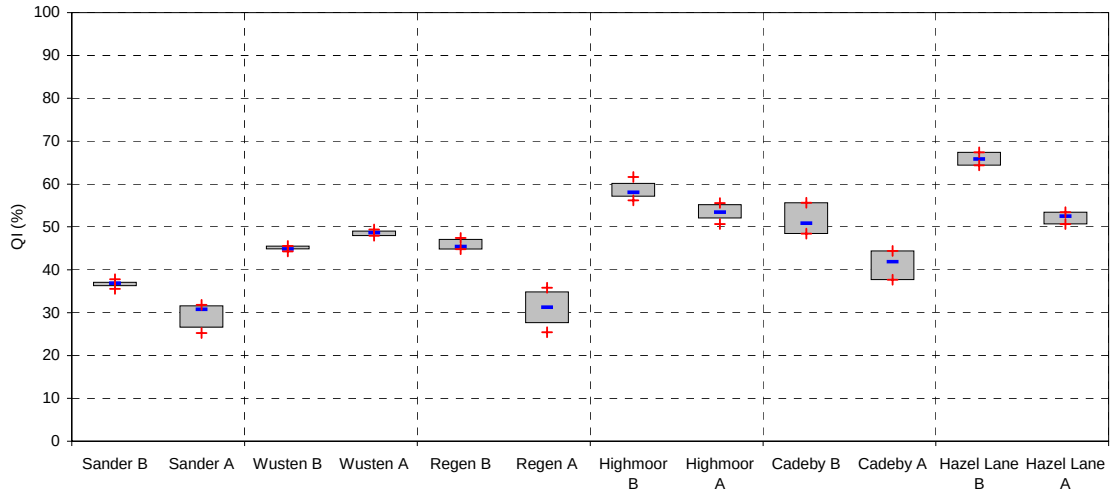

Figure 93. Comparison of QI% before (B) and after (A) Freeze-Thaw (F-T) cycles. Raw results in Annex 2 Table 12 and Table 17.

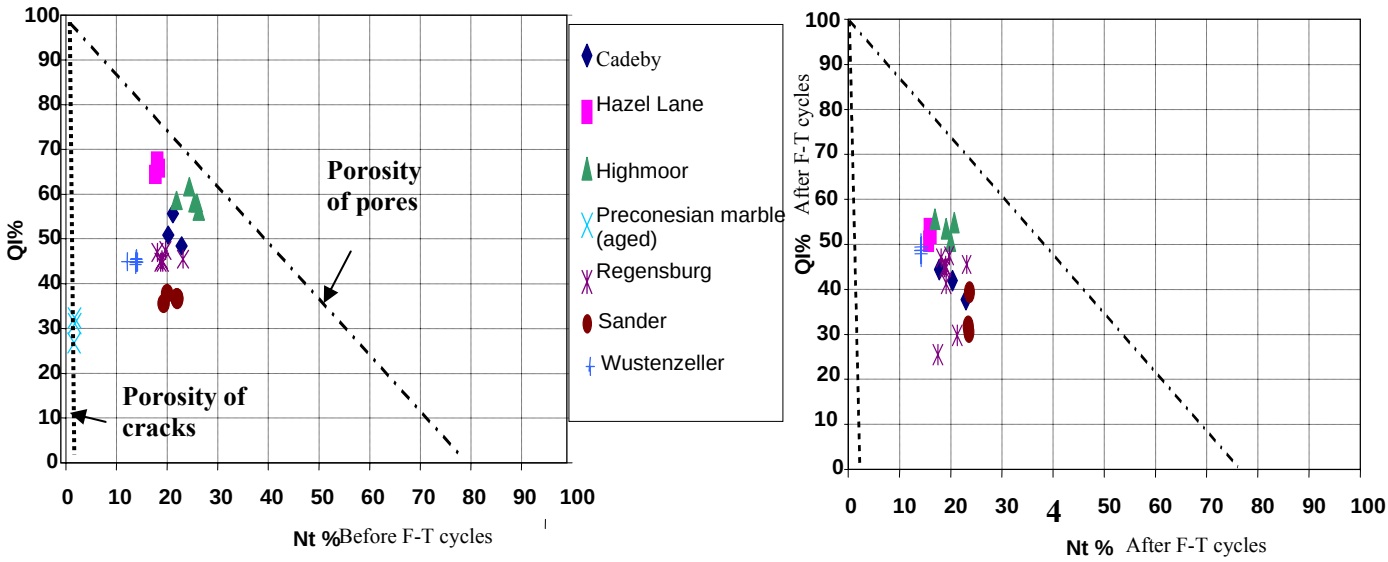

Figure 94. Diagram representing the porosity total (Nt) versus the quality index (QI%). It characterizes the shape of the pores (cracks or/and pores). On the left hand side, the diagram presents the results before weathering; on the right hand side, the results after F-T cycles; as the thermally aged Proconnesian marble was already represented on the first diagram and was used to verify that its porosity belongs to the porosity of cracks, the marble is not displayed on the diagram after F-T cycles.

VIII.3. Ultrasonic velocities

Concerning the ultrasonic velocities, comparable results as for the quality index can be observed. All lithotypes show a decrease of the ultrasonic parallel and perpendicular to the stone bedding (Figure 95 and Figure 96). The decrease of ultrasonic is probably more obvious parallel to the stone bedding than perpendicular.

This result confirms the propagation of cracks (macro and micro) parallel to the stone bedding, where the highest ultrasonic decrease is shown for Sander and Regensburg sandstone and Cadeby and Hazel Lane magnesium limestone.

The results, which are spread after artificial weathering, also illustrate the inhomogeneity of the decay. It is important to consider this observation when interpreting the results as the method of measurement may or may not reflect the entire specimen.
As it was observed for the quality index, Highmoor magnesium limestone also presents a decrease of ultrasonic velocity even if no visible decay could be noticed. Micro cracks reducing the ultrasonic velocity are probably also present in Highmoor stone.
Wüstenzeller sandstone slightly increases its ultrasonic velocity probably through a residual moisture content in the structure after the drying.

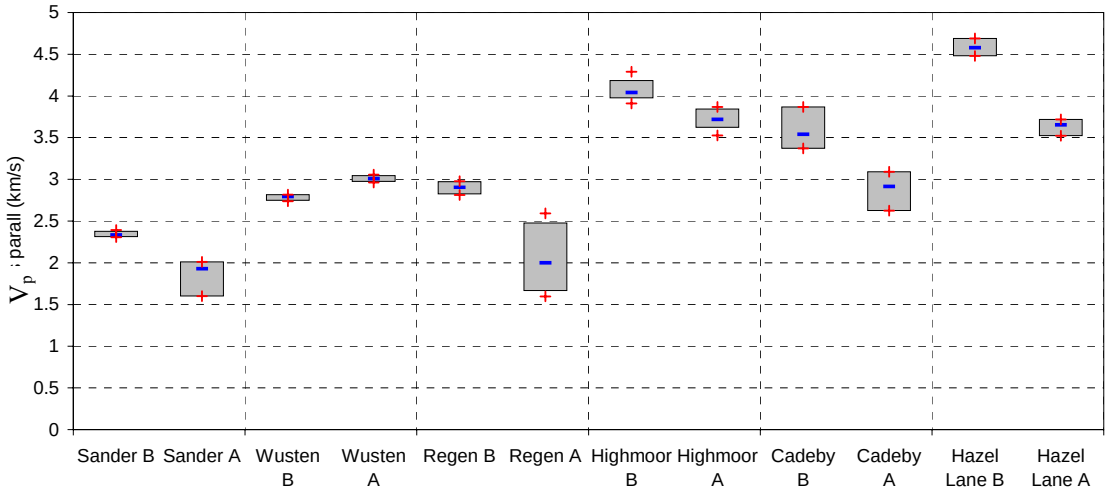

Figure 95. Comparison of the ultrasonic velocity parallel to the stone bedding before (B) and after (A) F-T cycles. Raw results in Annex 2 Table 13 and Table 18.

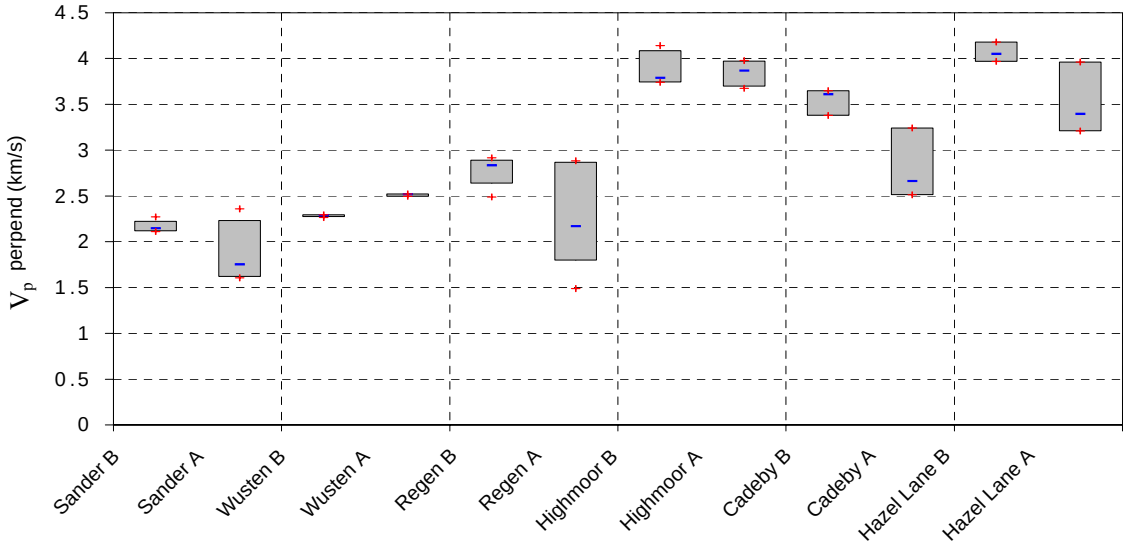

Figure 96. Comparison of the ultrasonic velocity perpendicular to the stone bedding before (B) and after (A) F-T cycles. Raw results in Annex 2 Table 13 and Table 18.

VIII.4. Dynamic modulus of elasticity

Dynamic modulus of elasticity also reveals an important decrease for the four stones highly weathered (Figure 97). Ultrasonic velocity and dynamic modulus of elasticity are connected to each other, and therefore when one decreases the other one should also decrease.
Highmoor magnesium limestone does not reveal a significant decrease of the dynamic modulus elasticity, as it was the case for the ultrasonic measurements parallel to the stone bedding. Ultrasonic velocity perpendicular to the stone bedding was not clearly decreased after artificial weathering. The dynamic modulus is also measured perpendicular to the bedding and then does not show variation after freeze-thaw cycles.

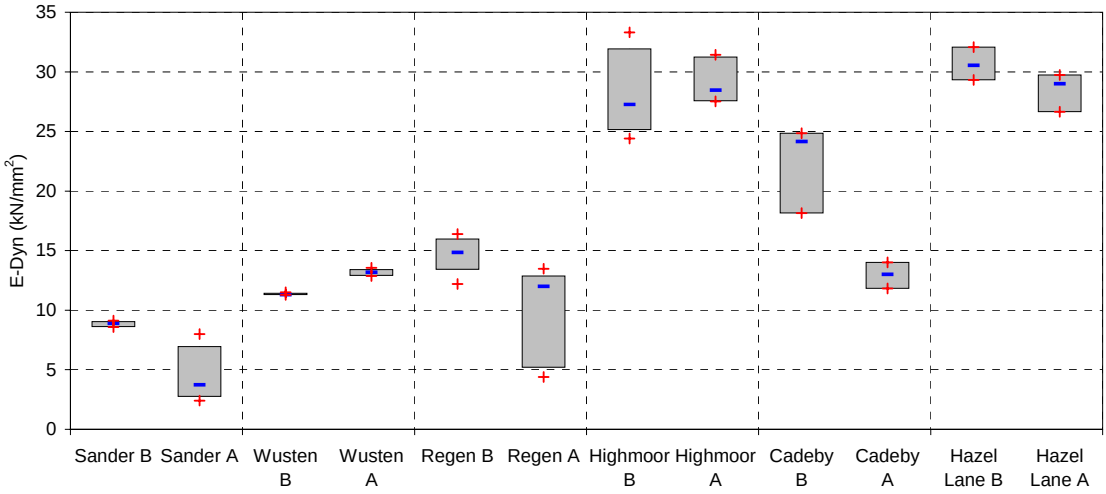

Figure 97. Comparison of the dynamic modulus of elasticity before (B) and after (A) F-T cycles. Raw results in Annex 2 Table 13 and Table 18.

VIII.5. Resume of changes in the structure

Quality index, ultrasonic velocities and dynamic modulus of elasticity show comparable results for all lithotypes. The decrease of these properties, quality index and ultrasonic specifically, seems to be related to the presence of micro and macro cracks, while the decrease of the dynamic modulus of elasticity seems to be more related to the presence of macro cracks in believe to the existence of microcracks through the quality index measurements (Figure 94). The three non-destructive measurements consider the entire specimen, reveal the inhomogeneity of the decay by widening the interval of significance and are influenced by the appearance of cracks in the material. These measurements are apparently a good indicator of the decay appearing in the structure at a micro scale. On the other hand, measurements on digital images of the grain contact after artificial weathering did not show any changes; the evolution of that property is not measurable on optical microscope.

IX. Changes in porosity

IX.1. Total porosity by water saturation

Total porosity by water saturation as well as the free porosity are measured on the entire specimen. No significant change of the total porosity can be observed on the sandstones (Figure 98).
For the sandstone, it can be assumed that a pore structure may have changed but without increasing the total porosity. Even the large cracks appearing in Sander and Regensburg did not enhance the total porosity.

In the other hand, the magnesium limestone does not show an increase in the volume of total porosity, especially Highmoor and Hazel Lane (Figure 98), but probably a redistribution of loose debris in the pore structure leading perhaps to the closing of certain pores (Fitzner, 1988). In case of partial saturation, collapse or compression of fine pores may also occur as they are emptied and a capillary under pressure results (Everett, 1961).
In all cases, the free porosity (N_{48}%) remains unchanged (Figure 99). There is no improvement of pore connectivity after freeze-thaw cycles.

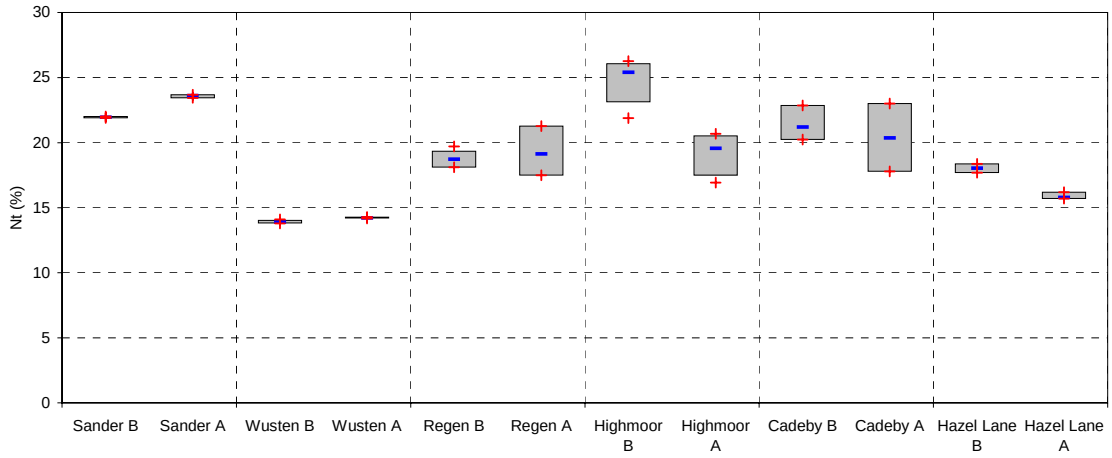

Figure 98. Comparison of the total porosity (Nt) before (B) and after (A) F-T cycles. Raw results in Annex 2 Table 12 and Table 17.

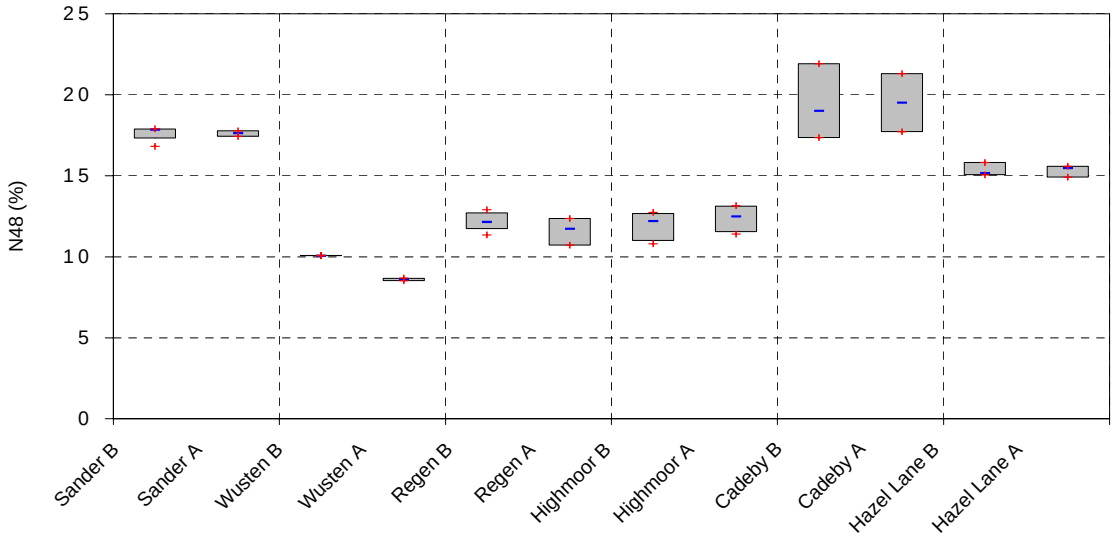

Figure 99. Comparison of the free porosity (N48) before (B) and after (A) F-T cycles. Raw results in Annex 2 Table 12 and Table 17.

IX.2. Total porosity by MIP and DIA

As it was observed and proved, decay of the stones after artificial weathering is heterogeneous. Therefore, mercury porosimetry as well as DIA are probably not the most accurate methods to evaluate changes in a whole material structure. Both methods use a part of a sample, which is probably not representative of the entire specimen.
The results of both methods are still presented. MIP porosity mainly reveals a spreading of the results (Figure 100). Nevertheless some few increases might be related to the amount of sample used to proceed to the measurement (0.5 cm^3), which might be highly influenced by the presence of micro cracks. Micro cracks may play a more important role on a small sample than an entire core sample.

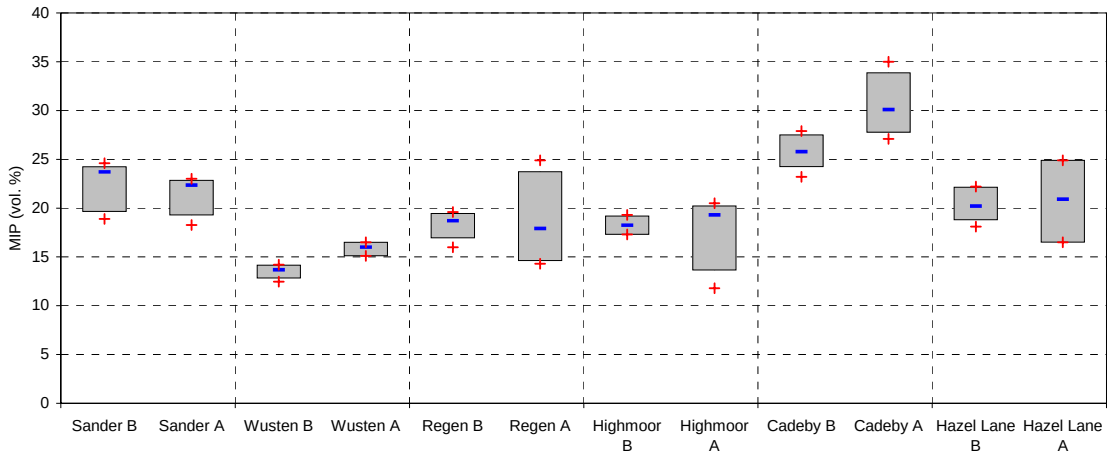

Figure 100. Comparison of the MIP porosity before (B) and after (A) F-T cycles. Raw results in Annex 2 Table 12 and Table 17.

DIA porosity shows different results such as an important increase of porosity for Cadeby magnesium limestone (Figure 101). The thin section prepared and analyzed presented cracks, which may lead to the increase observed (Figure 102). It proves that the heterogeneity of the sample has a main impact on the final result, and porosity measurements on such heteregoneous samples are probably more accurate when considering the entire sample and not a part of it, which is not really representative.

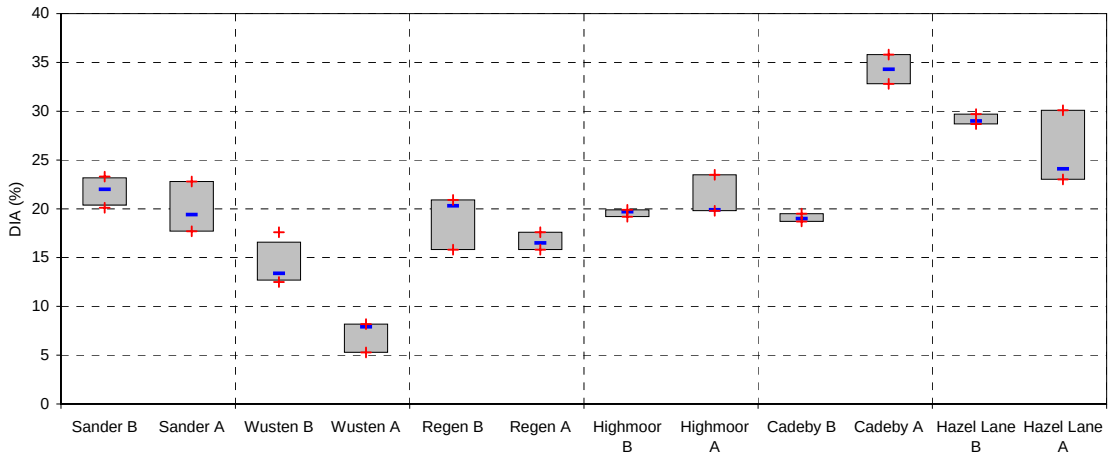

Figure 101. Comparison of the DIA porosity before (B) and after (A) F-T cycles. Raw results in Annex 2 Table 12 and Table 17.

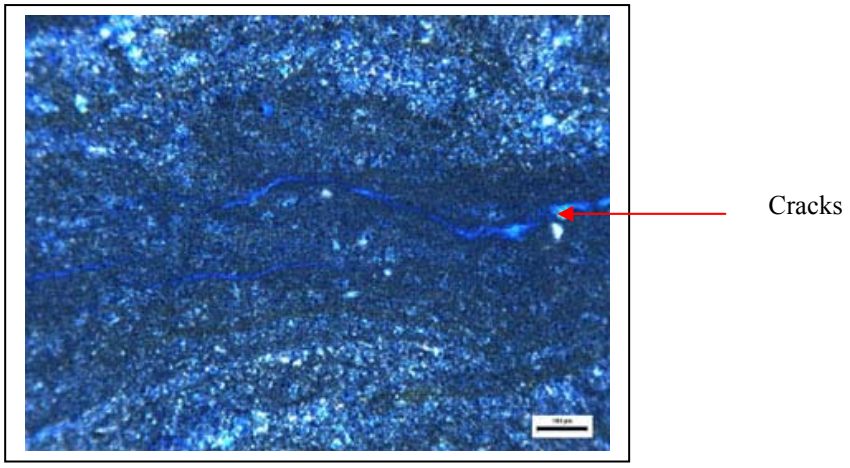

Figure 102. Picture at optical microscope of Cadeby limestone after F-T cycles showing the presence of cracks.

IX.3. Saturation coefficient S

The sandstones did not reveal real changes in the total porosity and free porosity after artificial weathering. Thus, the saturation coefficient is approximately the same as before freeze-thaw cycles (Figure 103).

On the other hand, the magnesium limestone showed a slight decrease of the total porosity (N_t), while the free porosity (N_{48}) remained stable. Therefore the ratio N_{48}/N_t necessarily increased, because more porosity of the material is naturally accessible to water by capillarity.

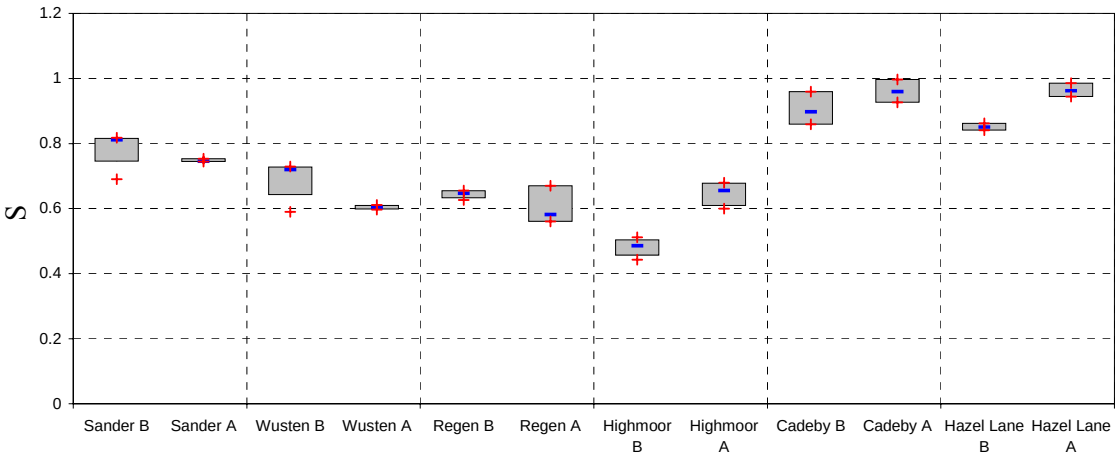

Figure 103. Comparison of the saturation coefficient S before (B) and after (A) F-T cycles. Raw results in Annex 2 Table 12 and Table 17.

IX.4. Pore size distribution

All diagrams related to the changes of the pore classes previously studied are presented in annex 1, Figures 127 to 133.
It is difficult to relate the results to weathering aspects as alterated sandstone Sander and Regensburg do not clearly reveal a change in the pore structure; only a decrease of the BET and therefore of the micro porosity below 2 nm can be observed. On the other hand, Wüstenzeller which from the ultrasonic and dynamic modulus of elasticity results is less to not weathered shows an increase of all pore ranges except over 5 µm. The compaction of clay aggregates, driving by flow of liquid water during freeze-thaw cycles may have reduced the largest pore range (filling of the pores), but increase the smaller porosity.

All limestones illustrate an increase of the pore volume 0.1-5 µm by MIP and DIA; DIA is probably not really reliable in this pore range. Nevertheless, increase of Highmoor and Cadeby are in agreement with MIP results. Pore volume > 5 µm is also increased from MIP measurements but broaden from DIA results; Hazel Lane results are largely spread probably due to the heterogeneity of the decay.

As Thomachot (2002) demonstrated freeze-thaw cycles cause a large dispersion of the pore access and accentuate heterogeneity of the porous network; it can lead to a decrease of fine pores (<2 µm) and the increase of large pores measured by mercury porosimetry; the break-up of grain contacts (Fitzner, 1988) or compression of pore walls due to internal growth of ice crystals may also involve pore enlargement.

Some of the changes in pore structure due to freeze-thaw cycles described in the literature can be recognized in the results (increase of larger pores), but several changes are too small to be

significant (decrease of smallest pores). Therefore, no general tendency could be identified from the reading of the porosity results according to the pore ranges determined before artificial weathering, pores < 0.1 µm; 0.1-5 µm and > 5 µm; the results depending largely on the methods used, are highly spread and are broaden for a same lithotype.
Therefore, it may be more realistic to observe and compare the evolution of the entire mercury intrusion diagram before and after artificial weathering.

As a first conclusion, all total porosity results (N_t, N_{48}, MIP, DIA) are mainly spread. As long as the results cover each other, there is no significant change. It can be also underlined that if total porosity (N_t) does not change, the sum of BET, 0.1-5 µm and > 5 µm must be constant.

Each stone is considered individually in order to observe better the evolution of the porosity on the entire mercury intrusion curve after freeze-thaw cycles (F-T).
For Highmoor magnesian limestone, the entire distribution is shifted in direction to the bigger pore entrances (Figure 104). The initial unimodal distribution centered on 1 µm becomes almost bi-modale and centered on 7 µm. Moreover, the distribution continues on the larger pores over 10 µm when before weathering it stopped at 7 µm. A decrease of small pores is then observed associated with an increase of the larger pore entrances.
Cadeby stone shows an important increase of the pore centered on 5 µm, three times higher after weathering than before (Figure 105). Augmentation of large pores on and over 10 µm is also noticed.
Distribution of Hazel Lane was initially spread from below 0.1 µm to over 100 µm. After freeze-thaw cycles the distribution has become unimodal and centered on 1 µm (Figure 106). Small pores and bigger pores disappeared.

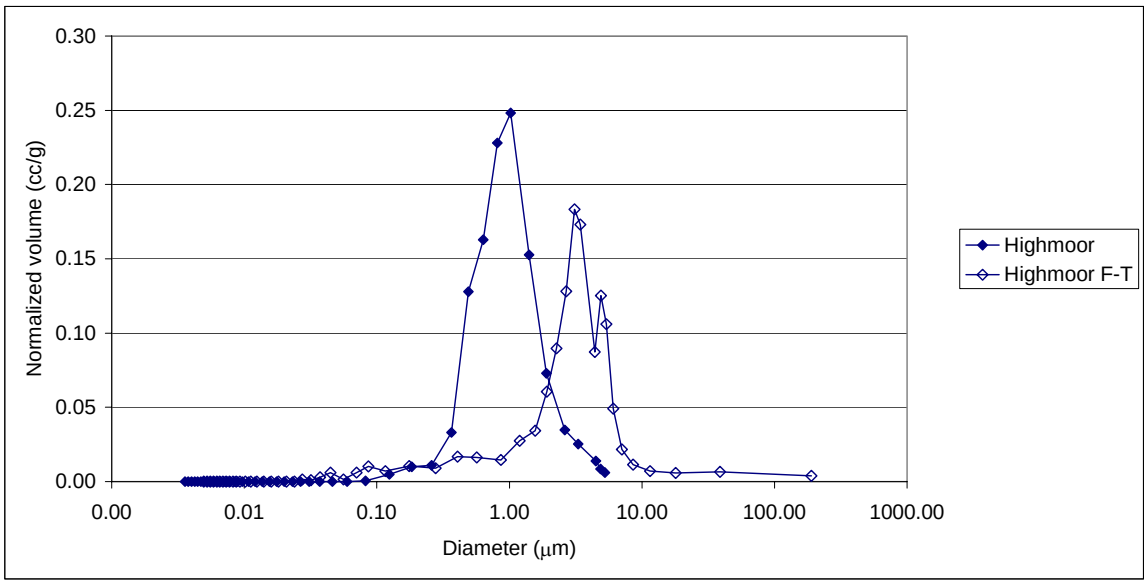

Figure 104. Pore size entry distribution by mercury porosimetry of Highmoor magnesian limestone before and after F-T cycles.

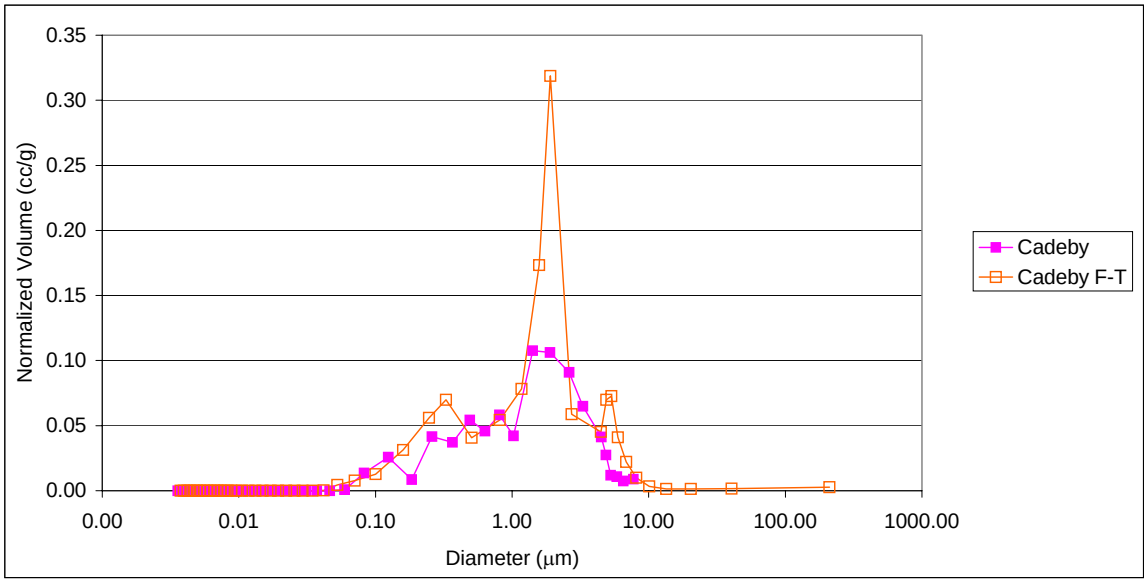

Figure 105. Pore size entry distribution by mercury porosimetry of Cadeby magnesian limestone before and after F-T cycles.

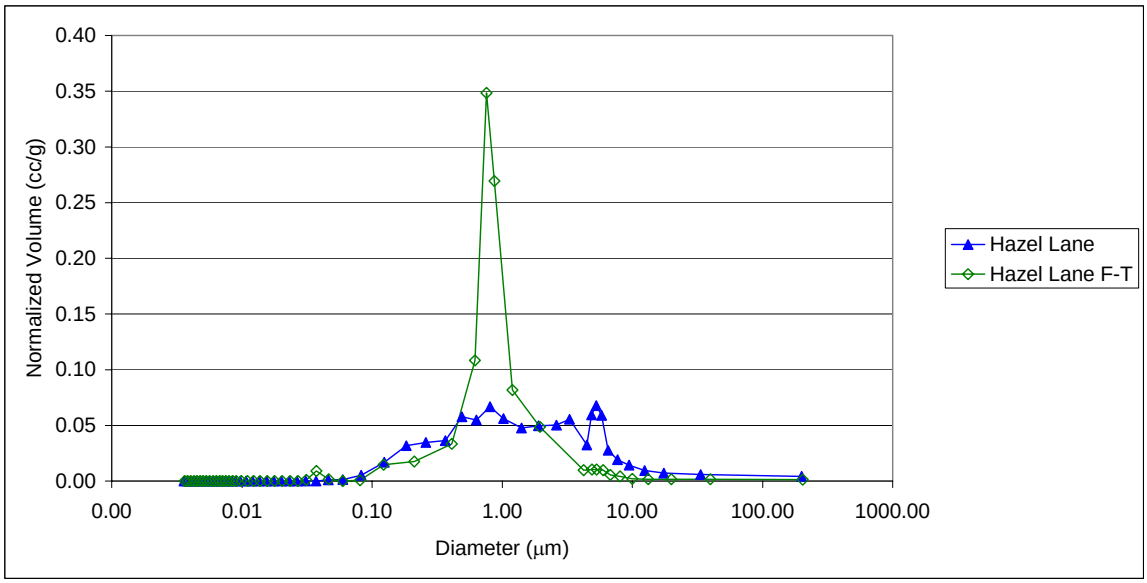

Figure 106. Pore size entry distribution by mercury porosimetry of Hazel Lane magnesian limestone before and after F-T cycles.

For the weathered sandstones similar observations can be made. Indeed, Sander sandstone does not reveal strong changes in the small pore range < 1 µm but an increase of bigger pores from 10 µm to 100 µm (Figure 107). For Regensburg, the increase of pore entrances is obvious on 1 µm, while the rest of the distribution remains the same (Figure 109).

Wüstenzeller seems to present a complete different evolution in the distribution of the pore entrances after freeze-thaw cycles (Figure 108). Indeed, it is after weathering shifted in direction to the smallest pores, and is spread from 0.1 µm to 100 µm. The larger pores clearly decreased. It might confirm the hypothesis of a clay aggregates compaction filling the larger pores and increasing the smaller pores (Fitzner, 1988).

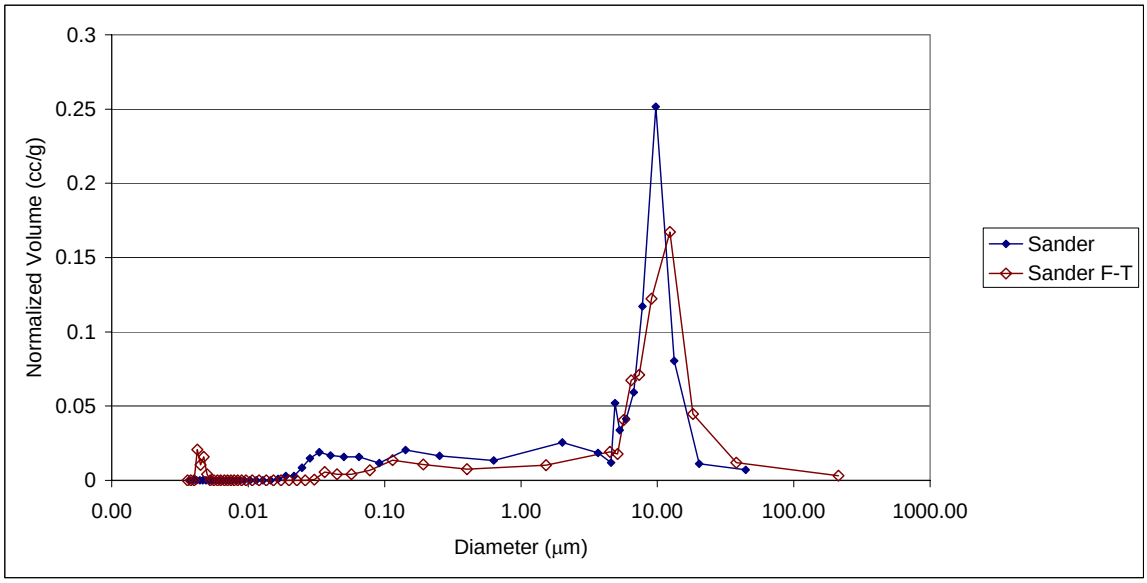

Figure 107. Pore size entry distribution by mercury porosimetry of Sander sandstone before and after F-T cycles.

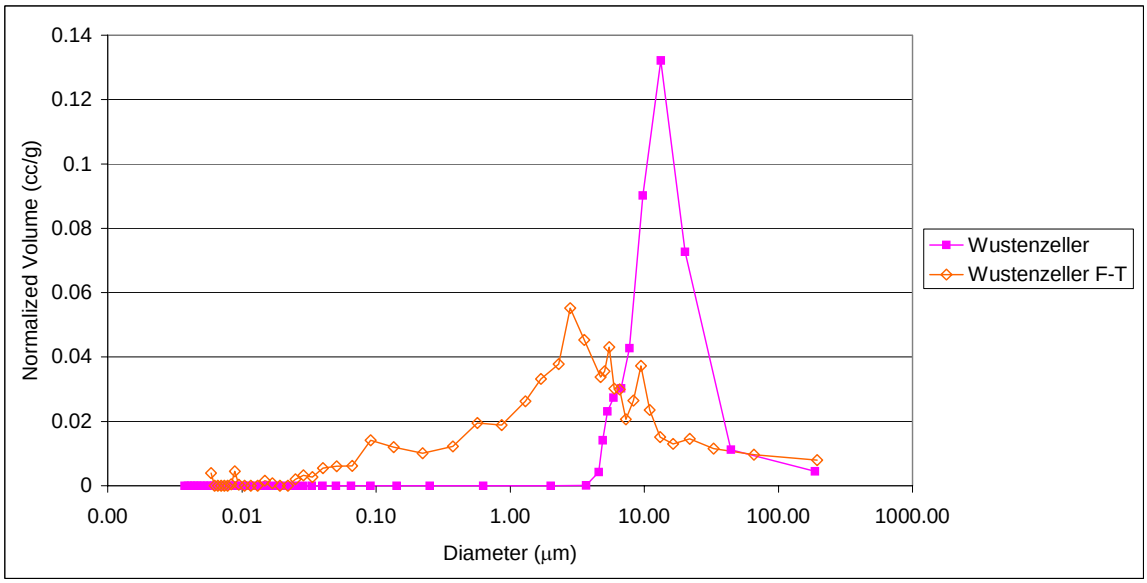

Figure 108. Pore size entry distribution by mercury porosimetry of Wüstenzeller sandstone before and after F-T cycles.

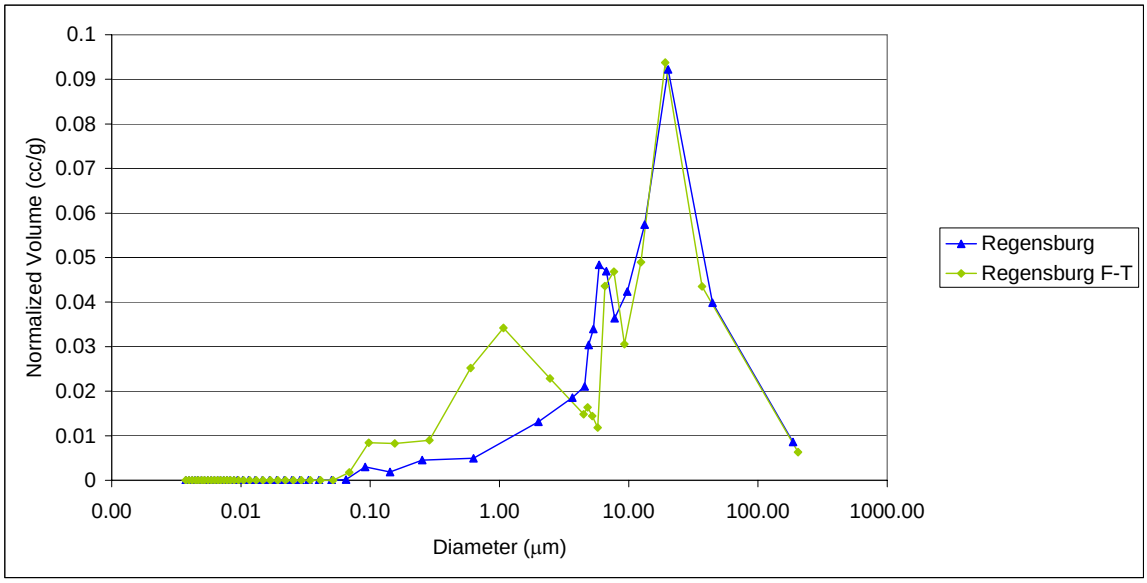

Figure 109. Pore size entry distribution by mercury porosimetry of Regensburg sandstone before and after FT cycles.

IX.5. Resume of changes in porosity properties

The purpose of this chapter is to identify clear properties and therefore variables, which will provide a fast and easy reading of the progression of the decay and the state of weathering. In order to be able to assess weathering we should be able to recognize the properties, which are affected the most. Apparently, porosity measurements and pore size distribution are not the easiest and clearest properties changed after weathering and proving that decay is actually going on. Even if porosity measurement before weathering were not necessarily linearly correlated, they gave at least the same range of results; before artificial weathering all methods provided a high pore volume < 0.1 µm for Sander sandstone or a low pore volume 0.1-5 µm for Wüstenzeller sandstone.

Nevertheless, it appears, that changes of pore size distribution can be easier detected and explained by looking at the entire mercury intrusion diagram. Thomachot (2002) also demonstrated the use of mercury porosimetry to identify changes in the pore structure. In general, all limestone show a more pronounced maximum after freeze-thaw cycles and centered around 1-5 µm, and rather no change in the total porosity (Figure 100). These results contradict Thomachot (2002) who explains a dispersion of the pore access after freeze-thaw cycles. The mechanism might be ice crystallization in the pores 1-5 µm and then an increase of these pores, a partial collapse of smaller pores under the pressure applied. Pore size distribution is uniformed after freeze-thaw cycles.

Sander sandstone does not present change besides an increase of the maximum (10-100 µm), and thus an increase of the total porosity. Wüstenzeller and Regensburg show wider pore distribution, where clear maximum disappeared.

X. Changes in hydric properties

X.1. Water uptake coefficient, W

A decrease of water uptake coefficient is observed for all lithotypes (Figure 110), and might be due to changes in the pores structure. However, as it was shown earlier, no specific changes in the pore classes defined before artificial weathering could have been identified such as the pore volume 0.1-5 µm, which was correlated with the water uptake on the fresh material. But it was also proved that after weathering these pore ranges are not valuable anymore and that it is the entire evolution of the pore entrance distribution, which has to be considered. Thus it is the pore range 0.1-5 µm, which is the most affected by the weathering. It can occur with a collapse of fine pore < 1 µm and an increase of larger pore 1-5 µm, or even with a new distribution of the pore range. The water uptake should represent the pore size, which is most significant for the stone. Thus the limestone with a new maximum around 5 µm should show an increase of the water uptake coefficient. For Sander sandstone, the pore size distribution is increased to the larger pores, while the distribution of Wüstenzeller and Regensburg present a wider distribution. There is therefore no evidence of a lower water uptake coefficient by the MIP curves for all stones. No real consistency in all pore size and W measurements can be emphasized.
Moreover, the freeze-thaw cycles can be qualified as "mild test" as water was not absorbed under pressure and the freezing period was in the air. Thus, ice can migrate to the outside of the stone and cause a compaction of pores and create formation of small cracks in the material. These cracks will decrease the QI (VIII.2) and can reduce the water uptake coefficient.

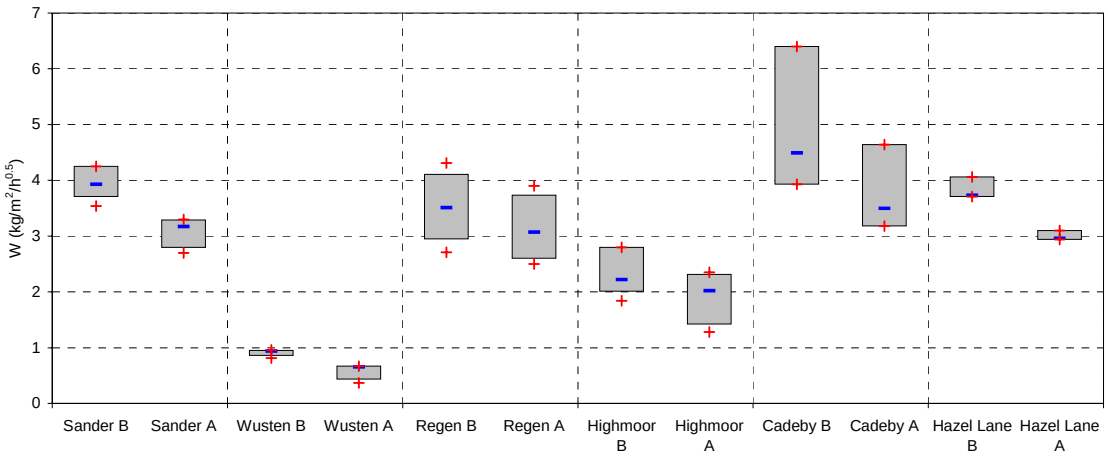

Figure 110. Comparison of the water uptake coefficient before (B) and after (A) F-T cycles. Raw results in Annex 2 Table 13 and Table 18.

The water absorption curves illustrate the lower water uptake after artificial weathering (Figure 111 and Figure 112), but also indicate a micro porosity which might be slower filled as the saturation is not completed and the curve is not linear, crossing the first curve and continuing slowly to increase; Hatched areas underline the decrease of capillarity of each stone.

It can be assumed that formation of clay packages by frost action may have occurred, but not all lithotypes do contain clay minerals. The increase of pore entrance around 1-2 µm on the MIP curves might be an indication of such a result.

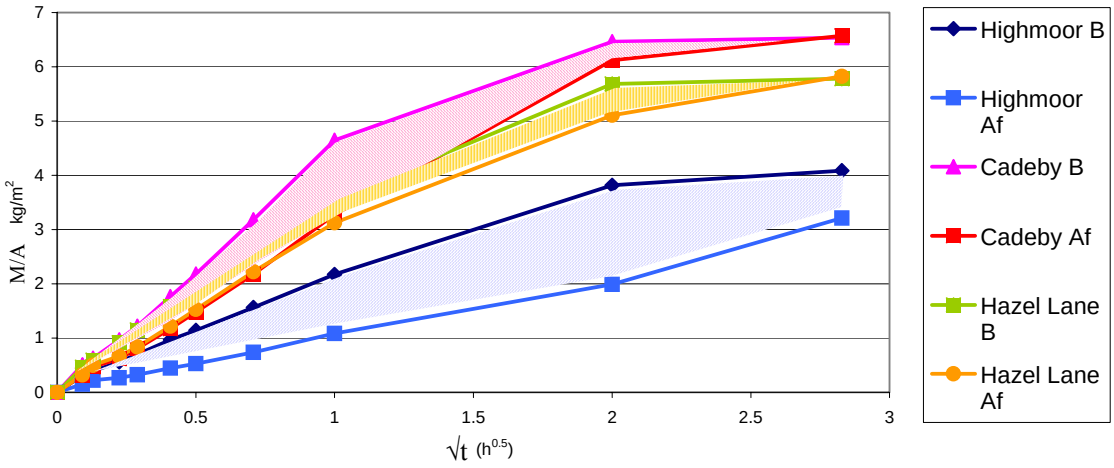

Figure 111. Comparison of the capillary curves of the magnesian limestone before (B) and after (A) F-T cycles.

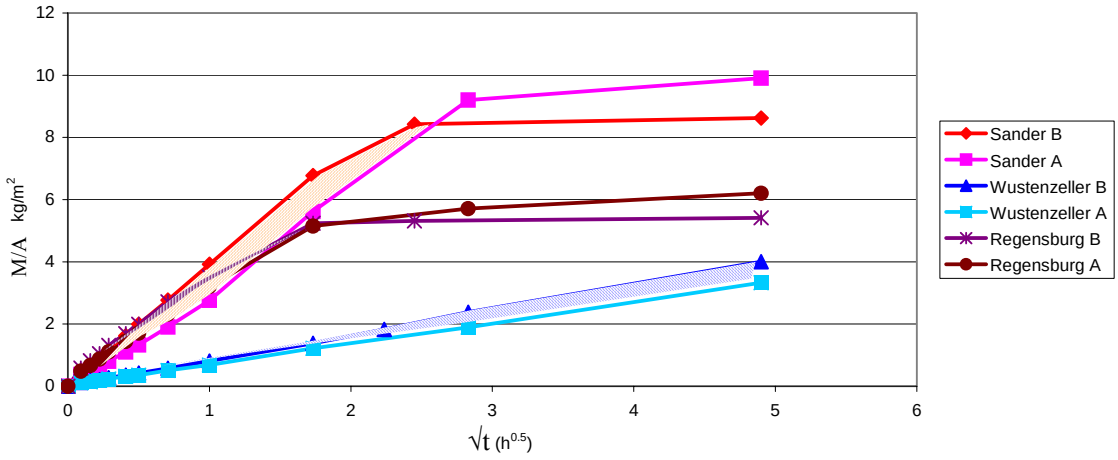

Figure 112. Comparison of the capillary curves of the sandstones before (B) and after (A) F-T cycles.

The capillary rise, B demonstrates a similar decrease as the water uptake coefficient for all lithotypes (Figure 113). As N_t and N_{48} remain more or less constant, B decreases when W decreases. It shows that pore structure changed but does not accelerate and augment the water absorption by capillarity. Capillary rise is obviously reduced after artificial weathering and might be due to the increase of larger pores, which slow down the capillary rise.

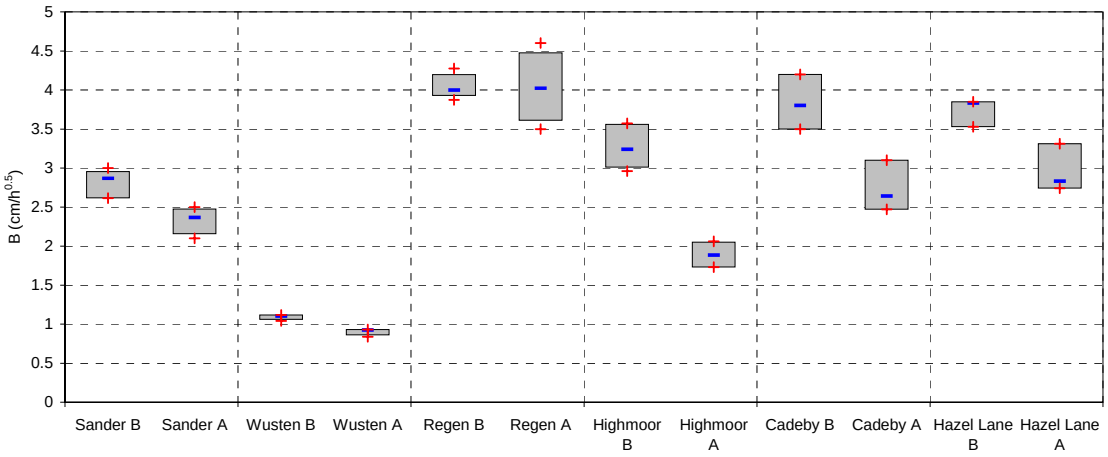

Figure 113. Comparison of the capillary rise (B-value) before (B) and after (A) F-T cycles. Raw results in Annex 2 Table 13 and Table 18.

X.2. Drying kinetics

Regensburg sandstones as well as Cadeby and Hazel Lane magnesium limestone reveal a strong increase of water flow rate g (liquid phase measured on the plateau) after artificial weathering (Figure 114), Sander sandstone presents a smaller increase. The evaporation rate is here measured and considered on the plateau during drying, so when it is still liquid water which is transported to the surface by capillarity. These four specimens showed open macro cracks on the side of the samples and presented macro cracks on the surface of the magnesium limestone especially.

Drying rate depends of the relative humidity inside and outside the material, the viscosity of the fluid but also on the surface roughness, which may increase the real surface for evaporation. The macro cracks visible on the surface and probably also some micro cracks as well as grain loss during freeze-thaw cycles may obviously increase the surface roughness of the material after weathering. Water flow rate is therefore accelerated.

Wüstenzeller sandstone and Highmoor magnesian limestone do not present increase of the water flow rate.

Therefore, it seems that the water flow rate is more related to macro open cracks, than to a real pore structure variation, but might be generally linked to an increase of the large pore 1-5 µm, which can be observed for all stones looking at the MIP curves.

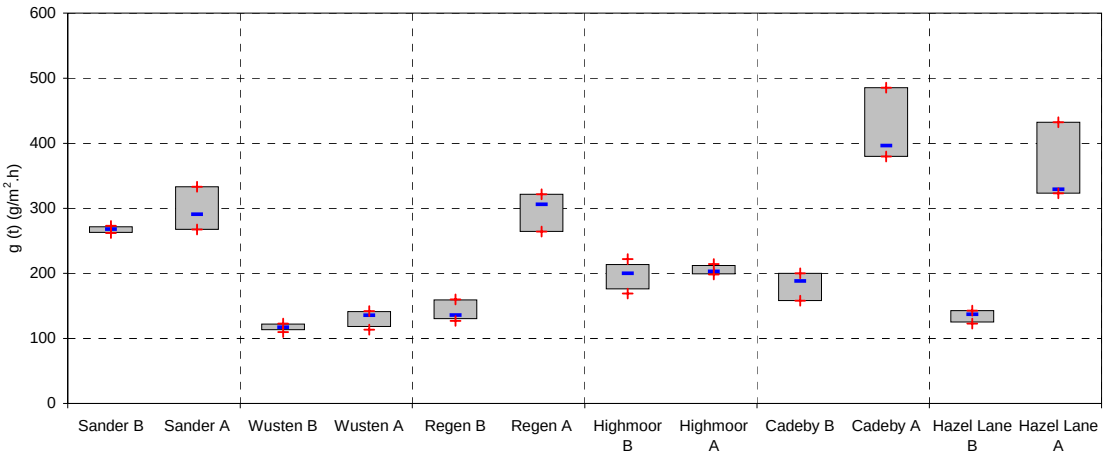

Figure 114. Comparison of the water flow rate g constant at the plateau during drying before (B) and after (A) F-T cycles. Raw results in Annex 2 Table 13 and Table 18.

Variation of the plateau after ageing illustrates well the important increase of drying rate of the four weathered lithotypes (Figure 115 and Figure 117).
The plateau and therefore the constant water flow rate during the capillarity phase of the drying is higher and shorter. It indicates a stronger evaporation during the capillary phase. This behavior may be related with the increase of the larger pores 1-5 µm, the increase of roughness and the presence of cracks on the surface of the sample. Moreover, the decrease of water flow by diffusion during drying of Sander and Regensburg sandstones is also stronger than before artificial weathering (Figure 115 and Figure 116). After the plateau the curves reveal a rapid diminution in the moisture content, the moisture content for Regensburg falls from 50% Residual Moisture to 20 % Residual Moisture after weathering, while before weathering it goes from 50% Residual Moisture to 48% Residual Moisture. Samples are dried faster after artificial weathering than when they are fresh.
Higher water vapor conductivity coefficient β from the surface to the air is also observed after artificial weathering, and especially for Sander and Regensburg; Wüstenzeller coefficient is stable (Figure 119).

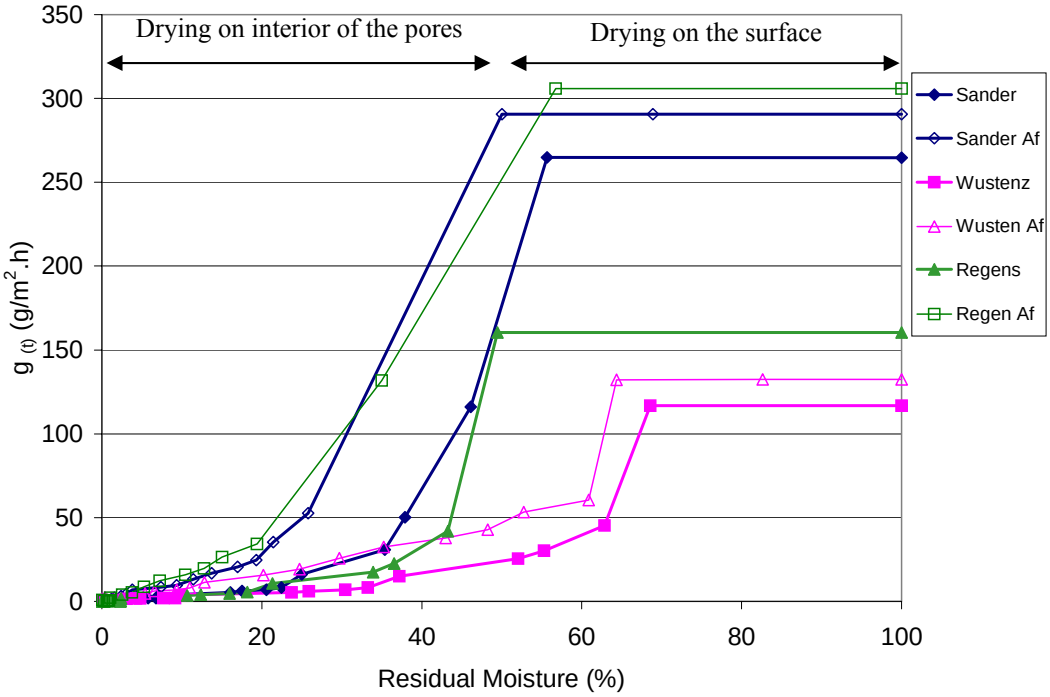

Figure 115. Comparison of the water flow rate during evaporation of the sandstones before (B) and after (A) F-T cycles.

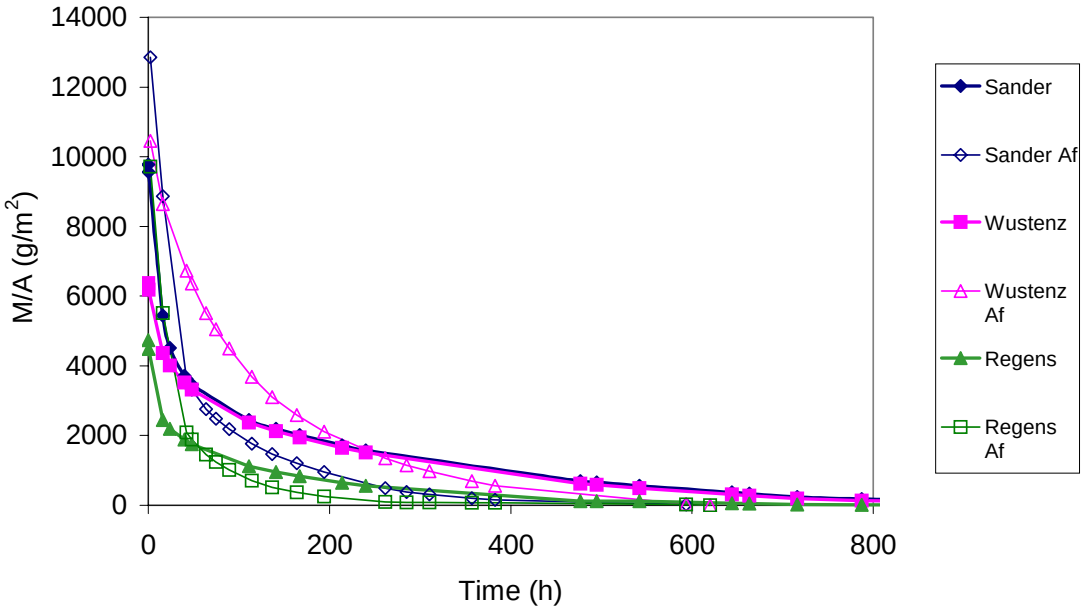

Figure 116. Drying curves of the sandstones before and after F-T cycles showing the weight loss as a function of time.

Concerning the magnesian limestone, the water flow rate is increased (higher plateau) and shorter (capillary phase is faster) but the curves remain comparable to the curves before weathering (Figure 117 and Figure 118). Curves before and after artificial weathering are almost parallel to each other. However, Highmoor seems to present a different behavior after weathering, with a longer plateau. The drying rate is more constant, followed by a quick drop of the drying rate during the diffusion phase. MIP curves show an important shift of the pore size from 1 µm to 5-10 µm. The increase of the large pore entrance may enhance the water flow rate during the drying by capillarity, the large reduction of pores < 1 µm may accelerate the drying by diffusion. Cadeby and Hazel Lane also show an important increase of the pore 1-5 µm, as well as cracks and surface roughness, which may explain the important increase of water flow rate and the fast drying of these stones. Finally, the water vapor conductivity coefficient β from the surface to the air is enhanced for the three limestones, Highmoor included (Figure 119)

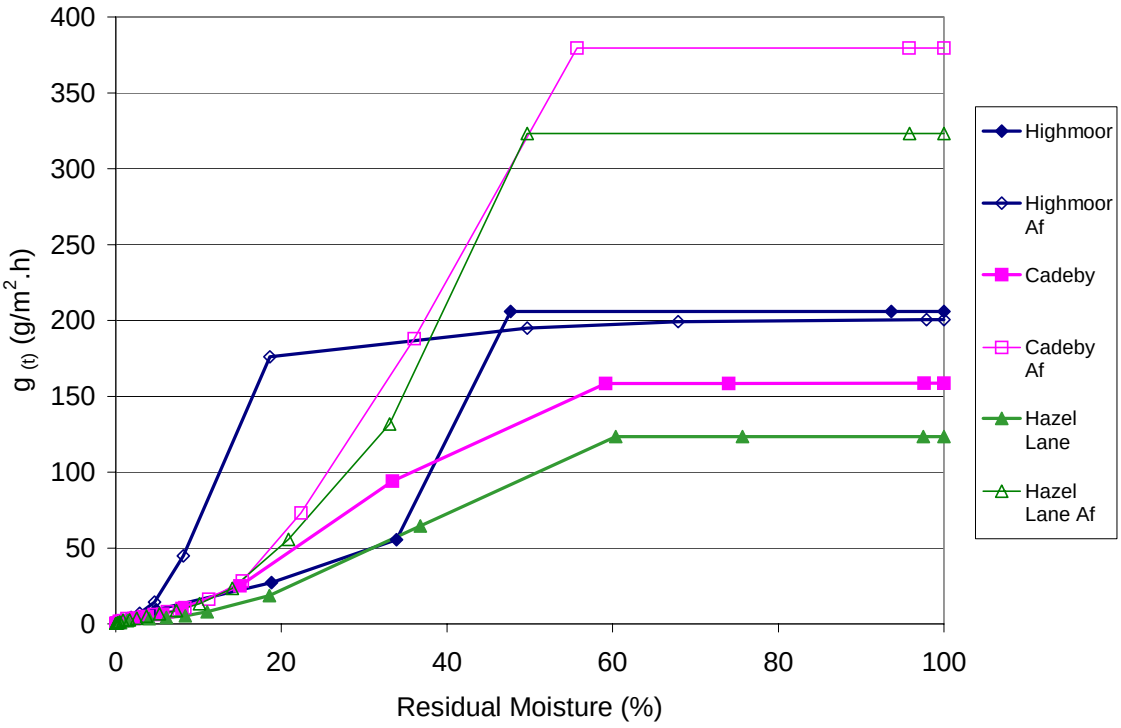

Figure 117. Comparison of the water flow rate during evaporation of the magnesian limestone before (B) and after (A) F-T cycles.

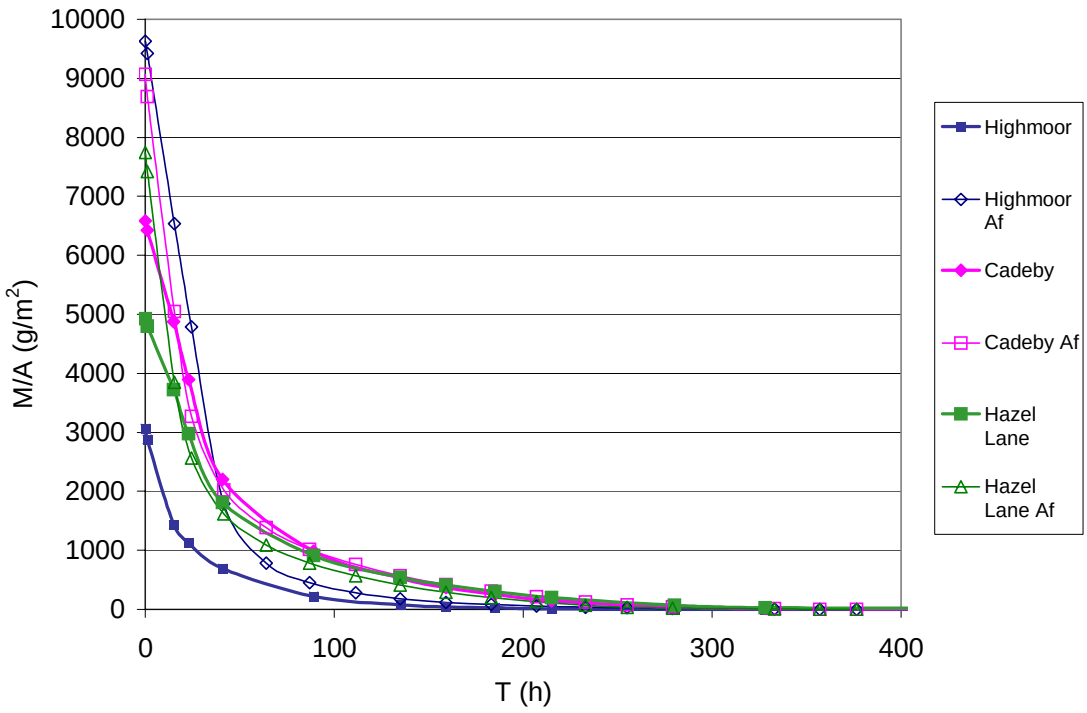

Figure 118. Drying curves of the magnesian limestone before and after F-T cycles showing the weight loss as a function of time.

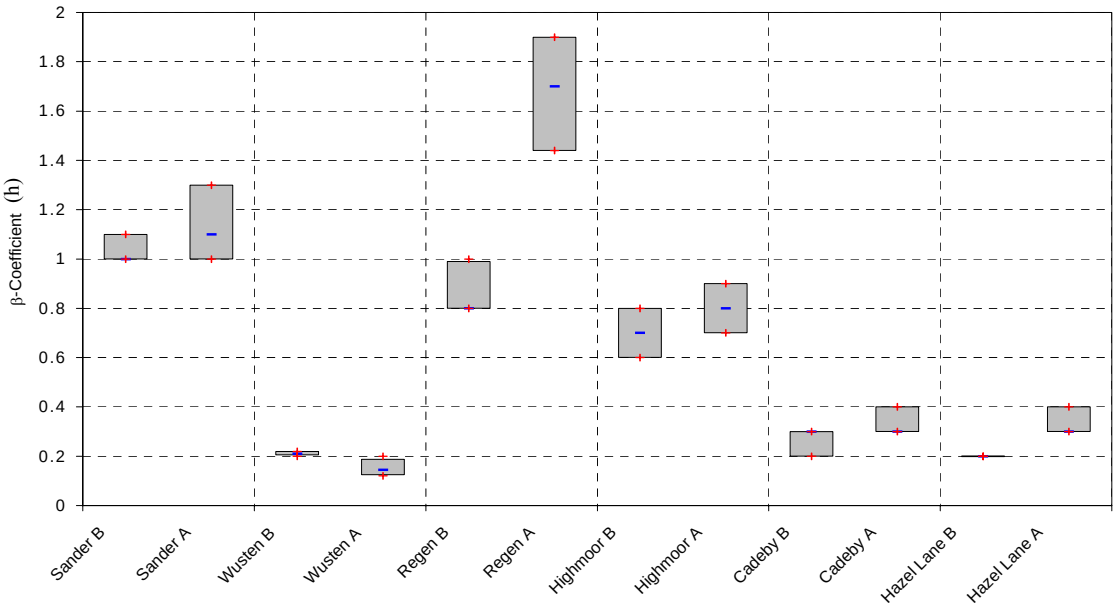

Figure 119. Comparison of the water vapor conductivity coefficient to the surface β before (B) and after (A) F-T cycles. Raw results in Annex 2 Table 13 and Table 18.

X.3. The water vapor diffusion resistance coefficient, μ-value

The measurement of the water vapor diffusion resistance coefficient is carried out on sample slices. Therefore, the most deteriorate part of the stone samples, presenting cracks, could not have been considered in the measurement. Slices necessarily avoid the large-scale decay, which could have been taken into consideration in the previous analysis as far evaporation kinetics and water vapor conductivity coefficient.

Only Cadeby and Hazel Lane magnesium limestone reveal a significant decrease of the water vapor diffusion resistance coefficient (Figure 120). However it seems logical that if water vapor conductivity to the surface is increased, the water vapor diffusion resistance should naturally decrease, the permeability being enhanced. It is proved with the drying curve versus time (Figure 116 and Figure 118) showing a faster drying after weathering than before. Also, the increase of large pores 1-5 μm may play an important role in increasing the water vapor permeability.

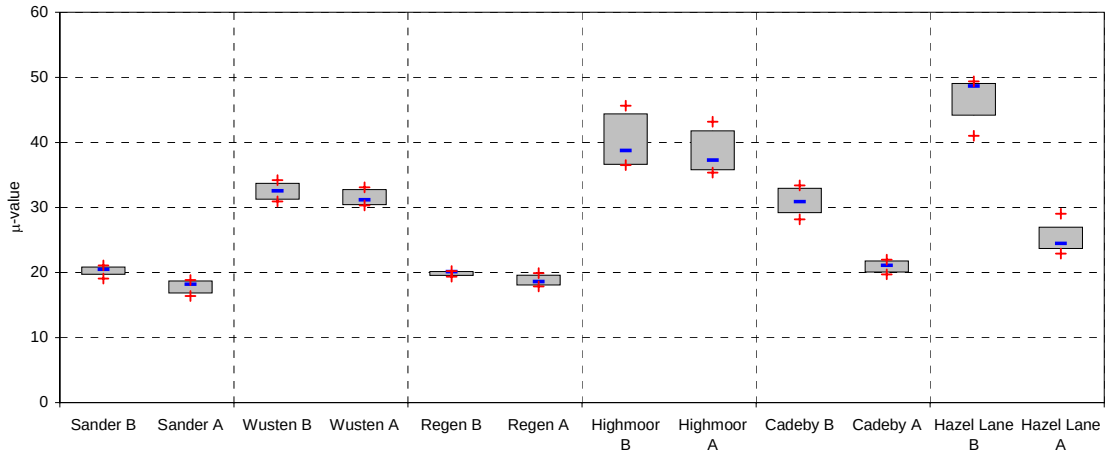

Figure 120. Comparison of the water vapor diffusion resistance coefficient μ before (B) and after (A) F-T cycles. Raw results in Annex 2 Table 13 and Table 18.

X.4. The hydric dilatation, ε-hydric

Increase of hydric dilatation is only observed for Sander sandstone (Figure 121). Sander already presented the highest hydric dilatation, which was probably due to its composition with a clay rich binder. Ice crystals could have been preferentially formed in the open spaces of the grain structures (Snethlage and Wendler, 1997). Movement and displacement within the structure may have been more important for Sander than for the other stones and may have lead to an increase of weakness of the intergranular bonds. The clay rich binder of Sander, playing a major role in the dilatation of the material, enhances the dilatation since the intergranular bounds are weaker. Wüstenzeller also contains some clay minerals, but the grain structure is not deteriorated after weathering, the strength is not affected and the hydric dilatation is stable. Regensburg, which also presented strong decay and open cracks, does not increase hydric dilatation. Its calcitic cement does not swell, dilatation remains the same than before weathering.

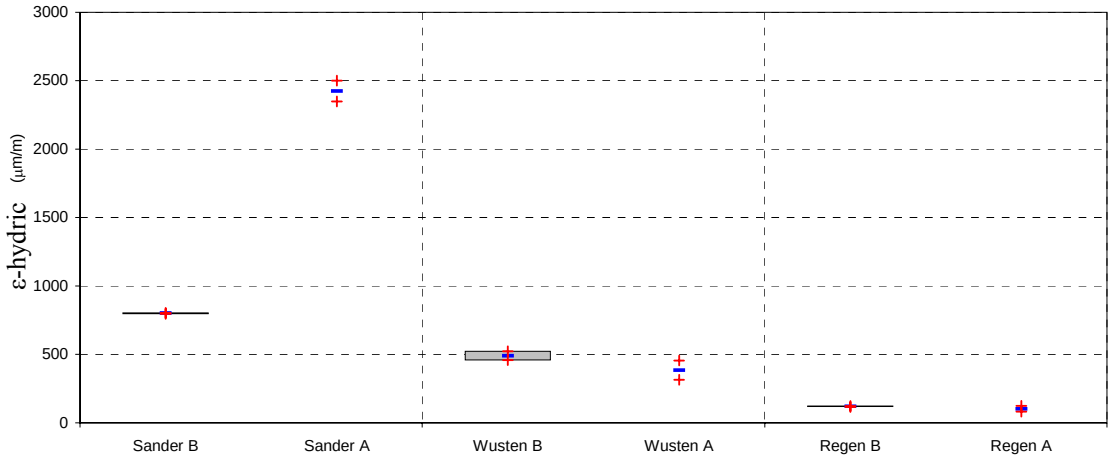

Figure 121. Comparison of the hydric dilatation of the sandstones before (B) and after (A) F-T cycles. Raw results in Annex 2 Table 13.

X.5. Resume of changes in hydric properties

Several changes have been pointed out. First of all, it is clear that artificial weathering by freeze-thaw cycles involves changes in all hydric properties, but at a different degree. A decrease of the water uptake coefficient was observed for all lithotypes, while an increase of the water flow rate by capillarity during drying as well as the water vapor conductivity occurred. These properties were all measured on the entire sample and should reveal the behavior of the whole structure. All these changes in hydric properties may have been linked to changes in the pore structure and especially the increase of larger pores 1-5 µm and over 10 µm as well as an increase of the surface roughness. Such changes in the pore access and accentuation of the heterogeneity of the porous network may lead to a decrease of the capillarity transport (Thomachot, 2002). Drying is enhanced as large pores present a more important interior surface open to evaporation and the surface roughness is largely increased.
Measurement of the drying rate seems to reveal clearly the state of weathering, as it shows real difference between highly deteriorated stones (open cracks) as Regensburg or Cadeby, less or no deteriorated stones (no visual decay) as Wüstenzeller or Highmoor.

XI. Changes in mechanical properties

XI.1. Biaxial flexural strength and static modulus of elasticity

Lithotypes presenting the most important visual decay (macro cracks) show also a decrease of the biaxial flexural strength (Figure 122). Artificial weathering may have broken intergranular bonds and increased weakness of the structure. Micro cracks may be present in the sample slices (macro cracks could not be seen in the sample slices) and may involve fast crack propagation inside the structure leading to the collapse of the material. Thus, Sander and Regensburg sandstones as well as Cadeby and Hazel Lane magnesium limestone show a decrease of the BFS. Such decrease of strength must be according to strength theory also related with a decrease of static modulus of elasticity (Figure 123). Deformation curves illustrate the decrease or increase of the biaxial flexural strength and static modulus of elasticity (Figure 124 and Figure 125).

On the other hand, Wüstenzeller sandstone and Highmoor limestone present an increase of the biaxial flexural strength, but the increase of static modulus of elasticity is not significant (Figure 122 and Figure 123). Concerning Wüstenzeller, it might be assumed that a clay aggregates compaction or dissolution occurred (see pore size distribution and ultrasonic velocity), quartz-quartz contacts might be brittle and thus increased the elasticity and strength of the material.

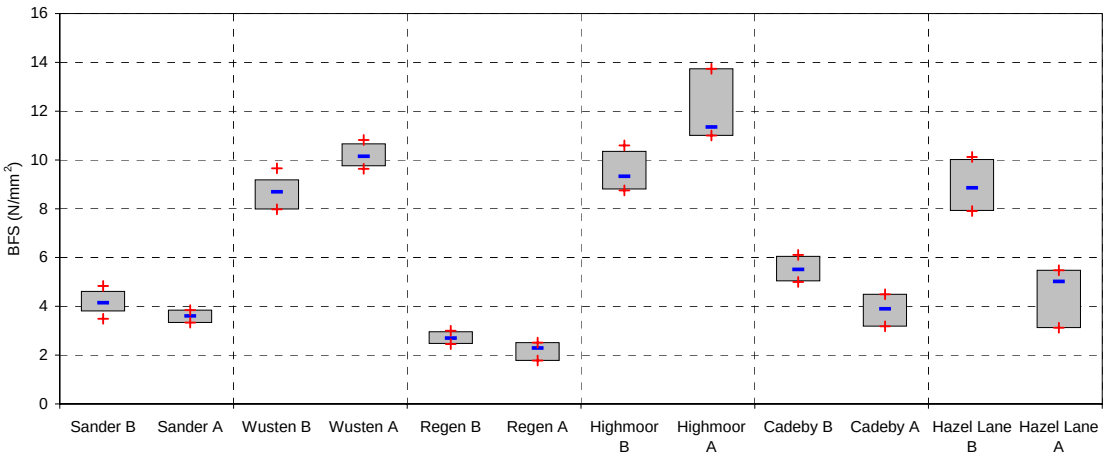

Figure 122. Comparison of the biaxial flexural strength before (B) and after (A) F-T cycles. Raw results in Annex 2 Table 13 and Table 18.

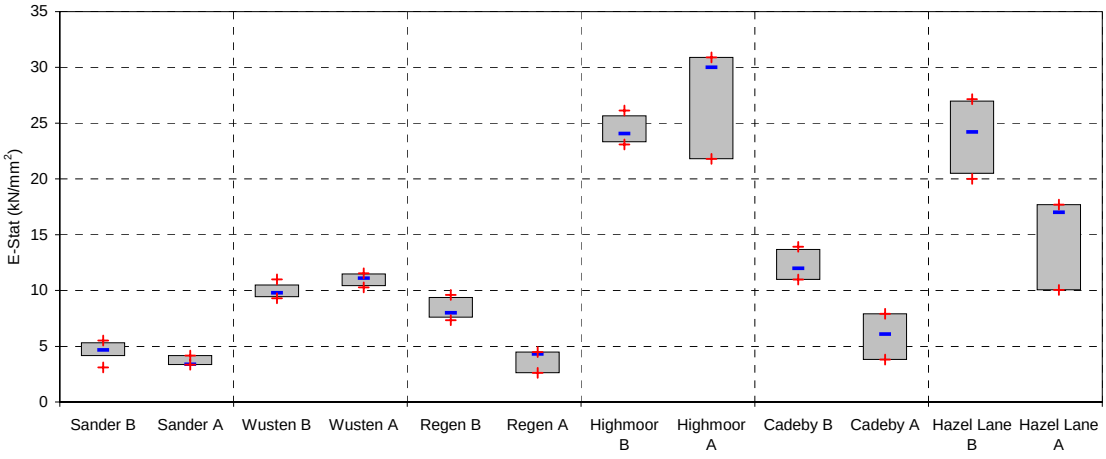

Figure 123. Comparison of the static modulus of elasticity before (B) and after (A) F-T cycles. Raw results in Annex 2 Table 13 and Table 18.

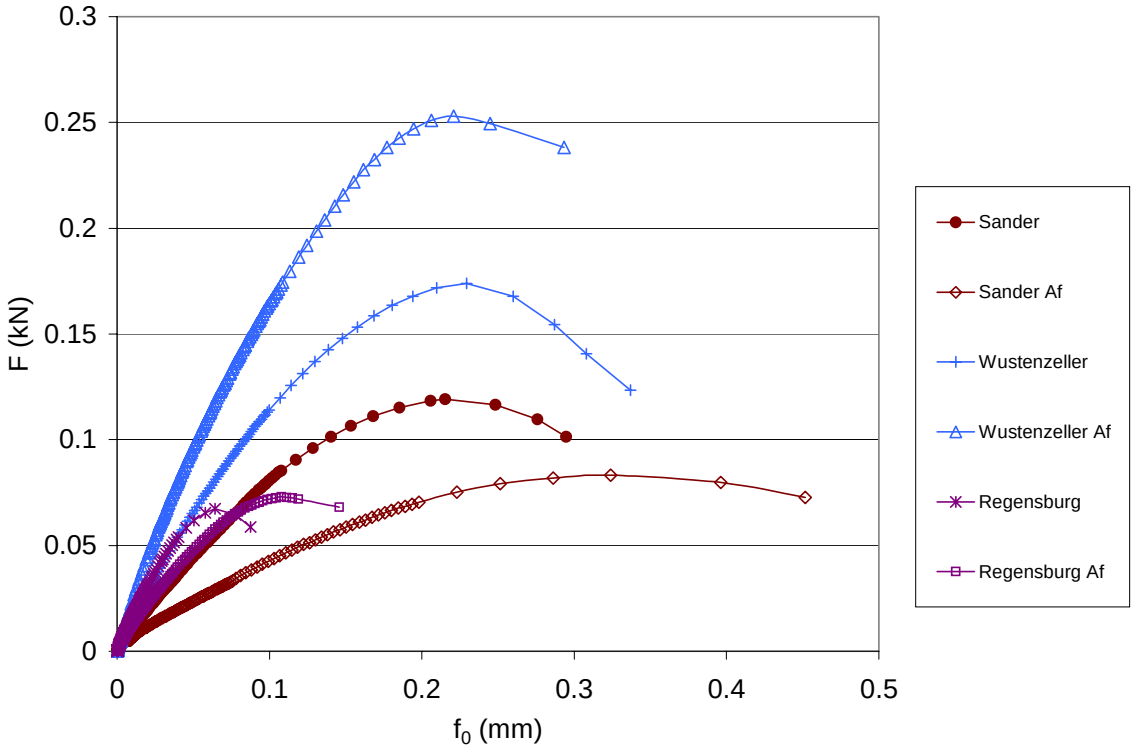

Figure 124. Deformation curves before and after F-T cycles of the sandstones.

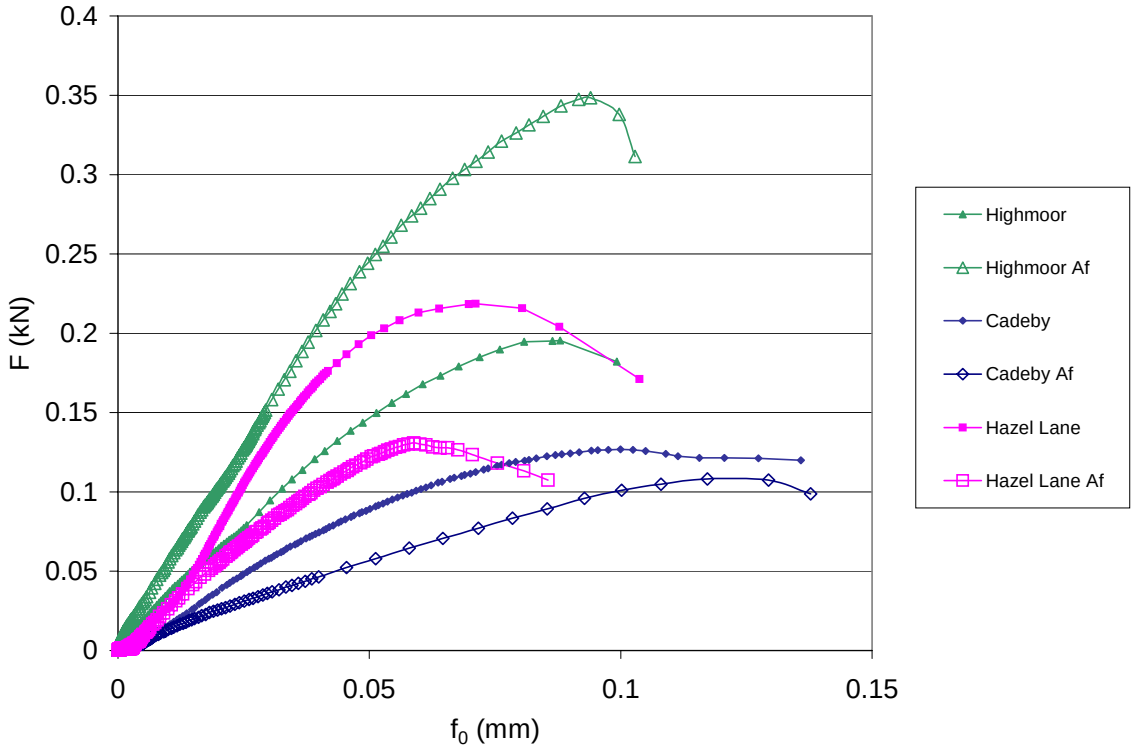

Figure 125. Deformation curves before and after F-T cycles of the magnesian limestone.

XI.2. Drilling resistance

As it was mentioned previously, the decay after artificial weathering is heterogeneous. A measurement of drilling resistance takes place on a surface of 19.5 mm^2 or 0.19 cm^2 (5 mm diameter). Therefore, a decrease of DRc is not really obvious for the different lithotypes (Figure 126). A slight diminution can be noticed but furthermore, the results are more spread after weathering than before. It reflects the heterogeneity of the results.

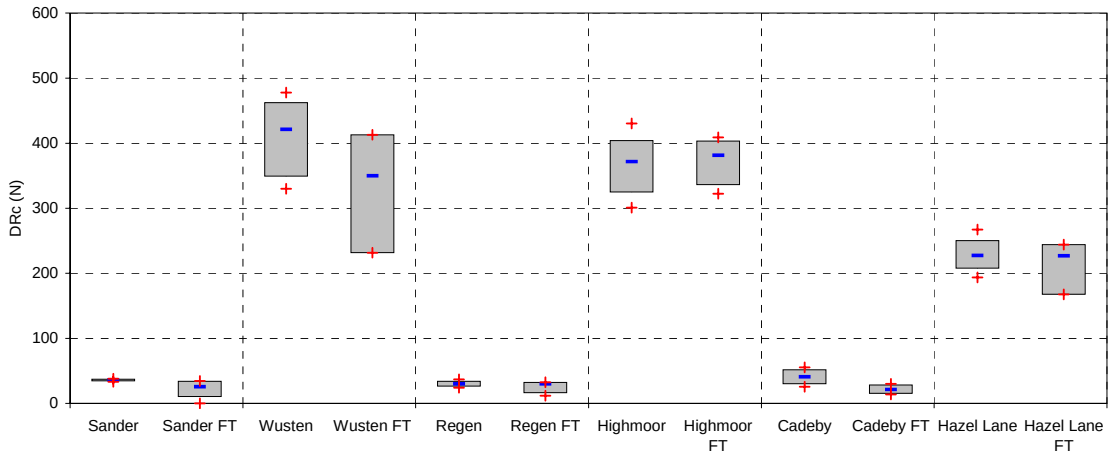

Figure 126. Comparison of the corrected drilling resistance before (B) and after (A) F-T cycles. Raw results in Annex 2 Table 13 and Table 18.

XI.3. Resume of changes in mechanical properties

Most important changes seem to be in the biaxial flexural strength and static modulus of elasticity. Both measurements proved a decrease of strength and elasticity for the most deteriorated stones. Elasticity properties seem to be even more affected than strength after artificial weathering.

The visually observed deterioration seems to be related with a loss of cohesion between grain boundaries and presence of micro cracks percolating in the structure and leading to the complete collapse of the material. It seems clear that decay of the macrostructure is linked to a loss of strength and elasticity of the material.

XII. Synthesis of material properties after freeze-thaw cycles

The previous chapter considered all direct relations between properties in order to understand their dependency and how physical and mechanical properties could be related to textural properties or non-destructive methods. After artificial weathering it was important to establish which properties are changed and reliable to effective decay observed on the lithotypes.
Methods of measurements are essential; measurements on lithotypes presenting a heterogeneous decay should be more considered as the whole samples than a part of it (pieces for the MIP measurements or DIA), which might not representative. It appears during this chapter that BET, MIP and DIA, porosity measurements in general, might not be accurate on partially weathered stone. Indeed, porosity measurements could have been more accurate on completely decayed stones, probably until breaking of the sample or even disintegration. In this case, most of the physical, mechanical and non-destructive methods could not have been carried out on the specimen. Therefore, it was a choice to reach a state of weathering where main macroscopic measurements could be carried out and detect what of these physical, mechanical properties and non-destructive methods are significantly changed during weathering process and could lead to macro decohesion of the structure. However, MIP measurements seem to still be helpful when the entire intrusion diagram is considered and compared to the fresh material. Changes in pore structure could have been underlined and reveal an increase of the largest 1-5 μm and over 10 μm.
Thus a coefficient of change for each "macro" property is determined. This coefficient is simply the ratio, for one property, between results obtained on the fresh specimen with results obtained on the same specimen after artificial weathering. In the case of this coefficient is equal to 1 that means that no changes appeared between before and after freeze-thaw cycles. A coefficient < 1 indicates a decrease of the value after weathering, a coefficient > 1 indicates an increase of the value. The Table 7 presents for each lithotype the coefficient of change for the properties on a "macro"scale and revealing weathering. It allows a direct reading of changes that occurred after artificial weathering. Therefore, it shows a decrease of the QI% and ultrasonic velocity for all specimens except for Wüstenzeller, a decrease of dynamic and static moduli of elasticity and biaxial flexural strength for all specimen except for Wüstenzeller and Highmoor, increase of water flow rate and water vapor conductivity to the surface for all stones except Wüstenzeller, and finally a decrease of the water vapor diffusion resistance coefficient for all stones except Wüstenzeller and Highmoor. These coefficients express changes occurred after artificial weathering.

	QI %	V_p parall (km/s)	V_p perpend (km/s)	E-Dyn (kN/mm2)	BFS (N/mm2)	E-Stat (kN/mm2)	DRc (N)	g (g/m2/h)	β	μ
Sander	0.8	0.8	0.9	0.5	0.9	0.9	0.8	1.1	1.1	0.9
Wustenzeller	1.1	1.1	1.1	1.2	1.2	1.1	0.8	1.1	0.7	1.0
Regensburg	0.7	0.7	0.9	0.7	0.8	0.5	0.9	2.2	2.0	0.9
Highmoor	0.9	0.9	1.0	1.0	1.3	1.1	1.0	1.0	1.6	1.0
Cadeby	0.8	0.8	0.8	0.6	0.7	0.5	0.6	2.3	1.3	0.7
Hazel Lane	0.8	0.8	0.9	0.9	0.5	0.6	1.0	2.7	1.7	0.5

Table 7. Coefficient expressing changes of the properties after F-T cycles. Most important changes are observed for properties linked to ultrasonic velocity and ultrasonic velocity itself, mechanical properties and water transport properties linked to evaporation and water vapor conductivity and permeability. They are the properties reflecting the decay of the material.

These changes related to "macro" scale properties can still be related to "micro" scale properties as pore entrance distribution before weathering and textural properties, established on the fresh lithotypes. A link should be made between variables and a correlation determined before artificial weathering and changes occurred after weathering. This is the main purpose of the study in order to assess weathering in the natural environment and will be further discussed in the conclusion.

The coefficient of variation expressing changes of properties after freeze-thaw cycles highlight the stones presenting an important decay as well as the stones apparently durable and resistant to weathering. Indeed, Wüstenzeller sandstone and Highmoor magnesian limestone are the most durable stones of the study. If we have a closer look at the pore entrance distribution as a function of the degree of alteration of each stone, some general observations can be established. In the Table 8 the type of distribution is associated with the different stones and as well the pore entrance distribution (PSD). This PSD is normalized to a porosity at 100 % in order to emphasize the role of the different pore ranges on the diverse stones. Previously, in the equation of correlation, the pore ranges was expressed in % vol of the porosity measured for every stone.
Durable stones seem to present a unimodal PSD from the MIP curves (IV.3). Moreover, Wüstenzeller sandstone reveals 97% of its PSD > 5 μm and 2.5% in the range 0.1-5 μm, while Sander and Regensburg sandstones show between 20 to 25 % of their PSD on the range 0.1-5 μm. Concerning Highmoor magnesian limestone more than 60% of its PSD is > 5 μm, while Cadeby and Hazel Lane magnesian limestone illustrate 70% of their PSD in the range 0.1-5 μm. The amount of pores < 0.1 μm is similar for the three limestone. Thus, the pore range 0.1-5 μm seems to be an essential factor in the state of weathering. This range of capillarity pores is also the most affected after weathering. It seems that this range associates pores where liquid water remains during the freezing process, and feed the larger pores where ice crystals can grow with liquid water.

Such changes in the microstructure involve the presence of microcracks, which propagate to produce macrocracks and the fracture and decay of the material. Thus, the biaxial flexural strength after freeze-thaw cycles (BFS $_{F-T}$) as well as the static modulus (E-Stat $_{F-T}$) are correlated with the pore vol. 0.1-5 μm on the fresh lithotypes (equations 124 and 125).
For the magnesian limestone the relation is clear:

BFS $_{F-T}$ = 16.26 – 0.59 MIP 0.1-5 μm ± 1.7 R^2 = 0.85 (124)

E-Stat $_{F-T}$ = 40.28 – 1.49 MIP 0.1-5 μm ± 5.7 R^2 = 0.75 (125)

For the sandstones, a better equation can be obtained when associating the pore range < 0.1 μm to the pore range 0.1-5 μm (equations 126 to 129); the influence of clay mineral might be important:

BFS $_{F-T}$ = 9.85 – 1.29 MIP 0.1-5 μm ± 0.7 R^2 = 0.73 (126)

BFS $_{F-T}$ = 10.86 + 5.25 MIP < 0.1 μm – 2.5 MIP 0.1-5 μm ± 0.7 R^2 = 0.97 (127)

E-Stat $_{F-T}$ = 10.85 – 1.38 MIP 0.1-5 μm ± 1.6 R^2 = 0.84 (128)

E-Stat $_{F-T}$ = 11.62 + 3.49 MIP < 0.1 μm – 2.3 MIP 0.1-5 μm ± 0.98 R^2 = 0.95 (129)

MgL = magnesian limestone; SS = Sandstone

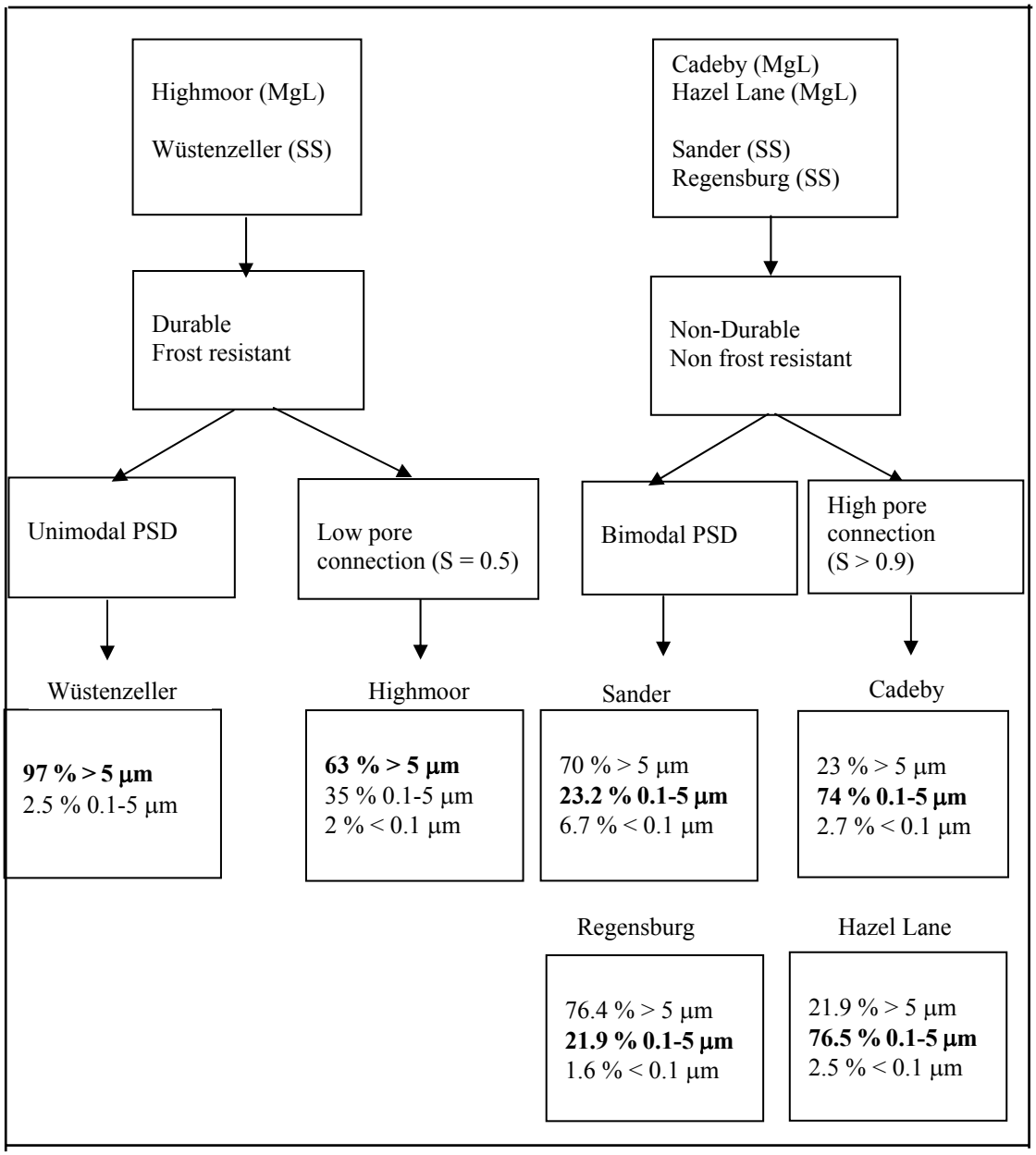

Table 8. Relation between the decay observed at a macro scale and the initial microstructure of the different stones. Bold indicates the pore range influencing the most durability of the stone. For assessing weathering degree the value before weathering must be considered.

D. CONCLUSION OF THE STUDY

XIII. Conclusion

The aim of this study is to provide a selection of tools to assess durability and susceptibility to weathering of natural stone, with an emphasis on sandstones and magnesian limestone.
Therefore, it was essential to draw models of correlation to underline the interdependency of various properties. From the analysis of the structure of the materials, their porosity, and their physical and mechanical properties, models were established for each lithotype. These models underline the main linear correlation linking direct observation of the structure and non-destructive methods to micro- and macro-structure. The effectiveness of non-destructive measurements and direct observation through optical microscopy in assessing the behavior of materials was highlighted. Thus, the study focused first on assessing the durability of new stone and then on evaluating the degree of deterioration of weathered stones.

Different points are highlighted in Chapter III to assess the durability of new stone. First, factor and correlation analyses are an excellent tool for the formulation of models and emphasize the relationship between different properties (water transport and mechanical) and material characteristics. Thus, models designed for the fresh magnesian limestone and the sandstone accentuate the properties needed for the stone to be more durable.
Indeed, for magnesian limestone, the shape of the pores seems to control the strength of the material. The pore shape can be determined from the calculation of the pore shape factor Psf through ultrasonic velocity measurement (equation 41) or evaluated through the quality index QI (equation 22 or equation 49 from the ultrasound parallel to stone bedding). Spherical pores (Hazel Lane and Highmoor) decrease the free porosity, are less deformable, limit the propagation of cracks and thus increase the strength and elasticity properties. But the determination of the pore shape alone is not enough to assess the durability of the limestone. Indeed, Highmoor is the only stone to be resistant to weathering and then the most durable. Highmoor presents a Hirschwald coefficient S very low (= 0.5) and reflects its poor pore connectivity. Moreover, it has more than 50 % of its pore entrance in the pore class > 5 μm (Annex 2 table 14). Highmoor is described as a dolo-microsparite magnesian limestone with fine dolomite crystals in micritic cement. It might be assumed that a real calcitic grain contact exists and the cement does not increase the microporosity. On the other hand, Cadeby and Hazel Lane both decayed after freeze-thaw cycles, were qualified as dolo-oomicrite magnesian limestone, and show a saturation coefficient S over 0.9 and present more than 70 % of their pore entrances in the pore class 0.1-5 μm. The importance of this pore class in the durability is proved by equation 124. The quantity of pores in the class < 0.1 μm is similar for the three stones. Thus, a high concentration of pore class 0.1-5 μm, defined by mercury porosimetry, describes the number of tube-like throats that increase water uptake and represents the main contributory factor to weathering. Therefore, for magnesian limestone, it is the association of spherical pores, low saturation coefficient and a pore class 0.1-5 μm concentration below 50 % of the total porosity volume that can assess durability (table 8).

Concerning sandstone, a determination of grain size distribution in thin section is apparently the principal step required. Fine sand (80-400 μm) should be present in an equivalent amount to medium sand (400-2000 μm), so that grains can be interlocked. If these conditions are satisfied, it may mean that grain contact is optimized, porosity and water transport is minimal and that the strength is enhanced. The presence of grain class 2-80 μm (silt or clay) decreases

the static modulus of elasticity, while determining the quantity of medium sand or ultrasonic velocity can assess the dynamic modulus of elasticity. Thus, grain size distribution controls strength and elasticity properties of sandstones. Moreover, it appears that Wüstenzeller, which is frost-resistant, presents a unimodal pore entrance distribution centered on the pore class > 5 μm (97 % of its pore entrances are > 5 μm; 3 % in the range 0.1-5 μm). Sander and Regensburg sandstones, which are largely decayed after freeze-thaw cycles, still have 70 % of their pore entrances measuring > 5 μm, but 20 to 25 % are in the range 0.1-5 μm. The susceptibility of the stone to weathering seems to be heightened due to the presence of the pores measuring 0.1-5 μm. Well sorted grain size distribution, particularly the inclusion of fine sand measuring 80-400 μm, improves grain contacts, and is directly correlated with the pore class 0.1-5 μm. For sandstones, it is clear that grain size distribution determines the pore structure and thus the durability of the material.

For both lithotypes, the concentration of pores within the range class 0.1-5 μm is the main parameter by which to assess durability. This range includes smaller pore entrances, which may feed with liquid water larger pores and larger pore entrances that may have grown in size during weathering. Finally, the correlation between static and dynamic modulus of elasticity was discussed and the relation proposed by Christaras et al (1994) was improved upon, as new results were closer to the zero and therefore more representative of the theory.

Once initial durability of new stone can be assessed, it is essential to identify the main parameters altered by weathering that may lead to deterioration and also help assess the degree of weathering after exposure. Therefore, the aim of Chapter IV is to identify, on a macro scale, the properties most affected by weathering and resulting in decohesion, from minimal loss of material to complete failure.

It has been highlighted that changes in structure and, particularly, changes in grain contact, are not visible through optical microscopy. Grain contact, which apparently controls pore structure and, thus, durability of sandstones, is not precise enough to detect and quantify weathering. It is essential to understand that grain contact is a principal parameter in determining the strength of the material but is not a key variable in evaluating weathering.

Thus, the main variables showing noticeable change after weathering are: ultrasonic velocity, dynamic modulus of elasticity and quality index, biaxial flexural strength and static modulus of elasticity, liquid water flow rate during drying, and water vapor diffusion resistance coefficient.

Ultrasonic velocity decreases with loss of strength, but no quantifiable correlation can be ascribed. The resulting decrease does highlight the sensibility of ultrasound to cracks developed during weathering, but cannot assess directly weathering of sandstone or magnesian limestone. Ultrasound can detect weathering only if a sample of unweathered stone can also be measured for comparison. It is the decrease of the ultrasound velocity that indicates a decrease of strength, but without previous control measurements, weathering cannot be measured. The alteration classification of marble (Galan, 1991; Köhler, 1991) was established from such comparisons of ultrasonic velocity measured on new and weathered material.

The literature has shown that these ultrasound readings, however, have no direct correlation with sandstones (Queisser, 1985). Nonetheless, weathering of sandstone can be assessed through comparison of these specific characteristics before and after exposure.

On the other hand, evolution of the mercury intrusion curves after weathering showed clearly that the pore class 0.1-5µm is the most changed after weathering. Most of the time, a peak between 1-5 µm appears on weathered stones. If the material does not show visible decay (cracks, grain disintegration) the presence of such a peak might be the only tool to assess weathering.

As Bell (1988) suggested porosity measurement alone may not be sufficient to provide a guide to durability. However, it has been demonstrated in this study that it is the association of microstructure (pore size distribution) with structural characteristics of the material (grain size distribution and pore shape), which are the tools to assess durability.

XIV. Summary sheet

MAGNESIAN LIMESTONES

- Identification of the shape of the pores by non-destructive methods:

- Determination of Pore shape factor Psf (equation 41) or
- Evaluation through the quality index QI (equation 22 or equation 49 from the ultrasound parallel to stone bedding).

⇨Spherical pores = less deformable = prevent from cracks propagation and increase elasticity properties.

- Determination of pore class 0.1-5 μm (MIP) < 50 % of the total porosity volume,

- Determination of the saturation coefficient S < 0.7

SPHERICAL PORES + LOW PORE CLASS 0.1-5 μM + LOW PORE CONNECTION
=
DURABILITY.

SANDSTONES

- Determination of the grain size distribution in thin section

- Fine sand (80-400 μm) = medium sand (400-2000 μm): grains interlocked

⇨Grain contact optimized = strength reinforced.

- Unimodal pore entrance distribution

- Pore class 0.1-5 μm < 10 % of the total pore volume

GRAIN SIZE DISTRIBUTION + PORE STRUCTURE
=
DURABILITY

XV. Work in prospect

Two main subjects for a future work appear clearly. It seems essential to enlarge the scale of the different results by including other lithotypes in the study. The system of linear correlation reveals differences and common points between the lithotypes, but in order to emphasize general rule, more diversified microstructure (different pore entrance distribution) and macrostructure should be added in the matrix of correlation. The study of the relation between static and dynamic modulus of elasticity associated the results of the present study on the magnesian limestone and sandstones with the previous work of Christaras et al (1994) and increase the scale of the study.

The methodology developed in this study can be used as a systematic method in order to integrate in the matrix all diversified lithotypes and draw for each lithotypes models of correlation and underline the variable common to all lithotypes, as it was done in this study.

The objective of this work was to find tools to assess weathering in the natural environment. Now that some models were drawn, it seems essential to verify these models with naturally weathered limestone and sandstones.
First, it would be necessary to corroborate the models with new fresh materials by measuring the main important properties proposed by the models. Then to analyze the same material naturally weathered in order to see the evolution of the properties but also to see if the state of decay can be identified.

Finally, the methodology developed in this study can have other application to the field of conservation. The question of weathering can be probably replaced by the question of treatment: can the efficiency of a treatment be assessed by holistic correlation? Such a work would allow to understand the influence of the microstructure and macrostructure on the effectiveness of a conservation treatment.

XVI. Zusammenfassung

Das Ziel der Untersuchungen war, Methoden bereit zu stellen, die Dauerhaftigkeit und die Verwitterungsbeständigkeit von Natursteinen mit besonderem Bezug auf Sandsteine und Kalksteine zu bewerten. Es erwies sich deshalb als wesentlich, modellhafte Korrelationen aufzustellen, welche die gegenseitige Abhängigkeit der verschiedenen Gesteinseigenschaften aufzeigen. Ausgehend von der Analyse der Gesteinsstruktur, der Porosität sowie der physikalischen und mechanischen Eigenschaften wurden solche Korrelationen für jede der ausgesuchten Gesteinsarten aufgestellt. Sie zeigen die Verbindungen zwischen den verschiedenen nicht zerstörenden Untersuchungsmethoden und der Mikro- und Makrostruktur der Gesteine auf. Die Ergebnisse unterstreichen die Bedeutung der zerstörungsfreien Messmethoden und der unmittelbaren Analyse der Gesteinsstruktur im Mikroskop, um das Materialverhalten zu bewerten. Die Untersuchungen konzentrierten sich zuerst auf die Bewertung der Dauerhaftigkeit von unverwitterten Gesteinen und dann später auf die Beurteilung der Materialveränderungen bei künstlich im Labor verwitterten Gesteinsproben. Als Verwitterungstest wurde der Frost-Tau-Wechselversuch nach DIN 52104 ausgeführt.

In Kapitel I wird der Stand des Wissens und der Technik behandelt. Es werden die Methoden erläutert, welche sich anerkanntermaßen zur Bestimmung der Eigenschaftsänderungen in Verlauf der Verwitterung eignen. Ferner wird begründet, welche Bestimmungsmethoden ausgewählt wurden. Die wichtigsten Methoden sind die Ultraschallmessung und die Mikrobohrhärte als nicht oder wenig zerstörende Messmethoden. Unter den physikalischen Eigenschaften sind die Wasser- und Wasserdampftransporteigenschaften, die Feuchtedehnung und das Trocknungsverhalten hervorzuheben. Unter den mechanischen Kennwerten wurden die Druckfestigkeit und Biegefestigkeit sowie der statische und der dynamische E-Modul ausgewählt.

Kapitel II enthält die Beschreibung der ausgewählten Gesteine und der angewendeten Messmethoden. Die ausgewählten Sandsteine umfassen das Spektrum der verschiedenen Bindemittel:

Der Sander Schilfsandstein besteht aus 78% Aggregaten, 8 % tonigem Bindemittel und 14% mikroskopisch sichtbarem Porenraum. Die direkten Kornkontakte betragen 35%.

Der Wüstenzeller Sandstein besteht aus 80 % Aggregaten, 9 % silikatischem Bindemittel und 11 % mikroskopisch sichtbarer Poren. Bei den Kornkontakten herrschen Langkontakte vor. Die direkten Kornkontakte betragen 80%.

Der Regensburger Grünsandstein ist ein Kalksandstein mit 42% Aggregaten, 47% calcitischem Bindemittel und 11% mikroskopisch sichtbarer Poren. Konkav-konvex und Langkontakte herrschen vor. Die direkten Kornkontakte betragen 45%.
Bei den ausgewählten Kalksteinen handelt es sich um permische Dolomit-Calcit-Kalksteine (Dolostones) aus der Gegend zwischen Nottingham und York in England.

Der Highmoor Kalkstein ist ein Dolo-Mikrosparit von weißer Farbe mit feinen Dolomitkristallen in mikritischer Matrix. Die Struktur zeigt wenige Kugelporen und ist sehr homogen. Die mittlere Korngröße und die Art der Kornkontakte sind wegen der geringen Korngröße nicht zu bestimmen.

Beim Cadeby Kalkstein handelt es sich um einen cremefarbenen Dolo-Oomikrit. Die Oolithe haben eine gelängte Form von rund 150 µm Durchmesser und berühren sich gegenseitig. Sie sind mit einem dünnen feinkristallinen Calcitzement umgeben.

Auch der Hazel Lane Kalkstein ist als Dolo-Oomikrit bezeichnet. Seine Farbe und Struktur ähneln dem Cadeby Kalkstein. Die Oolithe sind insgesamt runder, haben jedoch die gleiche Größe von 150 µm. Im Gegensatz zum Cadeby Kalkstein berühren sie sich nicht, sondern schwimmen in einer calcitischen Matrix.

Als Beispiel für ein besonders dichtes, aber trotzdem verwitterungsanfälliges Material wurde der Prokonnesische Marmor aus der Türkei ausgewählt. Der grobkörnige Marmor besitzt eine durchschnittliche Korngröße von 800 µm. Die Kornkontakte betragen 95 % und lassen lediglich eine geringe Rissporosität (Spaltporen) zu. Marmor eignet sich besonders für die Bestimmung des Verwitterungsgrades durch die Ultraschallgeschwindigkeit.

Im weiteren Verlauf von Kapitel II werden die Untersuchungsmethoden formelmäßig abgeleitet und erläutert: Rohdichte und Reindichte, wasserzugängliche Porosität, Quecksilber-Druckporosimetrie (MIP), Stickstoff BET, digitale Bildanalyse (DIA), Porenradienverteilung aus DIA, MIP und BET, Ultraschallgeschwindigkeit, Wasseraufnahmekoeffizient, Trocknungskinetik, Würfel-Druckfestigkeit, statischer und dynamischer E-Modul, Bohrwiderstand. Der Qualitätsindex QI basiert auf dem Vergleich zwischen tatsächlich gemessener und theoretisch aus der Zusammensetzung berechneten Ultraschall-geschwindigkeit. Er gibt Auskunft darüber, ob in der Struktur vorwiegend Rissporosität oder Hohlraum(Poren)-Porosität vorliegt. Eine weitere nützliche Variable stellt der Porenformfaktor PSF dar. Er beschreibt das Verhältnis der Ultraschallgeschwindigkeit im wassergesättigten zu der im trockenen Zustand.

Die Faktoranalyse wurde zur Berechnung der Korrelationen zwischen den variablen Eigenschaftsparametern gewählt. Die Variablen gehören fünf Kategorien an:

- Struktureigenschaften mit digitaler Bildanalyse und Qualitätsindex
- Zerstörungsfreie Messmethoden wie Ultraschallgeschwindigkeit, Bohrhärte und dynamischer E-Modul
- Porenraumeigenschaften mit Porenradienverteilung gemäß BET, MIP und DIA.
- Physikalische Eigenschaften mit allen Wassertransporteigenschaften
- Mechanische Eigenschaften mit hauptsächlich Biegezugfestigkeit und statischem E-Modul.

In den Kapiteln III - VII wird über die Ergebnisse zur Beurteilung der Dauerhaftigkeit von frischem Gestein berichtet. Faktoranalyse und lineare Regression haben sich sehr bewährt, die Beziehung zwischen den verschiedenen Materialeigenschaften herauszuarbeiten. Die Modelle, welche für frische Kalksteine und Sandsteine entwickelt wurden, liefern die

Voraussetzungen für die Beurteilung der Verwitterungsbeständigkeit von jeder der ausgewählten Gesteinsarten.

Bei Kalksteinen kontrolliert die Porengestalt die Festigkeit des Materials. Die Porengestalt kann aus der Berechnung des Porenformfaktors PSF mit Hilfe der Ultraschallgeschwindigkeit (41) oder durch den Qualitätsindex QI abgeleitet werden (22 oder 49). Kugelporen wie bei Hazel Lane and Highmoor Kalkstein erniedrigen die freie Porosität; sie sind weniger verformbar und begrenzen die Ausbreitung von Mikrorissen. Auf diese Weise erhöhen sie die Festigkeits- und Elastizitätseigenschaften. Aber die alleinige Bestimmung der Porenform ist nicht hinreichend, die Dauerhaftigkeit von Kalksteinen zu beurteilen. In der Tat ist der Highmoor-Kalkstein der einzige Kalkstein, der verwitterungsbeständig ist. Highmoor besitzt mehr als 50% seiner Poreneingangsradien in der Porenraumklasse > 5 µm. Petrologisch wird Highmoor als ein Dolo-Mikrosparit mit feinen Dolomitkristallen in mikritischem Zement beschreiben. Es kann angenommen werden, dass tatsächliche carbonatische Kornkontakte bestehen und dass der Zement den Anteil der Mikroporosität nicht erhöht.

Auf der anderen Seite werden Cadeby und Hazel Lane Kalkstein durch die Frost-Tauwechsel-Zyklen stark geschädigt. Sie besitzen mehr als 70% der Poreneingangsradien in der Porenklasse 0,1-5 µm und werden als Dolo-Oomikrite eingestuft. Die Porenklasse < 0,1 µm ist für alle drei Kalksteine vergleichbar. Deshalb kann die Porenradienklasse 0,1-5 µm, die mit Hilfe der Quecksilberporosimetrie bestimmt wurde, als kennzeichnend für die erhöhte Wasseraufnahme und die Verwitterungsbeständigkeit angesehen werden. Aus diesem Grunde besitzt im Falle der Kalksteine die Verbindung von Kugelporen und der Porenklasse 0,1-5 µm den verwitterungsbestimmenden Einfluss, sofern diese Poren weniger als 50% der Gesamtporosität ausmachen.

Bei den Sandsteinen ist die Bestimmung der Korngrößenverteilung an Dünnschliffen offensichtlich der wichtigste Schritt. Die Feinsandfraktion (80 – 400 µm) sollte in gleichen Mengen wie die Mittelsandfraktion (400 – 2000 µm) vorhanden sein. Wenn diese Bedingung erfüllt ist, sind die Kornkontakte optimal ausgebildet. Die Porosität und die Wassertransporteigenschaften haben ein Minimum und die Festigkeit ist erhöht. Das Vorhandensein der Korngrößenklasse 20 – 80 µm (Silt oder Ton) erniedrigt den statischen E-Modul. Auf der anderen Seite kann bei Sandsteinen der dynamische E-Modul von der Menge der Mittelsandfraktion und natürlich aus der Ultraschallgeschwindigkeit abgeleitet werden. Auf diese Weise bestimmt die Korngrößenverteilung die Festigkeit und die Elastizitätseigenschaften der Sandsteine.

Darüber hinaus lässt sich zeigen, dass der frostbeständige Wüstenzeller Sandstein eine monomodale Poreneingangsradienverteilung besitzt, welche ihr Maximum in der Porengrößenklasse >5 µm besitzt. 97% der Poreneingangsradien sind > 5 µm, nur 3 % in der Porenradienklasse 0,1 – 5 µm.

Der Sander und der Regensburger Sandstein, die durch die Frost-Tau-Zyklen weitgehend zerstört werden, besitzen immer noch 70% ihrer Poreneingangsradien in der Klasse > 5 µm, aber der Anteil der Porenradienklasse 0,1 - 5 µm beträgt 20 – 25 %. Die Anfälligkeit für Verwitterungsvorgänge scheint deshalb durch die Gegenwart der Porenklasse 0,1 - 5 µm

verstärkt zu werden. Bezüglich der Korngrößenverteilung lässt sich sagen, dass die Feinsandfraktion µm 80 - 400 µm die Kornkontakte verbessert. Sie ist direkt korreliert mit der Porenklasse 0,1 – 5 µm. Im Falle der Sandsteine erweist es sich als evident, dass die Korngrößenverteilung die Porenstruktur und damit die Verwitterungsbeständigkeit bestimmt.

Für Kalksteine und für Sandsteine gilt gleichermaßen, dass die Porenklasse 0,1 - 5 µm den hauptsächlichen Parameter darstellt, die Verwitterungsbeständigkeit zu beurteilen. Diese Porenklasse beinhaltet auch die kleineren Kapillarporen, welche die größeren Poren im Falle der Frost- und Salzverwitterung mit einem Nachschub an Wasser bzw. Salzlösung versorgen können.

Für alle Gesteine wurde die Korrelation zwischen statischem und dynamischem E-Modul untersucht. Die von Christaras et al (1994) vorgeschlagene Korrelation konnte nicht nur im Hinblick auf einen besseren Korrelationskoeffizienten wesentlich verbessert werden. Die neue Korrelationsgerade führt auch durch den Nullpunkt, was von der Theorie vorausgesetzt wird.

Kapitel VIII – XII: Nach der Bestimmung der Dauerhaftigkeitseigenschaften von frischen Gesteinen wurden die wichtigsten Parameter bestimmt, die sich durch die Verwitterung verändern und welche auf diese Weise die Verwitterung beeinflussen und zur Beurteilung des Verwitterungsverhaltens herangezogen werden können.

Aus diesem Grunde war es zunächst die Aufgabe, diejenigen Makroeigenschaften herauszufinden, welche durch die Verwitterung am meisten angegriffen werden und deshalb zu einer Entfestigung führen. Die Untersuchungen bestätigten, dass sich Veränderungen in der Struktur und vor allem Veränderungen bei den Kornkontakten mit Hilfe des Mikroskops nicht beobachten ließen. Die Kornkontakte, die offensichtlich die Porenstruktur und deshalb auch die Dauerhaftigkeit der Sandsteine beeinflussen, sind offenbar nicht genau genug zu bestimmen, um die eingetretenen Verwitterungsvorgänge nachzuweisen. Es ist deshalb wichtig zu wissen, dass die Kornkontakte die wichtigsten Parameter für die Festigkeit sind, dass sie aber andererseits keine Variable darstellen, die Verwitterungsvorgänge zu bewerten.

Die hauptsächlichen Eigenschaften, welche bemerkenswerte Veränderungen nach den Verwitterungstests aufweisen, sind die Ultraschallgeschwindigkeit, der dynamische E-Modul und der Qualitätsindex QI, daneben die biaxiale Biegezugfestigkeit und der statische E-Modul. Ebenso können auch die Trocknungsrate im ersten Trocknungsabschnitt und die Wasserdampfdiffusionswiderstandszahl herangezogen werden.

Die Ultraschallgeschwindigkeit nimmt zwar ebenso wie die Festigkeit ab; eine wirkliche Korrelation zwischen beiden Eigenschaften kann aber nicht hergestellt werden. Dies unterstreicht die besondere Empfindlichkeit der Ultraschallgeschwindigkeit gegenüber Rissen, wie sie durch Verwitterung entstehen. Sie ist aber nicht in der Lage, das Verwitterungsverhalten von Sandsteinen und von Kalksteinen absolut und in der gleichen Weise wie bei Marmor zu beschreiben. Durch die Messungen kann lediglich die Abnahme der Ultraschallgeschwindigkeit festgestellt werden, mit deren Hilfe man einen Verlust an Festigkeit erkennen kann. Wenn aber keine vorausgegangenen Messungen an unverwitterten Proben existieren, kann der Grad der Verwitterung nicht beurteilt werden. Vergleiche mit der

Literatur zeigen ebenfalls, dass die Ultraschallgeschwindigkeit keine direkte Korrelation bei den Sandsteinen mit der Verwitterung zulässt (Queisser, 1985).

Auf der anderen Seite zeigen die Kurven der Quecksilberporosimetrie nach den Verwitterungstests eindeutig, dass die Porenradienklasse 0,1 - 5 µm bei allen Gesteinen am meisten verändert wurde. In den meisten Fällen erscheint bei den verwitterten Gesteinen ein neues Maximum im Bereich von 1 – 5 µm. Sofern keine makroskopisch sichtbaren Verwitterungsphänomene wie Risse oder Absanden zu beobachten sind, scheint die Gegenwart eines derartigen neuen Maximums die einzige Möglichkeit zu sein, den Verwitterungsgrad zu erkennen.

Wie Bell (1988) vorgeschlagen hat, ist die bloße Messung der Porositätseigenschaften nicht ausreichend, einen Maßstab für die Verwitterung zu liefern. In dieser Untersuchung wurde jedoch gezeigt, dass die Verbindung von Mikrostruktureigenschaften (Porenradienverteilung) mit Struktureigenschaften wie Korngrößenverteilung und Porenform geeignete Werkzeuge darstellen, das Verwitterungsverhalten und die Verwitterungsbeständigkeit zu beurteilen.

Ausblick

Die Untersuchungen über die gegenseitige Abhängigkeit von statischem und dynamischem Elastizitätsmodul an Kalksteinen und Sandsteinen haben die bisherigen Ergebnisse auf diesem Gebiet entscheidend erweitert.

Die Untersuchungsstrategie, die in dieser Untersuchung angewendet wurde, kann als eine systematische Methode benutzt werden, um die unterschiedlichsten Gesteinstypen in die Korrelationsmatrix zu integrieren und für jeden Gesteinstyp entsprechende Relationen aufzustellen, welche die Gemeinsamkeiten und Unterschiedlichkeiten zu den anderen Gesteinstypen herausstreichen.

Zwei hauptsächliche Untersuchungsrichtungen erscheinen für die Zukunft wichtig zu sein. Es erscheint wesentlich, den Umfang der Ergebnisse durch Untersuchungen mit anderen Gesteinstypen zu vergrößern. Mit Hilfe linearer Korrelationen konnten Unterschiede und Gemeinsamkeiten zwischen den Gesteinstypen aufgedeckt werden, aber im Sinne einer generellen Regel sind weitergehende Informationen über die Mikrostruktur (z. B. eine feinere Einteilung der Porenradienklassen) und über die Makrostruktur in die Korrelationsmatrix einzubeziehen.

Das Ziel der Untersuchungen war, Methoden zu finden, das Verwitterungsverhalten in der natürlichen Umgebung zu beurteilen. Nachdem nun die Ergebnisse dieser Arbeit vorliegen, erscheint es wesentlich, diese Modelle anhand von natürlich verwitterten Kalksteinen und Sandsteinen zu überprüfen. Zu allererst wäre es nötig, die Modelle mit neuen, unverwitterten Materialien zu untermauern, indem die wichtigsten Eigenschaften bestimmt werden, die in dieser Untersuchung vorgeschlagen wurden. Sodann wäre es erforderlich, das gleiche Material, jedoch unter natürlichen Bedingungen verwittert, zu analysieren, um die Veränderung der Eigenschaften festzustellen, aber auch um nachzuweisen, ob der Verwitterungsgrad mit Hilfe dieser Parameter überhaupt bestimmt werden kann.

Darüber hinaus kann die Methodik, die in dieser Arbeit entwickelt wurde, auch weitere Anwendung im Bereich der Konservierung finden. Die Frage nach der Verwitterung kann wahrscheinlich ersetzt werden durch die Frage nach der Dauerhaftigkeit der Behandlungen. Es wäre der Frage nachzugehen, ob die Wirksamkeit einer Behandlung mit Hilfe der hier angewendeten holistischen Korrelationen beurteilt werden kann.

Die Ergebnisse, wie sich die Verwitterungsbeständigkeit eines Gesteins beurteilen lässt, können, für Kalksteine und Sandsteine getrennt, folgendermaßen zusammengefasst werden:

Kalksteine:

- Schritt 1:
  Bestimmung der Porenform durch zerstörungsfreie Methoden
  Bestimmung Porengestaltfaktor PSF nach Gleichung 41 oder
  Bestimmung des Qualitätsindex QI nach Gleichung 22 oder 49
  Bedingung: Kugelporen sind weniger verformbar und erhöhen Festigkeit und Elastizitätseigenschaften
- Schritt 2:
  Bestimmung der Porenradienklasse 0,1 – 5 µm mit MIP (Quecksilberdruckporosimetrie)
  Bedingung: Anteil dieser Porenradienklasse < 50 % an Gesamtporosität
- Folgerung:
  Vorherrschen Kugelporen + geringer Anteil Porenradienklasse 0,1 – 5 µm → bessere Verwitterungsbeständigkeit

Sandsteine:

- Schritt 1:
  Bestimmung der Korngrößenverteilung im Dünnschliff
  Bestimmung Feinsand (80 – 400 µm)
  Bestimmung Mittelsand (400-2000 µm)
  Bedingung: Wenn Feinsand = Mittelsand, dann bestmögliche Kornkontakte. Festigkeit erhöht.
- Schritt 2:
  Bestimmung Porenradienverteilung
  Bedingung: Vorherrschen monomodale Porenverteilung
  Bedingung: Porenklasse 0,1 – 5 µm < 10 % Gesamtporosität
- Folgerung:
  Korngrößenverteilung + Porenradienverteilung → bessere Verwitterungsbeständigkeit

XVII. Annex 1: Pore size distribution

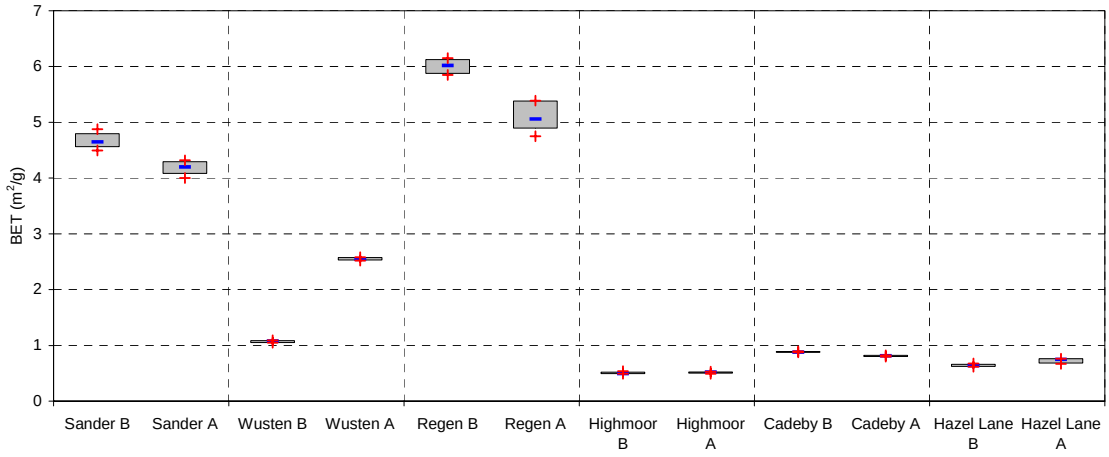

Figure 127. Comparison of the BET results before (B) and after (A) F-T cycles.

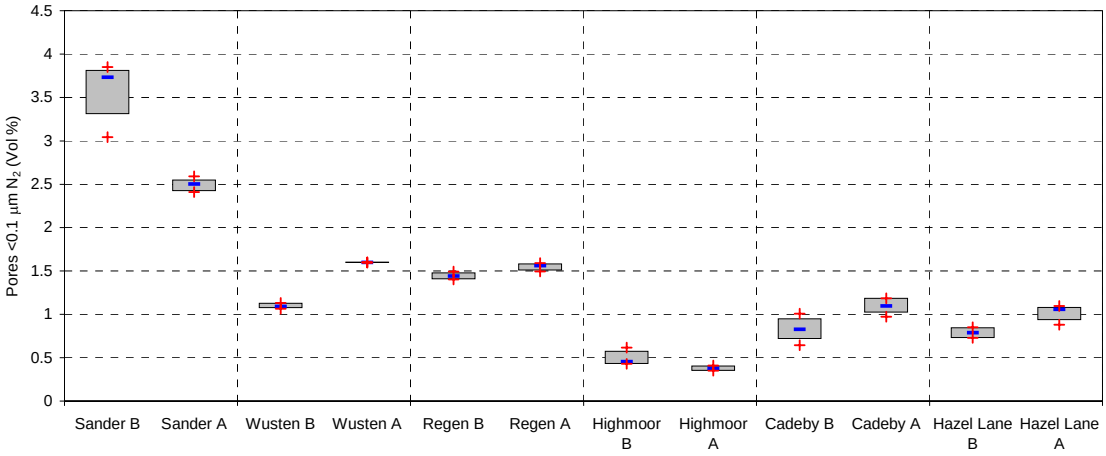

Figure 128. Comparison of the pores volume < 0.1 µm measured by N2 adsorption before (B) and after (A) F-T cycles.

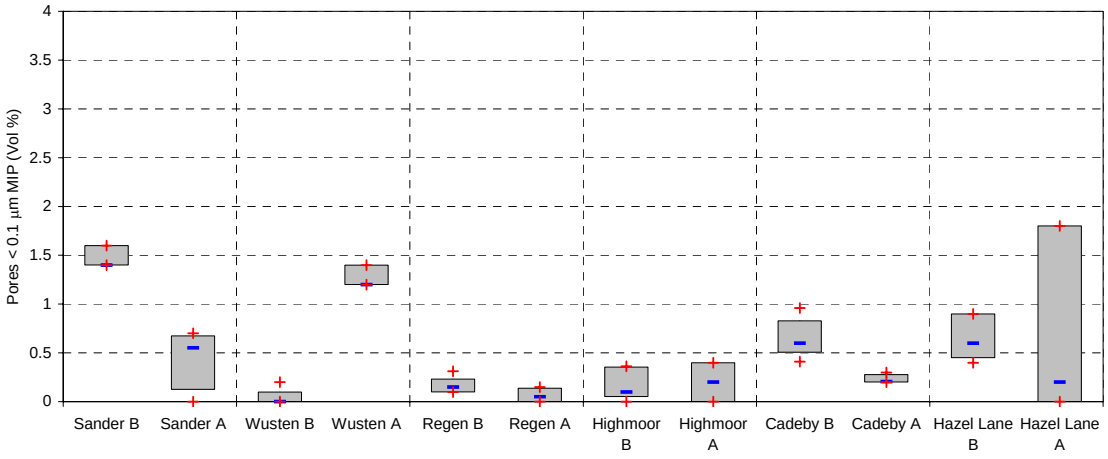

Figure 129. Comparison of the pores volume < 0.1 µm measured by MIP before (B) and after (A) F-T cycles.

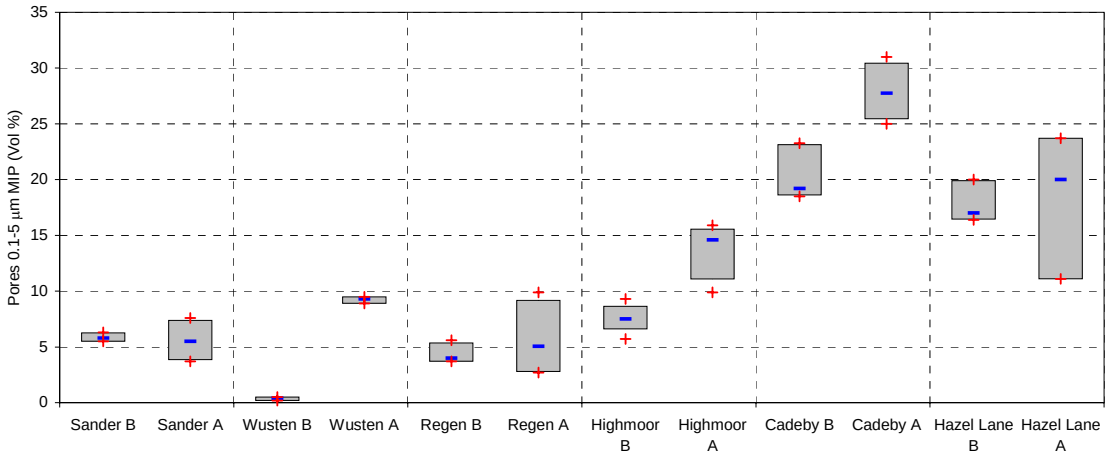

Figure 130. Comparison of the pores volume 0.1-5 µm measured by MIP before (B) and after (A) F-T cycles.

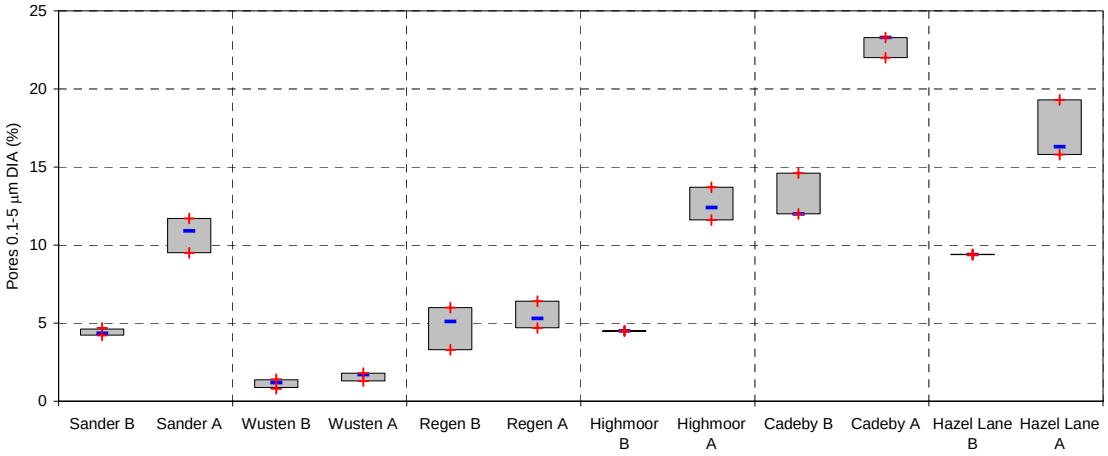

Figure 131. Comparison of the pores volume 0.1-5 µm measured by DIA before (B) and after (A) F-T cycles.

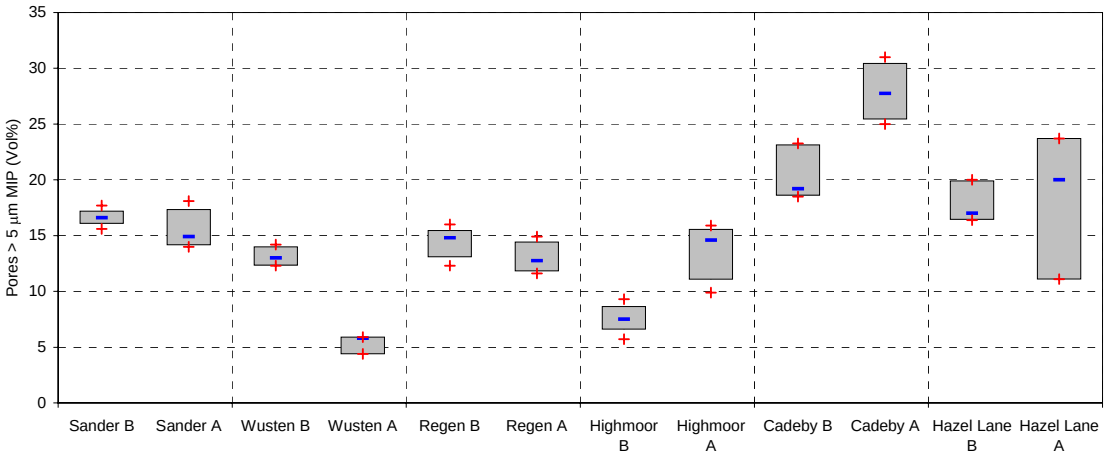

Figure 132. Comparison of the pores volume > 5 µm measured by MIP before (B) and after (A) F-T cycles.

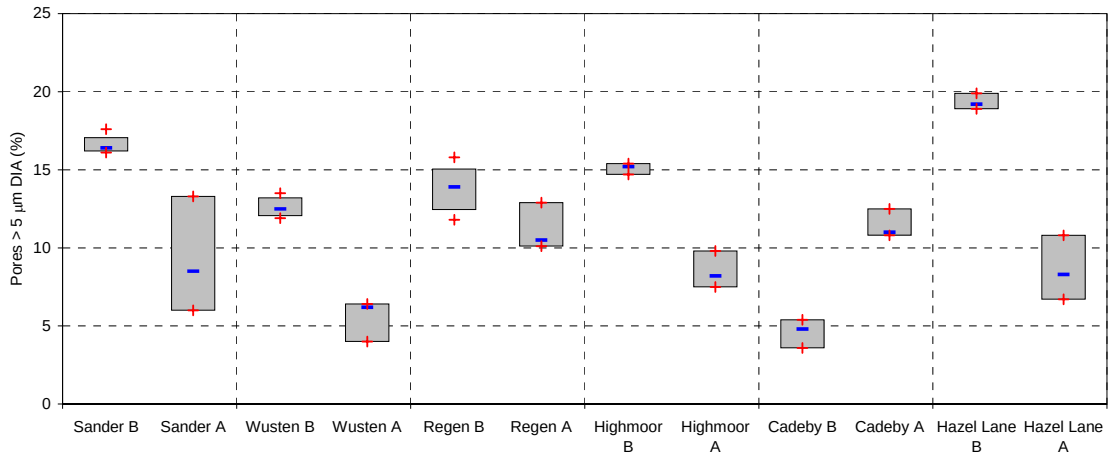

Figure 133. Comparison of the pores volume > 5 µm measured by DIA before (B) and after (A) F-T cycles.

XVIII. Annex 2: Raw results

XVIII.1. Fresh Sandstones

Label	Real Dens.(g/cm^3)	Apparent Dens. (g/cm^3)	Ql %	N_t (Vol%)	N_{48} (Vol%)	S-Coefficient	Air trapped porosity %	Gr 2 µm - 80 µm	Gr 80 µm - 400 µm	Gr 400 µm - 2000 µm	Mean Grain Diam. (µm)	Max Grain Diam. (µm)
Sander	2.7	2.2	37.8	17.4	17.9	0.7	4.0	82.0	17.9	0.0	166.0	199.0
Sander	2.7	2.1	35.6	20.0	17.9	0.7	4.1	75.0	25.0	0.0	168.0	202.0
Sander	2.6	2.1	36.9	19.3	16.8	0.8	5.2	78.0	22.0	0.0	164.0	200.0
Sander	2.6	2.1	36.5	21.9	17.8	0.8	4.0				169.0	198.0
Sander	2.6	2.0	36.9	22.0	17.8	0.8	4.2				168.0	201.0
Sander	2.6	2.1	36.9	22.0		0.8						
Sander	2.6	2.0		21.9		0.8						
Wustenzeller	2.7	2.3	45.6	13.9	10.1	0.6	3.7	14.7	39.4	45.9	175.0	272.0
Wustenzeller	2.7	2.3	44.9	12.1	10.1	0.6	3.8	13.0	45.0	42.0	178.0	300.0
Wustenzeller	2.7	2.4	44.3	11.1	10.1	0.7	4.0	15.0	40.0	45.0	179.0	323.0
Wustenzeller	2.7	2.3	45.5	13.8	10.1	0.7	3.8				180.0	315.0
Wustenzeller	2.7	2.3	44.9	13.9	10.1	0.7	3.9				174.0	295.0
Wustenzeller	2.7	2.3	44.9	14.1		0.7						
Wustenzeller	2.7	2.3	44.9	13.8		0.7						
Wustenzeller	2.7	2.3		14.0		0.7						
Regensburg	2.7	2.1	45.5	23.1	11.3	0.7	6.8	25.2	19.5	55.2	148.0	262.0
Regensburg	2.7	2.4	47.0	18.1	12.9	0.4	6.8	27.0	18.0	55.0	145.0	266.0
Regensburg	2.7	2.2	47.4	18.1	12.1	0.6	6.8	24.0	19.0	57.0	144.0	267.0
Regensburg	2.7	2.1	45.4	19.7	12.1	0.7	6.6				148.0	265.0
Regensburg	2.7	2.2	44.8	19.0	12.5	0.6	6.6				146.0	264.0
Regensburg	2.7	2.2	44.8	18.7		0.6						
Regensburg	2.7	2.2		19.1		0.7						

Table 9. Raw results of the fresh sandstones.

Results from:

Sattler L., 1992
Wolf-Dieter Grimm, 1990
Meng B., 1993

Label	MIP Porosity Vol.%	N_2 porosity % (< 0.1 µm)	Hg porosity % (< 0.1 µm)	Hg porosity % (0.1 µm - 5 µm)	Hg porosity % (> 5 µm)	DIA porosity % (> 5 µm)	DIA porosity % (0.1 µm - 5 µm)	DIA Nt %	Grain contact%	BET (m^2/g) N_2	C-value N_2	Us perpend.(km/s)	Us paral.(km/s)
Sander	23.9	3.7	1.4	6.2	17.7	17.6	4.3	21.2	36.4	4.9	67.1	2.2	2.4
Sander	24.6	3.6	1.6	5.8	16.6	16.4	4.2	23.3	31.8	4.7	67.8	2.1	2.2
Sander	23.7	3.8	1.6	6.3	16.6	16.3	4.7	20.1	33.2	4.6	67.1	2.3	2.3
Sander	18.9	3.9	1.4	5.5	16.7	16.5	4.4	22.8	34.5	4.5	66.2	2.1	2.3
Sander	20.4	3.0	1.4	5.5	15.6	16.1				4.7	66.8	2.1	2.3
Sander													
Sander													
Wustenzeller	12.5	1.1	0.0	0.2	12.3	12.2	1.4	13.3	87.8	1.1	61.4	2.3	2.8
Wustenzeller	14.2	1.1	0.2	0.5	14.2	13.5	1.1	17.6	80	1.0	68.8	2.3	2.8
Wustenzeller	13.7	1.1	0.0	0.5	13.8	12.9	0.8	12.5	75	1.1	60.7	2.3	2.7
Wustenzeller	13.2	1.1	0.0	0.4	12.4	11.9	1.3	13.5	79	1.1	57.7	2.3	2.8
Wustenzeller	14.1	1.1	0.0	0.2	13.0	12.5			85	1.0	68.8	2.3	2.8
Regensburg	19.3	1.4	0.3	4.0	14.9	14.3	3.3	20.9	35.4	6.0	63.9	2.9	2.9
Regensburg	18.7	1.4	0.2	3.7	16.0	15.8	5.1	20.3	47.2	5.9	62.4	2.9	3.0
Regensburg	19.6	1.4	0.2	3.7	14.8	13.9	6.0	15.8	45	6.2	65.0	2.8	3.0
Regensburg	17.9	1.5	0.1	5.6	13.9	13.1				5.9	63.2	2.8	2.9
Regensburg	16.0	1.5	0.1	5.1	12.3	11.8				6.1	64.7	2.5	2.8

Table 10. Raw results of the fresh sandstones.

Label	(UsS-UsD)/UsS	E-Dyn (kN/mm²)	W (kg/m²h^0.5)	B-value (cm/h^0.5)	g (g/m²/h) P1	β	t_c (h)	t_{eq} (h)	μ	Hydric dilatation (μm/m)	BFS (N/mm²)	E-Static (kN/mm²)	DRc (N)
Sander	0.1	8.9	3.5	**2.2**	264.0	1.0	48.0	1165.0	19.1	803.0	**5.2**	**4.21**	37.9
Sander	0.1	9.1	4.3	2.6	273.0	1.1	48.0	1165.0	20.5	796.0	4.4	5.2	36.7
Sander	0.1	8.6	4.3	3.0	268.0	1.0	48.0	1165.0	21.1	804.0	4.8	5.5	35.5
Sander	0.1	8.6	3.9	2.9	270.0	1.1	48.0	1165.0	20.4	799.0	3.5	3.1	36.3
Sander	0.1	9.0	3.9	2.6	262.0	1.0	48.0	1165.0	20.6		4.1	4.5	33.2
Sander			3.9	2.9							4.1	4.7	
Sander											4.1	4.7	
Wustenzeller	0.2	11.3	0.9	1.1	116.0	0.2	48.0	1165.0	33.2	458.0	**8.9**	9.5	447.0
Wustenzeller	0.2	11.3	0.9	1.1	117.0	0.2	48.0	1165.0	31.5	521.0	**8.7**	9.8	421.2
Wustenzeller	0.2	11.3	0.9	1.1	121.0	0.2	48.0	1165.0	30.9	459.0	8.7	10.5	368.1
Wustenzeller	0.2	11.5	0.8	1.1	123.0	0.2	48.0	1165.0	32.5	522.0	8.0	9.4	329.9
Wustenzeller	0.2	11.4	1.0	1.0	110.0	0.2	48.0	1165.0	34.2		8.7	10.5	477.8
Wustenzeller											8.0	9.3	
Wustenzeller											9.7	11.0	
Wustenzeller													
Regensburg	0.1	14.9	2.7	3.9	127.0	0.8	40.0	767.0	19.4	116.0	**3.1**	8	28.7
Regensburg	0.2	14.9	4.3	4.1	160.0	0.8	40.0	767.0	19.7	123.0	2.9	7.7	37.1
Regensburg	0.1	15.6	3.5	4.3	133.0	1.0	40.0	767.0	20.1	118.0	2.5	8.0	24.3
Regensburg	0.1	14.0	3.2	4.0	136.0	0.8	40.0	767.0	20.1	122.0	2.5	7.3	30.0
Regensburg	0.1	16.4	3.9	4.0	158.0	1.0	40.0	767.0	20.2		2.7	9.3	31.3
Regensburg											3.0	9.6	
Regensburg													

Table 11. Raw results of the fresh sandstones.

XVIII.2. Weathered Sandstones

Label	Real Dens.(g/cm^3)	Apparent Dens. (g/cm^3)	OI %	N_t (Vol%)	N_{48} (Vol%)	S-Coefficient	Air trapped porosity %	MIP Porosity Vol.%	N_2 porosity % (< 0.1 µm)	Hg porosity % (< 0.1 µm)	Hg porosity % (0.1 µm - 5 µm)	Hg porosity % (> 5 µm)	DIA porosity % (> 5 µm)
Sander	2.7	2.0	31.8	23.43	17.4	0.7	6.0	18.3	2.6	0.6	3.7	14.0	6.0
Sander	2.7	2.0	39.3	23.67	17.6	0.7	6.0	22.3	2.4	0.5	6.7	15.1	13.3
Sander	2.7	2.0	30.5	23.60	17.8	0.8	5.8		2.4				
Sander			25.3					23.0	2.5	0.7	7.6	14.7	8.5
Sander								22.4	2.5	0.0	4.3	18.1	
Wustenzeller	2.7	2.29	49.4	14.18	8.6	0.6	5.6	15.1	1.6	1.2	9.5	4.4	6.2
Wustenzeller	2.7	2.29	48.7	14.20	8.7	0.6	5.5	16.0	1.6	1.2	8.9	5.9	4.0
Wustenzeller	2.7	2.29	48.7	14.29	8.5	0.6	5.8	16.5	1.6	1.4	9.3	5.8	6.4
Wustenzeller	2.7	2.29	47.9	14.22	8.6	0.6	5.6		1.6				
Wustenzeller			47.9						1.6				
Regensburg	2.7	2.18	31.3	19.13	10.7	0.6	8.4	14.3	1.5	0.0	2.7	11.6	10.1
Regensburg	2.7	2.12	29.8	21.27	12.4	0.6	8.9	15.6	1.5	0.0	3.1	12.5	12.9
Regensburg	2.6	2.17	25.5	17.49	11.7	0.7	5.8	20.2	1.6	0.2	7.0	13.0	10.5
Regensburg			35.8					24.9	1.6	0.1	9.9	14.9	
Regensburg			33.9						1.6				

Table 12. Raw results of the weathered sandstones.

Label	DIA porosity % (0.1 µm - 5 µm)	DIA Nt %	BET (m^2/g) N_2	C-value N_2	Us perpend.(km/s)	Us paral.(km/s)	E-Dyn (kN/mm^2)	W (kg/m^2/h$^{0.5}$)	B-value (cm/h$^{0.5}$)	g (g/m^2/h) P1	β	BFS (N/mm^2)	E-Static (kN/mm^2)	µ
Sander	11.7	17.7	4	98.5	1.9	2.0	3.723	2.7	2.3	333.2	1.3	3.3	3.4	16.4
Sander	9.5	22.8	4.16	106.7				3.3	2.1	290.6	1.1	3.8	3.3	18.1
Sander			4.2	110.4	1.7	1.9	3.776	3.3	2.4	267.4	1.0	3.6	4.2	18.9
Sander	10.9	19.4	4.27	117	1.6	1.6	2.422	3.1	2.5					18.3
Sander			4.32	113.9										
Wustenzeller	1.7	7.9	2.6	72.6	2.5	3.1	12.863	0.7	0.9	113.4	0.1	9.6	10.9	31.7
Wustenzeller	1.3	5.3	2.5	69.7	2.5	3.0	12.96	0.7	0.9	132.3	0.1	10.2	10.3	30.3
Wustenzeller	1.8	8.2	2.5	73.2	2.5	3.0	13.225	0.4	0.8	138.9	0.2	10.1	11.5	33.1
Wustenzeller			2.58	71.5	2.5	3.0	13.176	0.6	0.9	142.2	0.2	10.8	11.3	30.7
Wustenzeller			2.54	73.3	2.5	3.0	13.562							
Regensburg	6.4	16.5	4.8	109.2	2.7	2.6	13.486	2.5	3.9	305.9	1.9	2.5	4.5	19.9
Regensburg	4.7	17.6	5.0	126.8	2.2	1.9	4.401	3.9	3.5	264.2	1.4	1.8	2.6	17.9
Regensburg	5.3	15.8	5.1	123.1	2.1	1.6	6.021	2.9	4.6	321.5	1.7	2.3	4.3	18.6
Regensburg			5.4	152.1	2.7	2.7	12	3.2	4.1					18.6
Regensburg			5.4	149.4	1.5	2.1	12.26							

Table 13. Raw results of the weathered sandstones.

XVIII.3. Fresh Magnesian Limestone

Label	Real Dens.(g/cm^3)	Apparent Dens. (g/cm^3)	QI %	N_t (Vol%)	N_{48} (Vol%)	S-Coefficient	Air trapped porosity %	MIP Porosity Vol.%	N_2 porosity % (< 0.1 µm)	Hg porosity % (< 0.1 µm)	Hg porosity % (0.1 µm - 5 µm)	Hg porosity % (> 5 µm)
Highmoor	2.9	2.1	58.1	25.9	12.2	0.5	13.7	18.3	0.5	0.4	7.5	9.3
Highmoor	2.9	2.1	56.2	26.3	12.8	0.5	13.5	17.3	0.5	0.4	7.5	9.4
Highmoor	2.9	2.2	58.1	25.4	12.6	0.5	12.8	19.3	0.4	0.1	9.3	11.5
Highmoor	2.9	2.2	58.6	21.9	11.2	0.5	10.7	19.1	0.6	0.1	8.0	11.0
Highmoor	2.9	2.2	61.7	24.4	10.8	0.4	13.6	17.3	0.4	0.0	5.7	12.3
Cadeby	2.9	2.3	55.6	21.2	19.0	0.9	2.2	25.8	1.0	0.6	23.3	3.2
Cadeby	2.9	2.3	50.9	20.2	17.4	0.9	2.9	27.1	0.8	0.6	23.0	3.9
Cadeby	2.9	2.2	48.4	22.9	21.9	1.0	0.9	27.9	0.8	0.4	19.2	8.3
Cadeby								25.3	0.9	0.7	18.7	5.9
Cadeby								23.2	0.6	1.0	18.5	4.1
Hazel Lane	2.9	2.3	65.8	18.4	15.8	0.9	2.5	22.2	0.7	0.9	19.8	1.5
Hazel Lane	2.8	2.3	64.4	17.7	15.1	0.9	2.6	20.2	0.8	0.5	16.4	3.3
Hazel Lane	2.9	2.3	67.4	18.0	15.2	0.8	2.9	19.5	0.7	0.4	17.0	2.1
Hazel Lane								18.1	0.8	0.6	16.5	1.0
Hazel Lane								22.1	0.9	0.9	20.0	1.2

Table 14. Raw results of the fresh magnesian limestone.

Label	DIA porosity % (> 5 µm)	DIA porosity % (0.1 µm - 5 µm)	DIA Nt %	BET (m^2/g) N_2	C-value N_2	Us perpend.(km/s)	Us paral.(km/s)	UsS/UsD	E-Dyn (kN/mm^2)
Highmoor	15.2	4.5	19.7	0.5	64.1	3.8	4.0	0.03	30.6
Highmoor	14.7	4.5	19.2	0.5	63.5	3.7	3.9	0.02	33.3
Highmoor	15.4	4.5	19.9	0.5	50.5	3.8	4.0	0.04	25.9
Highmoor				0.5	59.8	4.0	4.1	0.03	27.3
Highmoor				0.5	58.6	4.1	4.3	0.03	30.6
Cadeby	5.4	14.6	19.5	0.9	85.8	3.6	3.9	0.06	24.8
Cadeby	4.8	12.0	18.7	0.9	97.5	3.7	3.5	0.07	24.2
Cadeby	3.6	12.0	19.0	0.9	88.6	3.4	3.4	0.05	18.1
Cadeby				0.9	97.4			0.06	
Cadeby				0.9	95.9			0.06	
Hazel Lane				0.6	67.2	4.2	4.6	0.02	30.5
Hazel Lane	19.9	9.4	29.7	0.6	72.4	4.0	4.5	0.01	32.1
Hazel Lane	18.9	9.4	28.7	0.6	82.0	4.1	4.7	0.03	29.3
Hazel Lane	19.2	9.4	29.0	0.7	52.8	4.1	4.7	0.02	29.3
Hazel Lane				0.6	71.3			0.02	

Table 15. Raw results of the fresh magnesian limestone.

Label	W (kg/m^2/h$^{0.5}$)	B-value (cm/h$^{0.5}$)	g (g/m^2/h) P1	β	t_c (h)	t_{eq} (h)	BFS (N/mm^2)	E-Static (kN/mm^2)	μ	DRc (N)
Highmoor	2.8	3.0	205.0	0.2	23.0	280.0	8.7	24.1	45.6	348.7
Highmoor	2.8	3.1	222.0	0.2	23.0	280.0	9.7	26.1	40.5	377.5
Highmoor	2.2	3.2	200.0	0.3	23.0	280.0	10.6	23.1	36.5	430.5
Highmoor	2.2	3.6	183.0	0.2	23.0	280.0	9.0	24.0	37.0	371.5
Highmoor	1.8	3.6	169.0	0.1	23.0	280.0				301.0
Cadeby	3.9	3.8	158.0	0.2	41.0	328.0	5.9	13.9	32.5	34.6
Cadeby	4.5	3.5	188.0	0.3	41.0	328.0	5.0	13.0	33.4	25.7
Cadeby	5.0	4.2	200.0	0.3	41.0	328.0	6.1	11.0	30.9	48.4
Cadeby							5.1	11.0	30.2	55.5
Cadeby									28.2	41.0
Hazel Lane	4.1	3.5	123.0	0.2	41.0	328.0	9.7	26.4	47.3	267.2
Hazel Lane	3.7	3.8	131.0	0.2	41.0	328.0	10.1	27.2	48.7	221.8
Hazel Lane	3.7	3.9	143.0	0.2	41.0	328.0	7.9	22.0	48.7	193.4
Hazel Lane	3.7	3.9	143.0	0.2	41.0	328.0	8.0	20.0	49.4	227.4
Hazel Lane									41.0	232.8

Table 16. Raw results of the fresh magnesian limestone.

XVIII.4. Weathered magnesian limestone

Label	Real Dens.(g/cm^3)	Apparent Dens. (g/cm^3)	OI %	N_t (Vol%)	N_{48} (Vol%)	S-Coefficient	Air trapped porosity %	MIP Porosity Vol.%	N_2 porosity % (< 0.1 μm)	Hg porosity % (< 0.1 μm)	Hg porosity % (0.1 μm - 5 μm)	Hg porosity % (> 5 μm)	DIA porosity % (> 5 μm)
Highmoor	2.7	2.1	50.7	20.0	12.0	0.60	8.0	19.4	0.36	0.4	14.6	4.4	7.5
Highmoor	2.7	2.1	54.8	20.7	13.2	0.64	7.5	19.2	0.41	0.4	14.6	4.2	9.8
Highmoor	2.7	2.2	53.5	19.1	13.0	0.68	6.1	11.8	0.35	0.0	9.9	1.9	8.2
Highmoor	2.6	2.2	55.6	16.9	11.4	0.67	5.5	20.5	0.38	0.0	15.9	4.6	
Highmoor			53.4						0.40				
Cadeby	2.8	2.3	41.9	20.4	19.5	0.96	0.8	27.1	1.19	0.2	25.0	1.9	11.0
Cadeby	2.8	2.3	44.4	17.8	17.7	1.00	0.1	35.0	0.97	0.2	31.0	3.8	12.5
Cadeby	2.8	2.2	37.7	23.0	21.3	0.93	1.7	30.4	1.19	0.3	28.7	1.4	10.8
Cadeby								29.8	1.08	0.2	26.8	2.8	
Cadeby									1.10				
Hazel Lane	2.8	2.3	52.5	16.2	15.6	0.96	0.6	16.5	1.00	3.8	11.1	1.6	6.7
Hazel Lane	2.8	2.3	50.7	15.7	15.5	0.99	0.2	20.9	0.88	0.0	20.0	0.9	10.8
Hazel Lane	2.8	2.3	53.4	15.8	14.9	0.94	0.9	24.9	1.06	0.2	23.7	1.0	8.3
Hazel Lane									1.06				
Hazel Lane									1.10				

Table 17. Raw results of the weathered magnesian limestone.

Label	DIA porosity % (0.1 µm - 5 µm)	DIA Nt %	BET (m^2/g) N_2	C-value N_2	Us perpend.(km/s)	Us paral.(km/s)	E-Dyn (kN/mm^2)	W ($kg/m^2/h^{0.5}$)	B-value ($cm/h^{0.5}$)	g ($g/m^2/h$) P1	β	BFS (N/mm^2)	E-Static (kN/mm^2)	µ
Highmoor	12.4	19.9	0.52	122.03	3.7	3.5	27.6	2.35	2.06	200.5	**0.6**	11.4	21.8	37.1
Highmoor	13.7	23.5	0.53	109.77	4.0	3.8	28.5	2.2	2.03	214.3	**0.7**	13.7	30.0	43.2
Highmoor	11.6	19.8	0.51	168.34	3.7	3.7	27.5	1.28	1.73	205.4	**0.8**	11.0	34.9	37.5
Highmoor			0.49	202.9	3.9	3.9	31.0	1.84	1.74	198.4	**0.6**			35.3
Highmoor			0.52	152.84	4.0	3.7	31.4							
Cadeby	23.3	34.3	0.82	185.9	2.7	2.9	11.8	3.2	2.5	396.3	0.3	3.2	3.8	22.0
Cadeby	23.3	35.8	0.82	170.4	2.7	2.9	13.0	3.5	2.6	379.6	0.3	4.5	7.9	21.2
Cadeby	22.0	32.8	0.80	211.2	2.5	2.6	14.0	4.6	3.1	485.5	0.4	3.9	6.1	21.0
Cadeby			0.80	247.6										19.7
Cadeby			0.81	174.5										
Hazel Lane	16.3	23.0	0.76	210.4	3.4	3.7	29.0	3.0	2.8	329.3	0.3	5.0	17.0	29.0
Hazel Lane	19.3	30.1	0.76	145.8	3.2	3.5	26.6	2.9	3.3	323.2	0.3	5.5	17.7	24.4
Hazel Lane	15.8	24.1	0.69	145.8	3.5	3.7	29.7	3.1	2.7	432.2	0.4	3.1	10.0	24.9
Hazel Lane			0.67	145.8										22.9
Hazel Lane			0.75	141.5										24.5

Table 18. Raw results of the weathered magnesian limestone.

XVIII.5. Heated Proconnesian marble

Label	Real Dens.(g/cm^3)	Apparent Dens. (g/cm^3)	Ql %	N_t (Vol%)	N_{48} (Vol%)	S-Coefficient	Air trapped porosity %	Mean Grain Diam. (µm)	Max Grain Diam. (µm)	MIP Porosity Vol.%	N_2 porosity % (< 0.1 µm)
Proconnesian marble (heated)	2.7	2.7	40.5	1.7	1.5	0.9	0.2	611.0	830.0	1.4	0.1
Proconnesian marble (heated)	2.8	2.7	41.0	1.7	1.6	0.9	0.1	615.0	900.0	1.3	0.1
Proconnesian marble (heated)	2.7	2.7	40.4	1.6	1.4	0.9	0.2	609.0	1030.0	1.2	0.1
Proconnesian marble (heated)	2.8	2.7	41.0	1.7	1.6	0.9	0.1	610.0	995.0	1.3	0.1
Proconnesian marble (heated)	2.6	2.8	42.0	1.6	1.4	0.9	0.2	611.0	965.0	1.2	0.1

Table 19. Raw results of the heated Proconnesian marble.

Label	Hg porosity % (< 0.1 µm)	Hg porosity % (0.1 µm - 5 µm)	Hg porosity % (> 5 µm)	DIA porosity % (> 5 µm)	DIA porosity % (0.1 µm - 5 µm)	DIA Nt %	Grain contact%	BET (m^2/g) N_2	C-value N_2	Us perpend.(km/s)	Us paral.(km/s)
Proconnesian marble (heated)	0.0	0.6	0.8	1.0	0.9	1.9	90.0	0.09	86.8	2.1	2.6
Proconnesian marble (heated)	0.0	0.7	0.6	0.7	0.9	1.6	92	0.07	128.8	2.1	2.4
Proconnesian marble (heated)	0.0	0.4	0.8	0.6	0.9	1.5	92	0.08	136.5	2.2	2.4
Proconnesian marble (heated)	0.0	0.7	0.6	0.8	0.8	1.6	91	0.08	128.8	2.2	2.4
Proconnesian marble (heated)	0.0	0.4	0.8	1.0	0.3	1.3	90	0.07	136.5	2.2	2.4

Table 20. Raw results of the heated Proconnesian marble.

Label	UsS/UsD	E-Dyn (kN/mm^2)	W ($kg/m^2/h^{0.5}$)	B-value ($cm/h^{0.5}$)	g ($g/m^2/h$) P1	t_c (h)	t_{eq} (h)	β	BFS (N/mm^2)	E-Static (kN/mm^2)	µ	DRc (N)
Proconnesian marble (heated)	0.3	10.5	0.9	5.7	114.3	2.0	162.0	0.2	7.7	8.5	210.3	132
Proconnesian marble (heated)	0.3	11.3	0.8	5.2	112.2	2.0	162.0	0.2	7.8	8.7	227.0	138
Proconnesian marble (heated)	0.3	10.5	0.9	5.3	105.0	2.0	162.0	0.1	8.2	9.4	197.0	144
Proconnesian marble (heated)	0.3	11.3	0.8	5.2	112.2	2.0	162.0	0.2	7.8	8.7	227.0	140
Proconnesian marble (heated)	0.3	11.3	0.9	5.3	105.0	2.0	162.0	0.1	8.2	9.4	197.0	152

Table 21. Raw results of the heated Proconnesian marble.

XIX. References

Accardo G., Massa S.; Rossi-Doria P.; Sammuri, P.; Tabasso Laurenzi M, 1981, *Artificial weathering of Carrara marble: relationships between the induced variations of some physical properties*, International Symposium The Conservation of Stone II, Bologna, Vol. I, pp.243-273.

Alfes CH., 1991, *Relationship between the microstructure and fracture mechanics parameters of sandstones*, Fracture process in Concrete, Rocks and Ceramics, Ed. J.G.M. van Mier, J.G. Rots and A. Bakker, RILEM, pp.76-82.

Alfes CH., Breit W., Schiessl P., 1992, *Hardness testing for the measurement of stone degradation*, 7th International Congress on Deterioration and Conservation of Stone, Lisbon, pp. 771-780.

Alfes CH., Schiessl P., 1994, *Spannungsdehnungsverhalten, Schwinden und Kriechen von Sandsteinen*, Jahresberichte Steinzerfall – Steinkonservierung, Band 4, Verlag Ernst & Sohn, Berlin, pp. 3-18.

Andreola F., Leonelli C., Romagnoli M., 2000, *Techniques used to determine porosity*, The American Ceramic Society Bulletin, Vol. 79, No.7 pp. 49-52.

Andriani G., Walsh N., *Fabric, porosity and water permeability of calcarenites from Apulia (SE Italy) used as building and ornamental stone*, Bulletin of Engineering Geology and the Environment 62, pp. 77-84.

Aubry M.P., Lautridou J.P. 1974, *Relations entre propriétés physiques, gélivité et caractères microsturaux dans divers types de roches*, Bulletin Cent. Géomorphologie CNRS Caen, pp. 7-16.

Bell F.G., Dearman W.R., 1988, *Assessment of the durability of sandstones with illustrations from some buildings in the North of England*, Engineering Geology of Ancient Works, Monuments and Historical Sites, Rotterdam, pp. 707-716.

Bernabe Y., 1991, *Pore geometry and pressure dependence of the transport properties in sandstones*, Geophysics vol. 56., No4, pp. 436-446.

Böttger K.G., 1997, *Mörtel für die Erhaltung historischer Kalkputze: Haftmörtel, Hinterfüllmörtel und Kalkputze*, dissertation Bauhaus-Universität Weimar, pp. 57-58.

Boucher E.A., 1976, *Review porous materials: structure, properties and capillary phenomena*, Journal of materials science 11, pp. 1734-1750.

Bouineau A., 1978, *L'interet des essais non-destructifs utilises pour l'etude de la restauration des monuments et des sculptures*, Alteration et protection des monuments en pierres, RILEM, Paris, pp.1-29.

Bousquié P., 1979, *Structure et porosité de roches calcaires, relations avec perméabilité, ascension capillaire, gélivité, conduction thermique*, Dissertation Université Pierre et Marie-Curie Paris VI, 191p.

Brown C.E., 1993, *Use of principal-component, correlation, and stepwise multiple-regression analyses to investigate selected physical and hydraulic properties of carbonate-rock aquifers*, Journal of Hydrology, 147, pp.169-195. Elsevier Science Publishers.

Brunauer S., Emett P.H., Teller R., 1938, *Adsorption of gazes in multimolecular layers*, J. Amer. Chem. Soc., n.60, pp-309-318

Calleja L., Montoto M., Perez Garcia B., Suarez Del Rio L.M., Martinez Hernando A., Menendez Villar B., 1989, *An ultrasonic method to analyse the progress of weathering during cyclic salt crystallization laboratory tests*, La Conservazione dei Monumenti nel bacino del Mediterraneo, 1st International Symposium Bari, pp. 313-318.

Chan S.L., 1987, *Applications of stereological and image analytical methods for concrete testing*, in Pore structure and construction materials properties, vol.1, rilem congress, ed.Maso J.C. pp.111-118.

Chiesura G., 1985, *L'auscultation des materiaux par ultrasons sur monuments d'epoque romaine a Rome: quelques exmples d'application*, Vth International Congress on Deterioration and Conservation of Stone, Lausanne, vol1, pp.67-77.

Christaras B., Auger F., Mosse E., 1994, *Determination of the moduli of elasticity of rocks. Comparison of the ultrasonic velocity and mechanical resonance frequency methods with direct static methods*, Materials and Structures Vol.27, pp. 222-228.

Christensen P., Gudmundsson H., 1983, *Measurements of porosity in fresh and weathered sandstones by means of automatic image analysis*, Principles and applications of pore structural characterization, proceeding RILEM/CNR International Symposium Milan Italy, ed. Haynes J.M., Rossi-Doria P. pp.477-481.

Cultrone G., Sebastian E., Elert K., de la Torre M.J., Cazalla O., Rodriguez-Navarro C., 2004, *Influence of mineralogy and firing temperature on the porosity of bricks*, Journal of European Ceramic Society Vol. 24., pp. 547-564.

D'Have R., Motteu H., 1968, *Etude de la résistance au gel des matériaux de construction*, Buil. Batiment international 1, pp. 26-31.

Delesse M., 1848, Procédé mécanique pour déterminer la composition des roches, Annales des mines, quatrième série, tome XIII Paris pp.379-388.

Delgado Rodriguez J., Ferreira Pinto A., Rodriguez Costa D., 2002, *Tracing of decay profiles and evaluation of stone treatments by means of microdrilling techniques*, Journal of Cultural Heritage 3, pp.117-125.

Derski W., Izbicki R., Kisiel I., Mroz Z., 1989, Rocks and Soil Mechanics, Developments in Geotechnical Engineering Vol. 48, Elsevier, p.125.

Dessandier D., 1995*, Etude du milieu poreux et des propriétés de transfert des fluides du tuffeau blanc de Touraine, application à la durabilité des pierres en œuvre*, éd. BRGM, Orléans, doc.245. Dissertation.

Dethury H., 1828, *On the method proposed by Mr. Brard for the immediate detection of stones unable to resist the action of frost*. Annales de chimie et de physique, Paris Masson, 2ed, Vol. 38, pp. 160-192.

Dott R.H., 1964, *Wacke, graywacke, and matrix = what approach to immature sandstone classification*, Jour. Sed. Petrology, Vol.34, p. 629.

Dürrast H., Siegesmund S., 1999, *Correlation between rock fabrics and physical properties of carbonates reservoir rocks*, International Journal of Earth Science 88, pp. 392-408.

Eissa E.A., Kasi A., 1988, *Technical note, Relation between static and dynamic Young's moduli of rocks*, International journal of rocks mechanics and mining sciences & geomechanics abstracts, Vol.25, pp.479-482.

Ehrlich R., Crabtree S.J., Horkowitz K.O., Horkowitz J.P., 1991, petrography and reservoir physics I: objective classification of reservoir porosity, the American Association of Petroleum Geologists Bulletin v.75, No.10 pp. 1547-1562.

Ehrlich R., Bowers M.C., Rigger V.L., Prince C.M., 1997, *Detecting Permeability Gradients in Sandstone Complexes-Quantifying the effect of Diagenesis on fabric*, in Reservoir Quality Prediction in Sandstones and Carbonates, AAPG Memoir 69, American Association of Petroleum Geologists Oklama pp103-114

Everett D.H., 1961, *The thermodynamics of frost damage to porous solids*, Transactions of the Faraday Society 465, 57 part 8, pp.1541-1551.

Felix C., 1983, *Sandstone linear swelling due to isothermal water sorption*, Materials Science and Restoration Proceedings of the International Conference, pp. 305-310.

Fitzner B., Snethlage R., 1982, *Einfluβ der Porenadienverteilung auf das Vermitterungsverhalten ausgewählter Sandsteine*, Bautenschutz und Bausenierung 3, pp. 97-103.

Fitzner B., 1988, *Porosity properties of naturally or artificially weathered sandstones*, 6th International Congress on Deterioration and Conservation of Stone, Torun, pp. 236-245.

Fitzner B., Basten D., 1992, *Gesteinporosität – Klassifizierung, meßtechnische Erfassung und Bewertung ihrer Verwitterungsrelevanz*, Jahresberichte Steinzerfall – Steinkonservierung, Band 4, Verlag Ernst & Sohn, Berlin, pp. 19-32.

Folk R.L., 1954, *The distinction between grain size and mineral composition in sedimentary rock nomenclature*, jour. Geology, V. 62, p. 346.

Franzini M., 1984, *Degradazione del marmo per effetto di variazioni di temperatura*, Rendiconti Societa Italiana di Mineralogica e Petrologia, 39 (1) pp.47-58.

Galan E., Guerrero M.A., Vazquez F., Maert F., Zezza, 1991, *Marble weathering: relation between ultrasonic data and macroscopic observations*. The case of the Columns of the Court of the Lions at the Alhambra in Granada, 2nd. Internatinal Symposium on the Conservation of Monuments in the Mediterranean Basin, Geneva, pp.193-207.

Gebrande H., 1982, *Physikalische Eigenschaften der Gesteine*, Landolt-Bornstein Gruppe V, Band 1, Teilband b, Springer-Verlag Berlin 499pp.

Goins E., Reedy C.L., 2000, *Digital image analysis in microscopy for objects and architectural conservation*, in Objects speciality group post prints, vol.7, Philadelphia, Pennsylvania, pp.122-137.

Goudie A.S., 1999, *Experimental salt weathering of limestones in relation to rock properties*, Earth Surface Processes and Landforms 24, pp. 715-724.

Gregg S.J., Sing K.S.W., 1982, *Adsorption, Surface Area and Porosity,* second edition, Academic Press INC. p.111-193.

Grimm Wolf-Dieter, 1990, *Bildatlas Wichtiger Denkmalgesteine der Bundesrepublik Deutschland*, Arbeitsheft 50 – Bayerisches Landesamt für Denkmalpflege,

Guéguen Y., Palciauskas V., 1992, *Introduction à la physique des roches*, Hermann Ed. Paris p.89

Guerrero M.A., Vazquez M.A., Galan E., Zezza F., 1989, *The physical-mechanical properties and ultrasonic data as criteria for evaluation of calcareous stone decay*, La Conservazione dei Monumenti nel bacino del Mediterraneo, 1st International Symposium Bari, pp. 309-312.

Hart D., 1988, *the building magnesian limestones of the British Isles*, Building research Establishment report, Garston, Watford.

Haynes J.M., 1973, *Pore size analysis according to the Kelvin equation*, Material and Construction Vol.6 N.33., pp.209-213.

Hirschwald J., 1908, *Die Prüfung der natürlichen Bausteine auf ihre Wetterbeständigkeit*. Berlin: Verlag von Wilhelm Ernst and Sohn.

Hoffmann D., Niesel K., Wagner A., 1990, *Capillary rise and the subsequent evaporation process measured on colomns of porous material*, Ceramic Bulletin, Vol.69, No.3, pp.392-396.

Hoffmann D., Niesel K., Plagge R., 1996, *Relationship between pore structure and other physical-technical characteristics of stone*, Proceedings of the 8th International Congress on Detrioration and Conservation of Stone, Berlin, ed. Josef Rieder, pp.461-472.

Hoffmann D., Niedack-Nad M., Niesel K., 1996, *Evaporation as a feature of characterizing stone*, 8th International Congress on Deterioration and Conservation of Stone, Berlin, ed. Joseph Riederer, pp.453-459.

Honeyborn D.B., 1982, *The building limestones of France*, Building research establishment report, London.

Ide J.M., 1936, *Comparison of statically and dynamically determined Young's modulus of rocks*, proceedings of the National Academy of Sciences, Vol.22, pp. 81-92.

Judd W.R., Huber C., 1962, *Correlation of rocks properties by statistical methods*, International Symposium on Mining Research, Pergamon PressVol.2, pp.621-648.

Kaplan M.F., 1959, *Ultrasonic pulse velocity, dynamic modulus of elasticity, poisson's ratio and the strength of concrete made with thirteen different coarse aggregates*, reprinted from Rilem Bulletin, No.1, pp.2-15.

Kieβl, K. (1983) *Kapillarer und dampfförmiger Feuchtetransport in mehrschichtigen Bauteilen*, Rechnerische Erfassung und bauphysikalische Anwendung. Fachbereich Bauwesen, Hochschule Essen 123 S.

King M.S., 1970, *Static and dynamic elastic moduli of rocks under pressure*, Proc. 11th U.S. Symp. on Rocks Mechanics, Berkeley, pp.329-351.

King M.S, 1983, *Static and dynamic elastic properties of igneous and metamorphic rocks from the Canadian shield,* International Journal Rocks Mechanics Mineralogy science geomech., Vol.20, pp.237-241.

Köhler W., 1991, *Untersuchungen zu Verwitterungsvorgängen an Carrara-Marnor in Potsdam Sanssouci*, Berichte zu Forschung und Praxis der Denkmalpflege in Deutschland, Steinschäden - Steinkonservierung 2 Hannover, pp.50-53.

Kossev N.V., 1970, *Correlation between the physical and mechanical properties of rocks and degree of their weathering*, Proceedings of the Second Congress of the International Society for Rocks Mechanics, Beograd, pp.29-35.

Krtolica B., Crnkovié B., 1979, *Ultrasonic testing of stone quality*, 3rd International Congress on the Deterioration and Preservation of Stones, Venezia, pp. 219-225.

Kumar R., Bhattacharjee B., 2004, *Assessment of permeation quality of concrete through mercury intrusion porosimetry*, Cement and Concrete Research 34, pp. 321-328.

Larbi J.A., van Heess R.P.J., 2000, *a microscopical analytical method for characterisation of the original composition and constituents of (historical) mortars*, TNO report BT-Mk-R0081.

Lazzarini L., 1975, *Stones and marbles in Venice and their decay*, The conservation of stone I proceedings of the International Symposium Bologna, ed. R. Rossi-Manaresi, pp.169-189.

Lebart L., Morineau A., Fénelon J-P., 1979, Traitement des donnees statistiques, Dunod, pp.283-295.

Le Berre P., 1975, Méthodologie de prospection des granulats routiers a haute performance, Thèse de 3eme cycle Université de Paris VI.

Leonhardt H., Kiessl K., 1990, *Schnellbestimmung des Festigkeitsprofils verwitterter Oberflächenzonen alter Gebäude durch Bohrwiderstandsmessung*, Fraunhofer – Institut Für Bauphysik, Mitteilung 191.

Leroux L., Verges-Belmin V., Costa D., Degaldo Rodrigez J., Tiano P., Snethlage R., Singer B., Massey S., De Witte E., 2000, *Measuring the penetration depth of consolidating products : comparison of six methods*, 9th. International Congress on Deterioration and Conservation of Stone, Venice, Vol.2, pp. 361-369.

Lewin S., 1989, *The susceptibility of calcareous stones to salt decay*, in La Conservazione dei Monumenti del Bacino del Mediterraneo 1st International Symposium Bari, ed. Fulvio Grato, pp.59-63.

Mamillan M., 1972, *Connaissances actuelles pour mesurer le degre d'alteration des pierres et l'efficacite des methodes de traitement*, 1st. International Symposoium on the deterioration of building stones, La Rochelle, pp. 47-56.

Mamillan M., 1975, *Methodes d'essais physiques pour evaluer l'alteration des pierres des monuments*, The Conservation of Stone I, Bologna, Ed. Rossi-Manaresi, pp. 595-634.

McCreesh A., Ehrlich R., Crabtree S.J., 1991, *Petrography and reservoir physics II: Relating thin section porosity to capillary pressure, the association between pore types and throats size*, the American Association of Petroleum Geologists bulletin v.75, No.10 p. 1563-1578.

Meng B., 1993, *Characterization of pore structure for the interpretation of moisture transport*, in Conservation of Stone and other materials, vol.1, M.-J. Thiel Unesco Paris, pp.155-162

Mertz J.D., 1991, *Structure de porosité et propriétés de transport dans les grès,* Centre de géochimie de la surface, Strasbourg. Dissertation

Mueller, U., Hansen E. F., 2001, *Use of digital image analysis in conservation of building materials*, Proceedings of the 8th Euroseminar on Microscopy applied to buildings materials, Athens, Greece, pp.603-610)

Nicholson D.T., 2001, *Pore properties as indicators of breakdown mecanisms in experimentally weathered limestones*, Earth Surface Processes and Landforms 26, pp. 819-838.

Nieminen P., Uusinoka R., 1988, *The role of pore properties of rocks in the decay problem of building stones*, Engineering Geology of Ancient Works, Monument and Historical Sites, Maricos & Kouris eds, Rotterdam, pp. 809-813.

Niesel K., 1981*, Durability of porous building stone: importance of judgment criteria related to its structure*, the Conservation of Stone II, International Symposium, Bologna, Vol. 1, pp. 47-57.

Niesel K., 1983, *The weathering behavior of natural building stone*, Stone industries, october 1983, pp.30-31.

Pereira C.J., Rice R.W., Skalny J.P., 1988, *Pore structure and its relation to properties of materials*, in Pore structure and permeability of cementitious materials, Materials research society symposium proceedings by Roberts L.R., Skalny J.P., Vol.137, pp. 2-21.

Quesser A., Platen H.V., Fürst M., 1985, *Rebound and ultrasonic investigations on freestones of Bamberg area, F.R. Germany*, Vth International Congress on Deterioration and Conservation of Stone, Lausanne, Vol.1 pp.79-86.

RILEM 25-PEM, 1980, *Recommended tests to measure the deterioration of stone and to assess the effectiveness of treatment methods*, Bordas-Dunod.

Rondelet J., 1734-1829, Traité théorique et pratique de l'art de bâtir, Paris enclos du Pantheon, Tome 3 livre 5, pp. 75-103.

Rossi-Manaresi R., Tucci A., 1990, *Pore structure and the disruptive or cementing effect of salt crystallization in various types of stone*, Studies in Conservation 36, pp. 53-58.

Santamarinya J.C., Klein K.A., Wang Y.H., and Prencke E., 2002, *Specific surface: determination and relevance*, Can. Geotech. J., 39, 233-241.

Sattler L., 1992, *Untersuchungen zu Wirkung und Dauerhaftigkeit von Sandsteinfestigungen mit Kieselsäureester*, PhD dissertation, Bayerisches Landesamt für Denkmalpflege, München,

Sayed Ahmed M.I., Fayed L., Ibrahim H., 1999, *Geotechnical properties of some limestones of the Nile Valley*, Egypt, Kuwait J. Sci. Eng., 26 (1), pp.181-195.

Scheidegger A.E., 1960, *The physics of flow through porous media*, The Macmillan company, New-York, pp.17-30.

Shepherd R.G., Brice D.A., 1985, *Correlation of permeability and structure of modern and ancient point bars*, report unpublished, pp.5-10.

Schuh H., 1987, *Physikalische Eigenschaften von Sandsteinen und ihren verwitterten Oberflächen*, Münchner Geowissenschaftliche Abhandlungen, München, p.19.

Siegesmund S., Weiss T., Tschegg E.K., 2000, *Control of marble weathering by thermal expansion and rocks fabrics*, 9th nternational Congress on deterioration and conservation of stone, Venice, Vol. 1, pp. 205-213.

Simon S., Snethlage R., 1996, *Marble weathering in Europe – results of the Eurocar-Euromarble exposure programme 1992-1994*, 8th international Congress on Deterioration and Conservation of Stone, Berlin, pp.159-166.

Simon S., 2001, *Zur verwitterung und Konservierung Kristallinen Marmors, Untersuchungen zu physiko-mechanischen Gesteinskennwerten, zur Oberflächenchemie von Calcit und zur Anpassung und Überprüfung von Gesteinsschutzmitteln*, Dissertation, Ludwig-Maximilians-Universitat, Munchen, 256p.

Smorodinov M.I., Motovilov E.A., Volkov V.A., 1970, *Determinations of correlation relationships between strength and some physical characteristics of rocks*, Proceedings of the Second Congress of the International Society for Rock Mechanics, Beograd, 3-6 pp.35-37

Snethlage R., 1983, *Steinkonservierung mit einem beitrag von Hannelore Marschner*, Bayerisches Landesamt für Denkmalpflege, München, Arbeitsheft 22, pp.40-45.

Snethlage R., Wendler E., 1997, *Moisture Cycles and Sandstone Degradation*, Saving our Architectural Heritage: the Conservation of Historic Stone Structures, Ed. N.S. Baer and R. Snethlage, pp. 7-24.

Sparks D.S., 1986, *Soil physical chemistry*, CRC Press, p.41.

Tassios T.P., Mamillan M., 1985, *Valutazione structurale dei monumenti antichi*, Presentazione di Carlo Cestelli Guidi, Ed. Kappa, pp.15-30.

Thomachot C., Jeannette D., 2002, *Evolution of the petrophysical properties of two types of Alsatian sandstone subjected to simulated freeze-thaw conditions*, Siegesmund S., Weiss T., Vollbrecht A., Natural Stone, Weathering Phenomena, Conservation Strategies and Case Studies, Geological Society London, 205, pp. 19.32.

Tiano P. Filareto C., Ponticelli S., Ferrari M., Valentini E., 2000, *The conservation of monuments: A new method to evaluate consolidating treatments*, Int. journal for Restoration of Buildings and Monuments, vol. 6, No.2, pp.133-150.

Topal T., 2000, Freeze-thaw resistance of the Yazilikaya tuffs, 9th International Congress on Deterioration and Conservation of Stone, Venice, Vol.1, pp. 144-151.

Tourenq C., Fourmaintraux D., Denis A., 1971, Propagation des ondes et discontinuites des roches, Proceedings of the international Symposium on rocks mechanics, Nancy, France, I-1.

Valdeon L., Esbert R.m., Grossi C.M., 1992, *Hydric properties of some spanish building stones: a petrophysical interpretation*, Material issues in art and archeology III, Material Research Society Proc. Vol. 267, pp. 911-916.

Walsh J.B., Brace W., 1966, *Cracks and pores in rocks*, Proceedings of the first Congress of the International Society of Rocks Mechanics, pp643-646.

Wardlaw N.C., Cassan J.P., 1979, Oil recovery efficency and the rock-pore properties of some sandstone reservoirs, Bull. Can. Petr. Geol. 27, pp.117-138.

Williams H.F., Turner F.J., Gilbert C.M., 1982, Petrography, an introduction to the study of rocks in thin section, 2nd ed., Freeman and co, San Francisco, p. 327.

Wittmann F.H., Prim P., 1983, *Mesures de l'effet consolidant d'un produit de traitement*, Matériaux et Construction Vol.16 N.96 pp.235-242

Zeisig A., Siegesmund S., Weiss T., 2002, *Thermal expansion and its control on the durability of marble*, Natural Stone, Weathering Phenomena, Conservation Strategies and Case Studies, Geological Society, London, No. 205, pp.65-80.

Ann BOURGES
133, Avenue des Freres Lumiere
69008 LYON.
Tél. :33.(0)4.78.01.48.24
e-mail : ann.bourges@insa-lyon.fr

Born 26.01.1976 in Bordeaux
Single

EDUCATION

Currently
Since 2003

Ph.D. in mineralogy, laboratory of mineralogy, petrology and geochimistry - University Ludwig Maximilian-Münich (Germany), performed at the building material lab - Getty Conservation Institute-Los Angeles (USA).

↳ supervisor : Pr. Dr. Rolf Snethlage and Pr. Dr. Karl Thomas Fehr

Subject: Holistic correlation of chemical, physical and mechanical properties of selected natural stones for assessing durability and weathering in the natural environment.

2001-2002

Master DEA "Archeomaterials", laboratory CRPAA (Research Center of Applied Physics in Archeology), University Bordeaux III, Bordeaux.

↳ study performed at LRMH (Laboratory of Reaserch of Historical Monument) – Champs sur Marne. Magna cum laude.

2000-2002

Master DPEA Earthen Architecture, CRATerre, Grenoble (Special Degree of Architecture School)

↳ study performed at LRMH

1999-2000

Master DESS Physics in Archeology and museography, laboratory CRPAA, University Bordeaux III, Bordeaux

PROFESSIONAL BACKGROUND

Currently

INSA Lyon, laboratory GEMPPM (Study Group of Metals and Materials Physics)
Attache of research and teaching : charged to develop science for heritage conservation within materials ingineering laboratory.

2002-2005
3 years

Getty Conservation Institute, Building Materials section, **Los Angeles**
Research Lab Associate

↳ Project Manager "Magnesian Limestone" on decay of English magnesian limestone in collaboration with English Heritage. Budget and Scientific management.

↳ Development of a method for digital image analysis on porous materials.

↳ Ph.D topic :

- Statistical analysis of different lithotypes (sandstones, limetone and marble), in order to emphasize and link the mecanical properties (biaxiale flexural strength, modulus of elasticity static and dynamic, …) and the physical properties (water transport, evaporation kinetics, water vapor permeability, …) with the microstrure and the texture (poro Hg, water saturation, BET and digital image analysis in optical and environemental microscopy (ESEM Philips XL30-FEG) ;
- Development of non-destructives methods (ultrasound velocity, drilling resistance) in order to assess the physical-mechanical behavior of porous materials.

- Artificial weathering cycles (freeze-thaw) in order to assess and link the evolution of physical, mechanical behavior and the microstrucre of porous materials. The aim is to understand and anticipate decay of porous materials.

↳ Terra Project: Study of physical and mechanical properties of artificial adobe.

- Determination of the influence of water, liquid and vapor, on earthen material. Study of tranport properties, mechanical properties (swelling and shrinkage, uniaxial compressive strength and partial area compressive strength) and texture properties (influence of the particule size distribution).

2000-2002
9 months

LRMH, **Champ sur Marne**

Stone section

↳ Study of stabilized earthen plasters with bitumen and decorated surfaces of the Navrongo cathedral (2 months in the field).

- Different concentation of soft bitumen into a earthen material with a defined granolometry. Study of the hydrophobic and mechanical properties of these plasters ;
- Analysis of materials compatibility (swelling and shrinkage of clay minerals) ;
- Microstrural study of aggegates coating by the bitumen wrap ;
- Method to extract clay minerals for X-Ray Diffraction.

Metal and wood section

↳ Materials characterization of an altarpiece in the Luçon cathedral (XIX°s.). Compatibility tests of biocide products on these materials. «Oddy test» under controlled atmosphere.

Decorated surfaces section

Pigments, binders, and decay characterization of decorated surfaces in altar Saint-Jean - Toulouse (XIII°s.).

1999
4 months

UNESCO, Cultural Heritage, **Paris**

Arabic states section

↳ Collaboration on safeguard project of ancient towns and manuscripts in Mauritania.

1998-1999
10 months

CRPAA, **Bordeaux**

↳ Comparative study of ancient techniques of hydrophobic mortar and plasters applied in water tanks of the antique Laurium (Greece) and medieval tank of Sabra Al-Mansouryia (Tunisia).

- Analysis of motars and plasters in chalk by cathodoluminescence, thermal analysis, X-Ray diffraction, scanning microscopy. Study on pouzzolanique effect.

↳ Study of the texture, composition and pigments of decorated surfaces. Iconographic et technical study on the Huaca de la Luna site, valley Moche, Trujillo, Peru (2 months in the field).

OTHER COMPETENCE

Languages : English fluent
Spanish solid knowledge
Others : Travelling (America, Africa)
Sports : Natation, jogging

COMMUNICATIONS AND PUBLICATIONS

Paper in journal

Bourgès A., Joffroy T., Taxil G., 2002, *Les Surfaces décorées de la cathédrale de Navrongo "Our Lady of seven sorrows" au nord du Ghana*, in Coré n°12, pp. 43-50.

Publications after international conferences (selection committee and lecture committee)

Stefan Simon, Ann Bourgès, Mai 2005, *Correlation between composition and physico-mechanical properties of adobe*. Architecture, construction and conservation of earthen building in seismic areas, Lima, Peru, come out.

Ann Bourgès, Septembre 2004, *Conservation of Our Lady of the Seven Sorrows Cathedral And Safeguard of the decoration tradition of the Nankani women.* Colloquium Conservation of Decorated Surfaces on Earthen Architecture, 6 pages.

Ann Bourgès, Stefan Simon, Urs Mueller, Novembre 2003, *The interaction of earthen materials with water in vapor and liquid phase and influences on their weathering behaviour***.** 9th Conference on the Study and Conservation of Earthen Architecture, Yazd, Iran, 8 pages.

Ann Bourgès, Novembre 2003, *Research on earthen plaster stabilized with bitumen and polychrome decoration – Navrongo cathedral – North Ghana*. 9th Conference on the Study and Conservation of Earthen Architecture, Yazd, Iran, 10 pages.

Nowik W., Bourgès A., 2003, *Analyse du vernis des enduits peints de la cathédrale de Navrongo (Ghana)*. Colloque du GMPCA.